Next Generation Hybrid Optical & Wireless Systems for Converged Access Networking

Devika Dass

B.Tech, M.Tech

A dissertation submitted in fulfillment of the requirements

for the award of Doctor of Philosophy (Ph.D.)

to the

School of Electronic Engineering,

Dublin City University

Supervisors:

Dr. Colm Browning

Prof. Liam Barry

December 2023

Declaration

I hereby certify that this material, which I now submit for assessment on the program of study leading to the award of Doctor of Philosophy is entirely my own work, and that I have exercised reasonable care to ensure that the work is original, and does not to the best of my knowledge breach any law of copyright, and has not been taken from the work of others save and to the extent that such work has been cited and acknowledged within the text of my work.

Signed: 

ID No.: **19213004**

Date: **21 July 2023**

Dedicated to my grandparents, Mumma, Papa and Vasu.

Acknowledgement

First and foremost, I would like to thank my school teachers for helping me understand complex concepts so easily. Their knowledge and guidance have been invaluable to me. I would also like to thank my supervisors in the postgraduate program, Dr. Sumit Kumar Mishra and Prof. Kannadassan Dhanaraj, for their guidance and motivation to pursue a Ph.D.

I take this opportunity to thank my Ph.D. project supervisor, Dr. Colm Browning, for believing in my abilities and giving me the opportunity to carry out research at DCU. Without his excellent guidance, I wouldn't have accomplished this much in my career. I would also like to humbly thank my second supervisor, Prof. Liam Barry, for his support and guidance during my Ph.D. and for always ensuring that our lab has the best equipment.

Many thanks to the staff at DCU, Mr. Robert Clare and Mr. Conor Murphy, for their invaluable assistance in the lab. I would also like to express my gratitude to Dr. Aleksandra Kaszubowska-Anandarajah and Dr. Prince Anandarajah for their love and support, especially when I was new in the country. Additionally, I would like to thank my aunts, Ms. Ishita, Ms. Neelam and Ms. Inderjeet, for making me feel at home in Dublin.

I am very grateful to all my lab fellows for having fruitful discussions with me: Sean, Eamonn, Yi, Gaurav, Lakshmi, Prajwal, Mohab, Amol, Alison, Michael, Ankit, Marcos, Leidy, Rangana, Ahmed, Mahrokh and Muyiwa. They always make the lab a happy place to work in. I would not have enjoyed Dublin as much without the company of my good pals Amrutha, Greta, Brian, Anais, Jorge, Dovy, Carolyn, Romina, Shumailla, Margaret, Lorna, Mahshid and Chloé. Life was so much fun and easier when I spent time with these people.

I would also like to thank my homies Swati, Radhika, Anjali, Mehreen, Harsh, Shaivi,

Nitin and Varun for looking after me and supporting me from miles away. I am very lucky to have met Gaurav during my Ph.D., as he is the reason why I finished my thesis. My heartfelt thanks to him for always taking care of me, cracking the funniest jokes and supporting me through all of my mental breakdowns!

The important role my family has played in encouraging, motivating and supporting me is immeasurable, especially my grandparents and my cousins. I have doubted my potential many times, but this kindest person never stops praising me as if I were a superhero. Thanks to my lovely sibling, Vibhriti (aka Vasu), for always being my cheerleader and believing in me. And finally, I would like to thank my parents, Mr. Rohit Dass and Advocate Rashmi Sood, for giving me a life full of love and affection. They have made many sacrifices to ensure I receive the best education and have a healthy life. Without them, I would have never realized my dreams and for this, I am forever indebted to them.

List of Publications

Journal Publications

1. **Devika Dass**, L.Y. Dai, K. Bergman, X. Ouyang, P. Townsend, C. Roeloffzen and C. Browning, "Low Noise Ultra-Flexible SiP Switching Platform for mmWave OCDM & Multi-band OFDM ARoF Fronthaul," IEEE Photonics Technology Letters, 2023.

2. **Devika Dass**, A. Delmade, L. Barry, C. G. Roeloffzen, D. Geuzebroek, and C. Browning, "Wavelength & mm-Wave Flexible Converged Optical Fronthaul With a Low Noise Si-Based Integrated Dual Laser Source," Journal of Lightwave Technology, vol. 40, no. 10, pp. 3307-3315, 2022.

3. **Devika Dass**, M.T. Costas, L.P. Barry, S. O'Duill, C.G. Roeloffzen, D. Geuzebroek, G. Carpintero, R.C. Guzman and C. Browning, "28 GBd PAM-8 transmission over a 100 nm range using an InP-Si_3N_4 based integrated dual tunable laser module," Optics Express, vol. 29, no. 11, pp. 16563-16571, 2021.

4. **Devika Dass**, S. O'Duill, A. Delmade, and C. Browning, "Analysis of phase noise in a hybrid photonic/millimetre-wave system for single and multi-carrier radio applications," Applied Sciences, vol. 10, no. 17, p. 5800, 2020.

5. L. N. Venkatasubramani, **Devika Dass**, C. Browning, C. G. Roeloffzen, D. Geuzebroek, and L. Barry, "Bandwidth Re-configurable Wideband QAM-OFDM with Hybrid Integrated InP-Si_3N_4 Tunable Laser Source for Short-reach Systems," Journal of Lightwave Technology, 2023.

6. C. Browning, **Devika Dass**, P. Townsend, and X. Ouyang, "Orthogonal Chirp-division Multiplexing for Future Converged Optical/Millimeter-wave Radio Access Networks," IEEE Access, vol. 10, pp. 3571-3579, 2021.

7. M. Troncoso-Costas, **Devika Dass**, C. Browning, F. J. Diaz-Otero, C. G. Roeloffzen, and L. P. Barry, "Intra-Data Centre Flexible PAM Transmission System Using an Integrated Si_3N_4 Dual Laser Module," IEEE Photonics Journal, vol. 14, no. 1, pp. 1-6, 2021.

8. A. Delmade, L. P. Barry, **Devika Dass**, and C. Browning, "Multi-frequency 5G NR millimeter-wave signal generation over analog RoF link using optical frequency combs," Optics Communications, p. 129681, 2023.

9. L. Gonzalez-Guerrero, R. Guzman, M. Ali, A. Zarzuelo, J.C. Cuello, **Devika Dass**, C. Browning, L. Barry, I. Visscher and R. Grootjans, "Injection Locking Properties of a Dual Laser Source for mm-Wave Communications," Journal of Lightwave Technology, vol. 40, no. 20, pp. 6685-6692, 2022.

Conference Publications

1. **Devika Dass**, L. N. Venkatasubramani, L. Barry, C. G. Roeloffzen and C. Browning, "SiP based Hybrid Digital and Analog RoF mmWave 5G Transmission for Converged Optical Access Networks," in (CLEO) Conference on Lasers and Electro-Optics, 2023: IEEE. [Soon to be published online]

2. **Devika Dass**, A. Delmade, L. Barry, C. G. Roeloffzen, D. Geuzebroek, and C. Browning, "Flexible Optical and Millimeter-wave Analog-RoF transmission with a Silicon-based Integrated Dual Laser Module," in 2021 European Conference on Optical Communication (ECOC), 2021: IEEE, pp. 1-4.

3. **Devika Dass**, A. Delmade, L. Barry, C. G. Roeloffzen, D. Geuzebroek, and C. Browning, "Flexible V-band mmWave Analog-RoF transmission of 5G and WiGig signals using an InP-SiN Integrated Laser Module," in 2021 International Topical Meeting on Microwave Photonics (MWP), 2021: IEEE, pp. 1-4.

4. L. N. Venkatasubramani, **Devika Dass**, A. Delmade, C. G. Roeloffzen, D. Geuzebroek, and L. Barry, "Wideband QAM-OFDM with Hybrid Integrated InP-Si_3N_4 Tunable Laser Source for Short-Reach Systems," in European Conference and Exhibition on Optical Communication, 2022: Optica Publishing Group, p. Th2D. 4.

5. C. Browning and **Devika Dass**, "Flexible converged photonic and radio systems: A Pathway toward next generation wireless connectivity," in Photonic Networks and Devices, 2021: Optica Publishing Group, p. NeM4B. 2.

6. L. P. Barry, A. Delmade, **Devika Dass**, and C. Browning, "Role of Analogue Radio-over-Fibre technology beyond 5G," in Optical Fiber Communication Conference, 2022: Optica Publishing Group, p. Th1I. 1.

7. C. Browning, X. Ouyang, **Devika Dass**, G. Talli, and P. Townsend, "Orthogonal chirp-division multiplexing for performance enhanced optical/millimeter-wave 5G/6G communications," in 2021 Optical Fiber Communications Conference and Exhibition (OFC), 2021: IEEE, pp. 1-3.

8. L. Gonzalez-Guerrero, R. Guzman, M. Ali, J.C. Cuello, **Devika Dass**, C. Browning, L. Barry, I. Visscher, R. Grootjans and C.G. Roeloffzen, "InP-Si_3N_4 Hybrid Integrated Optical Source for High-purity Mm-wave Communications," in Optical Fiber Communication Conference, 2022: Optica Publishing Group, p. W3D. 7.

Contents

List of Figures

List of Tables

List of Acronyms

5G NR 5G New Radio

ARoF Analog Radio over Fiber

AWG Arbitrary Waveform Generator

BBU Baseband Unit

BER Bit Error Rate

CAGR Compound Annual Growth Rate

CO Central Office

C-RAN Centralized/Cloud Radio Access Network

CU Central Unit

DD Direct Detection

DD-LMS Decision-Directed Least Mean Square

DCN Datacanter Network

DCI Datacenter Interconnects

DFB Distributed-feedback Laser

DLM Dual Laser Module

D-RAN Distributed Radio Access Network

DRoF Digital Radio over Fiber

DSP Digital Signal Processing

DSB Double Sideband

DU Distributed Unit

EDFA Erbium-Doped Fiber Amplifier

EVM Error Vector Magnitude

FEC Forward Error Correction

FSR Free Spectral Range

FTTx Fiber to the x

IM Intensity Modulation

ISI Inter Symbol Interference

ISP Interney Service Provider

IT Information Technology

MRR Micro-ring Resonator

MZM Mach-Zender Modulator

mmWave millimeter wave

OCDM Orthogonal Chirp Division Multiplexing

OFDM Orthogonal Frequency Division Multiplexing

ONU Optical Network Unit

O-RAN Open Radio Access Network

OLT Optical Line Terminal

PAM Pulse Amplitude Modulation

PD Photodetector

PIC Photonic Integrated Circuit

PON Pasive Optical Network

RAN Radio Access Network

RF Radio Frequency

RIN Relative Intensity Noise

RoF Radio over Fiber

ROP Received Optical Power

RTO Real Time Oscilloscope

RU Radio Unit

SiP Silicon Photonics

SSB Single Sideband

SSMF standard Single Mode Fiber

TIA Trans-impedance Amplifier

VCSEL Verticle Cavity Surface Emitting Laser

VOA Variable Optical Attenuator

vRAN Virtual Radio Access Network

WAN Wireless Area Network

Wi-Fi Wireless Fidelity

WLAN Wired Local Area Network

WDM Wavelength division multiplexing

Next Generation Hybrid Optical & Wireless Systems for Converged Access Networking

– Devika Dass

Abstract

The rise in the number of internet connections, be it humans or machines, has led to demand for higher capacity and datarates on an individual level. This is further enhanced by the introduction of data-hungry applications that include augmented reality (AR), virtual reality (VR), artificial intelligence (AI), the Internet of Things (IoT), telemedicine and many more. With the ongoing increase in capacity demands from fixed-line and wireless networks, there is a drive to converge the vast bandwidth provided by optical access networks with the mobility provided by the wireless access networks to enable a range of multi-gigabit services to the end-users. Particular focus is paid to communication technologies, such as optical heterodyning and analog-radio-over fiber (ARoF), that support optical-wireless integration in a spectrally efficient and cost effective manner. Moreover, components and technologies in support of converged networks are deployed to enable high-capacity advanced modulation schemes and the use of very high frequency radio-frequency (RF) carriers. The photonic integrated circuits (PIC) will play a key role in the development of economic links as many transmitters and modulators can be integrated on a single chip.

In this work I present a novel, integrable, ultra-flexible and low noise optical source that can be employed to provide millimeter wave (mmWave) frequency transmission systems for high throughput applications in combination with advanced detection techniques. The wavelength flexibility feature of this optical source permits the best use of available fiber in a reconfigurable network environment while the ability to vary the RF carrier frequencies can allow different RF standards to be used, enabling future network upgrades to higher carrier frequencies in the THz range. This work also demonstrates a true optical-wireless multi-service convergence by pairing the ultra flexible silicon photonics (SiP) based sources with an optical switch fabric; enabling the dynamic provisioning of broadband, RoF and mmWave signals solely in the optical domain. Finally, for datacenter interconnects, the utilization of low noise optical transmitters to handle multi-level signaling, like PAM-N formats, is vital. The low noise optical source is deployed to provide high bandwidth intra-datacenter interconnect capability. Through these system demonstrations, this work highlights a platform to facilitate the flexible transmission of various service types throughout a fully converged optical network.

Introduction

The pre-existing and evolving data networks in today's world have assisted people in several ways through the COVID-19 pandemic, leading to a further rise in the demand for internet and cloud services. internet service providers (ISPs), information technology (IT), infrastructure providers and datacenters have seen this surge in demand primarily as a result of the shift towards home and remote working [1]. Apart from interconnectivity, cloud computing and storage have played an essential role in tracking and storing data of COVID-19 patients and the vaccination process. Datacenters have enabled digital commerce and online meetings, making digital infrastructure more important than ever before [2].

According to [3], at a 6 percent compound annual growth rate (CAGR), by 2023 the total number of internet subscribers is projected to grow to 66 percent of the global population as depicted in Fig. 1. The global devices and connections are growing at a CAGR of 10 percent, including both fixed and mobile devices. These trends induce demand for high capacity and bandwidths from both fixed-line and wireless data networks. Furthermore, demand for multi-gigabit services is inevitable in the near future, impelling many access network operators to look beyond download speeds towards improving upstream capacity [4] and presenting more symmetrical communication systems.

The increasing reliance on data networks underscores the significance of optical networks, and so far the optical backbone networks, i.e. core and metro networks, have played a critical role in meeting these demands. However, the growing demand for highly data-hungry applications depends on seamless integration of fixed-line and wireless networks. With the projected rise in the global machine-to-machine (M2M) connections, devices and internet users in the coming years, as evident from the IP traffic growth trends shown in Fig. 1, it becomes imperative to explore technologies to enhance the data carry-

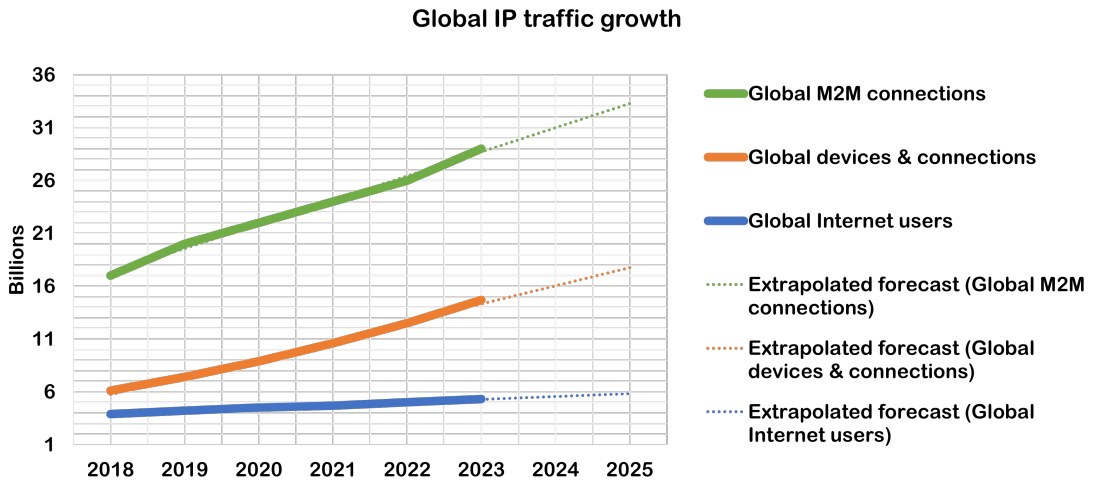

Fig. 1: The global IP traffic growth trends extracted from annual internet report [3] with linear extrapolation of growth trends for the years 2024 and 2025.

ing capacity of single fibers instead of simply resorting to the parallel fiber transmissions. This research area is of great interest as it enables the maximization of capacity on a single fiber while avoiding additional expenses and network space utilization. Additionally, it proves to be economically favorable for network operators, as it eliminates the need for deploying additional fibers and network components for scaling purposes.

Scaling the capacity of the access network can be achieved by deploying the latest technologies like switching to higher frequency ranges in wireless networks and high-order modulation formats in both fixed-line and wireless networks [5, 6, 7]. Also, the centralization of RANs in combination with Analog Radio over Fiber (ARoF) technology has recently been demonstrated to enhance access network performance [8, 9]. By embracing these advancements, the access network can support the increasing demands for data transmission and enable seamless integration of fixed-line and wireless access networks.

Utilizing optical heterodyning techniques for the generation of higher frequency ranges such as millimeter-wave (mmWave) and terahertz (THz) frequencies allows for the successful integration of fixed-line and wireless access networks. Furthermore, it can provide a cost-effective alternative to employing expensive high-bandwidth electrical components. It can facilitate seamless frequency switching between different wireless networks, ranging from 4G to 6G, thereby enhancing backward compatibility and enabling the coexistence of multiple networks forming a multi-service environment. Additionally, in

this multi-service environment, employing reconfigurable optical sources, switches and routers in combination with wavelength division multiplexing (WDM) technology can ensure efficient resource utilization and enables the network to cater to diverse service requirements [10, 11, 12, 13].

With the deployment of higher-order modulation formats, the ever-increasing demand for higher datarates can be sustained in fixed-line networks, such as datacenters, passive optical networks (PON) and Ethernet. On the other hand, the ARoF technology has drawn the attention of researchers to simplify and reduce the cost of equipment at the antenna site, which is expected to witness a massive rise in connections and antennas in the future wireless networks (as seen in Fig. 1). Thus, by utilizing these technologies, the access network can effectively meet the growing needs of data-intensive applications and services.

To support these advancements, fully integrable transceivers built with highly mass-producible, cost-effective materials are required. These transceivers should also have a smaller footprint compared to those made of III-V-based compounds. The concept of "Siliconize" photonics, which leverages widely available silicon materials, enables the production of inexpensive photonic devices on a large scale. This approach opens up possibilities for optical and electronic integration, leading to the development of smaller-sized devices.

Main Contributions

The main contributions of this thesis are:

⇒ *Optical-Wireless Convergence* – A novel hybrid integrated dual laser module (DLM) is characterized for the first time for its employment in ARoF transmission systems. Furthermore, the DLM is shown to provide a highly reconfigurable silicon photonics (SiP) platform for the development of integrated transceivers for 5G/6G mmWave applications. Wide tunability afforded by the integrated DLM in combination with advanced system design is a highly promising approach enabling photonic mmWave networking over an optical access infrastructure. This holds particular relevance for future converged optical networks exploiting flexibility in

the wavelength and frequency domain.

⇒ *Intra-Datacenter Transmission* – The low noise feature of the DLM is leveraged for transmitting a spectrally efficient high-order multi-level signal over a short-reach intra-datacenter link. The potential for mass production of the photonic integrated circuit (PIC) based design approach, the compatibility with surrounding electronic/optical silicon technologies and the facilitation of spectrally efficient intensity modulation/ direct detection (IM/DD) transmission, point toward the ability of the presented DLM to be a key component in a wider cost-efficient and scalable DWDM solution for future datacenter networks.

⇒ *SiP Platform for Reconfigurable Transceivers* – A mmWave ARoF fronthaul transmission of an emerging 6G waveform over a highly flexible SiP based wavelength and space switch fabric is demonstrated for the first time. This system highlights the potential of fully integrated SiP systems to be harnessed in support of the development of truly converged and flexible future access networks.

⇒ *Multi-service Environment* – The SiP platform is utilized for transmission of multiplexed waveforms that are compatible with cutting-edge technologies like PON, Wi-Fi and beyond 5G forming a multi-service optical access environment. Therefore, the concept of a truly converged optical access network scenario with the future coexistence of next-generation PON and 6G networks is portrayed for the fiber-to-the-room/fiber-to-the-building (FTTR/FTTB) scenario.

Thesis Structure

The thesis is organized as follows:

Chapter 1 explores various network architectures and emphasizes the importance of their convergence. It discusses widely deployed access networks and their classification based on the transmission medium. Additionally, it provides an overview of datacenter networks, which enable cloud-based sharing and computing applications and support large-scale data storage. Optical network convergence is a central concept in this thesis and a focus of emerging research in both the optical and wireless research communities. Therefore, this chapter motivates the need for convergence and outlines a vision for a truly

converged network, which influences later chapters. Finally, the chapter explores the role of PIC solutions in achieving network convergence, offering benefits like flexibility, reconfigurability, cost savings, and low energy consumption.

Chapter 2 focuses on capacity enhancement in optical and wireless networks in response to the increasing demand for device connections. It starts by exploring the potential of mmWave and THz frequencies in improving network capacity. Then the techniques for enhancing spectral efficiency through advanced modulation formats are discussed. Finally, the chapter provides an overview of three innovative optical-wireless convergence technologies: optical heterodyning, flexible optical sources and ARoF.

Chapter 3 focuses on the construction of SiP based ARoF mmWave transmission system, showcasing system-level convergence in optical access networks. It begins with a comprehensive description of a hybrid photonic integrated DLM, followed by a detailed characterization of its important parameters. The latter part of the chapter showcases the experimental implementation of the DLM in an optical heterodyne ARoF fronthaul link in centralized/cloud RAN (C-RAN) scenarios, involving both fiber-based and wireless mmWave links. The successful deployment of the novel laser module in a laboratory transmission environment demonstrates its potential for enabling the convergence of optical and wireless networks.

Chapter 4 explores advanced systems leveraging PIC technology to enhance reconfigurability in network infrastructure. It focuses on the transmission of multiplexed waveforms compatible with PON, Wi-Fi, and beyond 5G technologies over fronthaul RoF link in a C-RAN scenario using a low noise DLM. The concluding section showcases improved network reconfigurability achieved by incorporating SiP elements. An experimental demonstration highlights a flexible wavelength and space switched ARoF fronthaul transmission for an emerging 6G waveform and a low noise hybrid integrated laser.

Chapter 5 discusses the short-reach datacenter transmission employing high-order advance modulation format transmission using the low noise DLM. The wavelength tunability is added by the flexible DLM, supporting unamplified short-reach transmission over the entire C-band and parts of S and L bands while maintaining the requirement for low-complexity digital signal processing.

The conclusion and future work are discussed at the end of the thesis and consist of an

outline of all the chapters and a discussion of the potential future work that can be carried out based on the contributions of this thesis.

References

[1] Deloitte, "Covid-19 implications for data centers," 2020. [Online]. Available: https://www2.deloitte.com/content/dam/Deloitte/xe/Documents/About-Deloitte/mepovdocuments/mepov33/covid-19-implications-for-data-centers_mepov33.pdf

[2] P. Judge, "How the covid-19 pandemic has changed the data center business," 2020. [Online]. Available: https://www.datacenterdynamics.com/en/analysis/how-covid-19-pandemic-has-changed-data-center-business/

[3] Cisco, "Cisco annual internet report (2018˜2023) white paper," 2020. [Online]. Available: https://www.cisco.com/c/en/us/solutions/collateral/executive-perspectives/annual-internet-report/white-paper-c11-741490.html

[4] Nokia, "Nokia next−generation pon." [Online]. Available: https://onestore.nokia.com/asset/201150

[5] W. Hong, Z. H. Jiang, C. Yu, D. Hou, H. Wang, C. Guo, Y. Hu, L. Kuai, Y. Yu, Z. Jiang, Z. Chen, J. Chen, Z. Yu, J. Zhai, N. Zhang, L. Tian, F. Wu, G. Yang, Z.-C. Hao, and J. Y. Zhou, "The Role of Millimeter-Wave Technologies in 5G/6G Wireless Communications," *IEEE Journal of Microwaves*, vol. 1, no. 1, pp. 101–122, 2021.

[6] ZTE, "50G PON: New-Generation PON Technology After 10G PON," 2021. [Online]. Available: https://www.zte.com.cn/global/about/magazine/zte-technologies/2021/4-en/Expert-Views/1.html

[7] P. T. Dat, A. Kanno, N. Yamamoto, and T. Kawanishi, "Seamless convergence of fiber and wireless systems for 5G and beyond networks," *Journal of Lightwave Technology*, vol. 37, no. 2, pp. 592–605, 2018.

[8] C. Browning and D. Dass, "Flexible converged photonic and radio systems: A pathway toward next generation wireless connectivity," in *Photonic Networks and Devices*. Optica Publishing Group, 2021, pp. NeM4B–2.

[9] C. Lim and A. Nirmalathas, "Radio-over-fiber technology: Present and future," *Journal of Lightwave Technology*, vol. 39, no. 4, pp. 881–888, 2021.

[10] C. Browning, Q. Cheng, N. C. Abrams, M. Ruffini, L. Y. Dai, L. P. Barry, and K. Bergman, "A silicon photonic switching platform for flexible converged centralized-radio access networking," *Journal of Lightwave Technology*, vol. 38, no. 19, pp. 5386–5392, 2020.

[11] E. Ruggeri, C. Vagionas, R. Maximidis, G. Kalfas, D. Spasopoulos, N. Terzenidis, R. M. Oldenbeuving, P. W. van Dijk, C. G. Roeloffzen, N. Pleros *et al.*, "Reconfigurable Fiber Wireless fronthaul with A-RoF and D-RoF co-existence through a Si3N4 ROADM for Heterogeneous mmWave 5G C-RANs," *Journal of Lightwave Technology*, vol. 40, no. 16, pp. 5514–5521, 2022.

[12] J. Xia, T. Li, Q. Cheng, M. Glick, M. Crisp, K. Bergman, and R. Penty, "A Future Proof Reconfigurable Wireless and Fixed Converged Optical Fronthaul Network Using Silicon Photonic Switching Strategies," *Journal of Lightwave Technology*, 2022.

[13] X. Guan, W. Shi, J. Liu, P. Tan, J. Slevinsky, and L. A. Rusch, "Silicon photonics in optical access networks for 5G communications," *IEEE Communications Magazine*, vol. 59, no. 6, pp. 126–131, 2021.

Chapter 1

Network Architectures & Convergence

The current trends of increased demand for internet and cloud services have paved the path for further research on the convergence of fixed-line and wireless access networks. The high mobile bandwidth demands, for applications such as video streaming, cloud computing, IoT, etc., in particular, are driving the convergence of these network types. Leveraging the advantages of fiber access transport, such as high bandwidth and low latency, in wireless access networks has become a promising opportunity to meet these demands. In this chapter, the focus is on exploring network architectures and highlighting the significance of their convergence. The widely deployed access networks and their broad classification based on the transmission medium of information from the transport network to the end user and vice-versa are discussed. Later in the chapter, an overview of data center networks, which are large-scale data storage facilities that play a crucial role in enabling cloud-based sharing and computing applications, is presented. These networks are an essential component of the infrastructure that supports the processing and storage of vast amounts of data.

To meet the growing demand for popular services and applications, including AI, AR, VR, telemedicine, and the IoT, network operators must amalgamate various network architectures to exploit their respective advantages. This prompts inquiries into the feasibility of convergence, the relevant technologies and techniques, and the economics and energy efficiency associated with deploying such networks. This idea of optical network convergence is the key concept underpinning the work presented in this thesis and indeed is the focus of much emerging research both in the optical and wireless research

communities. Section 1.4 of this chapter describes the main drivers behind the need for convergence and outlines the vision of a truly converged network that motivates system level work presented in later chapters. In the final section of this chapter, the role of PIC solutions in achieving the aforementioned network convergences by offering increased flexibility, reconfigurability, cost savings, and low energy consumption is explored.

1.1 Optical Network Topologies

The classical service delivering network spans across a country or a large region, as shown in the architectural depiction in Fig. 1.1. The four areas of operations are a core network connecting two cities or countries, a metro network, a datacenter network and an access network connecting the end users to a local data network. This network layout is in line with leading service providers such as Domain 2.0 AT & T. The description of each type of network is given in the subsequent sections.

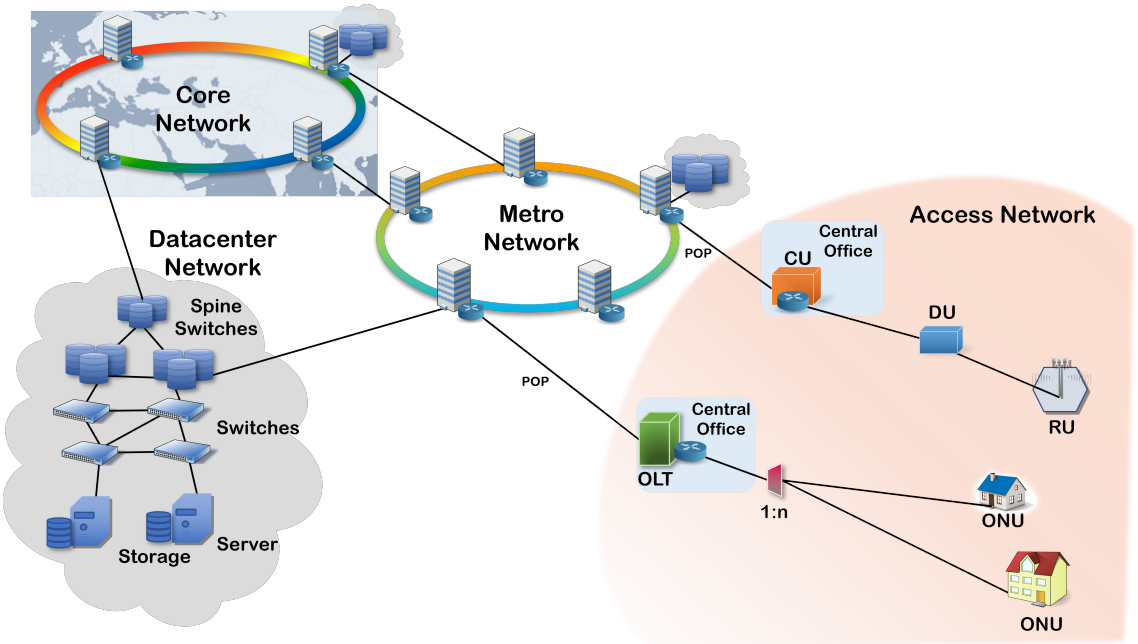

Fig. 1.1: A classical network with 3 tiers.

1.1.1 Core Networks

A core network, see Fig. 1.1, serves as the central infrastructure for transmitting, routing, and managing data traffic and is a fundamental component of a telecommunications

network. It acts as the backbone of the network (spanning 1000s km), connecting various access points, such as mobile devices, computers, and servers, and enabling seamless communication and data exchange between them. A core network is designed to handle large volumes of data ($\sim$ 800G line rate) in an efficient way across the network. Some of the functions performed by this network are data network management, routing and switching to ensure reliable connectivity, optimal performance and the delivery of various services to end-users.

The key characteristics of a core network are data routing of traffic over the most efficient paths using routing protocols and algorithms. Data switching is another characteristic of this network, where the switches in the network enable the connection and communication between different network nodes. Core networks also consist of management systems such as fault detection, performance monitoring, configuration management, security management and quality of service (QoS) management. The core network manages network resources, such as bandwidth, ensuring efficient utilization and optimal performance. Additionally, it enables interconnection between different networks and systems, facilitating seamless communication and data exchange.

1.1.2 Metro Networks

Metropolitan area networks (MANs) serve as a crucial link between businesses and residential users, connecting enterprises to core networks and residential users to the rest of the internet as shown in Fig. 1.1. This network segment spans cities, regions, districts, and municipalities, playing a vital role in broadband networking. The metro network consisted of an optical backbone, i.e. the open system interconnection (OSI) layer 0-3, with layer 1 transport and layer 2 framing, supplemented by an internet protocol (IP)/ multiprotocol label switching (MPLS) overlay for routing protocols. Points of presence (POP) along the metro network lead to distribution networks, where various access networking technologies are deployed, including coaxial cable, hybrid copper-fiber cable, passive optical networks, wireless technologies, and free space optical communication systems.

Enterprises can connect to the metro network via the plain old telephone system (POTS) distribution network or directly to a metro POP. The diverse range of communication technologies and customers connected to the metro network enables the provision

of various services, encompassing legacy voice, video, and data, as well as enterprise services, data center connectivity, and cloud connectivity. The emergence of cloud computing has further integrated cloud networking into the metro network, with metropolitan area clouds becoming an essential component of modern cloud businesses and business processes.

The metropolitan network incorporates various technologies across different layers. In the fiber layer, there is a requirement for transporting large amounts of data (up to $\sim$ 400G line rate), which has traditionally been achieved through synchronous optical network (SONET)/synchronous digital hierarchy (SDH). However, the industry is now transitioning towards packet-optical integration, utilizing technologies such as Ethernet and optical transport network (OTN). These technologies are then mapped onto optical wavelengths, which are configured by optical add-drop multiplexers (OADMs) at network nodes. The implementation of reconfigurable OADMs (ROADMs) enables end-to-end optical communication within the metro domain. To fulfill this objective, the deployment of ROADM technology has become prevalent.

1.1.3 Access Networks

The access network accounts for the transmission of all the human - or machine (in the IoT case) - centric data to the core/metro network, and is considered to be the 'last mile' in connectivity to subscribers. The key factors defining the access networks are the number of users/machines and the demand for bandwidth and speed which are driven by applications served. The broad classification of the type of access networks is based on the medium of transmission of information, which is wireless RF links for wireless access networks (WANs) and wireless local area networks (WLANs), and fixed-line copper/fiber connections for Ethernet, digital subscriber line (DSL), fiber to the x (FTTx) service and passive optical network (PON).

1.2 Classification of Access Networks

To meet the subscribers' requirements for data rate, mobility, and applications or services, network operators deploy different types of access networks. Fixed-line networks are

usually chosen for broadband services, while wireless networks are preferred for mobile links. A brief overview of the types of access networks is given below:

1. **WAN**: It is a high-capacity mobile network that uses RF links, typically in the microwave frequency range (300 MHz to 24 GHz), for information transmission. 3G networks provide voice and data transmission at a peak datarate of 2 Mbps. A peak datarate of 100 Mbps is provided by the subsequent release of 4G LTE and up to 20 Gbps from the 5G that is currently being deployed [1]. Unlike the predecessor 3G network which uses circuit switching, when entire information is transferred over a single connection, 4G LTE/5G sends information using packet switching, where information is divided into small packets which are then transmitted over different paths - thus utilizing the mobile network resources more efficiently. For additional analysis of this network type, please refer to subsection 1.2.1 for a comprehensive discussion.

2. **WLAN**: It is an ad hoc or fixed-line wireless access network connecting devices like mobile, laptops, home appliances, machines etc., present within a specific area using RF links typically in the microwave frequency range . An ad hoc network is a direct link between two or more devices to exchange information or share internet resources (e.g. Bluetooth and WiFi Direct). In the fixed network, a pre-existing infrastructure provides access to the internet via wireless access points like WiFi. Further discussion on this network category can be found in subsection 1.2.2, where a detailed discussion is provided.

3. **Ethernet**: It is a level-2 (data-link) protocol for fixed-line connection between the computers, switches, routers, processors, etc. located in a LAN to transmit and receive information bits encapsulated in a frame. It can be a point-to-point or point-to-multipoint network, depending upon the topology deployed in the network. Over 40 years, the ethernet speed evolved from 10 Mbps (10BASE-T) to 400 Gbps (CAT7) where the medium of transportation can be twisted pair, coaxial or fiber optic cables. Presently the Ethernet technology consortium (ETC) has developed a standardized specification for 800 Gigabit Ethernet (GbE) that relies on a configuration involving two instances of 400 GbE Physical Coding Sublayer/Forward Error Cor-

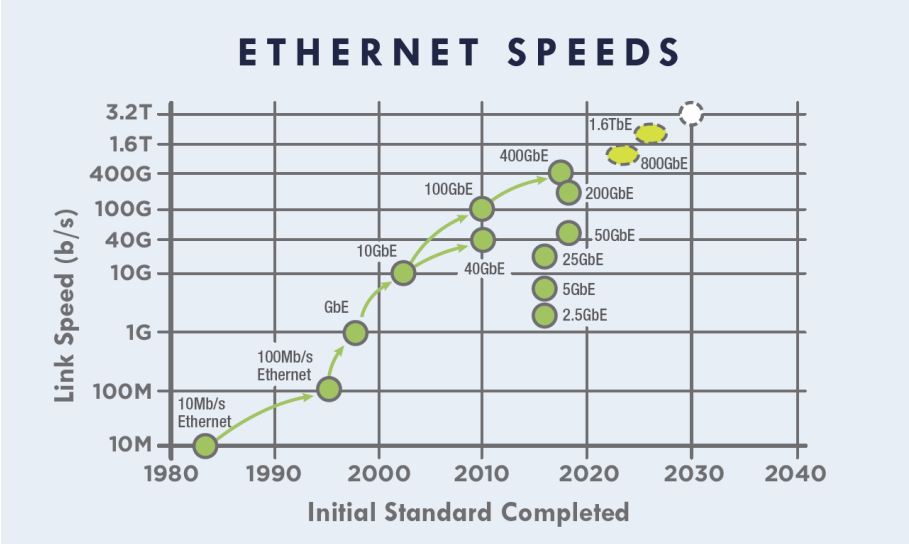

Fig. 1.2: Ethernet link speeds evolution over past 50 years and prediction for the next decade [3].

rection (PCS/FEC) [2]. Ethernet undergoes constant evolution in link speeds (see Fig. 1.2), incorporating innovations like Power over Ethernet (PoE) that enables device powering, Ethernet switching for optimized data routing, and advancements in fiber-optic Ethernet for enhanced high-speed and long-range communication.

4. **DSL**: It is a fixed-line broadband access technology that uses the existing twisted-pair copper telephone lines to deliver high-capacity data service to the subscribers. The combination of DSL and FTTx technologies are called G.fast, 212 MHz G.fast, and G.mgfast and have data speeds up to 800 Mbps, 2 Gbps, and 5-10 Gbps, respectively [4]. The integration of this technology with THz systems has been investigated recently [5].

5. **FTTx**: It is a fixed-line high-speed internet access network that connects x, where x is a home/building/node/curb/antenna to the Central Office (CO) using fiber links and are named FTTH, FTTB, FTTN, FTTC and FTTA respectively. These FTTx types are shown in Fig. 1.3.

6. **PON**: It is a fixed-line broadband access network, which connects several remotely deployed optical network units (ONUs) to central optical line terminals (OLTs) via a point-to-multipoint fiber network topology, as depicted in Fig. 1.3. In this case, each OLT is connected to multiple ONUs placed at subscriber sites through

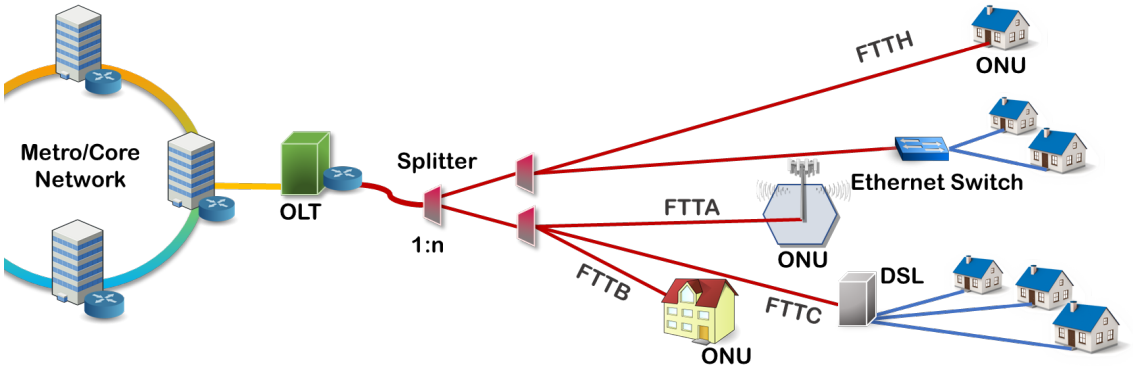

Fig. 1.3: Various configurations of FTTx architecture in PON.

an unpowered 1:n optical splitter/de-multiplexer. FTTx is a collective term used to encompass various types of fiber-to-the-x network architectures, including those based on PON technology. The specific configuration of FTTx networks depends on the precise placement of the remote ONU. For a more comprehensive analysis of this specific network type, please refer to subsection 1.2.3.

1.2.1 WANs

The latest generation of mobile networking technology is the 5G technology designed to provide faster data speeds, lower latency, and greater connectivity compared to previous generations of mobile networks. The key service classes of the 5G technology are ultra-reliable low latency (URLLC), enhanced mobile broadband (eMBB) and massive machine type communication (mMTC) [6, 7, 8]. Some service types, such as telemedicine and driverless vehicles, for example, will place stringent requirements on network reliability and latency and come within the URLLC service class. Whereas some services require high datarates and bandwidth, such as user-centric data traffic for services like VR, AR, high definition video play and multimedia services; these come in the service class of eMBB. The machine type communication (MTC) traffic is proliferating as the IoT is growing globally, as discussed in the introduction, shown in Fig. 1, which leads to connectivity among a massive number of devices. MTC traffic is assumed to be low in amount and delay insensitive. mMTC devices are bound to be cost effective, power efficient and have long battery life.

As we move toward the 6G era of communications, it is envisaged that some services

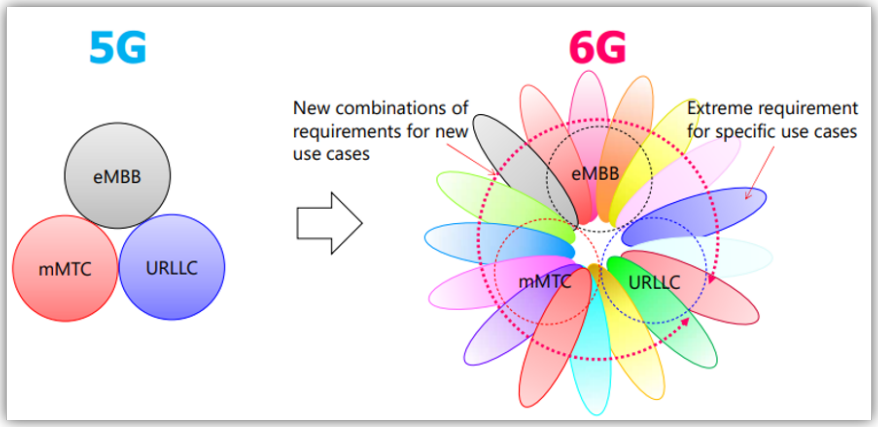

Fig. 1.4: 5G/6G service classes [6].

will require extreme performance through a combination of eMBB, mMTC and URLLC, and hence do not fall into the specific 5G services classes shown in Fig. 1.4. An example of an extreme use case is a remote robotic surgery, which is a combination of extreme performance provided by URLLC, for the communication link between doctor and hospital premises, and eMBB at the doctor's end to see 4k/8k live video streaming of the operation. Therefore, the applications of 5G/6G technology demand high datarate/capacity ($>$100 Gbps), extremely low latency ($<$1 ms) and proliferation in the number of users, devices and coverage area. To fulfill these demands, the 5G/6G technology will rely mainly on optical transport networks. Hence, the convergence of the 5G WAN-based technology with fiber-based access technologies, such as PON, can be highly advantageous for end-user service delivery and will be discussed in the later sections.

1.2.1.1 Classification of Radio Access Networks

Another important aspect of 5G communications is the radio access network (RAN) which is a type of WAN that specifically provides mobile device connectivity and whose architecture consists of two main modules; a radio unit (RU) and a baseband unit (BBU) as shown in Fig. 1.5. The remotely deployed RU defines the coverage of the network and provides the interface between the antenna in the cell and BBU: this is known as fronthaul and is typically based on the common public radio interface (CPRI). The BBU defines the capacity of the system and manages the signal processing and maintenance of the base station. Further division of BBU functionality in the distributed unit (DU) and central

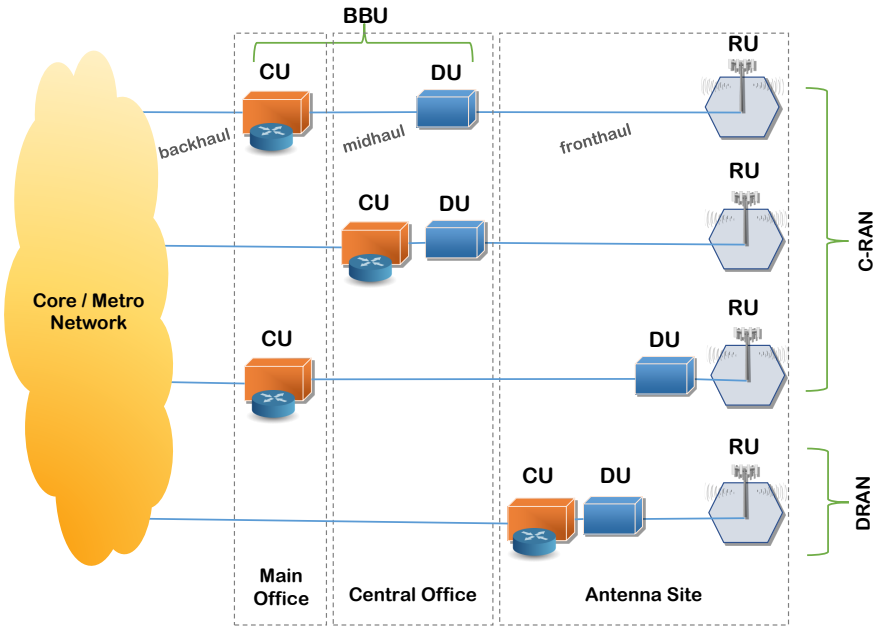

Fig. 1.5: Classification of RANs with various interfaces [11].

unit (CU) creates a new interface between the DU and CU called the midhaul (see Fig. 1.5). The DU is responsible for managing radio resources, quality of radio link and data processing whereas the CU provides centralized control and management of multiple DU resources.

The arrangement of RU, DU and CU varies with the specific use-case/service, transport option and physical/virtual network functions used in the network [9]. The distance between an RU and DU is in the range of 0-20 kilometers while the distance between the DU and CU can be up to tens of kilometers [10]. The interfaces between the RU, DU and CU are typically optical fiber based, making RANs a prime candidate for convergence or cooperation with optical access networks of a similar distance/topology i.e. PONs. These interfaces, as shown in Fig. 1.5 are classified as fronthaul, midhaul, and backhaul. They represent different sections of the network infrastructure that collectively enable the transmission of data signals, and control information in RANs. Fronthaul connects radio equipment or RU to the central processing unit i.e. either DU or a combination of CU and DU (BBU), midhaul acts as an intermediate link between fronthaul and backhaul, and backhaul connects aggregation points to the core network.

In simple terms, the RAN architectures are broadly classified as follows:

1. Distributed RAN (D-RAN):

The RU and BBU are colocated in the cell/antenna site as shown in Fig. 1.5. The cell sites are connected through a backhaul fiber link to the core network.

2. Centralized/ Cloud RAN (C-RAN):

   The location of RU with the antenna is in the cell site and the BBU, which constitutes the CU and DU, is at the centralized location between the cell site and the core network (referred to as the CO). The connection between the RU and BBU, is the fiber fronthaul. The C-RAN architecture is advantageous, especially in the case where there is a vast proliferation of cell sites. A detailed discussion of this is given in the next chapter 2.

3. Virtual RAN (vRAN):

   The vRAN is the same as C-RAN with the exception that CU and DU functionality at the CO are virtualized, typically through a software implementation on a local server, unlike the C-RAN which deploys proprietary hardware DUs and CUs.

4. Open RAN (O-RAN): The interface between the RU and DU, and DU and CU are open, such that the users can use multi-vendor components in the network. The open radio unit (O-RU), open DU (O-DU) and open CU (O-CU) components are specified by the O-RAN alliance and are software based server platforms.

In comparison with the existing RANs, C-RAN provides lower energy consumption, improved spectral efficiency, flexibility and scalability [12]. Moreover, C-RAN facilitates resource pooling, promotes environment-friendly infrastructure, enables virtualization of base stations, simplifies management and operation, facilitates coordination for interference mitigation, and supports smooth evolution to multiple technologies. [13]. Also, C-RAN/vRAN/O-RAN will be a preferable option for the deployment of small cells where the footprint and cost of the antenna site are crucial, especially for efficient support to massive MIMO [9, 13].

1.2.2 WLANs

WLAN is a type of computer network that allows devices to connect and communicate with each other wirelessly within a limited geographic area such as a building or campus.

In a WLAN, devices communicate with each other through access points (APs), which are connected to a wired network infrastructure, such as a router or a switch. The APs act as a bridge between the wired network and the wireless devices, providing access to the network resources and the internet.

Wi-Fi technology is a type of WLAN based on IEEE 802.11 standards and operates on various frequencies, including 2.4 GHz and 5 GHz bands. Wi-Fi technology has evolved significantly over a period of 20 years starting from 802.11b which offered a maximum speed of 11 Mbps on 2.4 GHz to 802.11ax which supports high-density environments and improves network efficiency, offering a maximum speed of 9.6 Gbps on 2.4 GHz and 5 GHz bands (refer to Table. 1.1).

WiGig (Wireless Gigabit) is a wireless communication standard based on the IEEE 802.11ad standard. It operates in the unlicensed 60 GHz frequency band and is designed to provide high-speed wireless data transfer between devices over short distances. WiGig uses beamforming technology to direct a focused beam of data between devices, which helps to improve reliability and reduce interference. It also supports multi-gigabit data rates, high-resolution video streaming, and low-latency wireless connections. The evolution of Wi-Fi technology is given in Table. 1.1.

Wi-Fi 6E is a recent addition to the 802.11ax family and utilizes an additional spectrum in the 6 GHz frequency band. This additional spectrum provides increased capacity and less interference, enabling faster speeds and more reliable connections by using technologies such as orthogonal frequency division multiple access (OFDMA) and multi-use

Table 1.1: Evolution of Wi-Fi technology

Year	Name	Standard	Datarate (Gbps)	Frequency (GHz)
1999	Wi-Fi 1	802.11b	0.011	2.4
1999	Wi-Fi 2	802.11a	0.054	5
2003	Wi-Fi 3	802.11g	0.054	2.4
2009	Wi-Fi 4	802.11n	0.6	2.4/5
2012	WiGig	802.11ad	7	60
2014	Wi-Fi 5	802.11ac	6.9	5
2019	Wi-Fi 6	802.11ax	9.6	2.4/5
2021	Wi-Fi 6E	802.11ax	9.6	2.4/5/6
2024	Wi-Fi 7	802.11be	~ 30	6

multiple inputs and multiple outputs (MU-MIMO). Wi-Fi 7 is under development and is expected to provide datarates up to 30 Gbps on the 6 GHz channel to support new applications such as autonomous vehicles and smart cities, which require high-performance, low-latency connectivity [14].

1.2.3 PONs

PON is a passive optical broadband access technology, that deploys time, wavelength or time and wavelength – division multiplexing (TDM, WDM, TWDM) technologies for data transmission. The three categories of PONs depicted in Fig. 1.6 are described below.

1. TDM PON: This technology deploys time division multiple access (TDMA), a method where each user (ONU) transmits data at a particular time slot at a predefined datarate. Data coming from all the ONUs over the same wavelength are multiplexed and upstreamed (US) to the OLT. Likewise, the time multiplexed data stream is sent over a single wavelength from OLT is downstreamed (DS) and broadcasted to all the ONUs.

2. WDM PON: Each ONU transmits data at a particular wavelength assigned to it, such that the total bandwidth of the PON is enhanced. All the information carrying

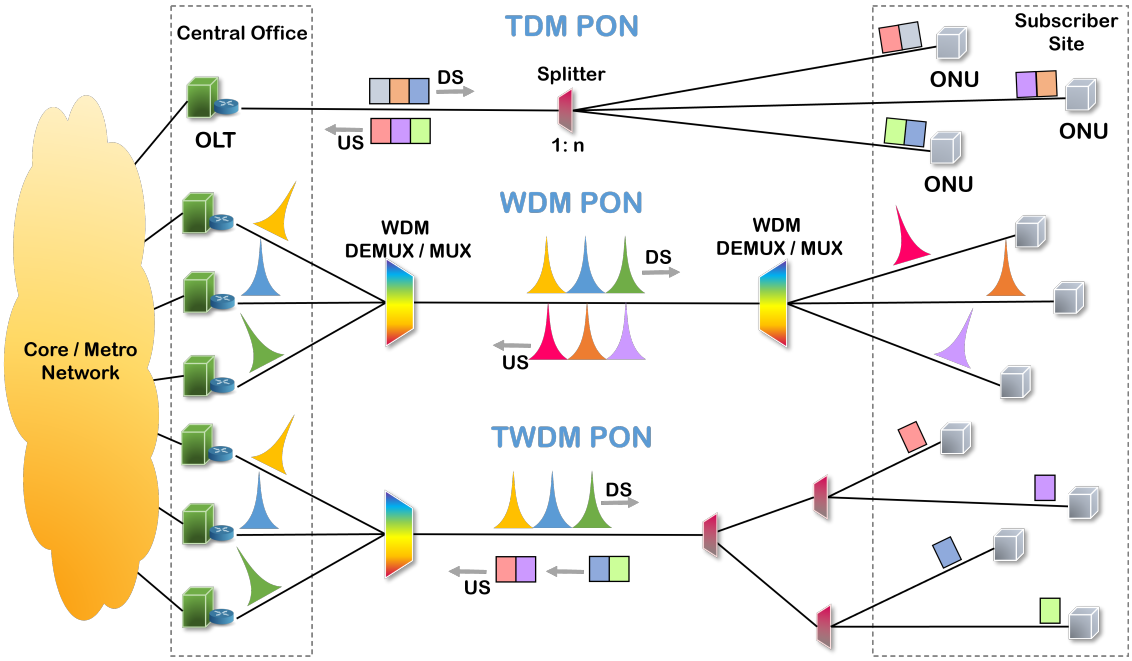

Fig. 1.6: Classification of PONs [15].

wavelengths are combined and upstreamed over a single fiber to an OLT. Similarly, the multiplexed wavelengths from the OLT are downstreamed to all the ONUs, demuxed at a remote node and each ONU is directed the desired wavelength.

3. TWDM PON: In this technology, four fixed wavelengths (optical carriers) are assigned to four OLTs, facilitating WDM transmission in the downstream direction with each ONU filtering the desired wavelength at the receiver. TDM is used in the upstream direction from ONU to OLT, where a laser operating in burst mode is deployed at each ONU. This technique is deployed in the NG-PON2 standard.

PON technology facilitates high bandwidth, multi-service transmission, high reliability and relatively low cost [16]. Fig. 1.7 shows the evolution of PON technology from Gigabit PON (GPON) with a downlink rate of 2.5 Gbps at 1480-1500 nm range to XG-PON/XGS-PON, also known as 10G-PON, with 10 Gbps downlink at 1575-1580 nm, where downlink means the link from the OLTs to the ONUs.

NG-PON was developed in order to increase the single wavelength rate, thereby improving the total rate using multi-wavelength multiplexing technology. The target network throughput of network operators for NG-PON is 50 Gbps, and IEEE and ITU-T are currently developing the follow-up evolution of PON technologies. IEEE formulated the NG-PON standard which is compatible with 10G-EPON, with a downlink rate of 25 Gbps and an uplink rate of 10 Gbps over a single fiber. They achieve a 50 Gbps bandwidth by binding two 25 Gbps channels. On the other hand, ITU-T/FSAN initiated 50G PON with single channel 50 Gbps uplink and downlink transmission in the O-band, fulfilling the re-

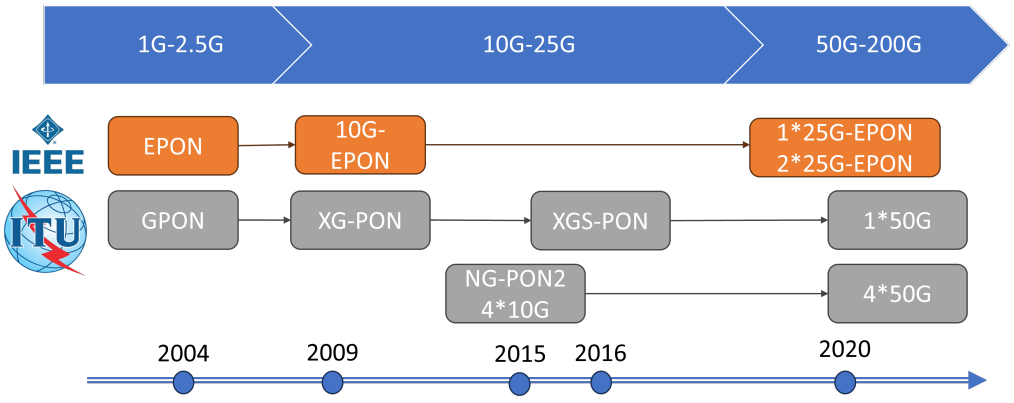

Fig. 1.7: PON roadmap [16].

quirements of home and enterprise users and (with a view to future network convergence) those of mobile fronthaul and backhaul also [16, 17].

1.3 Datacenter Networks

Datacenters are networks of storage and computing devices that are used by organizations to store critical applications and data. Datacenter networks (DCN) are also the backbone of cloud computing and are responsible for providing storage and computing resources for a wide range of applications. They consist of large data storage facilities that are connected through high-speed networks, enabling data to be shared and processed across multiple servers and data centers. The primary goal of DCNs is to provide highly available, scalable, and resilient services to support the needs of cloud computing applications. These networks are designed to handle large volumes of data traffic and provide high-bandwidth connectivity between data centers (inter-DC transmission), as well as between servers within a data center (intra-DC transmission) as depicted in Fig. 1.8. To

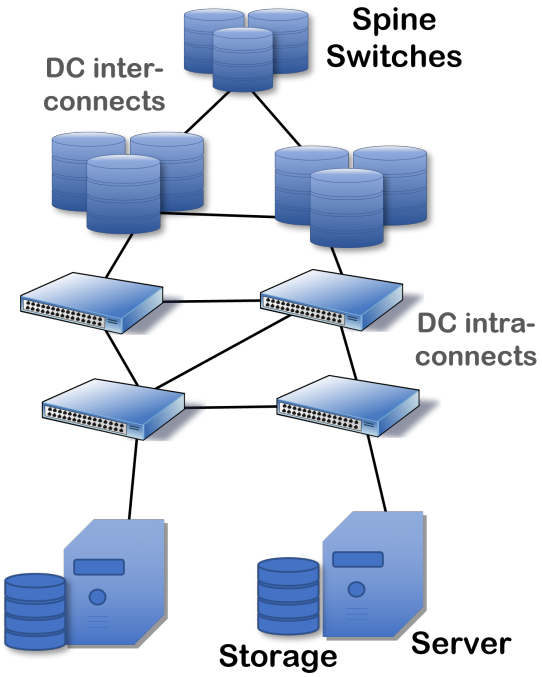

Fig. 1.8: An example of datacenter network.

achieve this, data center networks use a variety of higher layer technologies, including software-defined networking (SDN) and network function virtualization (NFV). These

technologies allow for greater flexibility and agility in network design, enabling administrators to dynamically allocate resources to meet the changing needs of their applications. A brief description of SDN and NVF network architectures is as follows:

1. SDN: It is a network architecture that involves the separation of the control plane from the data plane and the centralization of the network's intelligence in order to have a dynamic and efficient network configuration. This approach enables operators to manage the network comprehensively and consistently, regardless of the underlying network technology.

2. NFV: It focuses on virtualizing and consolidating network functions onto standard servers, switches, and storage, instead of dedicated hardware appliances. NFV aims to replace proprietary hardware with software applications, allowing network operators to deploy and manage network services more flexibly and cost-effectively.

In addition to providing connectivity and storage resources, DCNs also provide security and reliability features to ensure that data is protected and available at all times. This includes redundant hardware and power supplies, firewalls, and intrusion detection and prevention systems. The architecture of a DCN is shown in Fig. 1.8. Typically, datacenter networks can be classified into two categories: intra-datacenter and inter-datacenter networks. These two types of networks have distinct requirements in terms of topology, reliability, and bandwidth capacity due to their different roles and functions. The intra-datacenter networks connect machines or servers within the same building or campus, that spans $\sim$1 km distance, employing a combination of copper and optical cables. Intra-datacenter networks utilize a highly parallel fabric with diverse paths to ensure scalability and load balancing. Thousands of commodity-class servers and storage devices are interconnected by this network. On the other hand, inter-datacenter networks, which interconnect multiple datacenters, are more focused on point-to-point connections, featuring higher capacity per link and longer distances between interconnections, for example, connecting clusters located in different buildings within a 2 km campus area.

It is predicted that by 2025 global data growth will hit a rate of 175 zettabytes (ZB) [18], mainly due to the rise in the demand for advanced applications such as AI, IoT and AR amongst others. In addition, the rise in the number of devices and connection

growth globally, as discussed in the introduction, shown in Fig. 1, will a cause rise in the utilization of on-demand IT resources provided by datacenters, which will soon push the present datacenters' capacity to a maximum limit [19].

Moreover, stringent latency requirements ($<$1 ms) are demanded by the advanced services provided by 5G technology, especially those involving real-time interactions such as vehicle-to-vehicle communication, medical surgeries, manufacturing industries and online gaming. Such latency requirements, along with the extensive use of cloud-based services, are driving the development of ultra-high speed optical datacenter interconnects [20]. In addition to this, latency can be further reduced by bringing the computational and storage facilities near the data generators/sources in a concept termed as edge computing. A detailed discussion on improvement in datarate of intra datacenter interconnects is described in chapter 5.

Another aspect of DCN is switching bandwidth requirements that are driven by the volume of data traffic and the need for fast and reliable communication between servers and storage devices within the datacenter environment. To meet these high bandwidth requirements, DCN frequently utilizes high-speed switches that offer ample bandwidth capacities, such as switches with speeds of 10 Gbps, 40 Gbps, or 100 Gbps. Power consumption in DCNs is another major issue, prompting datacenter operators to consistently work towards adopting energy-efficient practices and technologies. Their goal is to reduce the environmental impact and lower operational costs associated with power usage while continuing to facilitate bandwidth scaling. This requirement in particular is driving current innovation in power efficient and high bandwidth photonic technologies for DCNs.

The storage systems in the datacenters have been improved in terms of memory access time, with the new Non-Volatile Memory Express (NVMe) technology enabling the access time in microseconds which is 1000X faster than the flash-enabled storage systems [21]. This is another factor that highlights the deficiency of current DC network speeds. The pre-existing fiber connections in the datcenters support datarate up to 16 Gbps, whereas Ethernet, a local area network of computers connected using wires, has been implemented with datarates from 10-100 Gbps. Small form-factor Pluggables (SFP) optical transceivers have been used as a common interface for both the copper and fiber

optics connections between switches and servers in DCNs, supporting the datarate of 1 Gbps.

The datarate 10 Gbps per data channel is supported by the SFP+ standard and has been widely adopted in DCNs as a single lane data channel interface. Furthermore, multiple optical lane interfaces such as 4-lane Quad SFP (QSFP) support 10-40 Gbps aggregate bandwidth and 8-lane Octal SFP (OSFP) supports 25 Gbps/lane with 200 Gbps per port aggregate bandwidth. PAM-4 modulation has been incorporated in the OSFP standard improving link bandwidth efficiency by a factor of two; supporting 50 Gbps/lane, resulting in an aggregate bandwidth of 400 Gbps [22]. Transceivers deploying 4-lane 100 Gbps with PAM-4, called QSFP double density (QSFP-DD), have been designed, characterized and tested [23, 24]. Hence, from the above short literature survey on the ongoing and future datacenter network requirements, the importance of exploring bandwidth and power efficient technologies, such as flexible/tunable optical solutions and advanced modulation, is emphasized [25].

In the last chapter 5 of this thesis, a discussion on the requirement and deployment of higher-order/advanced modulation formats in the short-reach intra-datacenter interconnects is presented.

1.4 Pathway to Converged Networks

As discussed, fiber access transport can provide the high bandwidths and low latencies required to sustain the growth of WANs and WLANs. Ultimately, this points to the effective convergence of optical and mobile networks segments and this technological concept will be a crucial aspect in meeting the ever-increasing demands of mobile users and enabling seamless and uninterrupted access to the digital world. The traditional approach to access networks has been to deploy separate wireless and optical infrastructures, but this approach is becoming increasingly inefficient due to the duplication of infrastructure and the need for increased capacity. As a result, the network operators are seeking to converge these networks to improve performance and reduce costs.

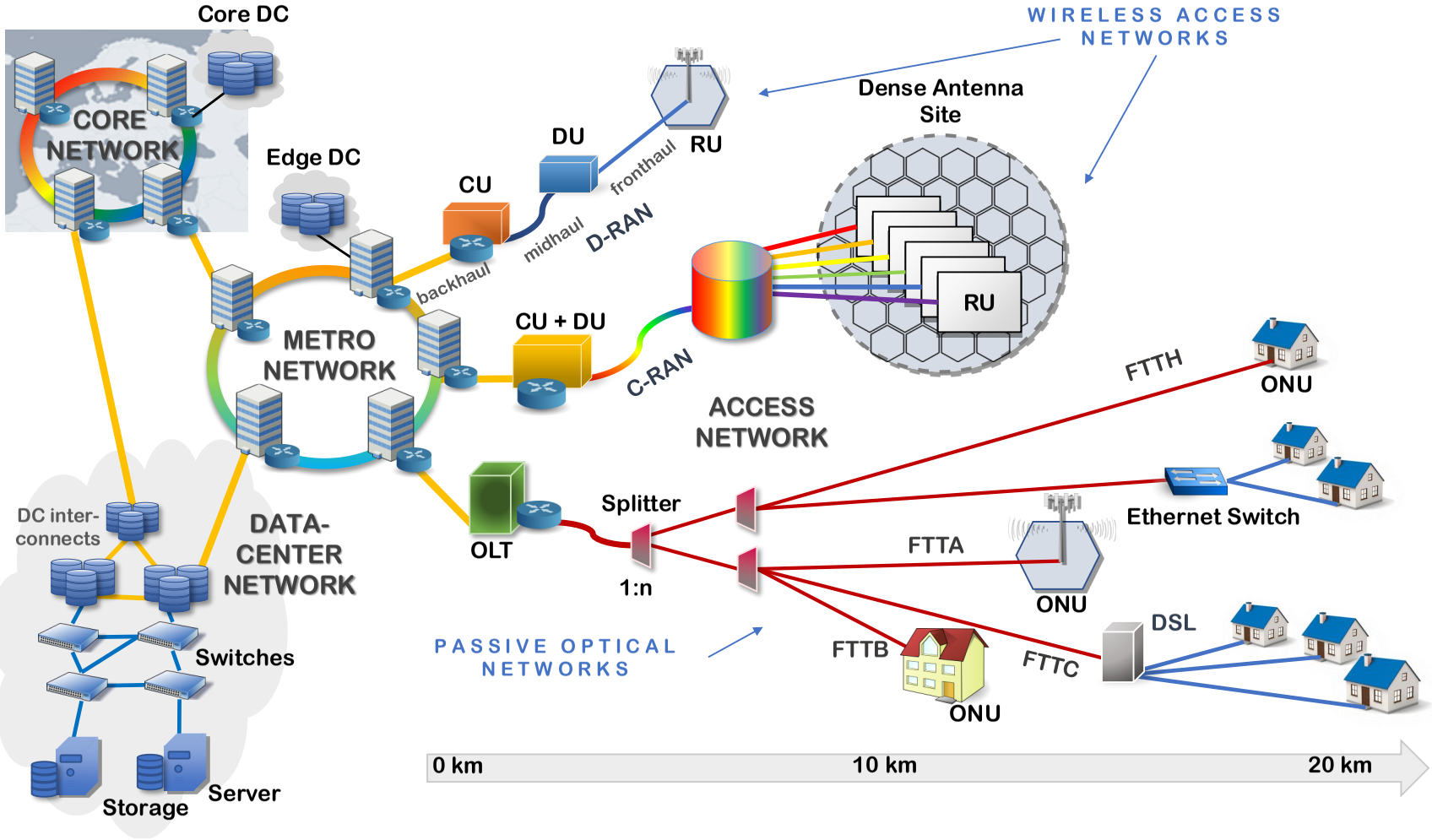

Fig. 1.9: Next-generatio converged optical access network.

Photonic convergence with traditional wireless networks facilitates higher bandwidth, speed of routing and transport, use of pre-existing multi-user access infrastructure and highly flexible networking, and also is an enabling technology for mmWave and THz systems. The development of flexible converged optical and wireless networks can be realized by deploying reconfigurable network components, that offer tunability both in operating wavelength used for optical transmission and also RF used for wireless transmission [26]. A future converged access network, as shown in Fig. 1.9, will be a coexistence of RAN and PON supporting various services and applications. The optical-wireless integrated RANs will have different placement options for CU, DU (the constituent parts of the baseband unit) and RU for specific network service types or applications. A DU can be placed at an intermediate distance between CU and RU (as shown at the top of Fig. 1.9), providing centralized processing for applications requiring high capacity, or next to the RU providing antenna site processing for latency sensitive applications [27, 28]. FTTA services can also be supported through current TWDM optical access systems also designed to cater for FTTB, FTTH, etc. [29, 30, 31].

For high-capacity wireless systems with dense antenna deployment and a large number of mobile users/devices, the C-RAN architecture - with CU and DU placed at CO and RU at cell site, as depicted Fig. 1.9 - provides reduced cost and complexity of RUs at the antenna sites [27, 11], helping to facilitate network scaling. Some recent works have demonstrated how this RAN architecture can be deployed in conjunction with centralized, flexible optical-based mmWave generation and spectrally efficient RoF transmission; serving to increase system throughput and flexibility while further reducing RU complexity [32, 33]. These aspects are particularly advantageous for future C-RAN deployments considering the ultra-dense deployment of the antenna sites required for high frequency wireless systems [34]. In order to fulfill the high capacity demanded by these dense antenna sites, an active remote node, like an optical switch, can be deployed to route wavelengths from CO to each RU in a WDM access network environment [35].

The incessant growth in required network capacity can only be catered for by the enhancement of fixed-line and wireless networks through the adoption of new communication techniques and technologies. The unification of isolated and independent networks with new technologies such as NFV, SDN and cloud computing, enables the 5G/6G

cloud-based network with agility, automation and flexibility. As mentioned earlier, the enhanced services promised by the 5G technology will rely mainly on the optical transport networks, to provide key performance indicators of latency, reliability and high capacity to the vastly increased number of users, devices and coverage areas. Using the optical transport of radio signals (e.g. fronthauling for 5G), will enhance the bandwidth of the mobile systems by many times. The information traveling at the speed of light between the CO and the antenna sites in 5G networks will increase the overall routing speed of the network. Hence, the seamless convergence of wireless and optical networks is highly advantageous. To further enhance the speed, scalability, datarate and reliability of the network, the storage and processing of the data should be brought closer to the data generators/antenna sites. Moreover, improving the capacity of the datacenter interconnects (DCIs) and their ability to interact with peripheral network types are also important aspects of the convergence of fixed-line and wireless networks. Therefore, extensive research in the field of convergence is essential.

Recently, ITU-T has released the recommendations for the requirements of PONs to incorporate 5G wireless fronthaul [36]. TDM PON (see Fig. 1.10 (a)) has been stated as a potential technology to support 5G [37]. [11] discusses the optical point-to-point, TDM and WDM interfaces for 5G RAN, and experimentally demonstrates 50 Gbps TDM PON transmission. Also, [38] predicts that 25 and 50 Gbps TDM PON leveraging the datacenter ecosystems, provides an ideal solution for midhaul and backhaul links in a 5G architecture, especially with dense antenna sites.

WDM PON is demonstrated as the predominant solution for the widespread implementation of 5G C-RAN in the future [39, 40]. A 5G PON architecture with WDM technology is shown in Fig. 1.10 (b). With the next-generation of WANs and WLANs predicted to leverage the advantages of optical fiber transmission extensively for backhaul and fronthaul, an onus is placed on the co-design of interfaces, baseband assets, and transmission systems to form fully integrated optical and wireless access technologies. This requires strong interdisciplinary research and WDM PON is a key enabling technology for this convergence [41, 42, 43, 44].

Furthermore, coherent WDM PON is another field of research for 5G technologies in order to increase the number of subscribers/devices in the network [45]. Extensive re-

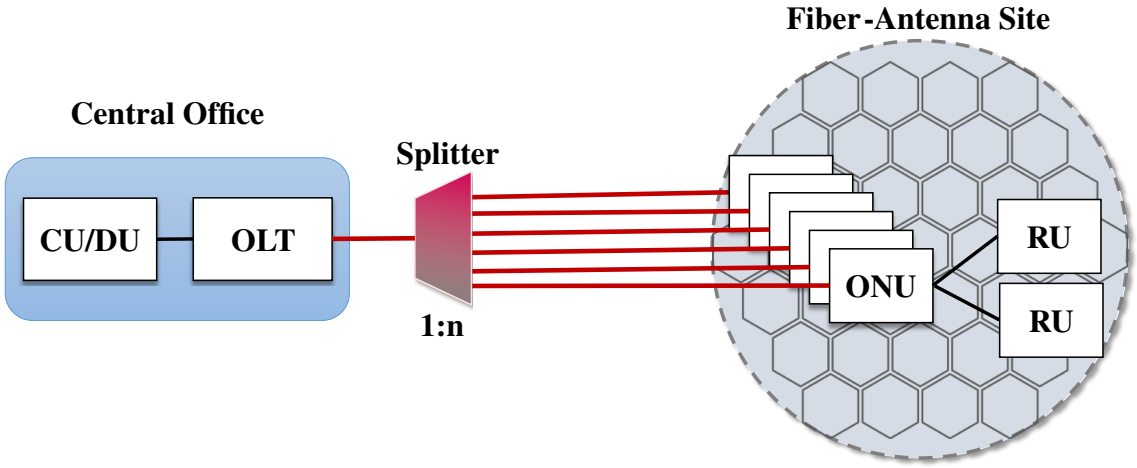

(a) 5G PON with TDM

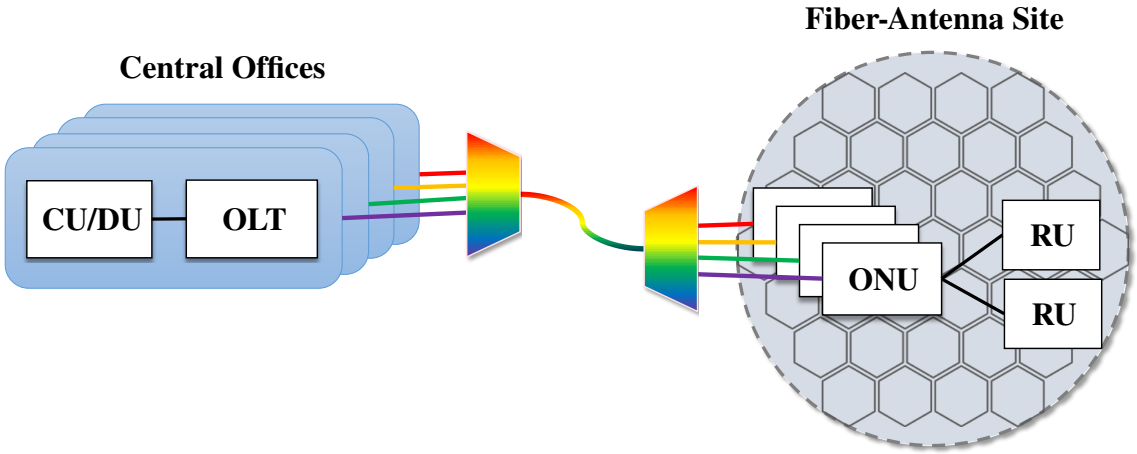

(b) 5G PON with WDM

Fig. 1.10: A depiction of prospective converged PON and 5G network with TDM and WDM technologies co-locating CU/DU and OLT in CO and ONU and RU at the antenna site.

search on planning and formation of 60 GHz fiber-wireless networks over existing GPONs infrastructure using 802.11ad and MT-MAC technologies is presented in [46]. The cloud-ification of 5G networks, where the traditional isolated and independent network is re-constructed to a virtualized cloud based network which shares datacenter IT resources is also a widely researched area [47, 48]. A brief discussion on this and the convergence of datacenter and access networks is given in chapter 5.

Another key enabling technology in support of efficient converged optical-wireless networks will be the development of mass-deployable flexible optical solutions. The clear need for such technology has led to a trend of adopting Silicon (Si) based PICs for data transmission in these future network types [49, 20, 50] which is discussed in the next

section.

1.5 PICs for Converged Networks

PICs provide a high level of integration, low power consumption, scalability, and reconfigurability, making them essential components in reconfigurable converged optical access networks. They enable service providers to deliver a wide range of services to multiple users on a single optical infrastructure while reducing costs and footprint and improving efficiency through photonic integration [51, 52]. PICs can be made from a variety of materials, each with its own set of advantages and disadvantages. Here are some of the most popular materials used for PIC developement:

1. Silicon: Silicon is becoming a popular material used for PICs due to its compatibility with complementary metal-oxide-semiconductor (CMOS) processing. Silicon photonics offers high performance, low cost, and scalability.

2. III-V materials: Materials like Indium Phosphide (InP) and Gallium Arsenide (GaAs) have high electron mobility and can operate at high frequencies, making them suitable for high-speed applications.

3. Silicon Nitride (SiN): SiN is a dielectric material that is compatible with CMOS processing. It has a low optical loss and can be used to make photonic waveguides, filters, and modulators.

4. Lithium Niobate ($LiNbO_3$): $LiNbO_3$ is a ferroelectric material that can be used to make high-performance modulators, switches, and filters. It has a high electro-optic coefficient, which means it can efficiently convert electrical signals to optical signals and vice versa.

Optical devices, such as lasers, manufactured using the above materials have previously been shown to exhibit extremely low noise and high optical power. The study of several hybrid integrated diode lasers with InP semiconductor optical amplifiers (SOAs) and Si_3N_4 based low-loss dielectric feedback circuits shows ultra-narrow intrinsic linewidth ($\sim$40 Hz), high output power (100 mW), record-wide spectral coverage (120 nm) and a

low level of relative intensity noise (RIN) of about −170 dBc/Hz [53]. The Si_3N_4 waveguide offers a longer photon lifetime, as compared to a lossy laser resonator, and leads to an increase in the coherence properties of on-chip light generation with the diode laser. An in-depth study of various optical sources that can enable flexible converged optical access is given in chapter 2.

Optical modulation is another key aspect of reconfigurable converged data networks where optical modulation can take place at the CO or the OLT or the datacenter node. Authors in [50] have shown a smart edge that is used to overlay 5G service on a PON downlink using small in-size and low-powered cascaded Si-based microring resonator modulators (MRM). Optical carrier reuse employed in [54] using Si-based microring resonators (MRRs) and MRMs and on-chip photodiodes (PDs) is an attractive solution for fully integrated optical transceivers in small-cell RUs. Using the optical carrier reuse scheme saves the costs of laser diode packaging. However, such a transceiver lacks tunability. Chen et al. suggest employing a SiP two-rings-coupled Mach Zehnder interferometer with a tunable bandpass filter in a mmWave RoF system to suppress the sideband signal while maintaining the optical carrier. This filter allows for tunability in the suppression band, making both the carrier and sideband signal adjustable and producing a frequency-flexible mmWave signal [55].

As datacenters prepare for the expected surge in demand for 100 Gbps and 400 Gbps modules, size and power consumption levels must be kept at low cost points that are difficult to achieve without the use of photonic integration and advanced packaging techniques. To meet the requirements of future optical networks, a platform is needed that can provide high performance, low powered, small form factor, and low-cost photonic transceivers [56]. The work in [57] examines the advancements in SiP technology for PAM transmission, with a focus on CMOS compatible photonics processes. It covers the performance metrics of SiP modulators, considerations for high-speed PAM transmission, driving strategies for optical PAM signals, and state-of-the-art Si based PAM modulators and integrated transmitters.

The following research works demonstrate the use of SiP as switches to enhance the reconfigurability of converged optical networks: Authors in [48] demonstrate the feasibility of using a SiP switching platform for digital RoF (DRoF) in optical fronthaul links.

Other studies have investigated the effectiveness of differential drive SiP Mach-Zehnder Modulator (MZM) and MRR based SiP switches for efficient ARoF service [58, 59]. A Si_3N_4 MRR based ROADM has been used in [60] to show the coexistence of multi-service mmWave ARoF and DRoF transmission in CRAN.

In this chapter, the various types of network architectures are presented. A significant emphasis is given to the convergence of the wireless and optical networks and PIC-based solutions have been proposed to achieve this. In chapter 2, the technologies to facilitate this convergence are discussed in detail.

References

[1] ETSI, "Why do we need 5g?," 2020.

[2] E. T. Consortium, "800 Gigabit Ethernet (GbE) Specification Rev. 1.1," 2020.

[3] E. Alliance, "2023 Ethernet Roadmap," 2023.

[4] G. ITU-T, "9701 Fast Access to Subscriber Terminals (G. fast)—Physical Layer Specification," *ITU-T recommendation, Series G: Transmission Systems and Media, Digital Systems and Networks*, 2014.

[5] J. M. Cioffi, K. J. Kerpez, C. S. Hwang, and I. Kanellakopoulos, "Terabit dsls," *IEEE Communications Magazine*, vol. 56, no. 11, pp. 152–159, 2018.

[6] N. DOCOMO, "White paper 5g evolution and 6g," 2020.

[7] B. Zong, C. Fan, X. Wang, X. Duan, B. Wang, and J. Wang, "6g technologies: Key drivers, core requirements, system architectures, and enabling technologies," *IEEE Vehicular Technology Magazine*, vol. 14, no. 3, pp. 18–27, 2019.

[8] M. Z. Chowdhury, M. Shahjalal, S. Ahmed, and Y. M. Jang, "6g wireless communication systems: Applications, requirements, technologies, challenges, and research directions," *IEEE Open Journal of the Communications Society*, vol. 1, pp. 957–975, 2020.

[9] N. Alliance, "5G RAN CU - DU network architecture, transport options and dimensioning," 2019.

[10] I. GSTR-TN5G, "Transport network support of imt-2020/5g," 2018.

[11] F. Saliou, P. Chanclou, L. A. Neto, G. Simon, J. Potet, M. Gay, L. Bramerie, and H. Debregeas, "Optical access network interfaces for 5g and beyond," *Journal of Optical Communications and Networking*, vol. 13, no. 8, pp. D32–D42, 2021.

[12] G. Kalfas, D. Tsiokos, N. Pleros, C. Verikoukis, and M. Maier, "Towards medium transparent MAC protocols for cloud-RAN mm-wave communications over next-generation optical wireless networks," in *2013 15th International Conference on Transparent Optical Networks (ICTON)*, pp. 1–4, IEEE, 2013.

[13] I. A. Alimi, A. L. Teixeira, and P. P. Monteiro, "Toward an efficient C-RAN optical fronthaul for the future networks: A tutorial on technologies, requirements, challenges, and solutions," *IEEE Communications Surveys & Tutorials*, vol. 20, no. 1, pp. 708–769, 2017.

[14] E. Reshef and C. Cordeiro, "Future Directions for Wi-Fi 8 and Beyond," *IEEE Communications Magazine*, vol. 60, no. 10, pp. 50–55, 2022.

[15] R. Q. Shaddad, A. B. Mohammad, S. A. Al-Gailani, A. Al-Hetar, and M. A. Elmagzoub, "A survey on access technologies for broadband optical and wireless networks," *Journal of Network and Computer Applications*, vol. 41, pp. 459–472, 2014.

[16] ZTE, "White paper on 50g-pon technology," 2020.

[17] ZTE, "50G PON: New-Generation PON Technology After 10G PON," 2021.

[18] D. Reinsel, J. Gantz, and J. Rydning, "Data age 2025: The evolution of data to life-critical," *Don't Focus on Big Data*, vol. 2, 2017.

[19] Y. Lu and H. Gu, "Flexible and scalable optical interconnects for data centers: Trends and challenges," *IEEE Communications Magazine*, vol. 57, no. 10, pp. 27–33, 2019.

[20] Q. Cheng, M. Glick, and K. Bergman, "Optical interconnection networks for high-performance systems," in *Optical fiber telecommunications VII*, pp. 785–825, Elsevier, 2020.

[21] J. S. Bozman, "Faster interconnects for nextgeneration data centers."

[22] J. David, "High-speed interconnects adapt to data centers' ever-changing signal, bandwidth, and density requirements."

[23] X. Zhang, D. Zheng, Z. Ying, Y. Li, M. Ding, D. Lam, S. Tu, R. Wu, X. Zhang, Y. Sun, *et al.*, "Integrated silicon photonics transmitter in 400gbase-dr4 qsfp-dd transceiver," in *2021 Optical Fiber Communications Conference and Exhibition (OFC)*, pp. 1–3, IEEE, 2021.

[24] H. Zhu, S. Anderson, N. Karfelt, L. Jiang, Y. Li, R. Boeck, H. Yamazaki, M. Wang, R. Kankipati, and R. Grzybowski, "Low-cost 400 gbps dr4 silicon photonics transmitter for short-reach datacenter application," *Nanomaterials*, vol. 11, no. 8, p. 1941, 2021.

[25] M. Hattink, L. Y. Dai, Z. Zhu, and K. Bergman, "Streamlined architecture for thermal control and stabilization of cascaded DWDM micro-ring filters bus," in *Optical Fiber Communication Conference*, pp. W2A–2, Optica Publishing Group, 2022.

[26] C. Browning and D. Dass, "Flexible converged photonic and radio systems: A pathway toward next generation wireless connectivity," in *Photonic Networks and Devices*, pp. NeM4B–2, Optica Publishing Group, 2021.

[27] P. Sehier, P. Chanclou, N. Benzaoui, D. Chen, K. Kettunen, M. Lemke, Y. Pointurier, and P. Dom, "Transport evolution for the ran of the future," *Journal of Optical Communications and Networking*, vol. 11, no. 4, pp. B97–B108, 2019.

[28] G.-K. Chang, M. Xu, and F. Lu, "Optical networking for 5g and fiber-wireless convergence," in *Springer Handbook of Optical Networks*, pp. 1031–1056, Springer, 2020.

[29] M. Erkılınç, D. Lavery, K. Shi, B. Thomsen, R. Killey, S. Savory, and P. Bayvel, "Bidirectional wavelength-division multiplexing transmission over installed fibre using a simplified optical coherent access transceiver," *Nature communications*, vol. 8, no. 1, pp. 1–10, 2017.

[30] T. Horvath, P. Munster, V. Oujezsky, and N.-H. Bao, "Passive optical networks progress: a tutorial," *Electronics*, vol. 9, no. 7, p. 1081, 2020.

[31] K. Asaka and J.-i. Kani, "Standardization trends for next-generation passive optical network stage 2 (ng-pon2)," *NTT Technical Review*, vol. 13, no. 3, pp. 80–84, 2015.

[32] D. Dass, S. O'Duill, A. Delmade, and C. Browning, "Analysis of phase noise in a hybrid photonic/millimetre-wave system for single and multi-carrier radio applications," *Applied Sciences*, vol. 10, no. 17, p. 5800, 2020.

[33] C. Browning, H. H. Elwan, E. P. Martin, S. O'Duill, J. Poette, P. Sheridan, A. Farhang, B. Cabon, and L. P. Barry, "Gain-switched optical frequency combs for future mobile radio-over-fiber millimeter-wave systems," *Journal of Lightwave Technology*, vol. 36, no. 19, pp. 4602–4610, 2018.

[34] S. Noor, P. Assimakopoulos, and N. J. Gomes, "A flexible subcarrier multiplexing system with analog transport and digital processing for 5g (and beyond) fronthaul," *Journal of Lightwave Technology*, vol. 37, no. 14, pp. 3689–3700, 2019.

[35] X. Pang, M. Beltrán, J. Sánchez, E. Pellicer, J. V. Olmos, R. Llorente, and I. T. Monroy, "Centralized optical-frequency-comb-based RF carrier generator for DWDM fiber-wireless access systems," *Journal of Optical Communications and Networking*, vol. 6, no. 1, pp. 1–7, 2014.

[36] I. Sup66, "5G wireless fronthaul requirements in a passive optical network context," *Geneva, Switzerland, Sep*, 2020.

[37] S. Kuwano, J. Terada, and N. Yoshimoto, "Operator perspective on next-generation optical access for future radio access," in *2014 IEEE International Conference on Communications Workshops (ICC)*, pp. 376–381, IEEE, 2014.

[38] E. Harstead, D. van Veen, V. Houtsma, and P. Dom, "Technology roadmap for time-division multiplexed passive optical networks (tdm pons)," *Journal of Lightwave Technology*, vol. 37, no. 2, pp. 657–664, 2018.

[39] I. Chih-Lin, J. Huang, R. Duan, C. Cui, J. Jiang, and L. Li, "Recent progress on C-RAN centralization and cloudification," *IEEE Access*, vol. 2, pp. 1030–1039, 2014.

[40] "High speed WDM-PON technology for 5G fronthaul network], author=Zhang, DeZhi and Zhe, Du and Jiang, Ming and Zhang, Jun, booktitle=Asia Communications and Photonics Conference, pages=S3K–8, year=2018, organization=Optica Publishing Group,"

[41] F. J. Effenberger and D. Zhang, "WDM-PON for 5G Wireless Fronthaul," *IEEE Wireless Communications*, vol. 29, no. 2, pp. 94–99, 2022.

[42] K. Honda, K. Hara, H. Nakamura, K. Sone, G. Nakagawa, Y. Hirose, T. Hoshida, and J. Terada, "WDM-PON management and control by auxiliary management and control channel for 5G mobile fronthaul," *Optics Express*, vol. 29, no. 26, pp. 42457–42470, 2021.

[43] T. Salgals, A. Ostrovskis, A. Ipatovs, V. Bobrovs, and S. Spolitis, "Hybrid ARoF-WDM PON Infrastructure for 5G Millimeter-wave Interface and Broadband Internet Service," in *2019 Photonics Electromagnetics Research Symposium - Fall (PIERS - Fall)*, pp. 2161–2168, 2019.

[44] G.-K. Chang, L. Cheng, M. Xu, and D. Guidotti, "Integrated fiber-wireless access architecture for mobile backhaul and fronthaul in 5G wireless data networks," in *2014 IEEE Avionics, Fiber-Optics and Photonics Technology Conference (AVFOP)*, pp. 49–50, IEEE, 2014.

[45] W. W. Shbair and F. I. El-Nahal, "Coherent passive optical network for 5g and beyond transport," *Optoelectronics Letters*, vol. 17, no. 9, pp. 546–551, 2021.

[46] G. Kalfas, N. Pleros, L. Alonso, and C. Verikoukis, "Network planning for 802.11 ad and MT-MAC 60 GHz fiber-wireless gigabit wireless local area networks over passive optical networks," *Journal of Optical Communications and Networking*, vol. 8, no. 4, pp. 206–220, 2016.

[47] Huawei, "5g-oriented data center facility."

[48] J. Xia, T. Li, Q. Cheng, M. Glick, M. Crisp, K. Bergman, and R. Penty, "A Future Proof Reconfig-

urable Wireless and Fixed Converged Optical Fronthaul Network Using Silicon Photonic Switching Strategies," *Journal of Lightwave Technology*, 2022.

[49] K. Yamada, T. Tsuchizawa, H. Nishi, R. Kou, T. Hiraki, K. Takeda, H. Fukuda, Y. Ishikawa, K. Wada, and T. Yamamoto, "High-performance silicon photonics technology for telecommunications applications," *Science and Technology of Advanced Materials*, 2014.

[50] X. Guan, R. Dubé-Demers, W. Shi, and L. A. Rusch, "Heterogeneous optical access networks: Enabling low-latency 5g services with a silicon photonic smart edge," *Journal of Lightwave Technology*, vol. 39, no. 8, pp. 2348–2357, 2021.

[51] R. Soref, "The past, present, and future of silicon photonics," *IEEE Journal of selected topics in quantum electronics*, vol. 12, no. 6, pp. 1678–1687, 2006.

[52] D. Thomson, A. Zilkie, J. E. Bowers, T. Komljenovic, G. T. Reed, L. Vivien, D. Marris-Morini, E. Cassan, L. Virot, J.-M. Fédéli, *et al.*, "Roadmap on silicon photonics," *Journal of Optics*, vol. 18, no. 7, p. 073003, 2016.

[53] K.-J. Boller, A. van Rees, Y. Fan, J. Mak, R. E. M. Lammerink, C. A. A. Franken, P. J. M. van der Slot, D. A. I. Marpaung, C. Fallnich, J. P. Epping, R. M. Oldenbeuving, D. Geskus, R. Dekker, I. Visscher, R. Grootjans, C. G. H. Roeloffzen, M. Hoekman, E. J. Klein, A. Leinse, and R. G. Heideman, "Hybrid Integrated Semiconductor Lasers with Silicon Nitride Feedback Circuits," in *Photonics*, vol. 7, p. 4, Multidisciplinary Digital Publishing Institute, 2020.

[54] M. Lyu, W. Shi, and L. A. Rusch, "Silicon photonic subsystem for broadband and rof detection while enabling carrier reuse," *Optics Express*, vol. 28, no. 10, pp. 14897–14907, 2020.

[55] Y.-H. Chen, K.-H. Chen, J.-H. Yan, T. A. Nguyen, K.-M. Feng, and M.-C. M. Lee, "Integrated Tunable Sideband Suppressor for Optical Carrier Reuse in Millimeter-Wave Radio-Over-Fiber Transmission," *Journal of Lightwave Technology*, vol. 40, no. 9, pp. 2696–2702, 2022.

[56] B. R. Koch, E. J. Norberg, B. Kim, J. Hutchinson, J.-H. Shin, G. Fish, and A. Fang, "Integrated silicon photonic laser sources for telecom and datacom," in *Optical Fiber Communication Conference*, pp. PDP5C–8, Optica Publishing Group, 2013.

[57] W. Shi, Y. Xu, H. Sepehrian, S. LaRochelle, and L. A. Rusch, "Silicon photonic modulators for PAM transmissions," *Journal of Optics*, vol. 20, no. 8, p. 083002, 2018.

[58] C. Browning, Q. Cheng, N. C. Abrams, M. Ruffini, L. Y. Dai, L. P. Barry, and K. Bergman, "A silicon photonic switching platform for flexible converged centralized-radio access networking," *Journal of Lightwave Technology*, vol. 38, no. 19, pp. 5386–5392, 2020.

[59] C. Browning, A. Gazman, N. Abrams, K. Bergman, and L. P. Barry, "256/64-QAM multicarrier analog radio-over-fiber modulation using a linear differential drive silicon Mach-Zehnder modulator," in *2018 International Topical Meeting on Microwave Photonics (MWP)*, pp. 1–4, IEEE, 2018.

[60] E. Ruggeri, C. Vagionas, R. Maximidis, G. Kalfas, D. Spasopoulos, N. Terzenidis, R. M. Oldenbeuving, P. W. van Dijk, C. G. Roeloffzen, N. Pleros, *et al.*, "Reconfigurable Fiber Wireless fronthaul

with A-RoF and D-RoF co-existence through a Si3N4 ROADM for Heterogeneous mmWave 5G C-RANs," *Journal of Lightwave Technology*, vol. 40, no. 16, pp. 5514–5521, 2022.

Chapter 2

Optical Fronthaul Technologies & Architectures

As discussed in the introduction, the growing number of device connections is fueling a demand for increased capacity, which is driving the development of capacity-enhancing techniques and technologies in access networks and datacenters. As an illustration of this trend, [1] shows a remarkable 100-fold increase in the number of 5G connections between 2019 and 2023, from 13 million to 1.4 billion. This chapter begins by exploring methods for enhancing capacity in both wireless and optical networks. As the standardization of millimeter-wave and terahertz (THz) range frequencies for 5G and 6G networks has been proposed by organizations such as ITU and IEEE, it is crucial to discuss the ways in which these high-frequency carriers can help augment network capacity. Therefore, the first section of this chapter offers a brief discussion of this topic. The next section delves into the techniques for improving the spectral efficiency of high-frequency links through the implementation of advanced single and multi-carrier advanced modulation formats. Finally, the chapter presents a comprehensive overview of three cutting-edge optical-wireless convergence technologies, namely ARoF, optical heterodyning, and flexible optical sources.

2.1 Capacity Enhancement Techniques

2.1.1 Millimeter Wave

In mobile communications, a shift of information carriers from microwave frequencies (3G, 4G and 5G) to mmWave and THz frequencies (5G and 6G) is seen due to many reasons. Firstly, the availability of a vast amount of spectrum at these higher frequencies including the free license band at 60 GHz. Secondly, frequency reuse is possible as the transmission range for mmWave and THz is short because of high atmospheric attenuation and penetration losses. Thirdly, higher frequencies correspond to shorter wavelengths and hence the antenna size is smaller, allowing complex antenna arrays to be built on PCBs or chips more easily [2]. A peak datarate of 20 Gbps can be achieved with mmWave communication and massive antenna arrays [3]. An electromagnetic spectrum is shown in Fig. 2.1.

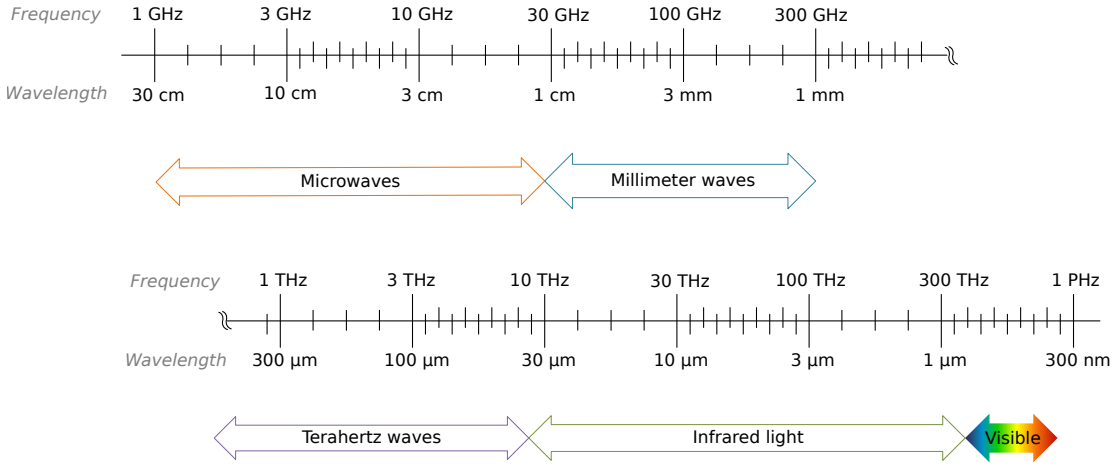

Fig. 2.1: Electromagnetic spectrum.

Looking ahead to 2030, the rapid growth of technologies like virtual reality (VR), vehicle-to-vehicle, tropospheric vehicular networks, lower earth orbit (LEO) satellite networks, and oceanic information networks will eventually saturate the 5G network [4]. Therefore, 6G performance specifications will exceed the datarates and bandwidths provided by 5G, with the network expected to be an intelligent mobile communication platform. THz frequencies have been proposed as a potential addition to the frequency bands for 6G communications [5, 4]. The Horizon 2020 program by the European Commis-

sion has sponsored various beyond 5G projects, including TERRANOVA, which aims to achieve Tb/s wireless connectivity through innovative THz technologies, to provide optical network-like quality of experience in beyond 5G systems [3]. Further European research activities into high capacity THz links for 6G mobile are currently underway through the Smart Network and Services Joint Understanding (SNS JU) between the European Commission and 6G Industry Association (6G-IA) [6].

The use of mmWave communications has already been standardized as a physical layer option for wireless personal area networks (WPAN) in IEEE 802.15 Task Group 3c (TG3c) at the 57–64 GHz band, as well as for short-range applications like wireless docking and display in IEEE 802.11ad (WiGig) at 60 GHz [2]. 5G New Radio (NR) has been divided into two bands by the Third Generation Partnership Project (3GPP). The first band is referred to as the FR1 band, spanning from 410 to 7125 MHz, while the second band is commonly known as the mmWave band or FR2 band, covering a range from 24.25 to 52.6 GHz [7]. Apart from the limited frequency bands at 3.5 GHz and 4.9 GHz, numerous countries have made available a range of mmWave bands for 5G New Radio (5G NR) communications in the Ka-band, Q-band, and even E-band [8].

The beyond 5G wireless network will require support for significantly higher mobile data volume, more connected devices, higher user data rates, longer battery life for low-power devices, and reduced end-to-end delay compared to 4G networks. An approach to combine of mmWave systems and small cell technology is promising to meet these requirements. However, there are still challenges to overcome, such as providing scalable, affordable, and flexible mobile back/front/mid-haul (X-haul) to connect high-capacity small cells back into the metro/core network [9, 2].

The demand for high-speed data transfer has led to the development of spectrally efficient mmWave communication. The 60 GHz unlicensed wireless mmWave band provides around 7 GHz of bandwidth [10]. This increased bandwidth allows for higher data transfer rates, but it also requires more efficient utilization of the available spectrum. In order to achieve data rates of 100 Gbps, a spectral efficiency of at least 14 bit/s/Hz is needed, which means for every Hz of bandwidth, at least 14 bits of information must be transmitted. However, current modulation techniques and transceiver components are not capable of achieving this level of spectral efficiency [5]. Hence, the focus on advanced modula-

tion formats has become a necessity for achieving higher spectral efficiency, which will be discussed in the next section.

2.1.2 Advanced Modulation formats

Encoding information on RF or optical carriers by their modulation enables the transmission of information over long distances and the study and development of data modulation techniques has always been the center of attention for the network operators and the research community in both wireless and optical networks. A comprehensive study of new modulation techniques deployed in a network and a comparative analysis of different modulation techniques based on service delivered (type of service delivered in a network entails its capacity, latency and budget) is useful in selecting the most suited modulation format for a given networking application. The flowchart, see Fig. 2.2, presents a broad classification of the types of modulation techniques that are analog and digital modulation. Under analog modulation there are two main categories: continuous wave (CW) and pulse modulation. In CW modulation an analog signal alters the amplitude (AM), phase (PM) or frequency (FM) of another higher frequency CW analog signal which carries the information end-to-end in a network. Pulse modulation is a technique where an analog information signal is sampled and the resulting samples modulate a pulse train that serves as a carrier. In pulse modulation, the amplitude, duration, or position of the pulses in the pulse train are varied to represent the amplitude or value of the samples, which allows the analog signal to be transmitted as a series of pulses. The amplitude variation of the pulse is two levels for Non-Return-to-Zero (NRZ) and Return-to-Zero (RZ) pulse modulation techniques, while in Pulse Amplitude Modulation (PAM), multiple levels can be assigned to represent a greater range of analog signal amplitudes. An analog Quadrature Amplitude modulation (QAM) operates by transmitting AM signals on the in-phase and quadrature components of the same carrier frequency [11].

Digital modulation techniques are classified based on the number of bits that form a symbol. The modulation schemes where a binary digit (or bit) information stream consisting of an array of 0s and 1s, modulates the amplitude, phase and frequency of a higher frequency CW analog signal are called Amplitude Shift Keying (ASK), Phase Shift Keying (PSK) and Frequency Shift Keying (FSK), respectively. A symbol consisting of two

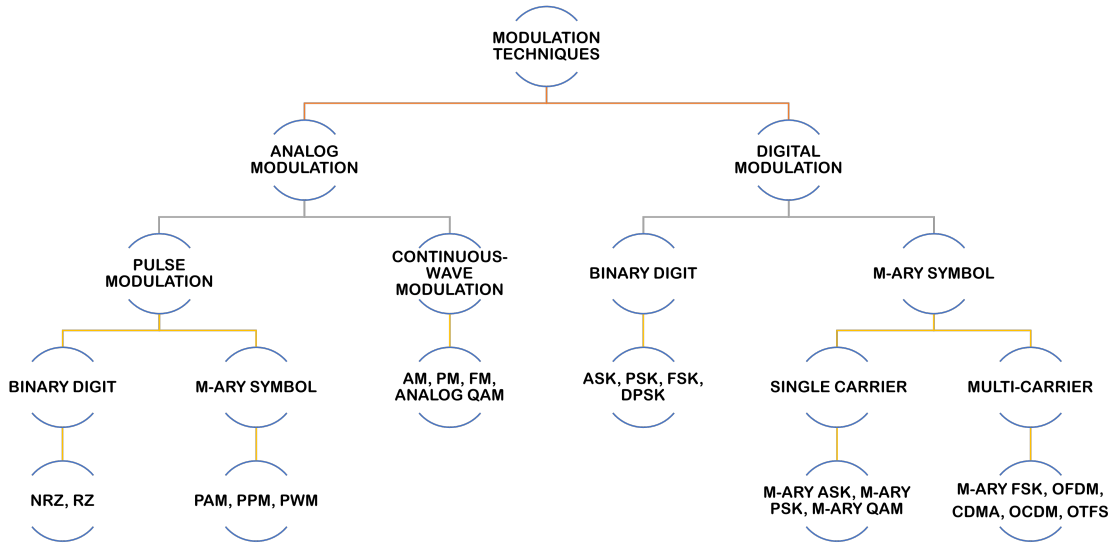

Fig. 2.2: Classification of modulation formats based on the type of information, carrier and number of bits.

or more bits of information is called an M-ary symbol, where M represents the number of bits conveyed by each symbol. When an analog carrier signal is modulated with M-ary symbols for amplitude, phase, or frequency, the modulation technique is called M-ary ASK, M-ary PSK, or M-ary FSK, respectively. If the amplitude and phase of an analog carrier signal are simultaneously modulated by an M-ary symbol, the technique is called M-ary QAM.

In a multi-carrier modulation, a large bandwidth is divided into smaller sub-bands (also called subcarriers), and each sub-band is modulated with information. Modulating the subcarriers with M-ary symbols leads to modulation techniques such as M-ary FSK, Frequency Division Multiplexing (FDM), Orthogonal Frequency Division Multiplexing (OFDM), Code Division Multiple Access (CDMA), Optical Code Division Multiplexing (OCDM), and Orthogonal Time Frequency Space (OTFS). For traditional multi-carrier modulation formats, such as M-ary FSK and FDM, the range of frequency components used can lead to a relatively large bandwidth occupation. To improve spectral efficiency, orthogonality is introduced between the adjacent frequency components in a given frequency band. Orthogonality means that the product of cross-correlation between the two adjacent frequencies is zero. The most widely used multi-carrier modulation technique is

OFDM. In OFDM, the transmission frequency band is divided into multiple subcarriers and each subcarrier is orthogonal (in frequency) to each other. Therefore, the orthogonality principle allows OFDM subcarriers to overlap with one another without impacting detection - thereby facilitating enhanced spectral efficiency. These orthogonal subcarriers are modulated using a digital modulation scheme, like QAM, and transmitted simultaneously. The next two subsections discuss single and multi-carrier modulation schemes suitable for various applications in the context of a converged network.

2.1.2.1 Pulse Amplitude Modulation

PAM is a single optical carrier multi-level modulation scheme and has become a successor to NRZ in today's DC networks and Gigabit Ethernet standards as discussed previously in sections 1.3 and 1.2, respectively. Figure 2.3(a) shows a two-level NRZ encoding scheme at a symbol rate of 10 GBd, where each symbol represents one bit and thus the datarate of this signal is 10 Gbps. The two-level NRZ signal has one eye opening as shown in Fig. 2.3(b) and the information bit '0' or '1' is assigned amplitude values of either -1 or 1, see 2.3(c). The PAM-4 signal encodes one symbol with two bits, i.e. '00', '01','10' and '11' and has four distinct levels as shown in Fig. 2.4(a), doubling its spectral efficiency with respect to NRZ at the same symbol rate - with a 10 GBd PAM-4 signal equating to a data rate of 20 Gb/s. The PAM-4 eye diagram, see Fig. 2.4(b), portrays four distinct levels, with the amplitude difference between each level reduced to 1/3 that of the NRZ eye.

As discussed in the previous subsection 2.1.1, ETC has standardized the specification for 800 GbE which is achieved using two 400 GbE interfaces. The IEEE Standard 802.3bs includes the adoption of 4×100G (4 wavelength channels each carrying 100 Gbps) PAM-4 with intensity modulation and direct detection (IM/DD) as a standardized solution for the 400 GbE interface [12]. IEEE working groups have standardized 400G transceivers that apply 4×100G PAM-4 or 8×50G PAM-4 technology [13, 12, 14, 15].

In an effort to further increase spectral efficiency while maintaining the simplicity and cost effectiveness of IM/DD solutions, many recent research works, including work here presented later in chapter 5, have proposed the use of 8-level PAM for both datacenter and access applications [16, 17, 18, 19]. With a PAM-8 signal each symbol represents three bits, forming an 8-level encoding scheme with each level conveying '000', '001',

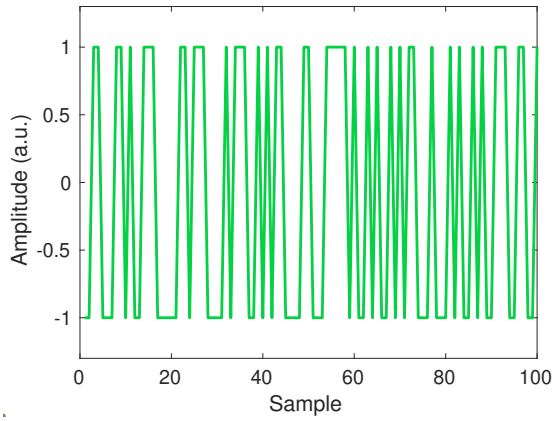

(a) NRZ time domain signal representation

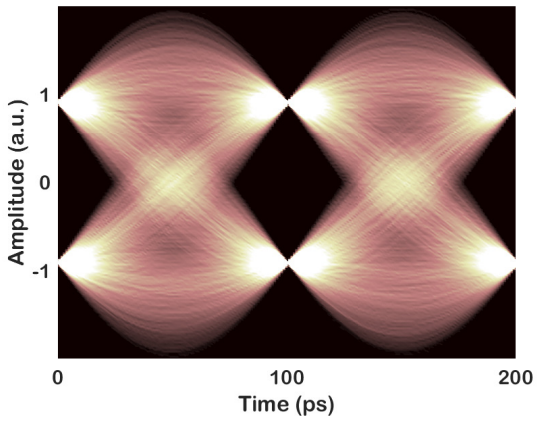

(b) Eye diagram of NRZ

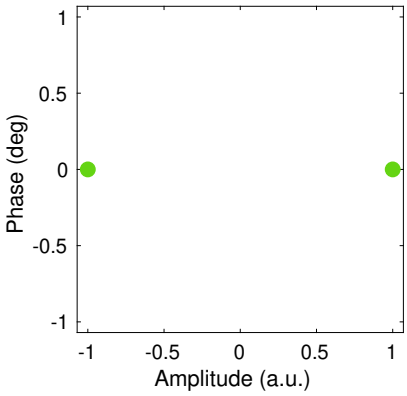

(c) Constellation of NRZ

Fig. 2.3: NRZ signal with 10 GBd symbol rate and 10 Gbps datarate.

‘010’, ‘011’,‘100’, ‘101’, ‘110’, or ‘111’, tripling its spectral efficiency with respect to NRZ. For example, a 10 GBd NRZ and PAM-8 signals (shown in Fig. 2.5(b)) will have the same spectral occupancy but with data rates of 10 Gbps and 30 Gbps, respectively. This is formulated using $D = Slog_2M$, where D is the datarate, S is the symbol rate and M is the number of levels of symbols in a modulation scheme.

An eye diagram of 10 GBd PAM-8 signal, in Fig. 2.5(c), shows overlapped symbols of the PAM-8 signal in one symbol time period, depicting eight distinct levels. As the number of levels in the eye diagram quadruples with respect to the equivalent NRZ signal, the difference, in terms of amplitude, between each level is reduced to 1/7 that of NRZ; ultimately placing a much higher requirement on channel signal-to-noise ratio (SNR) for comparative performance.

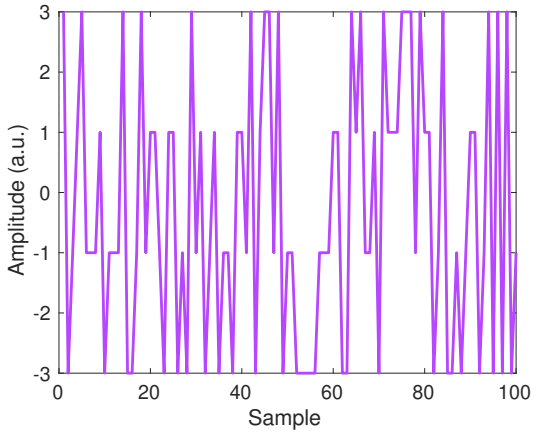

(a) PAM-4 time domain signal representation

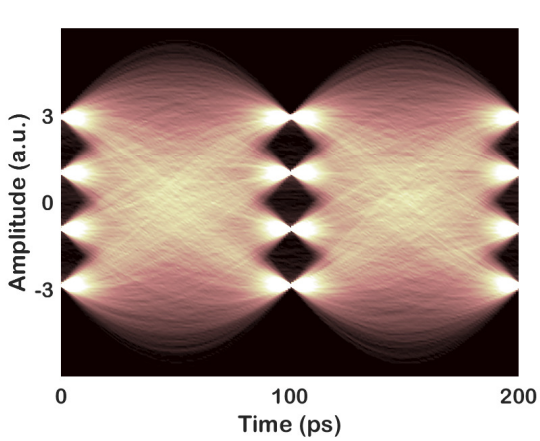

(b) Eye diagram of PAM-4

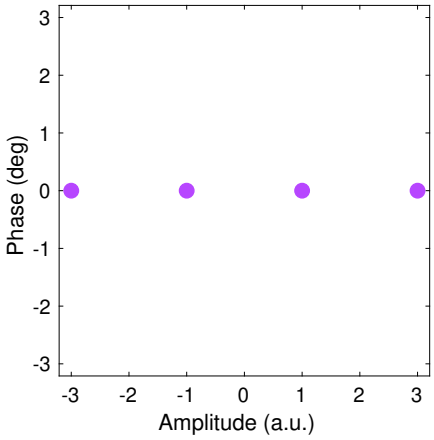

(c) Scatter plot of PAM-4

Fig. 2.4: PAM-4 signal with 10 GBd symbol rate and 20 Gbps datarate.

Telecommunication systems often face a trade-off between the need to increase the datarate per channel while also expanding the number of channels. In order to increase the datarate of a signal, the bandwidth must be increased. However, as the bandwidth is widened, the number of channels that can be accommodated simultaneously within a fixed frequency band decreases. To help strike a balance between maximizing data rate and optimizing channel quantity in telecommunications systems, pulse shaping/filtering of single-carrier modulation signals can be used to restrict the signal's bandwidth without loss of information. Nyquist pulse shaping is a solution that can be utilized for these scenarios, where the information carrying signal is band-limited by a filter whose cut-off frequency is set at the Nyquist frequency - which is half the signal's baud rate. This technique increases the efficiency of the system by achieving a desired finite transmission

bandwidth while eliminating inter-symbol interference (ISI) introduced by the channel. A system employing Nyquist criteria for zero ISI has absolute finite bandwidth but the

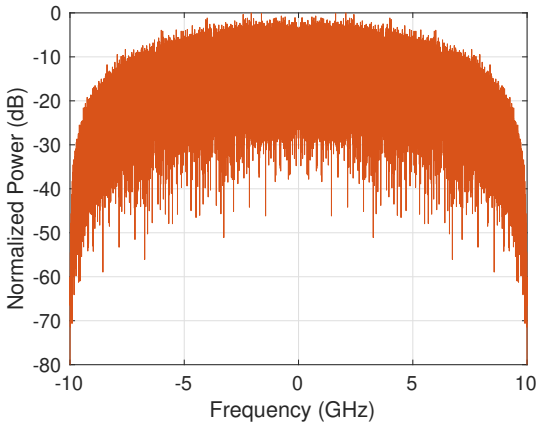

(a) PAM-8 frequency spectrum

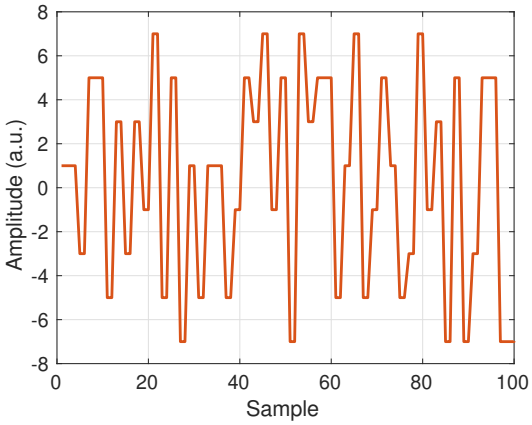

(b) PAM-8 time domain signal representation

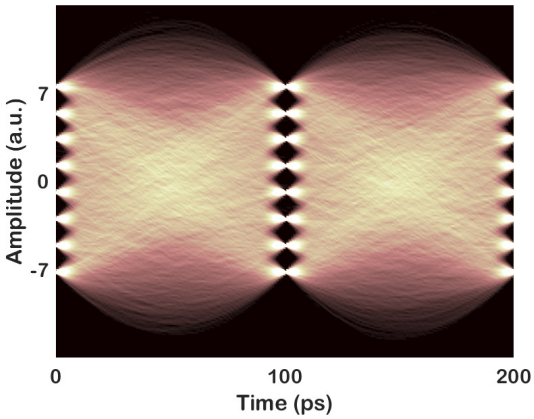

(c) Eye diagram of PAM-8

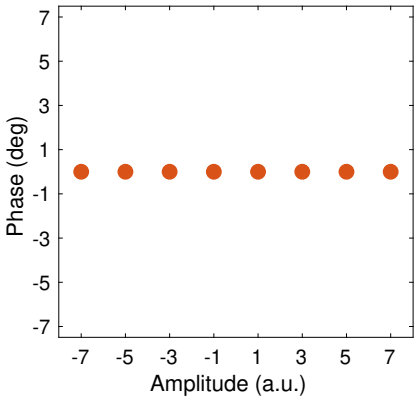

(d) Scatter plot of PAM-8

Fig. 2.5: PAM-8 signal with 10 GBd symbol rate and 30 Gbps datarate.

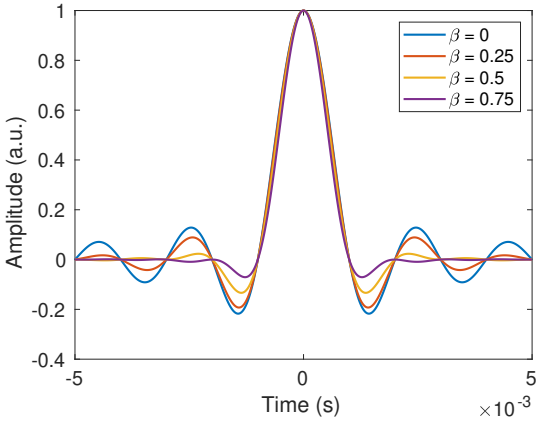

(a) Time domain

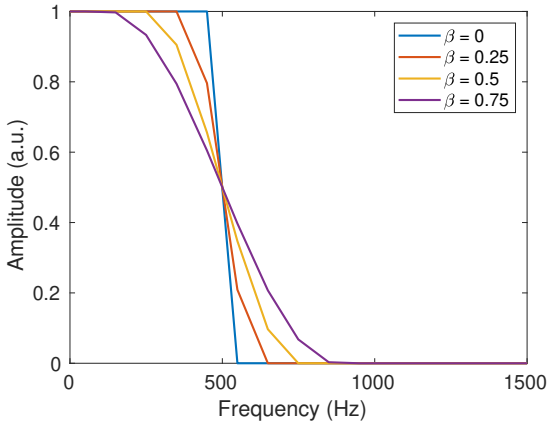

(b) Frequency Domain

Fig. 2.6: Raised cosine filter profiles for different values of roll-off β for symbol duration T= 1 ms and sampling frequency of 100 kHz.

corresponding time waveform is non-causal and lasts infinitely, hence such systems are not physically realizable.

The raised cosine filter implementation is portrayed in Fig. 2.6, where time and frequency domain filter profiles are shown in Fig. 2.6 (a) and (b) respectively. Raised cosine filtering when implemented on the signal in the frequency domain for infinite bandwidth, a fast rate decay in the time domain is ensured. Observing the curves with $\beta = 0.75$ in Fig. 2.6, it is inferred that the smoother the roll-off in the frequency domain, the faster is decaying of Sinc pulse in the time domain. However, for the limited bandwidth signal utilized in the system, the Sinc pulse in the time domain must be truncated finitely to some length sufficiently enough to have a small ISI. The equation of the raised cosine filter coefficient (h_{rc}) is given below:

Time Domain representation of raised cosine filter coefficient $h_{rc}(t)$:

$$h_{rc}(t) = \frac{\sin(\pi t/T)}{\pi t/T} \cdot \frac{\cos\left(\frac{\pi\beta t}{T}\right)}{1-\left(\frac{\pi\beta t}{T}\right)^2} \tag{2.1}$$

Frequency Domain representation of raised cosine filter coefficient $H_{rc}(f)$:

$$H_{rc}(f) = \begin{cases} T & \text{for } 0 \le |f| \le \frac{1-\beta}{2T} \\ \frac{T}{2} \cdot \left[1+\cos\left(\frac{\pi T}{\beta} \cdot (|f| - \frac{1-\beta}{2T})\right)\right] & \text{for } \frac{1-\beta}{2T} < |f| \le \frac{1+\beta}{2T} \\ 0 & \text{for } |f| > \frac{1+\beta}{2T} \end{cases} \tag{2.2}$$

where T is the symbol period and β is the roll-off factor. The steepness of the slope of the roll off is defined by the roll-off factor β of the filter function and also controls the bandwidth of the filter. It is typically a value between 0 and 1, where 0 corresponds to a rectangular pulse shape and 0.75 corresponds to the slowest roll-off as shown in Fig. 2.6. The bandwidth of the spectrum is given as:

$$BW_{baseband} = \frac{1+\beta}{2T} \tag{2.3}$$

$$BW_{passband} = \frac{1+\beta}{T} \tag{2.4}$$

By keeping the bandwidth of the filter at Nyquist frequency, i.e. setting the cutoff fre-

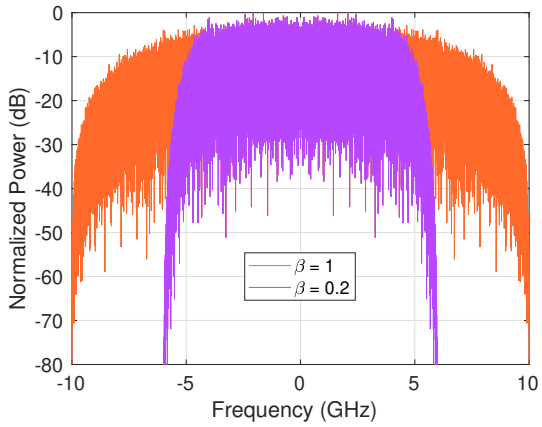

Fig. 2.7: Filtered frequency spectrum of PAM-8 signal.

quency of the filter to a frequency equal to half the signal's symbol rate - the 3 dB point of the signal - the filtered signal is attenuated by approximately 50% in terms of power and 70.7% in terms of voltage (root mean square). This attenuation level of power/voltage represents a reasonable compromise between preserving signal power/voltage and increasing the channel capacity. At frequencies below the 3 dB point, the filter allows the signal to pass with minimal distortion, ensuring that essential information is preserved. The frequencies above the 3 dB point are attenuated, band-limiting the signal and preventing aliasing or ISI. For example, Fig. 2.7 shows a raised cosine filter applied to a PAM-8 signal with $\beta = 0.2$ and $\beta = 1$ showing the bandwidth difference of $\sim$4 GHz. The β of 1 preserves the original bandwidth of the signal. However, the β of 0.2 reduces the bandwidth of the 10 GBd signal to $\sim$ 6 GHz, which is close to the Nyquist frequency, i.e. 5 GHz for this 10 GBd signal. However, this reduces the optical signal to noise ratio (OSNR) of the filtered signal compared to the unfiltered signal, causing degradation of Bit Error Rate (BER) versus the received optical power performance of the filtered signal.

From the standpoint of high datarate FDM-based PAM transmission: taking a standard 10 GBd PAM-8 signal, depicted in Fig. 2.8 (a), and filtering in the manner described above, allows the transmission of an increased number of channels within the fixed frequency band as shown in Fig. 2.8 (b). The unfiltered 10 GBd PAM-8 signal occupies 20 GHz of bandwidth whereas the filtered 10 GBd PAM-8 signal with the roll-off factor of the filter, β, is 0.2 occupies $\sim$ 12 GHz. This bandwidth can further be reduced by reducing the value of β to 0.1.

Another way to mitigate channel distortion and ISI on the received signal is by employing the least mean square (LMS) equalization. LMS equalization is a widely used adaptive equalization technique in digital communication systems. LMS equalization can be particularly effective in PAM systems where the ISI can be significant and difficult to remove using the traditional single-tap equalization technique, where channel estimate is a ratio of received and transmitted training sequences. The adaptive nature of the LMS algorithm allows it to adapt to changes in the channel response over time, making it well-suited for applications where the channel conditions may be dynamic.

A block diagram of an adaptive filter is shown in Fig. 2.9. The input signal to the linear filter is denoted as x(n), while the corresponding output signal is y(n). The adaptive

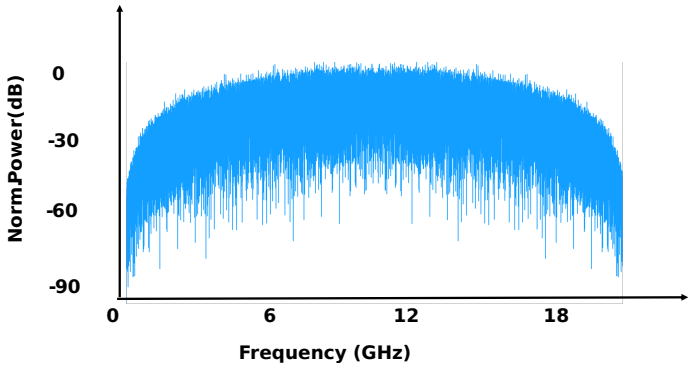

(a) Unfilterd 10 GBd PAM-8 signal

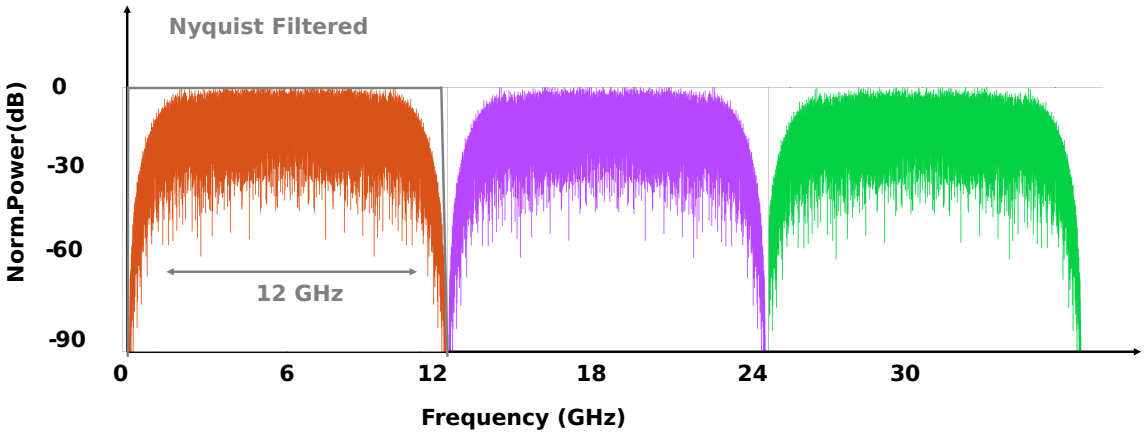

(b) Nyquist filtered 10 GBd PAM-8 signal

Fig. 2.8: Representation of enhancement of spectral efficiency using Nyquist filtering, further increasing the number of channels within a fixed frequency range.

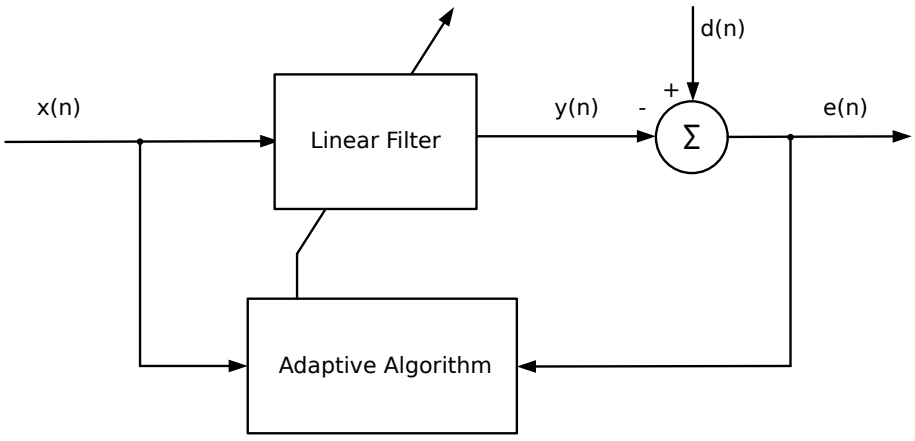

Fig. 2.9: Adaptive filter.

filter also takes an additional input signal d(n), which is the desired or primary input that is the error-free training sequence and generates an error signal e(n) which represents the difference between d(n) and y(n) and is used to adjust the weights of the equalizer. The

adaptive filter can utilize different filter types, such as finite impulse response (FIR) or infinite impulse response (IIR) filters, and the coefficients of the linear filter are adjusted iteratively by an adaptive algorithm to minimize the mean square power of the error signal e(n). To update the coefficients of an adaptive FIR filter using the LMS algorithm, the adaptive filter:

1. Calculates the output signal y(n) from the FIR filter using the filter input vector $x(n) = [x(n)x(n-1)...x(n-N+1)]^T$ and the filter coefficients vector $w(n) = [w_0(n)w_1(n)...w_{N-1}]^T$. The output signal is $y(n) = w^T(n)\,x(n)$.

2. Calculates the error signal $e(n)$ using the equation $e(n) = d(n) - y(n)$.

3. Updates the filter coefficients by using the equation $w(n+1) = w(n) + \mu\, e(n)\, x(n)$, where μ is the step size parameter of the adaptive filter.

The step size in the LMS algorithm plays a crucial role and needs to be carefully adjusted. A small step size ensures low excess mean square error but leads to slow convergence. On the other hand, a large step size enables fast adaptation but may compromise stability. Adjusting the step size dynamically during the adaptation process based on specific characteristics of the system, such as bit error rate, allows for improved system performance and stability [20].

2.1.2.2 Orthogonal Frequency Division Multiplexing

OFDM is a multicarrier modulation technique used to transmit data over orthogonal subcarriers such that the frequency spectrum is used efficiently. Data is split into parallel streams and each OFDM symbol comprises a number of orthogonal frequencies carrying each data stream. This results in a relatively long symbol period compared to a serial system having the same total datarate. Symbols with a long time duration are less affected by ISI and require relatively simple frequency domain equalization. In addition, a guard band interval called a cyclic prefix (CP) is added to each OFDM symbol. Implementing a CP involves taking a copy of a portion of the end of a given OFDM symbol and appending it to the beginning of that symbol. Originally used to combat multi-path effects wireless channels, the CP serves to eliminate the effects of ISI and intra-symbol interference and

can be effectively used to overcome the effects of dispersion in optical fiber - provided a prefix of sufficient length is designated. Unlike FDM, the orthogonality of the carrier frequencies avoids the requirement for frequency guard bands between OFDM subcarriers, enabling them to overlap. The spectrum of each OFDM subcarrier has a Sinc function shape with significant side lobes over a frequency range. This results in the overlapping of many subcarriers across the OFDM signal bandwidth. For this reason, OFDM is sensitive to frequency offset and phase noise [21].

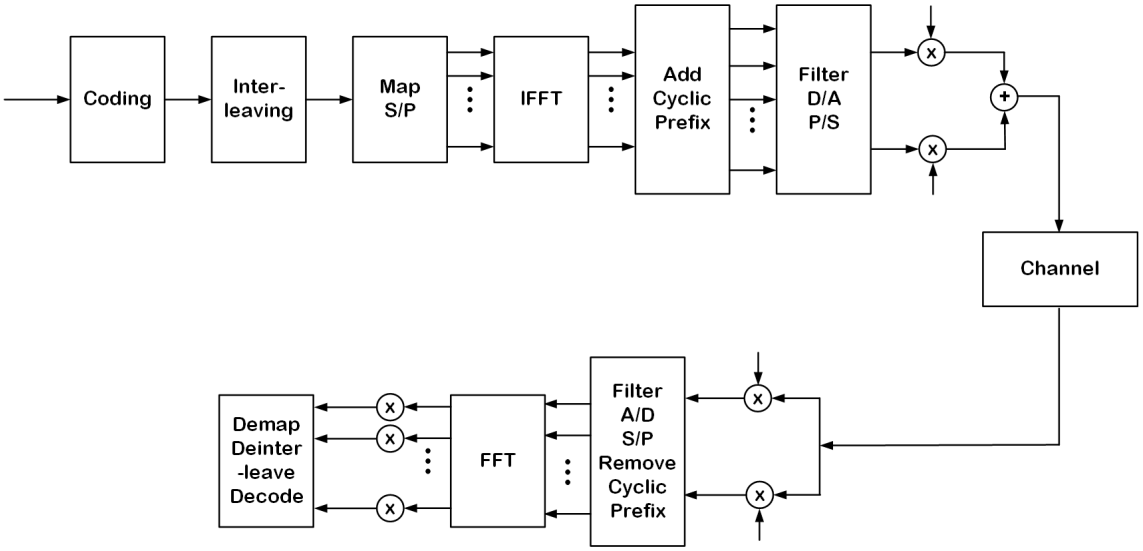

Fig. 2.10: OFDM modulation and demodulation [21].

A block diagram of the OFDM modulation and demodulation processes is shown in Fig 2.10. The OFDM symbols are generated by modulating a set of subcarriers by data streams. Before the modulation process, the serial data is coded, typically in the form of QAM data symbols, and interleaved before conversion into parallel streams as shown by the serial-to-parallel (S/P) operation at the transmitter side (see in Fig. 2.11 parallel OFDM symbols). The parallel data streams are passed through the inverse fast Fourier transform (IFFT). The input of the IFFT is the complex vector $X = [X_0\ X_1\ ...\ X_{N-1}]^T$, where each entry in the vector X typically represents complex valued QAM symbols and N is the size of the IFFT. The time domain output symbol is described through the discrete version of the IFFT (IDFT):

$$x_m = \frac{1}{\sqrt{N}} \sum_{k=0}^{N-1} X_k \, exp\left(\frac{j2\pi km}{N}\right) \qquad \text{for } 0 \leq m \leq N-1 \tag{2.5}$$

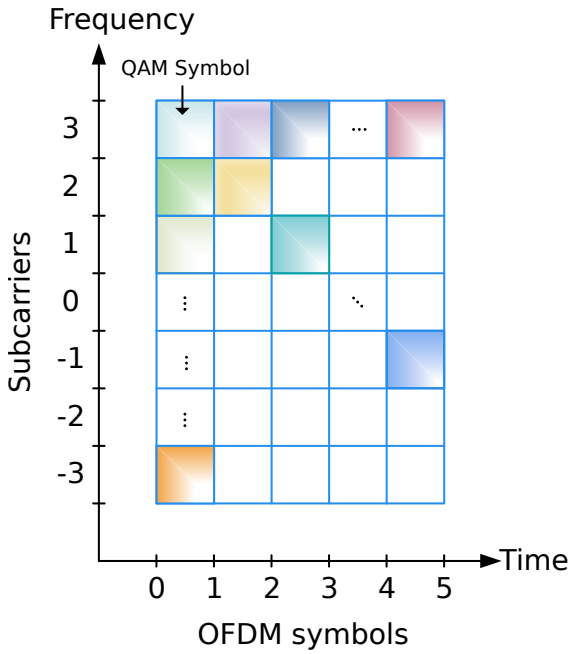

Fig. 2.11: Representation of a block of OFDM symbols with each subcarrier modulated by a QAM symbol.

This operation modulates the frequency domain (FD) inputs (i.e. the QAM symbols X_k) onto a set of orthogonal subcarriers which are then multiplexed to form the output time domain (TD) signal. Unused subcarrier frequencies are nulled by using zeros as inputs to the corresponding IFFT frequency bins (i.e. setting $X_k = 0$ where desired). This operation is equivalent to oversampling the signal in the TD. Zero padding in the FD in this way is an advantageous feature because it performs flexible subcarrier nulling and oversampling in one operation (through the IFFT). Also, because it is implemented in the FD (on a subcarrier basis) it means that non-integer oversampling can be easily achieved, without having to perform time consuming up and down sampling processes which are required for TD resampling. After the IFFT operation, the CP is added and the signal is transformed from parallel to serial (P/S) data stream. The transmitted sequence with CP is $x_{CP}(i) = [x_{N-G}(i) \ldots x_{N-1}(i), x_0(i) \ldots x_{N-1}(i)]^T$, where G is the length of CP. The in-phase (I) and quadrature (Q) components of the complex TD OFDM signal are up-converted by mixing with the I and Q components of an RF (typically intermediate frequency) carrier, respectively, before recombination to form a real valued signal ready for transmission. A 390 MHz bandwidth OFDM signal is depicted in Fig. 2.12 (a) and (b) in the time and frequency domain, respectively and Fig. 2.12 (c) shows a constellation of the signal.

For optical IM/DD systems, the I and Q components of the OFDM signal are added and used to modulate an optical carrier, transmitted over an optical fiber channel and directly detected using a standard photodiode. At the receiver side, the electrical signal is filtered, the I and Q components are separated and down-converted. The signal is then converted into parallel streams of OFDM symbols and each (time domain OFDM) symbol's CP is removed. The OFDM symbols, $y = [y_0\ y_1\ ...\ y_{N-1}]^T$, are passed through fast Fourier transform (FFT), resulting in a complex vector

$$Y_k = \frac{1}{\sqrt{N}} \sum_{m=0}^{N-1} y_m\, exp\left(\frac{-j2\pi km}{N}\right) \qquad \text{for } 0 \leq k \leq N-1 \tag{2.6}$$

where Y_k represents the received complex (QAM) symbols. The channel estimation and equalization are applied to the received QAM symbols and binary data is produced after the removal of zeroes and QAM demodulation.

A single tap equalization is used to recover the transmitted data from the received signal by calculating the channel estimate H_k which is the ratio of the transmitted/desired training sequence X_k^{TS} and the received training sequence Y_k^{TS} in the frequency domain. The channel estimate is expressed as:

$$H_k = \frac{Y_k^{TS}}{X_k^{TS}} \tag{2.7}$$

Therefore at the receiver side, the effect of channel H_k and the addition of noise W_k on the received signal will be:

$$Y_k = H_K X_k + W_k \tag{2.8}$$

After equalization, the recovered transmitted signal $\hat{X_k}$ is represented as:

$$\hat{X_k} = \frac{Y_k}{H_k} = X_k + \frac{W_k}{H_k} \tag{2.9}$$

The setback of single-tap equalization is that if the H_k is very small, the noise is enhanced.

Noise Processes associated with optical OFDM systems: The main disadvantage of optical OFDM generation is the peak-to-average power ratio (PAPR) and sensitivity to phase noise and frequency offset. PAPR refers to the ratio between the maximum power

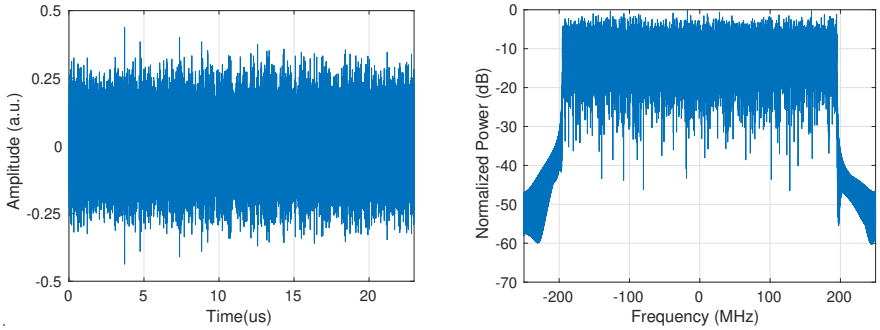

(a) OFDM in time domain (b) OFDM in frequency domain

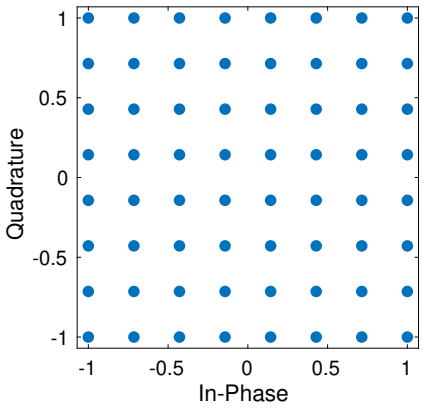

(c) Constellation of 64-QAM OFDM

Fig. 2.12: Time and frequency domain representation of 390 MHz wide OFDM with 1600 subcarriers and datarate of 2.3 Gbps with 64-QAM constellation diagram.

level of the OFDM signal and its average power level. In OFDM systems, the modulation scheme inherently requires the addition of many subcarriers which often leads to signal peaks that can be significantly higher than the average power level and can be observed in Fig. 2.12 (a). The high power peaks can cause distortion and nonlinearity in optical amplifiers (and indeed electrical amplifiers at the transmit and receive sides of the communication system). When the signal peaks exceed the amplification range or saturation level of the amplifier, it can introduce unwanted out-of-band (OOB) power. This OOB power can result in interference with neighboring channels or spectral regions, leading to degraded system performance and potential interference with other systems. Addressing the PAPR issue in optical OFDM systems is crucial to mitigate the adverse effects of high power peaks.

Clipping is a simplistic technique that is typically implemented to reduce the PAPR

and involves limiting the signal amplitude to a maximum level set by a defined threshold. This clipping process helps reduce the dynamic range of the signal, effectively lowering the PAPR. Aside from helping to overcome non-linear distortion effects, clipping is an effective way to prevent distortion caused by exceeding the dynamic range of digital-to-analog converters (DACs) and analog-to-digital converters (ADCs), ensuring relatively greater utilization of the available quantization levels.

Optical OFDM systems are also sensitive to phase noise and frequency offset. Variations in the frequency and phase of the receiver's local oscillator (LO) with respect to the carrier of the received signal can cause a loss of orthogonality between subcarriers, negatively impacting system performance. Phase noise refers to random fluctuations in the phase of the transmitted signal, which can impair the detection and decoding of data at the receiver. Both phase noise and frequency offset can cause inter-carrier interference (ICI) in OFDM systems, resulting in a degradation of the BER performance.

The relationship between the time variation of phase and its effect on the received constellation can be described as follows:

1. *Phase Errors*: When there are phase errors in the received signal, the QAM constellation points may rotate or shift from their ideal positions. This rotation or shifting can result in ISI and cause the received symbols to deviate from their intended locations as shown in the example 4-QAM signal constellation diagram in Fig. 2.13. If the rotation is enough to displace the received symbol sufficiently far away from its ideal location, the receiver may not be capable of accurately decoding the symbol. For a fixed phase error θ_0, the received OFDM symbols will be $y_m = x_m e^{j\theta_0}$ and their FFT will be $Y_k = X_k e^{j\theta_0}$.

2. *Frequency Errors*: Frequency errors can cause a time-varying phase shift in the received signal. This time-varying phase shift introduces phase variations that affect the positioning of the constellation points over time. The amount of phase variation depends on the rate of change of frequency error. If the frequency error is large or changes rapidly, the constellation points may undergo several rotations, leading to symbol overlapping and increased error rates. For a fixed frequency offset Δf between transmitter and receiver, whose center frequency is f_c, the shifted frequency

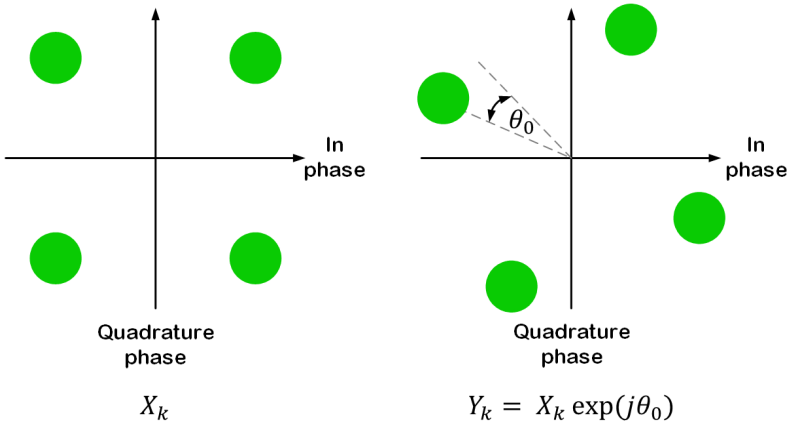

Fig. 2.13: QAM-4 constellation rotation due to phase noise.

is given by $f_r = f_c + \Delta f$ and the corresponding linear variation of phase $\theta(t)$ with respect to time is $\theta(t) = \Delta f t$.

Channel Estimation: The insertion of training symbols (TS) to the OFDM signal at the transmitter facilitates channel estimation. As previously discussed in section 2.1.2, channel estimation provides important information about the transmission channel and enables efficient digital compensation of optical transmission impairments such as chromatic dispersion (CD) and polarization-mode dispersion (PMD). The accuracy of channel estimation in optical transmission systems is frequently hindered by the presence of optical noise. To enhance the precision of channel estimation, a technique known as time-domain averaging is employed. Equation 2.7 above, and the related discussion, describes how channel estimates can be obtained through the use of an OFDM TS. Obtaining many channel estimates in this manner, using TSs at different time intervals in the OFDM signal allows the construction of a channel matrix as shown in Fig. 2.14. The time-domain averaging approach involves averaging the channel matrices obtained, in time, for each frequency subcarrier as shown in Fig. 2.14. This means that the averaging is done over consecutive channel estimates, to achieve the channel estimation based on the temporal variations of channel response. However, utilizing multiple training symbols necessitates additional transmission overhead, decreasing the overall throughput of the system. To address this issue, an intra-symbol frequency-domain averaging (ISFA) based method was proposed [22]. In this method, the averaging is performed over the estimated channel matrices $H_{k,n}^{ISFA}$ for multiple adjacent frequency subcarriers k in the same training symbol n,

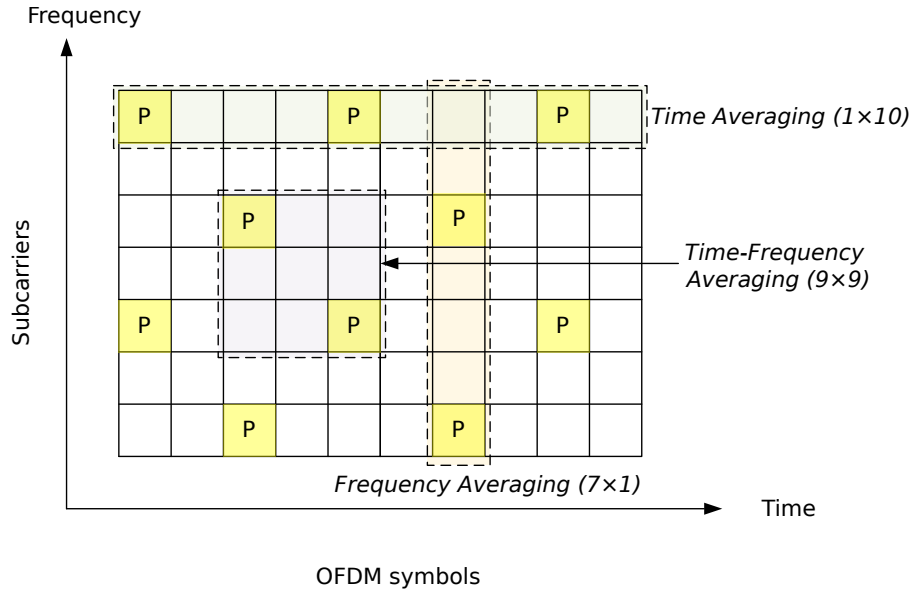

Fig. 2.14: Representation of time-averaging, frequency-averaging and time-frequency averaging channel estimation techniques [23]. Here 'P' indicates the beginning of the training symbols.

instead of using multiple training symbols as shown in Fig. 2.14. This approach reduces overhead and simplifies processing. Hence, ISFA can provide more accurate channel estimation with reduced overhead compared to time-based averaging, as it leverages the inherent frequency correlations within the symbol, assuming that the channel variations are relatively small over the neighboring subcarriers within the same symbol. The ISFA process can be represented by the following equations:

The frequency domain representation of the signal received at the OFDM receiver:

$$Y_{k,n} = H_{k,n} X_{k,n} + W_{k,n} \tag{2.10}$$

where $Y_{k,n}$ is the received signal on subcarrier k in symbol n, $X_{k,n}$ is the transmitted signal on subcarrier k in symbol n, $H_{k,n}$ is the channel response on subcarrier k in symbol n, and $W_{k,n}$ is the complex Gaussian noise on subcarrier k in symbol n. The ISFA method involves averaging the estimated channel response matrices for adjacent subcarriers within the same TS:

$$H_{k,m}^{ISFA} = \frac{1}{L} \sum_{l=-\frac{L-1}{2}}^{\frac{L-1}{2}} H_{k+l,m} \tag{2.11}$$

In this equation, $H_{k,m}^{ISFA}$ represents the estimated channel response for subcarrier k in

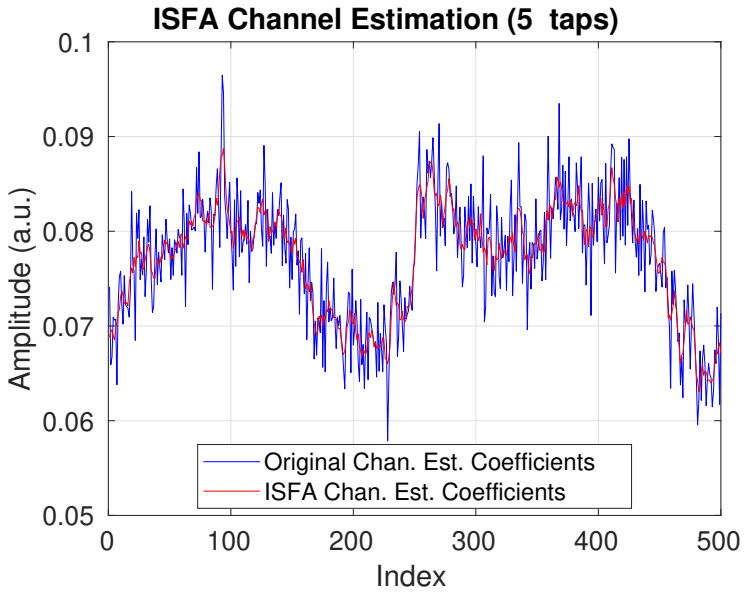

Fig. 2.15: A comparison between single tap equalizer, shown in blue, and ISFA equalizer, shown in red.

symbol m using the ISFA method. The averaging window spans L subcarriers, where L is an odd number. The index l ranges from $-\frac{L-1}{2}$ to $\frac{L-1}{2}$, indicating the subcarriers included in the averaging window. The channel response for each of these subcarriers, $H_{k+l,m}$, is summed up and then divided by L to obtain the averaged channel response $H_{k,m}^{ISFA}$. This process averages out noise effects giving a smoother channel estimate that is more representative of the actual channel response, compared to a non-averaged variant as shown in Fig. 2.15. The improved estimated channel response using the ISFA method is then used to equalize the received signal for data detection:

$$\hat{X}_{k,n} = \frac{Y_{k,n}}{H_{k,n}^{ISFA}} \tag{2.12}$$

where $\hat{X}_{k,n}$ is the equalized data on subcarrier k in symbol n.

This technique is used to compensate for the distortion introduced by the channel during transmission. The idea is to undo the effects of the channel on the received signal by applying an inverse channel response. The resulting equalized signal should closely resemble the original transmitted signal. It is noteworthy that ISFA is most effective on channels with frequency dependent variation than time-domain averaging, however for linear channels the effectiveness of ISFA and time-domain averaging is very similar for

the same averaging window size [24]. Moreover, the window size of the ISFA must be optimized to minimize the BER of the recovered signal without losing frequency resolution for transmission through a highly frequency dependent channel noise [24]. Another averaging technique that can be used is time-frequency averaging, depicted in Fig. 2.14, which gives an estimate of both time and frequency varying channels. This technique is deployed in LTE technology.

2.2 Convergence Technologies and Architectures

In this section, convergence techniques that enable the seamless integration of wireless and optical networks are explored. The primary objective of achieving true convergence is to effectively transport wireless signal information over the existing or future optical transport infrastructure. It is essential to note that wireless access networks require the transmission of both mobile and fixed broadband data and, due to the high capacity and vast bandwidth requirements of modern communication systems, optical transport systems prove to be the most viable solution for efficiently carrying such large volumes of data. The information from wireless signals can be modulated onto an optical carrier in various ways, each offering its own advantages and considerations. These methods encompass different approaches to encode and transmit the wireless signal information over the optical medium, ensuring optimal performance and compatibility with the existing network infrastructure.

In this section, the generation of mmWave/THz using optical heterodyning - a vital support for high-speed wireless communications- is discussed initially. Optical heterodyning for the generation of frequencies covering the wide range of mmWave/THz bands mainly relies on the utilization of flexible optical sources. These sources, which can include various types of lasers and integrated optical devices enable tunable carrier generation, offering versatility and adaptability to different applications and system requirements.

Finally, an extensive discussion on various RoF technologies is given. By employing advanced techniques and technologies, RoF enables the transmission of mmWave signals over optical fibers, effectively harnessing the benefits of both wireless and optical domains. Later, the evolution of RAN architecture to facilitate the widespread deployment of (mmWave enabled) remote antenna sites and support for efficient network management is discussed. The role of C-RAN architecture in supporting the integration of wireless and optical networks is further highlighted. Additionally, the challenges and impairments associated with transporting analog data signals over an optical channel are examined, with the strategies for their mitigating also discussed. Through a comprehensive examination of these topics, insight will be provided into the convergence of future optical and wireless

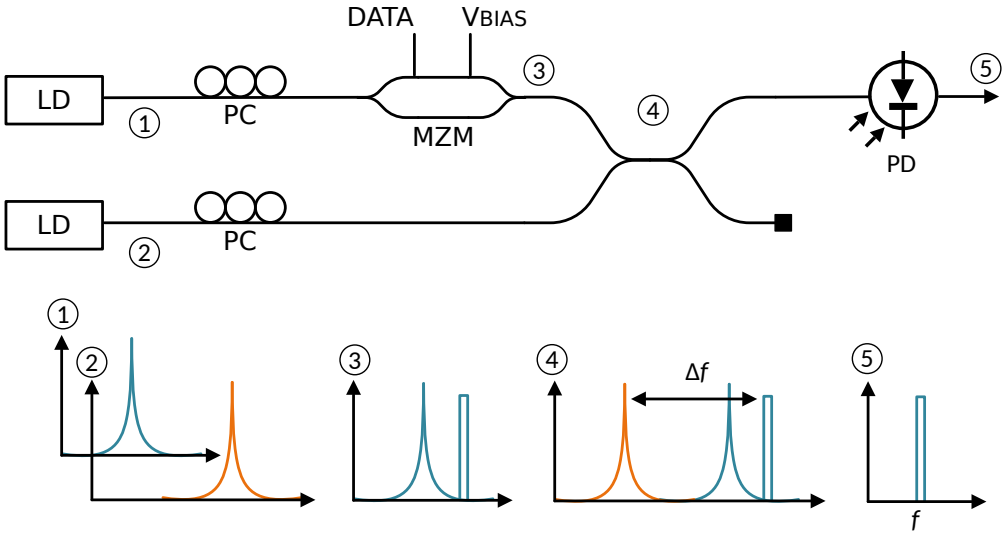

Fig. 2.16: Generation of mm-wave using optical heterodyning.

networks and the methods employed to maximize their potential.

2.2.1 Optical Heterodyning

The recent inclusion of mmWave frequencies in 5G specifications has paved the way for the widespread commercialization and deployment of mobile communications systems, initially utilizing carrier frequencies between 25 and 39 GHz. The enormous bandwidth demands envisioned for future applications such as autonomous vehicles (AV) and virtual reality (VR), coupled with the continued proliferation of small cell antenna sites, means that the expansion to higher mmWave, and even THz, frequencies is inevitable as we transition to the next generation of mobile communications [25].

The extent to which mmWave communications can be leveraged for future wireless systems depends greatly on the ability to easily generate mmWave frequency carriers. The difficulty and expense currently associated with generating high quality carriers in this frequency range, by purely electronic means, hinder the potential wide deployment of these systems. An alternative method for mmWave generation is optical heterodyning (depicted in Fig. 2.16) which involves the photo-mixing of two optical components, spaced by a mmWave frequency 'Δf', on a high speed Photo Diode (PD) - producing a beat term mmWave carrier/signal 'f' at the output of the PD. The photodetector produces a photocurrent that is proportional to the total optical intensity falling on it, i.e. the square

of the total electric field amplitude and can be described as follows:

$$I_{PD} \propto [E_3 cos(\omega_3 t + \phi_3) + E_2 cos(\omega_2 t + \phi_2)]^2 \tag{2.13}$$

$$I_{PD} \propto E_3^2 cos^2(\omega_3 t + \phi_3) + E_2^2 cos^2(\omega_2 t + \phi_2) + 2E_3 E_2 cos(\omega_3 t + \phi_3) cos(\omega_2 t + \phi_2) \tag{2.14}$$

The

$$I_{PD} \propto \frac{1}{2}E_3^2 + \frac{1}{2}E_2^2 + 2E_3 E_2 cos(\omega_3 t + \phi_3) cos(\omega_2 t + \phi_2) \tag{2.15}$$

where E_3, ω_3 and ϕ_3 are the electric field amplitude, angular frequency and phase components of the modulated optical carrier (spectrum numbered '3' in Fig. 2.16) and E_2, ω_2 and ϕ_2 are the electric field amplitude, angular frequency and phase components of the unmodulated optical carrier (spectrum numbered '2' in Fig. 2.16). Ignoring the part of the signal that lies outside the bandwidth of the PD, the resulting heterodyned signal has the power proportional to the product of the electric field amplitudes and at the frequencies $(\omega_3 t + \phi_3)$ and $(\omega_2 t + \phi_2)$. If the phase component of both the optical carriers is equal, i.e. $\phi_3 = \phi_2 = \phi$, the resulting signal using the trigonometric identity $cosAcosB = \frac{1}{2}cos(A-B) + \frac{1}{2}cos(A+B)$ is

$$I_{PD} \propto 2E_3 E_2 (\frac{1}{2}cos((\omega_3 + \omega_2)t + 2\phi) + \frac{1}{2}cos((\omega_3 - \omega_2)t) \tag{2.16}$$

The above equation shows the heterodyned signal where the desired frequency component is $E_3 E_2 cos((\omega_3 - \omega_2)t)$ at a frequency $(\omega_3 - \omega_2)$ shown as spectrum numbered '5' in Fig. 2.16.

Through the deployment of tunable optical sources in such a heterodyne system, the relative ease of optical carrier generation, operation over a wide bandwidth/frequency range, avoidance of costly high frequency electronic components and the continued development of small form factor integrated microwave/mmWave photonic components makes heterodyning a highly promising contender for high frequency communications in the 5G and 6G eras [26, 27]. Indeed, the inherent compatibility of optical heterodyning with optical distribution and transport makes it a prime candidate for use in future converged networks.

In the context of optical heterodyne systems, high frequency radio carriers can be

produced by the use of optical carrier pairs which may or may not be coherent with one another:

1. **Coherent optical sources**: When optical carriers derived from the same optical source (e.g. from an optical comb source - see section 2.2.1.1) beat at the PD, and have no relative path difference after transmission, a stable and pure RF signal is generated at the output of the PD. This occurs in part because the phase noise of both the optical carriers are inherently matched leading to optical phase noise cancellation as the carriers undergo mixing through the heterodyne process. In addition, as the optical carriers originate from the same source, they have the same thermal drift resulting in a fixed frequency difference between the optical carriers. Heterodyning of such a pair, therefore, results in an RF beat signal with a high level of frequency stability (i.e. no frequency offset). It is important to note that if the relative path difference approaches the coherence length of the optical carriers, it can add phase noise to the RF beat signal. Even though comb sources produce low noise RF beat signals, they have limited variability in frequency separation and wavelength tunability.

2. **Non-coherent optical sources**: When two optical carriers generated from independent laser sources beat at the PD, an RF signal with phase noise and frequency offset is produced. The phase noise of each of the optical carriers is different and adds up to form the total phase noise of the RF beat signal. Moreover, the thermal drift of each laser is different, hence the frequency of the RF signal drifts over time (i.e. time varying frequency offset). These considerations effectively mean that the lasers with low phase noise and high stability are required for high performance optical heterodyne systems [27, 28] - impacting their relative cost and complexity. In general, the advantage of using non-coherent independent tunable sources for optical heterodyning is that a variable frequency separation can be achieved such that an RF beat signal across mmWave, sub-THz and THz ranges can be easily generated.

2.2.1.1 Optical Frequency Combs

An optical frequency comb (OFC) generates a series of equidistant optical carriers with a fixed frequency separation and correlated phase. Figure 2.17 illustrates an example of such a source's spectral output. The properties of OFCs are commonly characterized by their carrier spacing (f_r), also known as the free spectral range (FSR), and the measure of coherence between the carriers, called the offset frequency (f_0). The n is the number of optical modes generated by the comb source and the frequency of the nth optical mode is given by $f_n = nf_r + f_0$. The multiple lines in the optical frequency domain correspond to a train of very short optical pulses in the time domain, with a repetition rate of $T_r = 1/f_r$. The width of these pulses represents the spectral bandwidth of the optical frequency comb, meaning that a narrower pulse corresponds to a broader spectral range for the comb. OFCs are widely deployed for the generation of highly spectrally efficient superchannels. A combination of multiple optical carriers that are closely spaced in the spectrum can be encoded with higher order modulation formats to form superchannels. These superchannels fulfill the previously mentioned bandwidth requirements with transmission rates exceeding 100 Gb/s per channel, while simultaneously maximizing spectral efficiency.

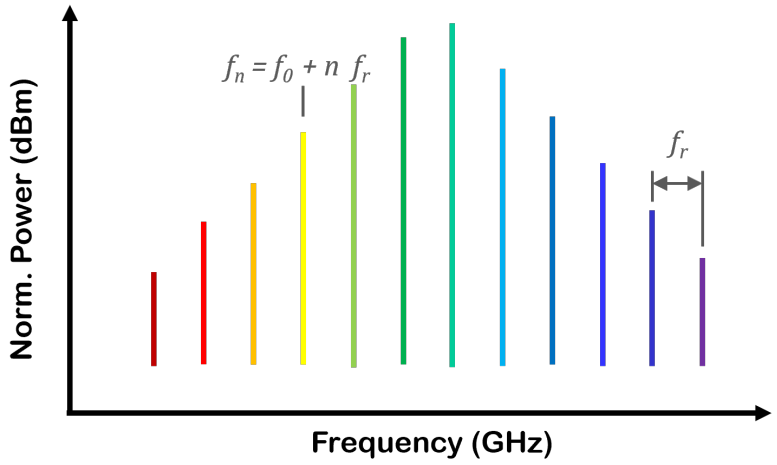

Fig. 2.17: Representation of an optical frequency comb source.

OFCs ensure a consistent and stable frequency separation between the optical carriers, enabling the reduction or elimination of guard bands in advanced WDM systems and facilitating compensation for fiber nonlinearities. When the input power to a fiber exceeds

a certain threshold, nonlinearities arise and distort the transmitted information irreparably. However, the phase correlation among the optical carriers in OFCs can be utilized to mitigate these nonlinear effects and significantly recover the transmitted data. This phase correlation is crucial for pushing the limits of fiber transmission capacity and distance beyond previously estimated boundaries, as demonstrated in the referenced article [29]. Moreover, OFCs offer a limited degree of flexibility in the FSR, making it straightforward to adapt a single source to different modulation formats and symbol rates, as discussed in another study [30]. Some of the technologies used for generating optical frequency combs include mode-locking, Kerr effect in microresonators, parametric processes, electro-optic modulation, and gain switching [31, 32, 33].

2.2.1.2 Flexible Optical Sources

Optical devices based on photonic integration have shown the potential to be a key element of evolved optical networks and have drawn a lot of attention in recent years. Increasingly, flexible optical technologies such as tunable lasers, optical switch fabrics and active remote nodes are being proposed as a means to incorporate high bandwidth and low latency WDM networking in the access domain [34, 35, 36, 37]. From the perspective of a converged network operating in such a dynamic environment, the ability to assign pairs of optical carriers in a flexible manner across a wide wavelength range for remote mmWave carrier generation would be highly advantageous.

A discrete approach to optical heterodyning involves the use of two independent tunable lasers whose wavelengths are separated by the desired mmWave frequency. This method can provide a high level of tunability – but such operation typically requires the use of bulky and expensive sources as well as phase locking. Comb based solutions such as gain-switched optical frequency combs (GS-OFCs) [38] and mode locked lasers (MLLs) [39] can provide pairs of coherent carriers for heterodyning but lack a high degree of tunability in operational wavelength and carrier frequency spacing, respectively. Integrated dual laser solutions providing higher levels of tunability have also been proposed using two distributed Bragg reflector (DBR) lasers [40, 41] with Carpintero et al. showing flexible THz operation on a hybrid InP-polymer platform. The advantages of SiP are exploited by Hulme et al. [42] demonstrating mmWave carrier generation from 1-112

GHz with a wavelength tuning range of 42 nm using a dual external cavity laser (ECL) integrated SiP circuit.

SiP integrated circuits (PICs) are preferable to discrete semiconductor devices due to their compact size, high yield, and potentially lower cost [43]. As mentioned in section 1.5, the development of optical sources, modulators and detectors with Si, that are compatible with CMOS processing, have the potential to enable fully integrated transceiver solutions and are the subject of many research with various approaches described in [44, 45, 46]. Outside of the SiP approach, compact laser designs such as the fiber Bragg grating (FBG)-based sources in [47] provide extremely low RIN (- 165 dBc/Hz), while the liquid crystal-based device in [48] gives full C-band tunability.

2.2.2 Radio over Fiber Technologies

RoF is a communication technology that uses optical fiber to transmit RF signals over long distances. The basic idea behind RoF is to convert the RF signals into optical signals and then transmit them over the optical fiber, where they experience low loss and enhanced channel capacity. At the receiving end, the optical signals are converted back into RF signals for further processing and transmission. The congestion in the lower microwave frequencies by the increasing demand for wireless bandwidth has created a significant strain on the lower microwave spectral region. As a result, there has been a push to transition wireless operations to the mmWave region, which offers a substantial bandwidth advantage. One of the ways to modulate the IF signal onto the mmWave carrier is achieved by using optical heterodyning in conjunction with ARoF technology which is discussed in detail in section 3.2.

Radio-over-Fiber transport schemes: There are three types of transport schemes in RoF: baseband-over-fiber, RF-over-fiber and intermediate frequency(IF)-over-fiber. These schemes are visually represented in Fig. 2.18, illustrating their respective architectures and signal flow.

- **Baseband-over-fiber** – In this scheme, also referred to as DRoF, single carrier binary modulated signals are typically transmitted over fiber. In the downstream (core/metro network to antenna site), the ethernet signal that arrives at the CO is

re-framed and converted from electrical to optical (E-O) signal for binary transmission (NRZ/RZ) over the optical channel to the antenna site where the DU and RU are located. At the antenna site, the received optical signal is converted to an electrical (O-E conversion) signal by a PD and modulated into an OFDM signal. The resulting digital signal is converted to an analog signal through a DAC. This signal is filtered, upconverted using an RF carrier, amplified and transmitted via an an-

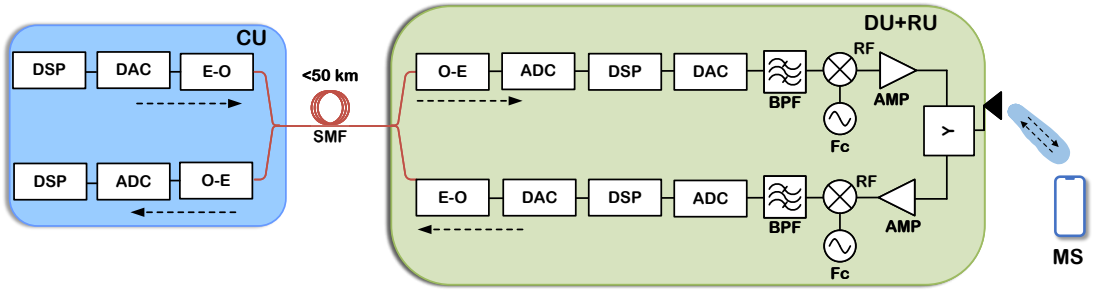

(a) DRoF

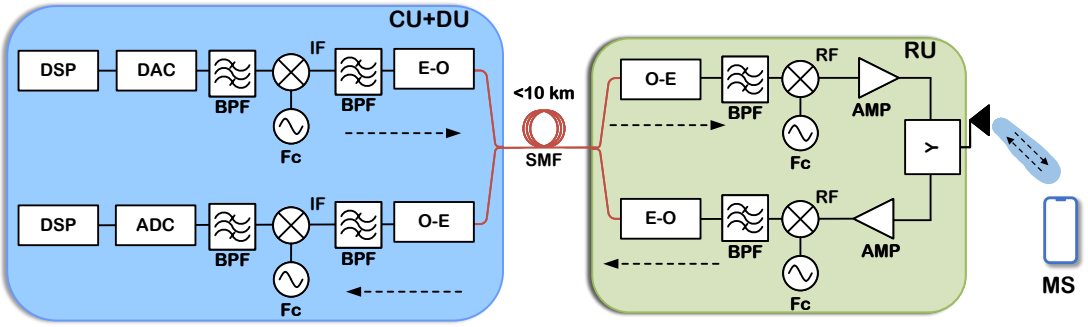

(b) IFoF

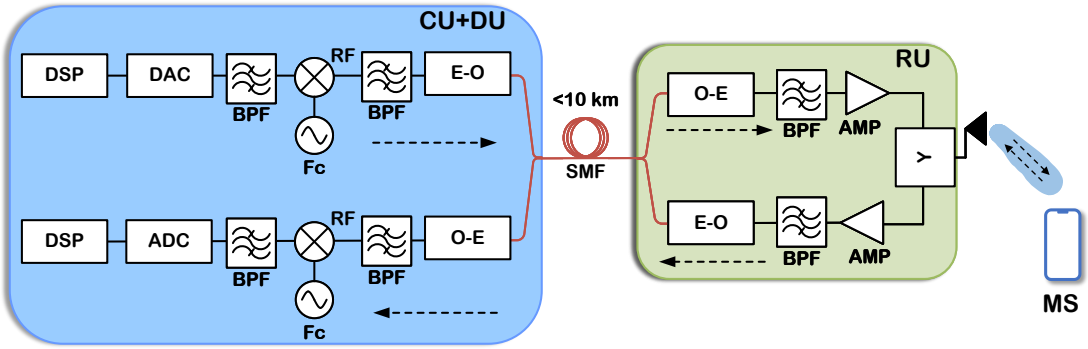

(c) RFoF

Fig. 2.18: Transport of baseband signal over fiber in DRoF scheme and wireless signals over fiber in ARoF scheme.

tenna to the mobile station (MS). The schematic is depicted in Fig. 2.18 (a). In the upstream (antenna site to core/metro network), RF signals (OFDM) from MS are downconverted and demodulated at the RU and DU. After E-O, the binary stream is used to modulate an optical carrier for transmission back to the CO. The DRoF approach benefits from using relatively low speed optoelectronic devices and minimizes the effect of fiber chromatic dispersion as the transmission bandwidths are typically < 20 GHz. However, inefficiencies associated with the requirement to digitize multi-carrier mobile signals to a binary level, remote digital signal processing the additional cost of up/down-conversion processes required at the antenna site, all detract from the DRoF scheme and hinder its ability to facilitate network scaling.

- **IF-over-fiber** – The IF-over-fiber (IFoF) scheme involves modulation of an optical carrier with the information carrying IF signal as shown in Fig. 2.18 (b). In the downstream, the ethernet to baseband signal re-framing, digital to analog conversion, filtering and upconversion to an IF carrier takes place. Then the IF signal is modulated onto an optical carrier before being transmitted over the optical fiber. At the antenna site, the signal undergoes O-E conversion, filtering, upconversion to an RF/mmWave frequency and amplification before being transmitted wirelessly by an antenna to the MS. In upstream, the RF signal from the MS is downconverted to IF, amplified and filtered before the E-O conversion and optical transmission back to CO. This approach allows flexibility in the assigned carrier frequency over the optical channel which has two main advantages: (i) IFs can be chosen such that they are supported by limited RF bandwidth characteristics of low cost optical modulators and PDs and (ii) multiple RF signals can be assigned different IFs allowing electrical domain multiplexing before optical transmission. The latter allows scaling of the transport capacity of a single optical carrier in the converged network.

- **RF-over-fiber** – In the RF-over-fiber (RFoF) scheme is similar to IFoF, however, the microwave/mmWave signals at the desired wireless transmission frequency are directly modulated onto an optical carrier for fiber transmission. Compared to other schemes, this approach completely eliminates the need for frequency upconversion or downconversion at the remote antenna sites (see Fig. 2.18 (c)), simplifying the

overall system design. However, implementing RFoF systems requires high-speed PDs and optical modulators, which can increase the implementation cost. Additionally, the presence of fiber chromatic dispersion poses a challenge in RFoF links and limits the optical transmission distance. Chromatic dispersion is prominent in longer fiber lengths and higher frequency signals, resulting in dispersive fading that further degrades SNR and overall link performance of RFoF signal [49, 50, 51].

The RFoF and IFoF are collectively called ARoF as the signal modulating the optical carrier is a product of continuous-wave (IF or RF) modulation technique (see Fig. 2.2). Table 2.1 showcases the classification of RoF based on the modulation formats employed for modulating the optical carrier. As mentioned earlier, DRoF systems make use of baseband modulation formats, whereas ARoF systems employ modulation formats with single or multiple RF carriers. A detailed comparison between the ARoF and DRoF schemes is discussed in the next section.

2.2.2.1 Evolution of RoF's competing schemes: ARoF and DRoF

In its early stages, the primary goal of RoF technology was to address the problem of spectral congestion in the lower microwave frequency range. It aimed to provide an effective solution for distributing mmWave signals over optical fiber, offering advantages over traditional over-the-air transmissions that suffer from high propagation losses. By combining the strengths of both wireless and optical technologies, RoF had the potential to unify core/metro networks into a converged infrastructure supporting both wireless and wired connectivity.

During the mid-2000s, the rapid expansion of optical fiber networks prompted extensive research on RoF technology, with a focus on utilizing existing optical metro WDM

Table 2.1: Classification of RoF based on the modulation formats

RoF	Modulation Formats
DRoF	NRZ, RZ, PAM, PPM, PWM
ARoF	AM, PM, FM, ANALOG QAM, ASK, PSK, FSK, DPSK, M-ARY ASK, M-ARY PSK, M-ARY QAM, M-ARY FSK, OFDM, CDMA, OCDM, OTFS

and PON infrastructures. As a solution to address nonlinearity in analog optical links, the concept of DRoF transport emerged. The aspect of transporting information at higher datarates is somewhat fulfilled by the DRoF technology in 5G networks. DRoF transport formed the basis for standards such as Common Public Radio Interface (CPRI) and Open Base Station Architecture Initiative (OBSAI), where wireless signals were directly digitized and transmitted over optical links. The CPRI is a protocol used for transmitting data between the BBU and the remote RU in a DRAN. It enables the efficient transfer of digital signals carrying both control and user data over a fronthaul link. In multi-sector and multi-antenna configurations, the total bit rate for the CPRI fronthaul links can be calculated using the formula:

$$B_{CPRI} = 2\,S\,A\,f_s\,b_s\,(16/15)\,LC \tag{2.17}$$

where S is the number of sectors (part of the hexagonal cell) in configuration, A is the number of antennas per sector, f_s is the sample rate, which is typically 15.36 MS/s per 10 MHz of radio bandwidth, b_s is the number of bits per sample. For LTE, this is usually 15 bits, while for UMTS, it is 8 bits [52]. The factor '2' accounts for the separate processing of the in-phase I and Q samples and '16/15' represents the additional overhead information in the CPRI protocol. LC is the line coding factor, which is either 10/8 or 66/64, depending on the chosen CPRI net bit rate option. By plugging in the appropriate values for S, A, f_s, b_s, and LC, the total bit rate for the CPRI fronthaul links in the given configuration can be calculated.

By mid 2010s, research on RoF technology shifted its focus toward strategies for achieving ultra-high-speed wireless transmission. This shift was driven by the growing demand for seamless wireless connectivity due to the widespread use of affordable smart portable devices. The 4G Long-Term Evolution-Advanced (LTE-A) mobile network deployed CPRI based DRoF fronthaul in a D-RAN architecture as shown in Fig. 2.19. However, this transmission method suffers from low bandwidth efficiency due to the requirement to transmit IQ baseband binary signal samples. As a result, the effective data rate of the transport is decreased [53, 54]. The authors in Ref. [52], have shown the aggregate CPRI for 3 sector LTE antenna sites at different radio bandwidths in Fig. 2.20.

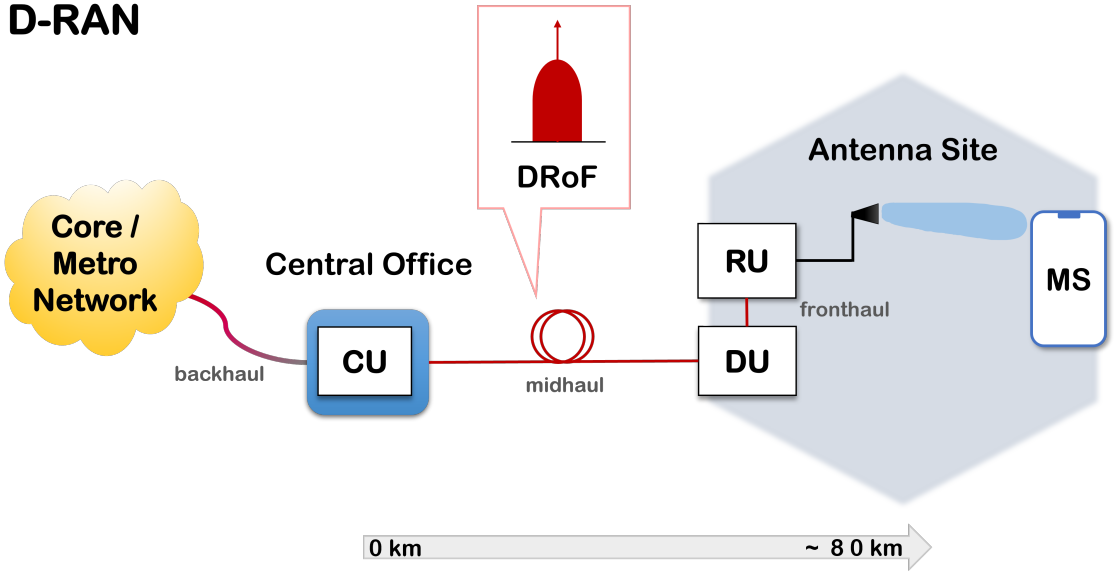

Fig. 2.19: D-RAN RoF transport scheme.

The graph shows that in a high connectivity configuration of three sectors, eight antennas, and a 100 MHz bandwidth, the required CPRI line rate is 148 Gb/s, which is clearly prohibitively high in the context of widely deployed and low cost RoF systems. Therefore, in order to facilitate the scaling of the network (5G and 6G), in terms of both antenna deployment and overall capacity, changes to traditional binary level DRoF techniques are required.

In recent years, extensive research in the field of DRoF has been undertaken to overcome its limitations, including CPRI compression and flexible quantization algorithms, aimed at enhancing spectral efficiency and addressing the bandwidth challenge [55]. This has led to the emergence of Enhanced CPRI (eCPRI) standard which can increase the efficiency of DRoF fronthaul links by enabling flexible assignment processing functions between the access network units. Researchers have also explored various approaches to digitized transport, considering different sampling theories [56]. This approach has proven highly efficient for distributing wireless signals in the lower microwave frequency range, thanks to the widespread availability and maturity of DACs and ADCs. However, its applicability for mmWave signal distribution is still constrained by the availability and affordability of suitable ADC/DAC components [49]. Within this context, many recent works have proposed the use of more advanced single and multi-carrier modulation formats, broadly categorized as DRoF and ARoF, respectively, for fronthaul transmission

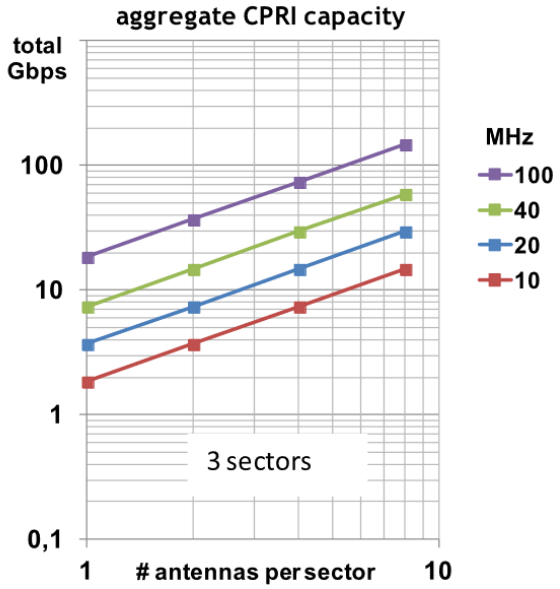

Fig. 2.20: The combined CPRI line rates for a site with three sectors versus the number of antennas used for various radio bandwidths [52].

[57, 58, 59].

There has been a growing interest in utilizing RoF technology as an analog transport scheme, particularly with the advancements and standardization efforts for 5G networks. ARoF is increasingly seen as a viable option for mobile fronthaul systems, potentially serving as a far more spectrally efficient alternative to CPRI transport. As capacity becomes the key driving factor behind network evolution, the necessity (for today's DRoF technologies) to digitize wireless signal to a binary level for optical fronthaul acts as a bottleneck. In the context of converged networking for mobile fronthaul, ARoF entails the transmission of the mobile signal (typically OFDM) in its native format. This allows the avoidance of DACs/ADCs at the remote site and also exploits the inherent high spectral efficiency of the wireless multi-carrier modulation format. Ultimately these factors facilitate network scaling and reduced RU cost and complexity. These factors, coupled with future network capacity requirements, make ARoF an even more attractive option for future mobile fronthaul systems underpinning beyond 5G and 6G [49].

2.2.2.2 ARoF in C-RANs

The mobile traffic growth and introduction of highly data driven technologies have led to a rapid expansion of wireless networks. This demand for high capacity mandates the use

of optical fiber infrastructure for transporting radio signals as it offers several advantages and enables new architectural configurations. Furthermore, to support high antenna site proliferation, a vast number of small cells (micro- and picocells) and high traffic flow in the 5G networks, there is a shift to C-RAN architectures that are in convergence with the optical fiber infrastructures. For network operators, it is vital to have a highly efficient and cost effective transition from currently deployed D-RAN architectures to the future RAN architectures, as shown in Fig. 2.19 and Fig. 2.21 respectively.

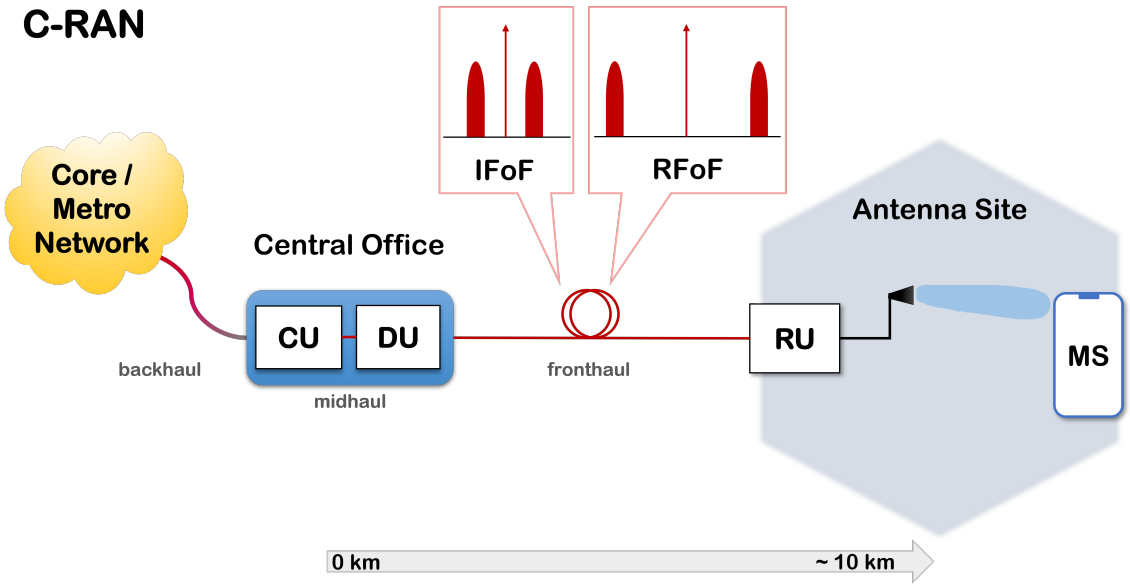

Fig. 2.21: C-RAN RoF transport schemes.

To simplify the RUs in 5G networks, a C-RAN architecture is highly advantageous, especially for dense cell sites. Centralization allows for the consolidation of resources, enabling effective control and coordination of a large number of antenna sites. This approach streamlines network operations and optimizes resource allocation, leading to enhanced network performance and scalability. A highly centralized implementation such as this emphasizes the role of optical transport between the CO and the RU - fronthaul.

ARoF provides several advantages when deployed in C-RAN architecture. Firstly, it enables the deployment of very low cost RUs, in the case of RFoF, as there is no requirement for up/down-conversion of the information and thus reduces the digital signal processing (DSP) complexity at the RU. Secondly, it supports baseband DSP and management functions at the CO. Thirdly, ARoF leverages the huge capacity of fiber in a more spectrally efficient way compared to DRoF by multiplexing multiple relatively low band-

width radio signals onto a single optical fiber, allowing for fronthauling to many deployed RUs over a shared fiber infrastructure.

Finally, through combination with optical heterodyning (see section 2.2.1), ARoF's aforementioned advantages can be leveraged to provide mmWave and THz capabilities for future centralized and widely deployed radio systems. This concept is explored through experimental demonstrations described in chapters 3 and 4 which will show practical methods to incorporate such functionality into future converged optical networks.

2.2.2.3 ARoF Challenges

The major concerns of the ARoF transport scheme include analog channel impairments such as fiber chromatic dispersion, transceiver nonlinear distortions, the limited dynamic range of DAC/ADC and intolerance to phase noise and frequency offset. Fiber chromatic dispersion refers to the phenomenon where different wavelengths of light travel at different speeds in an optical fiber and this phenomenon limits the transmission distance of the multi-carrier ARoF link. It specifically affects the double sideband signals by dispersive fading as the two sidebands after traveling the dispersive fiber undergo different phase shifts relative to the optical carrier. In dispersive fading the received RF power exhibits periodic variations with complete nulling at certain points, depending upon fiber dispersion parameter, link length and RF frequency [50].

Transceiver nonlinear distortions during the E-O and O-E conversion can cause signal distortions and impair the quality of the transmitted signals, especially with high PAPR. The limited dynamic range of the DAC and electrical amplifiers used in the ARoF system is another concern. As mentioned earlier, the dynamic range of a DAC refers to its ability to accurately represent a wide range of signal amplitudes. In ARoF systems, the attempts to mitigate both the nonlinearity from the transceivers and the limited dynamic range of the DAC can lead to an increased carrier-to-signal power ratio (CSPR). This means that the power of the carrier signal is much higher compared to that of the desired signal, which can result in reduced signal quality and increased susceptibility to interference and distortions. Modulation techniques to improve the power allocated to the signal can be employed to improve the performance of the link.

Another challenge is the reduced tolerance to phase noise and frequency offset. Phase

noise refers to random fluctuations in the phase of the transmitted signal, which can occur due to various factors such as oscillator imperfections. Frequency offset, on the other hand, refers to the deviation of the carrier frequency from its intended value. ARoF systems are more sensitive to phase noise and frequency offset compared to digital-based systems, making it necessary to implement techniques to minimize their impact.

Overall, these impairments and limitations pose challenges for ARoF systems, as they set a ceiling on the signal-to-noise ratio (SNR) that can be achieved. Despite these challenges, researchers and engineers are actively working on developing techniques and strategies to mitigate these impairments and improve the performance of ARoF systems [60, 61, 59].

When it comes to transmitting low-frequency signals, directly modulated lasers can be used as transmitters, providing a straightforward approach. However, for higher microwave and mmWave frequencies, ARoF systems typically require external modulators, as the laser's bandwidth is limited. In scenarios where multiple carriers are involved, the ARoF link, as depicted in Fig. 2.21, is prone to intermodulation distortions (IMD) caused by the nonlinearity of both microwave and optical components within the optical link. Moreover, the chromatic dispersion deteriorates the signal fidelity, resulting in the broadening of the frequency tones which further limits the transmission length over the optical fiber.

2.2.2.4 RoF modulation techniques

To mitigate the effects of chromatic dispersion induced dispersive fading and IMD induced power penalties, different optical carrier modulation schemes can be implemented. A modulator is a device that uses electrical signals to manipulate a beam of light. Modulators can vary the phase, amplitude, polarization and combination of amplitude and phase of an optical carrier. One example of an optical modulator is the Mach-Zehnder modulator (MZM) which is based on a Mach-Zender interferometer with phase modulators on each arm that imparts a phase shift on the electric field in either arm. Figure 2.22 shows a dual drive MZM with drive voltage inputs $V_1(t)$ and $V_2(t)$ and bias voltage input V_{bias}. The DC bias voltage controls the relative phase offset between the two arms resulting in a sinusoidal transfer function. When the MZM is driven by equal drive voltages with

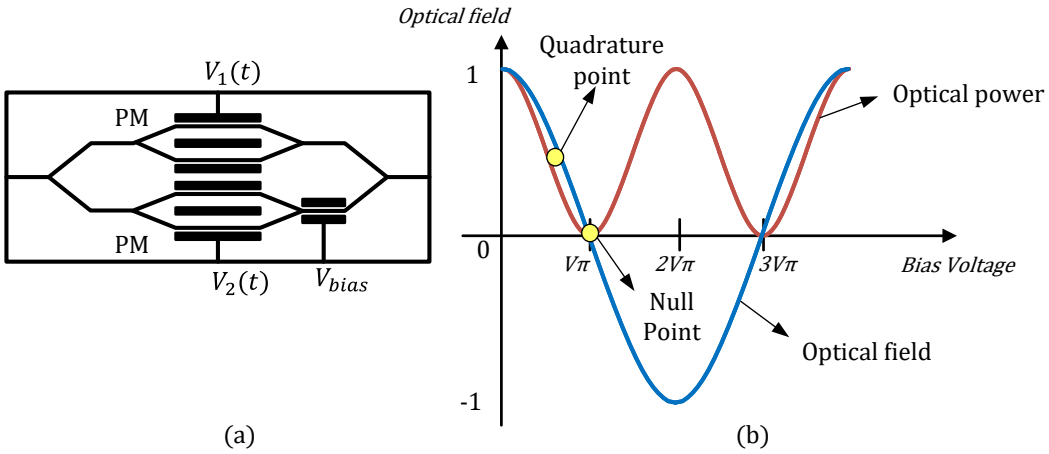

Fig. 2.22: Schematic of dual-drive MZM with sinusoidal transfer function.

opposite signs, for example, $V_1(t) = V(t)/2$ and $V_2(t) = -V(t)/2$, it is called a push-pull operation. The optical field C at the output of the MZM is expressed as

$$C = A\,cos\left(\frac{\pi}{V_\pi}\frac{V(t)}{2} + \frac{\Phi_{bias}}{2}\right) \tag{2.18}$$

where A is the amplitude of the signal, Φ_{bias} is the additional phase shift induced to one of the MZM arms by the bias voltage. The field/power transfer function describes the relation between the optical field/power and the electrical driving voltage. From the graph in Fig. 2.22, it is noted that linear intensity modulation can be achieved with a $V_\pi/2$ bias voltage (quadrature point) and field modulation is achieved at V_π (null point).

The specific modulation technique generated depends on the bias operation and drive voltage of the MZM, and various modulation techniques are summarized in Fig. 2.23. The operation of MZM at $V_\pi/2$ produces an optical double sideband (ODSB) signal, as shown in Fig. 2.23 (a). For the generation of optical single sideband modulation (OSSB), the dual drive MZM is used, which has two electrical voltage input ports for driving the modulator. The two driving voltages have equal amplitude and 90° phase shift and the bias voltage applied is $V_\pi/2$ (see Fig. 2.23 (b)) The OSSB modulation has gained significant popularity among the various generation techniques to alleviate chromatic dispersion and IMD [62, 63, 64]. By employing OSSB modulation, high-quality optical mmWave signals can be efficiently generated as the OSSB averts the penalty imposed by the optical

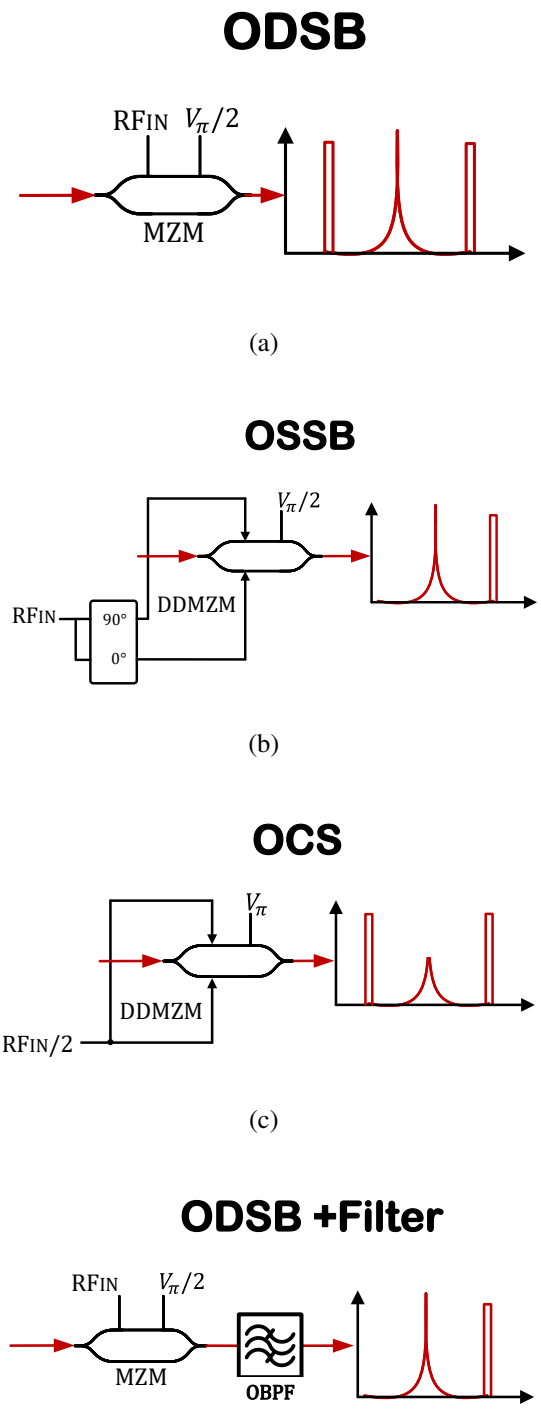

Fig. 2.23: Optical carrier modulation techniques. The single drive MZM is used to generate ODSB signal. The dual-drive MZM in a push-pull configuration generates OSSB.

fiber, i.e. dispersive fading on the ODSB signals. Optical carrier suppression (OCS), illustrated in Fig. 2.23 (c), is achieved with an MZM operating at the minimum transmission

point and driven with an RF signal at half of the desired frequency. The utilization of the OCS scheme in MZMs necessitates high RF power for achieving an adequate modulation depth. However, this amplification of RF power can exacerbate nonlinearity in the front end of the system. In Fig. 2.23 (d), a schematic demonstrates the removal of one of the sidebands through the application of an external filter. This technique has been successfully implemented using fiber Bragg gratings (FBGs) [65, 66] and chirped fiber gratings [67]. Nevertheless, a limitation of the filtering scheme arises from the inflexibility caused by the fixed frequency of the gratings, preventing easy adaptation to potential changes in the wireless frequency [49].

This chapter discusses the technologies facilitating high-capacity optical and wireless converged networks. In chapter 3, these technologies are employed for developing converged optical-wireless networks.

References

[1] Cisco, "Cisco annual internet report (2018˜2023) white paper," 2020. [Online]. Available: https://www.cisco.com/c/en/us/solutions/collateral/executive-perspectives/annual-internet-report/white-paper-c11-741490.html

[2] L. Wei, R. Q. Hu, Y. Qian, and G. Wu, "Key elements to enable millimeter wave communications for 5G wireless systems," *IEEE Wireless Communications*, vol. 21, no. 6, pp. 136–143, 2014.

[3] Z. Zhang, Y. Xiao, Z. Ma, M. Xiao, Z. Ding, X. Lei, G. K. Karagiannidis, and P. Fan, "6G wireless networks: Vision, requirements, architecture, and key technologies," *IEEE Vehicular Technology Magazine*, vol. 14, no. 3, pp. 28–41, 2019.

[4] W. Hong, Z. H. Jiang, C. Yu, D. Hou, H. Wang, C. Guo, Y. Hu, L. Kuai, Y. Yu, Z. Jiang, Z. Chen, J. Chen, Z. Yu, J. Zhai, N. Zhang, L. Tian, F. Wu, G. Yang, Z.-C. Hao, and J. Y. Zhou, "The Role of Millimeter-Wave Technologies in 5G/6G Wireless Communications," *IEEE Journal of Microwaves*, vol. 1, no. 1, pp. 101–122, 2021.

[5] T. S. Rappaport, Y. Xing, O. Kanhere, S. Ju, A. Madanayake, S. Mandal, A. Alkhateeb, and G. C. Trichopoulos, "Wireless communications and applications above 100 GHz: Opportunities and challenges for 6G and beyond," *IEEE access*, vol. 7, pp. 78 729–78 757, 2019.

[6] 6G SNS. [Online]. Available: https://smart-networks.europa.eu/

[7] T. ETSI, "138 104 V15. 5.0. 5G; NR; Base Station (BS) radio transmission and reception (3GPP TS 38.104 version 15.5. 0 Release 15, 2019–05)."

[8] W. Hong, Z. H. Jiang, C. Yu, J. Zhou, P. Chen, Z. Yu, H. Zhang, B. Yang, X. Pang, M. Jiang, Y. Cheng, M. K. T. Al-Nuaimi, Y. Zhang, J. Chen, and S. He, "Multibeam Antenna Technologies for 5G Wireless Communications," *IEEE Transactions on Antennas and Propagation*, vol. 65, no. 12, pp. 6231–6249, 2017.

[9] I. A. Alimi, A. L. Teixeira, and P. P. Monteiro, "Toward an Efficient C-RAN Optical Fronthaul for the Future Networks: A Tutorial on Technologies, Requirements, Challenges, and Solutions," *IEEE Communications Surveys Tutorials*, vol. 20, no. 1, pp. 708–769, 2018.

[10] 3GPP, "Study on scenarios and requirements for next generation access technologies," *Technical Specification Group Radio Access Network, Technical Report 38.913*, 2016.

[11] Z. D. Lathi, "Modern Digital and Analog Communication Systems (The Oxford Series in Electrical and Computer Engineering) by BP."

[12] "IEEE Standard for Ethernet - Amendment 10: Media Access Control Parameters, Physical Layers, and Management Parameters for 200 Gb/s and 400 Gb/s Operation," *IEEE Std 802.3bs-2017 (Amendment to IEEE 802.3-2015 as amended by IEEE's 802.3bw-2015, 802.3by-2016, 802.3bq-2016, 802.3bp-2016, 802.3br-2016, 802.3bn-2016, 802.3bz-2016, 802.3bu-2016, 802.3bv-2017, and IEEE 802.3-2015/Cor1-2017)*, pp. 1–372, 2017.

[13] "Ieee standard for ethernet – amendment 7: Physical layer and management parameters for 400 gb/s

over multimode fiber," *IEEE Std 802.3cm-2020 (Amendment to IEEE Std 802.3-2018 as amended by IEEE Std 802.3cb-2018, IEEE Std 802.3bt-2018, IEEE Std 802.3cd-2018, IEEE Std 802.3cn-2019, IEEE Std 802.3cg-2019, and IEEE Std 802.3cq-2020)*, pp. 1–72, 2020.

[14] "IEEE Standard for Ethernet - Amendment 4: Physical Layers and Management Parameters for 50Gb/s, 200Gb/s, and 400Gb/s Operation over Single-Mode Fiber," *IEEE Std 802.3cn-2019 (Amendment to IEEE Std 802.3-2018 as amended by IEEE Std 802.3cb-2018, IEEE Std 802.3bt-2018, and IEEE Std 802.3cd-2018)*, pp. 1–87, 2019.

[15] "400G-ER4-30 Technical Specification 1.0," 2023. [Online]. Available: https://100glambda.com/specifications/send/2-specifications/12-400g-er4-30-technical-specification-1-0

[16] Y. C. Wang, H. H. Lu, C. Y. Li, P. H. Chew, Y. B. Jheng, W. S. Tsai, and X. H. Huang, "A high-speed 84 gb/s vsb-pam8 vcsel transmitter-based fiber–ivllc integration," *IEEE Photonics Journal*, vol. 10, no. 5, pp. 1–8, 2018.

[17] L. Sun, C. Wang, J. Du, C. Liang, W. Zhang, K. Xu, F. Zhang, and Z. He, "Dyadic probabilistic shaping of PAM-4 and PAM-8 for cost-effective VCSEL-MMF optical interconnection," *IEEE Photonics Journal*, vol. 11, no. 2, pp. 1–11, 2019.

[18] M. Chagnon, M. Osman, M. Poulin, C. Latrasse, J. F. Gagné, Y. Painchaud, C. Paquet, S. Lessard, and D. Plant, "Experimental study of 112 Gb/s short reach transmission employing PAM formats and SiP intensity modulator at 1.3 μm," *Optics express*, vol. 22, no. 17, pp. 21 018–21 036, 2014.

[19] C. Browning, M. Ruffini, B. Cardiff, and L. P. Barry, "Single lane 168 gb/s pam-8 short reach transmission using an eam with receiver skew compensation," in *2018 European Conference on Optical Communication (ECOC)*. IEEE, 2018, pp. 1–3.

[20] M. Reuter and J. R. Zeidler, "Nonlinear effects in LMS adaptive equalizers," *IEEE Transactions on Signal Processing*, vol. 47, no. 6, pp. 1570–1579, 1999.

[21] J. Armstrong, "Ofdm for optical communications," *Journal of lightwave technology*, vol. 27, no. 3, pp. 189–204, 2009.

[22] X. Liu and F. Buchali, "Intra-symbol frequency-domain averaging based channel estimation for coherent optical OFDM," *Optics express*, vol. 16, no. 26, pp. 21 944–21 957, 2008.

[23] I. The MathWorks. Channel Estimation. [Online]. Available: https://www.mathworks.com/help/lte/ug/channel-estimation.html

[24] Q. Yang, N. Kaneda, X. Liu, and W. Shieh, "Demonstration of frequency-domain averaging based channel estimation for 40-Gb/s CO-OFDM with high PMD," *IEEE Photonics Technology Letters*, vol. 21, no. 20, pp. 1544–1546, 2009.

[25] H. Tataria, M. Shafi, A. F. Molisch, M. Dohler, H. Sjöland, and F. Tufvesson, "6g wireless systems: Vision, requirements, challenges, insights, and opportunities," *Proceedings of the IEEE*, 2021.

[26] S. Alavi, M. Soltanian, I. Amiri, M. Khalily, A. Supa'at, and H. Ahmad, "Towards 5g: A photonic based millimeter wave signal generation for applying in 5g access fronthaul," *Scientific Reports*, vol. 6, no. 1, pp. 2045–2322, 2016.

[27] C. Browning, H. H. Elwan, E. P. Martin, S. O'Duill, J. Poette, P. Sheridan, A. Farhang, B. Cabon, and L. P. Barry, "Gain-switched optical frequency combs for future mobile radio-over-fiber millimeter-wave systems," *Journal of Lightwave Technology*, vol. 36, no. 19, pp. 4602–4610, 2018.

[28] D. Dass, S. O'Duill, A. Delmade, and C. Browning, "Analysis of phase noise in a hybrid photonic/millimetre-wave system for single and multi-carrier radio applications," *Applied Sciences*, vol. 10, no. 17, p. 5800, 2020.

[29] V. Vujicic, C. Calo, R. Watts, F. Lelarge, C. Browning, K. Merghem, A. Martinez, A. Ramdane, and L. P. Barry, "Quantum dash mode-locked lasers for data centre applications," *IEEE Journal of selected topics in quantum electronics*, vol. 21, no. 6, pp. 53–60, 2015.

[30] P. Zhu, J. Li, L. Niu, Y. Xu, Y. Chen, X. Xie, X. Chen, B. Guo, Z. Chen, and Y. He, "Optical comb-enabled cost-effective ROADM scheme for elastic optical networks," in *Optical Fiber Communication Conference*. Optica Publishing Group, 2014, pp. W3B–5.

[31] M. Imran, P. M. Anandarajah, A. Kaszubowska-Anandarajah, N. Sambo, and L. Potí, "A survey of optical carrier generation techniques for terabit capacity elastic optical networks," *IEEE Communications Surveys Tutorials*, vol. 20, no. 1, pp. 211–263, 2018.

[32] P. M. Anandarajah, S. P. Ó. Dúill, R. Zhou, and L. P. Barry, "Enhanced optical comb generation by gain-switching a single-mode semiconductor laser close to its relaxation oscillation frequency," *IEEE Journal of Selected Topics in Quantum Electronics*, vol. 21, no. 6, pp. 592–600, 2015.

[33] P. M. Anandarajah, R. Zhou, R. Maher, M. D. G. Pascual, F. Smyth, V. Vujicicand, and L. P. Barry, "Flexible optical comb source for super channel systems," in *Optical Fiber Communication Conference*. Optica Publishing Group, 2013, pp. OTh3I–8.

[34] J. S. Zou, S. A. Sasu, M. Lawin, A. Dochhan, J.-P. Elbers, and M. Eiselt, "Advanced optical access technologies for next-generation (5g) mobile networks," *Journal of Optical Communications and Networking*, vol. 12, no. 10, pp. D86–D98, 2020.

[35] P. Iovanna, F. Cavaliere, F. Testa, S. Stracca, G. Bottari, F. Ponzini, A. Bianchi, and R. Sabella, "Future proof optical network infrastructure for 5G transport," *Journal of Optical Communications and Networking*, vol. 8, no. 12, pp. B80–B92, 2016.

[36] C. Browning, Q. Cheng, N. C. Abrams, M. Ruffini, L. Y. Dai, L. P. Barry, and K. Bergman, "A silicon photonic switching platform for flexible converged centralized-radio access networking," *Journal of Lightwave Technology*, vol. 38, no. 19, pp. 5386–5392, 2020.

[37] X. Guan, R. Dubé-Demers, W. Shi, and L. A. Rusch, "Heterogeneous optical access networks: Enabling low-latency 5g services with a silicon photonic smart edge," *Journal of Lightwave Technology*, vol. 39, no. 8, pp. 2348–2357, 2021.

[38] C. Browning, H. H. Elwan, E. P. Martin, S. O'Duill, J. Poette, P. Sheridan, A. Farhang, B. Cabon, and L. P. Barry, "Gain-switched optical frequency combs for future mobile radio-over-fiber millimeter-wave systems," *Journal of Lightwave Technology*, vol. 36, no. 19, pp. 4602–4610, 2018.

[39] A. Delmade, C. Browning, T. Verolet, J. Poette, A. Farhang, H. H. Elwan, R. D. Koilpillai, G. Aubin,

F. Lelarge, A. Ramdane *et al.*, "Optical heterodyne analog radio-over-fiber link for millimeter-wave wireless systems," *Journal of Lightwave Technology*, vol. 39, no. 2, pp. 465–474, 2020.

[40] G. Carpintero, S. Hisatake, D. de Felipe, R. Guzman, T. Nagatsuma, and N. Keil, "Wireless data transmission at terahertz carrier waves generated from a hybrid inp-polymer dual tunable dbr laser photonic integrated circuit," *Scientific reports*, vol. 8, no. 1, pp. 1–7, 2018.

[41] Y. Liu, Q. Tang, L. Zhang, X. La, L. Zhao, W. Wang, and S. Liang, "Dual-wavelength dbr laser integrated with high-speed eam for thz communications," *Optics express*, vol. 28, no. 7, pp. 10 542–10 551, 2020.

[42] J. Hulme, M. Kennedy, R.-L. Chao, L. Liang, T. Komljenovic, J.-W. Shi, B. Szafraniec, D. Baney, and J. Bowers, "Fully integrated microwave frequency synthesizer on heterogeneous silicon-iii/v," *Optics express*, vol. 25, no. 3, pp. 2422–2431, 2017.

[43] P. Dong, Y.-K. Chen, G.-H. Duan, and D. T. Neilson, "Silicon photonic devices and integrated circuits," *Nanophotonics*, vol. 3, no. 4-5, pp. 215–228, Aug. 2014. [Online]. Available: https://www.degruyter.com/view/journals/nanoph/3/4-5/article-p215.xml

[44] A. Abbasi, J. Verbist, L. A. Shiramin, M. Verplaetse, T. De Keulenaer, R. Vaernewyck, R. Pierco, A. Vyncke, X. Yin, G. Torfs, G. Morthier, J. Bauwelinck, and G. Roelkens, "100-Gb/s Electro-Absorptive Duobinary Modulation of an InP-on-Si DFB Laser," *IEEE Photonics Technology Letters*, vol. 30, no. 12, pp. 1095–1098, 2018.

[45] S. Chen, W. Li, J. Wu, Q. Jiang, M. Tang, S. Shutts, S. N. Elliott, A. Sobiesierski, A. J. Seeds, I. Ross, P. M. Smowton, and H. Liu, "Electrically pumped continuous-wave III-V quantum dot lasers on silicon," *Nature Photonics*, vol. 10, no. 5, p. 307, 2016.

[46] B. R. Koch, E. J. Norberg, B. Kim, J. Hutchinson, J.-H. Shin, G. Fish, and A. Fang, "Integrated silicon photonic laser sources for telecom and datacom," in *Optical Fiber Communication Conference*. Optica Publishing Group, 2013, pp. PDP5C–8.

[47] P. A. Morton and M. J. Morton, "High-Power, Ultra-Low Noise Hybrid Lasers for Microwave Photonics and Optical Sensing," *J. Lightwave Technol.*, vol. 36, no. 21, pp. 5048–5057, Nov. 2018. [Online]. Available: https://ieeexplore.ieee.org/document/8319492/

[48] J. De Merlier, K. Mizutani, S. Sudo, K. Naniwae, Y. Furushima, S. Sato, K. Sato, and K. Kudo, "Full c-band external cavity wavelength tunable laser using a liquid-crystal-based tunable mirror," *IEEE Photonics Technology Letters*, vol. 17, no. 3, pp. 681–683, 2005.

[49] C. Lim, Y. Tian, C. Ranaweera, T. A. Nirmalathas, E. Wong, and K.-L. Lee, "Evolution of radio-over-fiber technology," *Journal of Lightwave Technology*, vol. 37, no. 6, pp. 1647–1656, 2019.

[50] H. Schmuck, "Comparison of optical millimetre-wave system concepts with regard to chromatic dispersion," *Electronics Letters*, vol. 31, no. 21, pp. 1848–1849, 1995.

[51] U. Gliese, S. Norskov, and T. Nielsen, "Chromatic dispersion in fiber-optic microwave and millimeter-wave links," *IEEE Transactions on microwave theory and techniques*, vol. 44, no. 10, pp. 1716–1724, 1996.

[52] T. Pfeiffer, "Next generation mobile fronthaul and midhaul architectures," *Journal of Optical Communications and Networking*, vol. 7, no. 11, pp. B38–B45, 2015.

[53] A. De la Oliva, J. A. Hernandez, D. Larrabeiti, and A. Azcorra, "An overview of the CPRI specification and its application to C-RAN-based LTE scenarios," *IEEE Communications Magazine*, vol. 54, no. 2, pp. 152–159, 2016.

[54] D. Apostolopoulos, G. Giannoulis, N. Argyris, N. Iliadis, K. Kanta, and H. Avramopoulos, "Analog radio-over-fiber solutions in support of 5G," in *2018 International Conference on Optical Network Design and Modeling (ONDM)*. IEEE, 2018, pp. 266–271.

[55] D. Che, "Digital SNR adaptation of analog radio-over-fiber links carrying up to 1048576-QAM signals," in *2020 European Conference on Optical Communications (ECOC)*. IEEE, 2020, pp. 1–4.

[56] J. Wang, Z. Yu, K. Ying, J. Zhang, F. Lu, M. Xu, and G.-K. Chang, "Delta-sigma modulation for digital mobile fronthaul enabling carrier aggregation of 32 4G-LTE/30 5G-FBMC signals in a single-λ 10-Gb/s IM-DD channel," in *2016 Optical Fiber Communications Conference and Exhibition (OFC)*. IEEE, 2016, pp. 1–3.

[57] L. Breyne, G. Torfs, X. Yin, P. Demeester, and J. Bauwelinck, "Comparison between analog radio-over-fiber and sigma delta modulated radio-over-fiber," *IEEE Photonics Technology Letters*, vol. 29, no. 21, pp. 1808–1811, 2017.

[58] W. Li, A. Chen, T. Li, R. V. Penty, I. H. White, and X. Wang, "Novel digital radio over fiber (drof) system with data compression for neutral-host fronthaul applications," *IEEE Access*, vol. 8, pp. 40 680–40 691, 2020.

[59] A. Delmade, C. Browning, A. Farhang, N. Marchetti, L. Doyle, R. Koilpillai, L. Barry, and D. Venkitesh, "Performance analysis of analog if over fiber fronthaul link with 4g and 5g coexistence," *J. Opt. Commun. Netw.*, vol. 10, no. 3, pp. 174–182, Mar 2018. [Online]. Available: http://jocn.osa.org/abstract.cfm?URI=jocn-10-3-174

[60] X. Liu, "Hybrid digital-analog radio-over-fiber (DA-RoF) modulation and demodulation achieving a SNR gain over analog RoF of> 10 dB at halved spectral efficiency," in *2021 Optical Fiber Communications Conference and Exhibition (OFC)*. IEEE, 2021, pp. 1–3.

[61] C. Browning, A. Delmade, Y. Lin, J. Poette, H. H. Elwan, and L. Barry, "Phase noise robust optical heterodyne system for reduced complexity millimeter-wave analog radio-over-fibre," in *European Conference on Optical Communication*, Sept. 2019.

[62] G. Smith, D. Novak, and Z. Ahmed, "Technique for optical SSB generation to overcome dispersion penalties in fibre-radio systems," *Electronics letters*, vol. 33, no. 1, pp. 74–75, 1997.

[63] C. Lim, M. Attygalle, A. Nirmalathas, D. Novak, and R. Waterhouse, "Analysis of optical carrier-to-sideband ratio for improving transmission performance in fiber-radio links," *IEEE Transactions on Microwave Theory and Techniques*, vol. 54, no. 5, pp. 2181–2187, 2006.

[64] P. S. Devgan, D. P. Brown, and R. L. Nelson, "RF performance of single sideband modulation versus

dual sideband modulation in a photonic link," *Journal of Lightwave Technology*, vol. 33, no. 9, pp. 1888–1895, 2014.

[65] J. Park, W. Sorin, and K. Lau, "Elimination of the fibre chromatic dispersion penalty on 1550 nm millimetre-wave optical transmission," *Electronics Letters*, vol. 33, no. 6, pp. 512–513, 1997.

[66] E. Vourch, D. Le Berre, and D. Herve, "Lightwave single sideband wavelength self-tunable filter using an InP: Fe crystal for fiber-wireless systems," *IEEE Photonics Technology Letters*, vol. 14, no. 2, pp. 194–196, 2002.

[67] J. Marti, J. Fuster, and R. Laming, "Experimental reduction of chromatic dispersion effects in lightwave microwave/millimetre-wave transmissions using tapered linearly chirped fibre gratings," *Electronics Letters*, vol. 33, no. 13, pp. 1170–1171, 1997.

Chapter 3

Converged Optical-Wireless Transmission Systems

The preceding chapters have outlined various techniques, technologies and architectural considerations that can be employed to enable high-capacity converged optical-wireless transmission systems. In this chapter, several of the previously discussed elements are amalgamated to construct a SiP based ARoF mmWave transmission system, showcasing the true system-level convergence in an optical access network.

The chapter begins with a comprehensive description of a pioneering hybrid integrated laser that is used in system-level work (presented later in this chapter). A detailed characterization, which encompasses several crucial parameters such as wavelength tunability, output power, side mode suppression ratio (SMSR), RIN, linewidth, and FM noise follows. Furthermore, this section also explores the potential applications of this laser device, illustrating its versatility and wide-ranging utility.

In the latter part of the chapter, section 3.2 details the practical implementation of the hybrid integrated laser in two distinct optical heterodyne ARoF fronthaul link scenarios. These hybrid transmission scenarios involve the integration of both a 10 km fiber-based link and a wireless mmWave link spanning up to 2 meters. By employing the SiP based ARoF mmWave transmission system, this work demonstrates the successful deployment of the novel laser device in an end-to-end laboratory transmission environment, underscoring its potential to provide a platform for the convergence of optical and wireless networks.

3.1 SiP Source Description & Characterization

3.1.1 Device Design

A schematic outline of the photonic integrated circuit based DLM, provided by Lionix International, is shown in Fig. 3.1 (a). The device consists of two lasers denoted as L1 and L2 (outlined in Fig. 3.1 (a) in grey). Each laser consists of a gain, phase and cavity section along with associated 2×2 symmetric Mach-Zehnder Interferometer based tunable couplers (MZI-TC) [1] (labeled in Fig. 3.1 (a) as cavity coupler (CC), PD/L1 output coupler (OC), PD/L2 OC). An additional MZI-TC (labeled in Fig. 3.1 (a) as a PD coupler) is used to control light to the photodetectors (PDs). The DLM was fabricated using two InP based reflective semiconductor optical amplifiers (SOAs) which are hybrid coupled to two Si_3N_4 feedback circuits. Both SOAs are designed to have the same gain spectra and support a wavelength range over 100 nm. Each feedback circuit consists of two microring resonators (MRRs) in a Vernier configuration, creating an MRR based external cavity laser (MRR-ECL). The phase section, the MRR and the MZI-TC are thermo-optically controlled with associated on-chip micro-heaters (highlighted in red in Fig. 3.1 (a)). The hybrid assembly process used by the manufacturer - Lionix International - is described in [2].

Each SOAs' left facet is coated with high reflective material to reduce cavity losses and the right facet is coated with low reflective material to facilitate lasing in the external cavity [3, 4]. The PIC consists of two Si_3N_4 feedback circuits, each incorporating a pair of MRRs. Both pairs of MRRs on the chip exhibit circumferences of 787.119 µm and 813.336 µm, and free spectral ranges (FSRs) of 1.7242 nm and 1.668 nm respectively. The corresponding FSRs are calculated by using the following formula:

$$FSR_\lambda = \frac{\lambda^2}{n_g L} \tag{3.1}$$

where the wavelength $\lambda = 1550$ nm, group index of the waveguide n_g is 1.7703 and the ring circumference is L. Multiple round-trips through the two MRRs yield a longer, low loss, cavity length and narrow spectral filtering of the wavelength, producing a single mode output [2]. Tuning of the single mode output can be achieved by varying the voltage

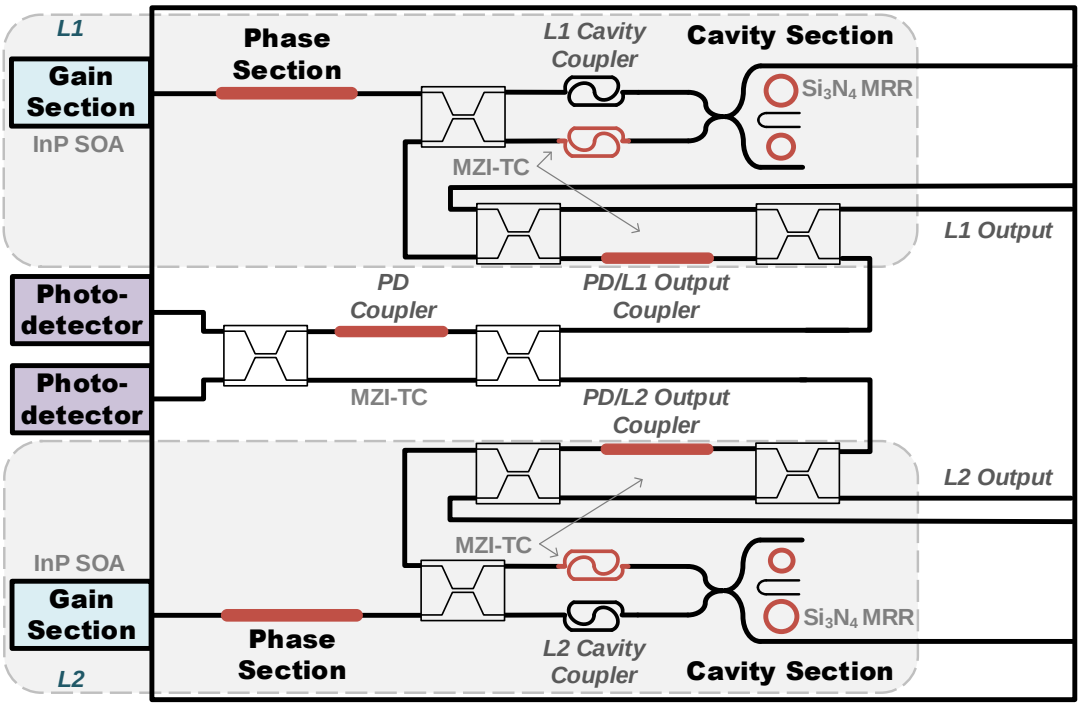

(a) PIC schematic

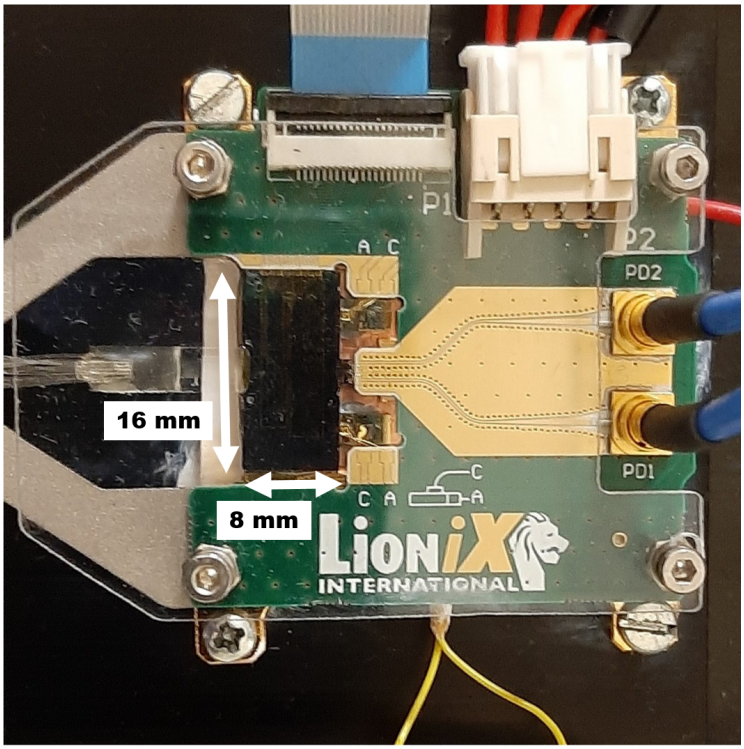

(b) Photograph

Fig. 3.1: Dual tunable InP-Si_3N_4 laser module.

of the micro-heater associated with each ring. The amount of light fed back to the gain and cavity sections of a laser is controlled by the thermally adjustable phase section and cavity coupler. The light from lasers L1 and L2 is directed to couplers PD/L1 and PD/L2 respectively, where the relative light power directed to either the on-chip detectors or the output fibers can be set. Finally, the on-chip PDs include a PD coupler, which controls the power level that is coupled to each PD. The PDs can be used for power monitoring or to enable on-chip optical heterodyne operation. A photograph of the InP-Si_3N_4 hybrid integrated DLM is shown in Fig. 3.1 (b).

3.1.2 Device Characterization

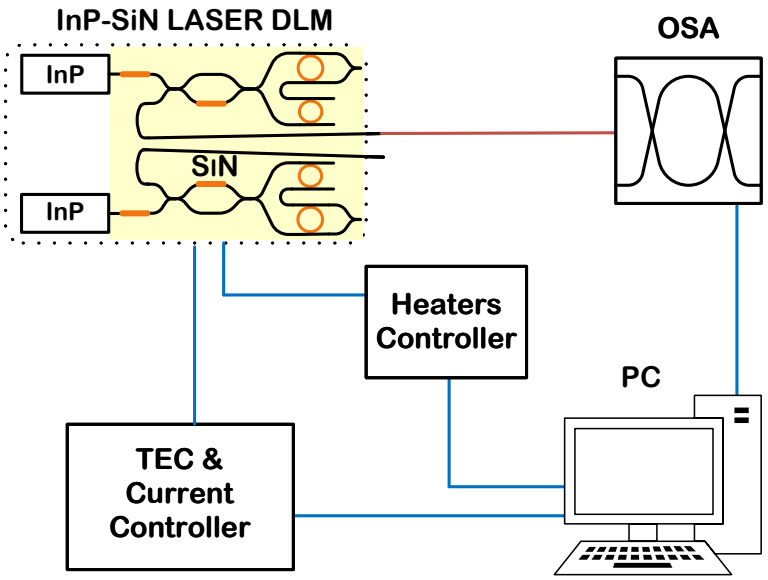

Fig. 3.2: Characterization setup with automated software control of TEC and current source, DLM's micro-heater controllers and OSA.

A schematic of the characterization setup is given in Fig. 3.2. For the characterization of the device, the temperature of the laser module was maintained at room temperature (20°C) using a laser diode thermo-electric cooler (TEC) connected to the temperature sensor IC inserted in the module. Each laser had an isolator connected to the fiber output and was operated one at a time for individual characterization. The gain current for both lasers was set to 100 mA. To observe the effects of tuning MRRs in the feedback circuit,

the phase sections and the cavity coupler sections were biased at 0 V throughout the characterization. The voltage of the micro-heater associated with the PD/L1 and PD/L2 output couplers was kept constant at 15 V to maximize optical power at the fiber output of both lasers, for the above bias settings. For each laser on the chip the tuning map and the SMSR, shown in Fig. 3.3 and Fig. 3.4, respectively, were obtained by observing the output wavelength characteristics using an OSA while varying the voltage applied to the micro-heaters associated with the two MRRs[1]. Fine tuning was achieved by changing the voltage bias to the rings' micro-heaters by a relatively small step size of 0.1 V, within the range of 0 V to 10 V.

The DLM's wavelength tuning maps, presented in Figs. 3.3 (a) and (b), show the tuning ranges for L1 (from 1470 nm to 1540 nm) and L2 (from 1510 nm to 1575 nm), respectively. This reduction in coverage (with respect to that supported by both SOAs) and the difference in wavelength ranges exhibited by L1 and L2 are attributed to the respective spectral dependencies of the cavity coupler MZI-TCs [5], which were biased at 0 V during characterization. Altering these bias conditions allows the lasers' wavelength coverage to be tuned. For the settings used for characterization, the DLM exhibits a tuning range of 100 nm, covering most of the S-band, all of the C-band and parts of the L-band. Figs. 3.4 (a) and (b) show that an SMSR of greater than 50 dB is achieved across the whole range of wavelengths for the gain and bias settings used during this characterization.

The fiber coupled output powers of L1 and L2 as a function of gain current (with all other bias settings fixed) were measured independently and are shown in Figs. 3.5 (a) and (b). Fig. 3.5 (a) shows the power-current (P-I) curves when the heaters associated with each lasers' output coupler and cavity coupler MZI-TCs were biased at 15 V and 0 V respectively (the conditions used for wavelength and SMSR characterization), while Fig. 3.5 (b) shows P-I curves when these bias conditions were set to maximize the output power at higher gain currents. The power drops exhibited by all P-I curves are explained by the fact that while the biasing configurations in the external cavities remain constant, increasing the gain current results in refractive index changes in the gain waveguide; serving to slightly shift the lasing mode out of resonance with the MRR-based Vernier filter [2]. Fig. 3.5 (a) shows threshold currents for L1 and L2 of 29 mA and 10

[1] See Appendix B for values corresponding to these graphs

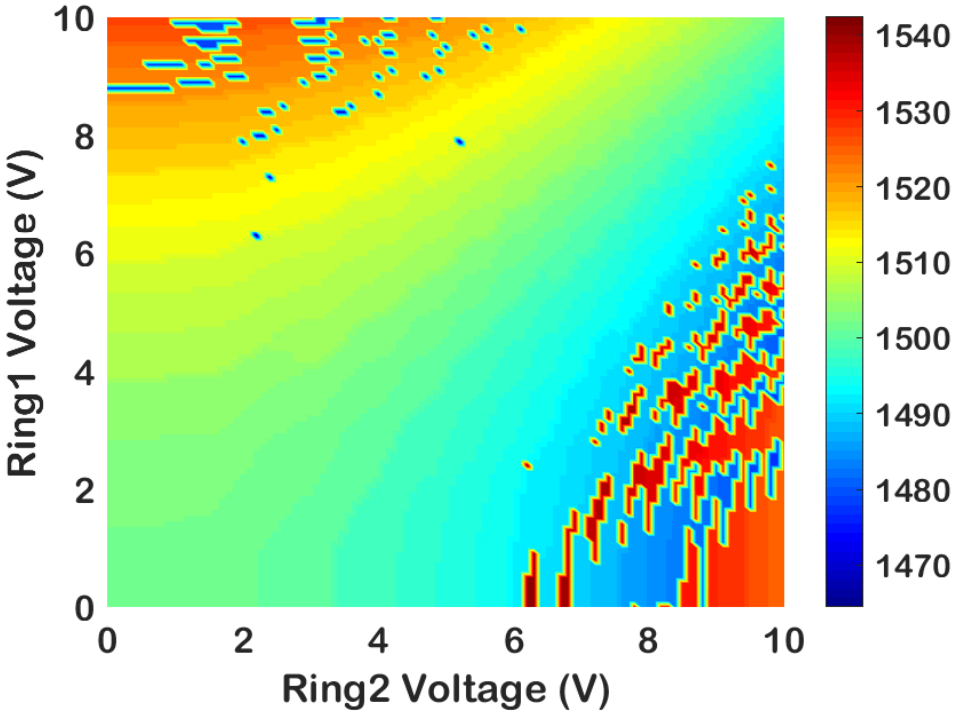

(a)

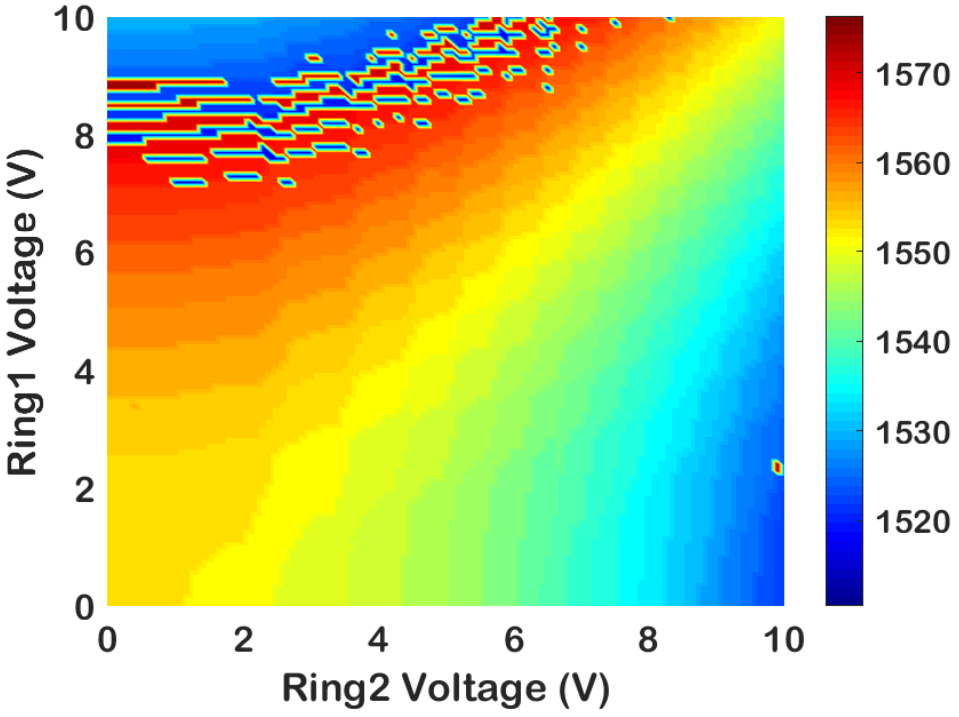

(b)

Fig. 3.3: (a) and (b) are tuning maps of the wavelength versus voltage on the ring section for L1 and L2 respectively.

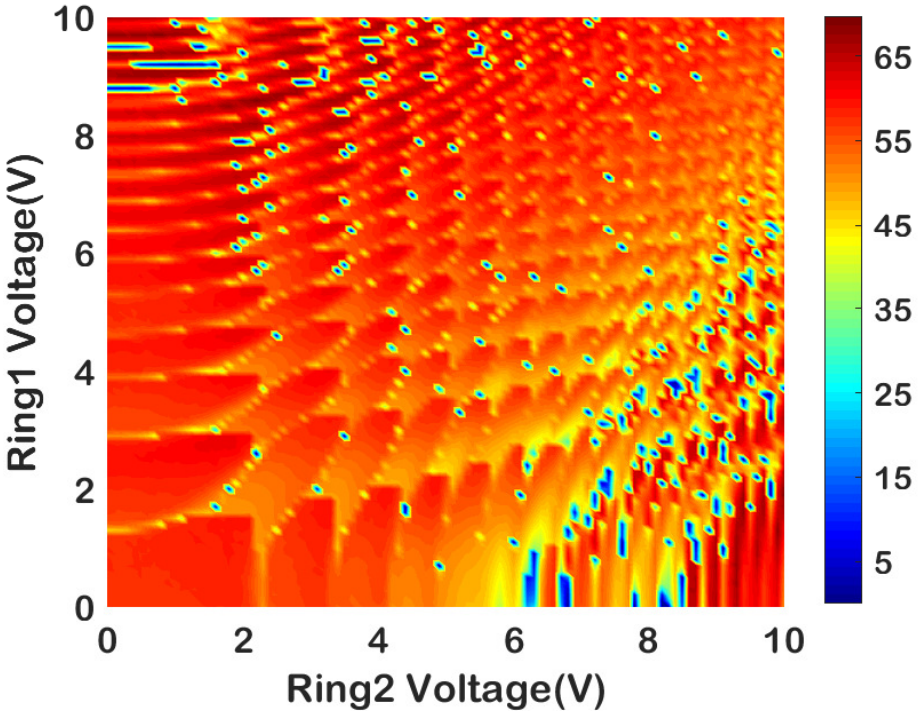

(a)

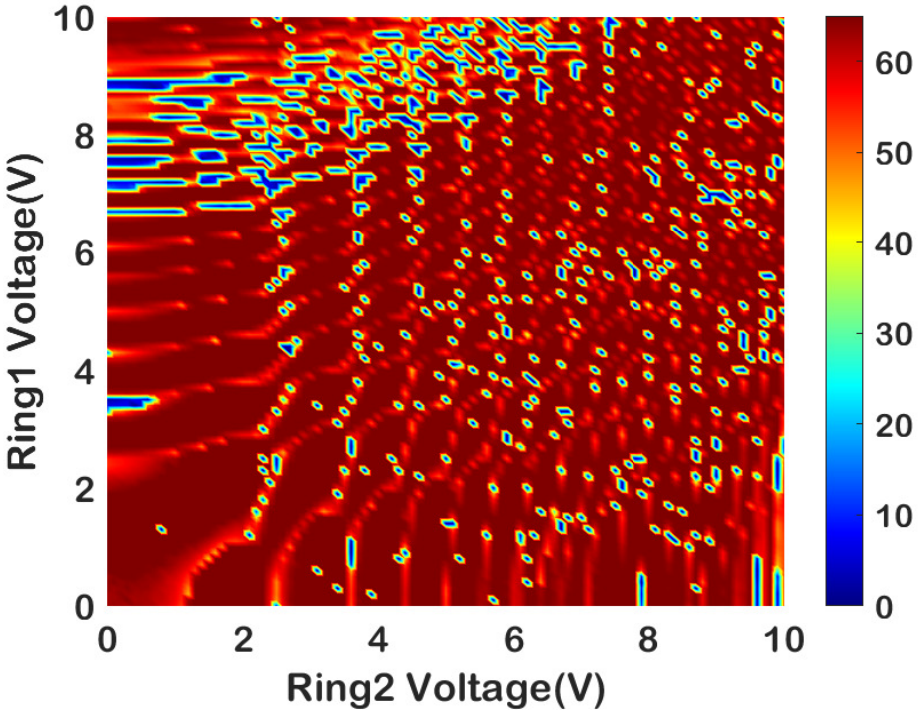

(b)

Fig. 3.4: (a) and (b) are SMSR values versus voltage on the ring sections for L1 and L2 respectively.

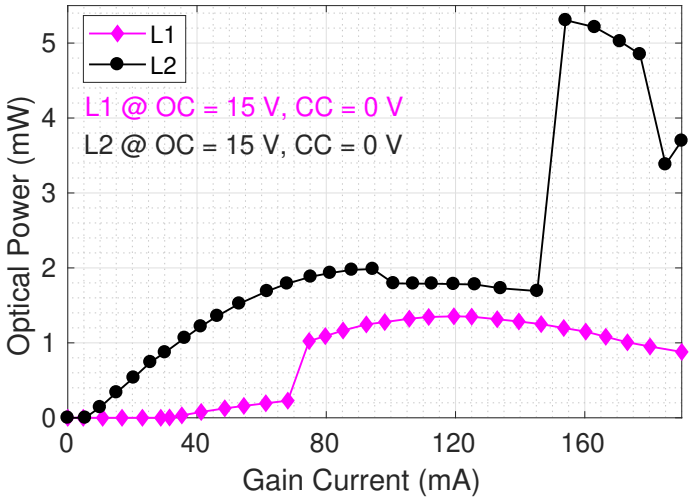

(a)

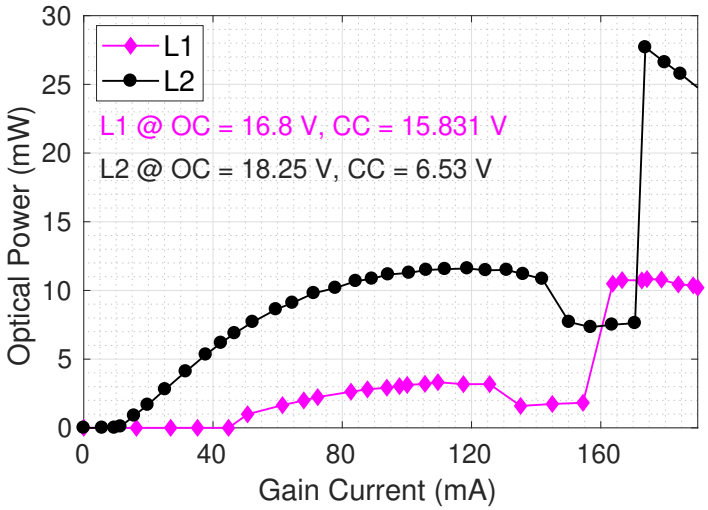

(b)

Fig. 3.5: (a) and (b) are the optical power of L1 and L2 versus gain current with different bias conditions of the MZI-TCs given in the inset.

mA respectively. While biasing conditions do impact the threshold current, this relatively large variation between L1 and L2 is attributed to differences in chip-to-chip coupling losses, and potentially to small differences in respective SOA reflectivities. This loss also impacts the maximum achievable output power for both lasers. Nevertheless, Fig. 3.5 (b) shows that powers $>$ +10 dBm can be achieved using both L1 and L2 through suitable tuning of the output coupler and cavity coupler MZI-TCs.

Fig. 3.6 (a) and (b) show the output power for both lasers as the MRRs are tuned when the heaters associated with each lasers' output coupler and cavity coupler MZI-TCs were

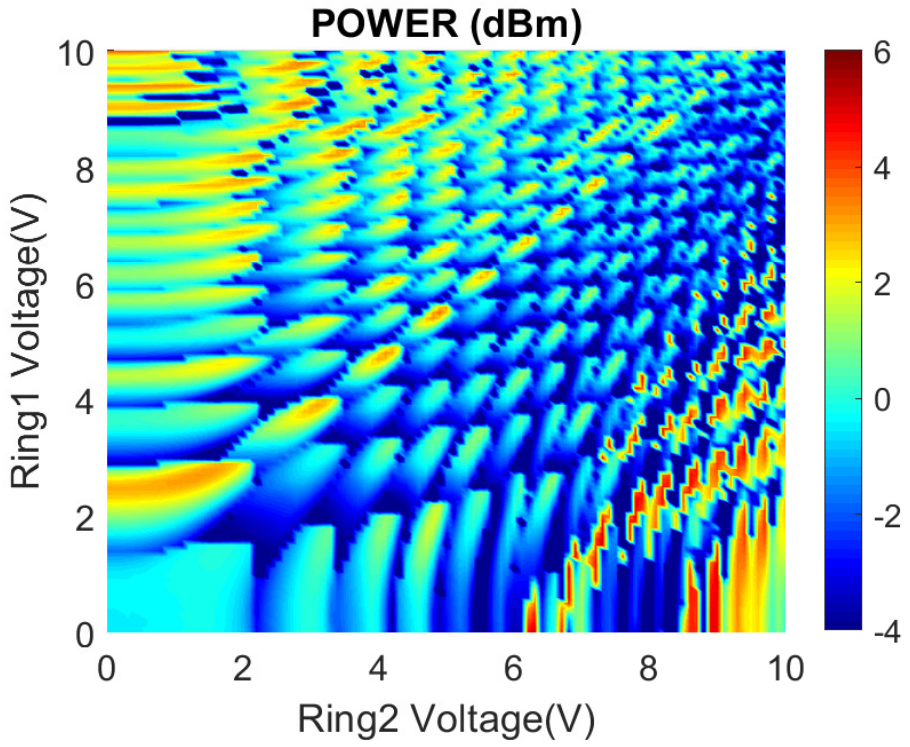

(a)

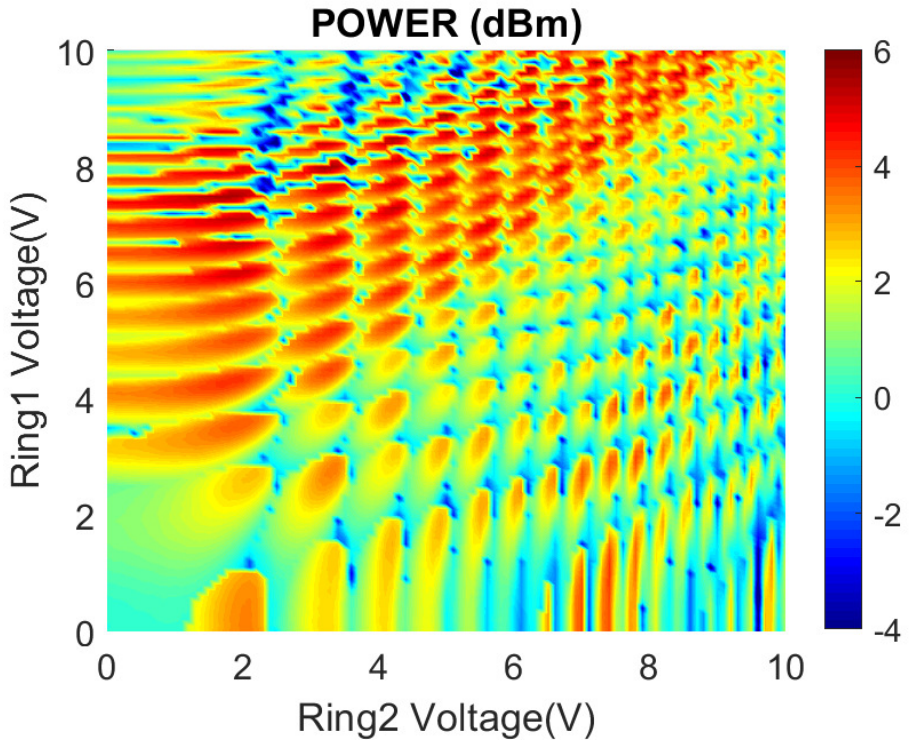

(b)

Fig. 3.6: (a) and (b) are power versus voltage on the ring section for L1 and L2 respectively.

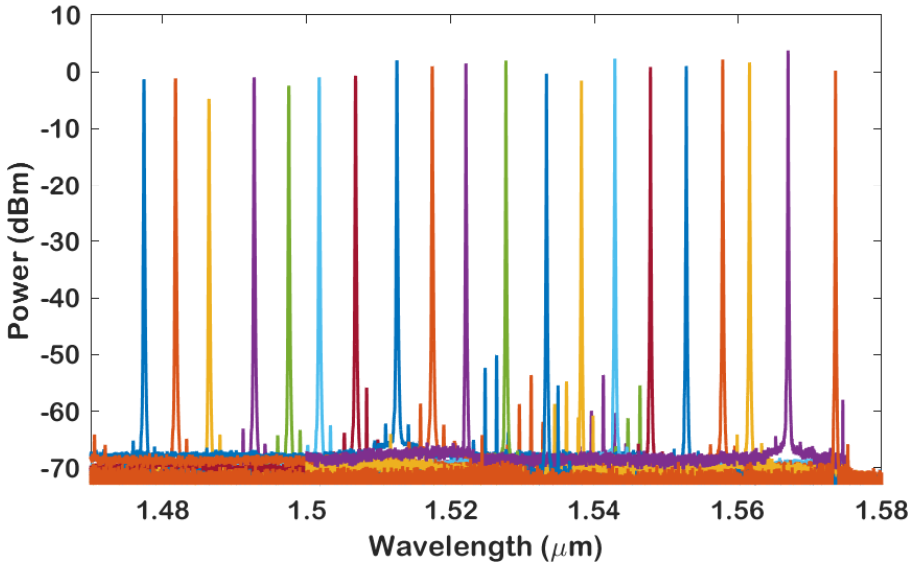

Fig. 3.7: Superimposed spectra of L1 and L2 over 100 nm tuning range.

biased at 15 V and 0 V respectively. Figs. 3.6 (a) and (b) show some regions that indicate deterioration in output power. These regions arise at MRR bias settings for which the oscillating cavity mode is off-resonance with the Vernier filter to some degree. In some cases, this deterioration could be alleviated by appropriate tuning of the phase sections. The optical spectra corresponding to a selection of wavelengths across the device's full tuning range (about 100 nm) are superimposed and presented in Fig. 3.7.

3.1.2.1 Intensity, Phase & Frequency Fluctuations

Fluctuations in intensity, phase, and frequency are observed in the output of a semiconductor laser, even when the laser is biased with constant current and negligible current fluctuations. The primary sources of noise in semiconductor lasers are spontaneous emission and photons emitted at the electron-hole recombination, with spontaneous emission dominating the overall noise. Spontaneously emitted photons introduce random phase and amplitude perturbations to the coherent field, resulting in random fluctuations in both intensity and phase. Due to the relatively high rate of spontaneous emission events caused by a relatively large value of spontaneous emission rate (approximately 10^{12} per second), these fluctuations occur rapidly, with a time scale as short as 100 ps. Intensity fluctuations impact the RIN, while phase fluctuations contribute to a finite spectral linewidth when semiconductor lasers operate at a constant current. Since these fluctuations can af-

fect the performance of lightwave systems, it is crucial to assess their magnitude [6]. The fluctuating power of a laser, denoted as $P(t)$, arises from spontaneous emission and can be characterized as deviations from an average power value, P_0:

$$P(t) = P_0 + \delta P(t) \tag{3.2}$$

Relative intensity Noise: The noise induced by the random fluctuations in the intensity of the optical source attributed to the spontaneous generation of photons is called relative intensity noise. These fluctuations occur as a result of the inherent quantum nature of stimulated emission, spontaneous emission and also noise from the electrical supply. The statistical characterization of RIN can be accomplished by using a power spectral density that is dependent on the frequency of the noise. This power spectral density of RIN is commonly represented on a logarithmic scale, measured in units of decibels per hertz (dB/Hz). The mathematical definition of total RIN (RIN_T) is given by the mean-square power of the intensity fluctuations to the square of the average optical power of the signal.

$$RIN_T = \frac{\langle \delta P(t)^2 \rangle}{\langle P_0 \rangle^2} \tag{3.3}$$

where the time average $\langle \delta P(t)^2 \rangle$ arises from the autocorrelation function $\langle \delta P(t) \delta P(t + \tau) \rangle$ evaluated at time $\tau = 0$. The total RIN in the frequency domain is represented in the form of the power spectral density of RIN and is given by the integral of RIN ($R(\nu)$), over all frequencies [7]:

$$RIN_T = \int_0^\infty R(\nu) d\nu \tag{3.4}$$

where ν is the optical frequency (in Hz). The spectral density amplitude fluctuations have a minimum of the standard Poisson limit in classical states of light. To this Poisson limit, some excess intensity noise may be added and thus the RIN_T constitutes both Poisson RIN and excess RIN. The excess RIN remains unchanged through system propagation, however, the Poisson RIN depends on the losses in the system [7]. The laser noise RIN measurements were performed using a method similar to that outlined in reference [4]. In the RIN measurement setup, shown in Fig 3.8 (a), the laser was connected to an isolator the optical output was fed into a high bandwidth ($\sim$20 GHz) Thorlabs DXM20AF PD

with an inbuilt bias tee and an impedance-matching circuit. The AC signal was amplified using an SHF 806E electrical amplifier and fed to a Rohde & Schwarz FSW50 electrical spectrum analyzer (ESA) to measure the power across the 0-20 GHz frequency band. The intensity fluctuations in the optical signal generated by a laser source are detected by a high speed PD that generates an electrical output with power that is proportional to the power intensity fluctuations. The photocurrent generated at the PD is:

$$I(t) = I_{PC} + i_{shot}(t) + i_{thermal}(t) \tag{3.5}$$

where I_{PC} is the deterministic part of the current and written as:

$$I_{PC}(t) = RP(t) \tag{3.6}$$

where $P(t)$ is the fluctuating power of a laser, and R is the responsivity of the PD. The term $i_{shot}(t)$ is the shot noise component of the current which is generated due to random photon-electron conversions that cause fluctuations in the photocurrent of PD. The term $i_{thermal}(t)$ denotes the thermal noise component in the photocurrent due to the random motion of electrons in a conductor.

The RIN is ideally expressed as:

$$RIN = \frac{\langle R^2 \delta I_{PC}^2(t) \rangle}{R^2 I^2(t)} = \frac{\langle \delta I_{PC}^2(t) \rangle}{I^2(t)} = \frac{\langle \delta P_{AC}^2(t) \rangle}{P_{DC}^2(t)} \tag{3.7}$$

where $P_{AC}^2(t)$ and $P_{DC}^2(t)$ are the associated power fluctuations of the photocurrent and the average power of the photocurrent respectively. The $P_{AC}^2(t)$ is calculated as:

$$RIN(1/Hz) = \frac{P(t) - P_{thermal}(t)}{RBW I^2(t) \Omega G} \tag{3.8}$$

where $P_{thermal}(t)$ is the thermal noise power of the system, RBW is the resolution bandwidth of the ESA, I(t) is the photocurrent at the PD, Ω is the load resistance and G is the electrical amplifier gain. We can also calculate the RIN in decibel (dB):

$$RIN(dB/Hz) = P_{AC}(dB) - P_{DC}(dB) \tag{3.9}$$

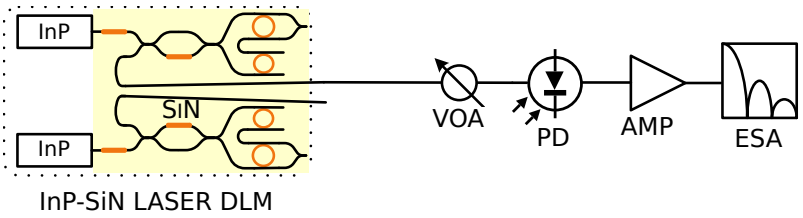

(a)

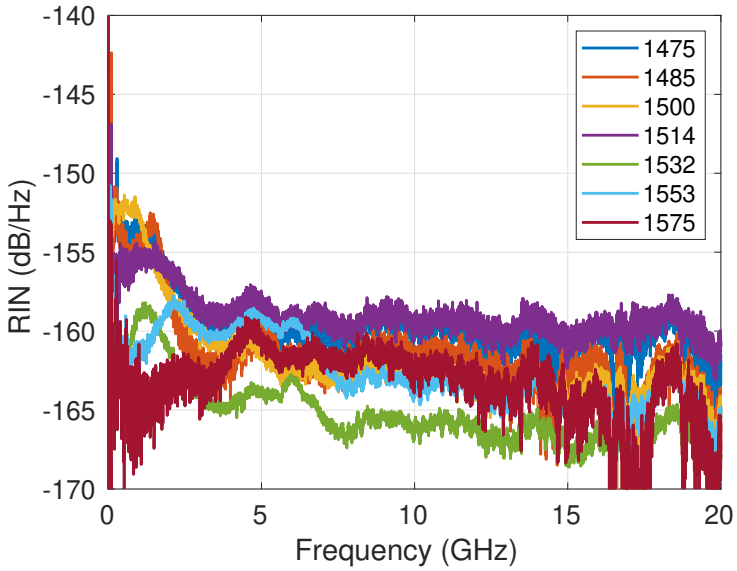

(b)

Fig. 3.8: (a) RIN measurement setup and (b) RIN measured at different wavelengths.

In this setup and RIN calculation; having accurately measured thermal noise, the shot noise ($I^2(t)\Omega$) contribution is subtracted from $P(t)$. Therefore the lowest possible measurable RIN value, which can be accurately measured, would be a few dB below the shot noise RIN limit of:

$$RIN_{shot} = 2q/I(t) \tag{3.10}$$

where q is the value of elementary electric charge, and $I(t)$ is the photocurrent at PD. $I(t)$ depends on the average laser power, and in the measurements, the photocurrent is typically 6.2 mA. This implies a shot noise RIN limit of the order of -163 dB/Hz. As the laser RIN reduces to below the calculated shot noise RIN, the accuracy of the laser RIN measurement is degraded, and this is evidenced by the additional noise in the RIN measurements (Fig. 3.8) as the RIN values approach -165 dB/Hz. A selection of measured

RIN profiles across the 100 nm tuning range[2] of the dual tunable device is shown in Fig. 3.8 (b). For all wavelengths, low frequency RIN below 2.5 GHz, does not exceed −153 dB/Hz, while at higher frequencies up to 20 GHz, RIN reduces to values within the range of −160 dB/Hz to −165 dB/Hz. Later, in chapter 5, RIN is presented as a constraining factor that significantly influences the performance of IM/DD systems that utilize digital multi-level signaling.

Linewidth & FM noise: Understanding phase noise is particularly important for advanced modulation formats that rely on encoding information in the carrier phase. As mentioned earlier, spontaneous emission introduces random phase fluctuations, which can be seen as frequency variations. The linewidth of a laser diode refers to the broadening of the spectral distribution of light emitted by the laser, primarily caused by phase noise. These phase fluctuations are a result of two main factors contributing to the frequency noise. Firstly, electronic carrier noise leads to changes in the refractive index and causes the laser's frequency to fluctuate. Secondly, there is the laser's inherent phase noise, which originates from the spontaneous emission of photons into the laser's mode [8]. Furthermore, the phase noise can be characterized statistically by analyzing the power spectral density of the frequency fluctuations, which is referred to as the Frequency Modulated (FM)-noise spectrum. In this study, both the linewidth and the FM-noise spectrum are measured to assess and describe the characteristics of the phase noise accurately.

The linewidth of each laser of the DLM is measured using the delayed self heterodyning (DSH) technique [9]. The DSH experimental setup employed in this study is depicted in Fig. 3.9 (a). This technique is used to measure the narrow linewidth which cannot be resolved by an optical spectrum analyzer (OSA). Here, L1 and L2 were thermo-optically tuned over the S, C and L bands, as shown in the Table. 3.1 and the linewidth is measured for each wavelength. The current to the gain section was set to 170 mA and 100 mA for L1 and L2 respectively. Each laser had an isolator connected to the fiber output. The optical output from each laser was split into two parts and decorrelated by adding a path delay via a 25 km standard single-mode fiber (SSMF) in one arm. The other arm was modulated by a high power 22 dBm RF signal at 2 GHz. The optical signals from

[2]The values corresponding to optical output for these measurements are presented in Appendix B

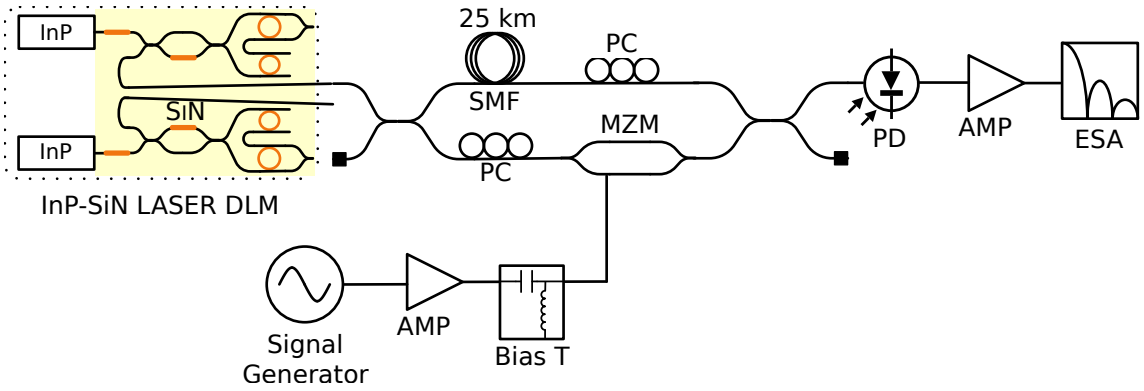

(a)

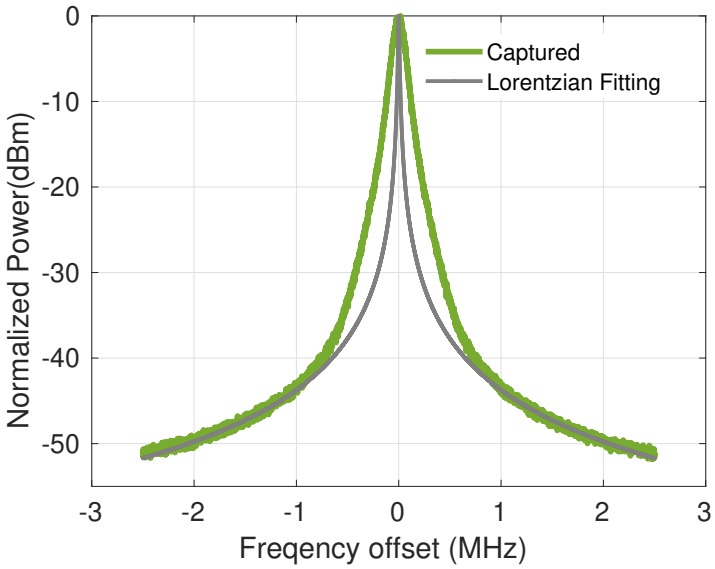

(b)

Fig. 3.9: (a) Delayed self heterodyning setup for linewidth measurement and (b) optical linewidth of L2 at 1536 nm with Lorentzian curve fitting.

the two arms were combined and fed to a 30 GHz PD. The electrical output of the PD was amplified and the linewidth of the beat tone was observed at the ESA (50 GHz bandwidth). Fig. 3.9 (b) shows the Lorentzian curve fitting on the received electrical spectrum of linewidth. The width of the measured spectrum is wider than the Lorentzian line curve due to the presence of flicker noise that gives a Gaussian profile to the measured spectrum. The linewidth estimation can also be done using Voigt curve fitting, which will produce a line curve that is a convolution of Lorentzian and Gaussian functions. However, in this work, the linewidth is estimated using the Lorentzian curve fitting only. The Lorentzian spectral width (−3 dB) was measured by dividing the width of the spectrum 20 dB below

the peak by 20, which in Fig. 3.9 (b) is roughly 14 kHz. The linewidth measured at different wavelengths[3] generated by thermo-optically tuning each laser is given in Tab. 3.1, indicating that the linewidth is <25 kHz for both lasers. This also indicates that the laser module has low phase noise (with the relation between linewidth and phase noise presented in the following measurement system). From Table 3.1, a small fluctuation in linewidth (due to different operating conditions for each wavelength) can be observed, but the values remain < 25 kHz across the full tuning range.

Table 3.1: Lorentzian Linewidths of DLM over 100 nm tuning range.

Laser 1		**Laser 2**	
Wavelength (nm)	Linewidth (kHz)	Wavelength (nm)	Linewidth (kHz)
1492	9	1517	10
1501	14	1527	10
1503	15	1536	14
1512	19	1547	11
1522	18	1557	19
1532	25	1567	20

The FM noise spectrum provides a comprehensive description of the noise processes contributing to the overall phase noise [10, 11]. To calculate the optical linewidth, the white noise component of the FM noise spectrum is utilized. This study undertakes an empirical assessment of the FM noise spectrum by employing a phase noise measurement technique that was previously developed [10]. The aim is to experimentally characterize the properties and behavior of the FM noise spectrum in a controlled environment.

The setup for phase noise measurement is similar to DSH, with the exception that a phase modulator is utilized as illustrated in Fig. 3.10 (a). The system measures the emitted light from L1, which was driven by a gain current of 170 mA, resulting in an optical power of 6.8 dBm at a wavelength of 1523 nm. Additionally, the phase noise of the optical signal from L2, operating at a wavelength of 1552 nm and with an optical power of 7 dBm, was measured when driven by a gain current of 100 mA. The optical signal from a laser is divided into two parts, one part was delayed by 25 km of SSMF to decorrelate it from the original/other signal. The other part is phase-modulated using a phase modulator driven by a high power 20 dBm 1 GHz RF signal, generating second-order harmonics. The light from both arms was combined and the resulting signal was detected using a

[3]The values corresponding to optical output for these measurements are presented in Appendix B

PD (20 GHz bandwidth). The detected heterodyne signal exhibits copies of the doubled linewidth at 1 GHz harmonics, which were captured by a real-time oscilloscope (4×10^6 samples captured over 400 ns). This allows post-processing of the signal for analysis and extraction of the FM noise spectrum and calculation of the optical linewidth [10].

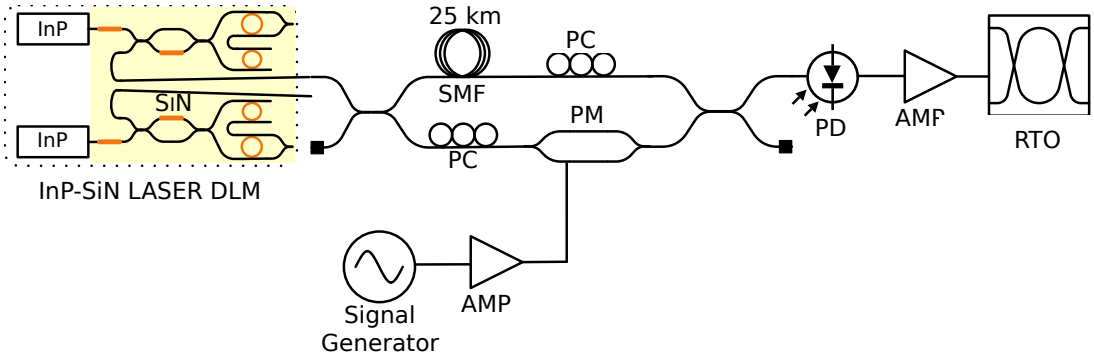

(a)

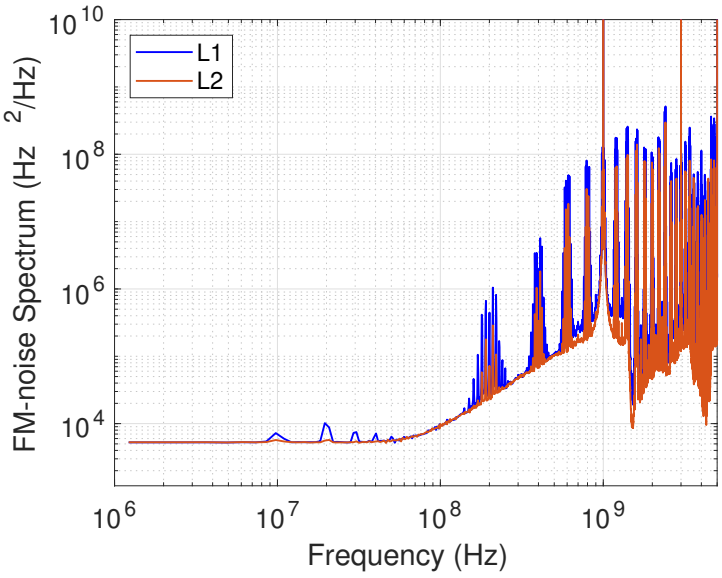

(b)

Fig. 3.10: (a) The phase noise measurement setup and (b) spectrum for L1 at 1523 nm and L2 at 1550 nm.

The FM noise spectrum represents the power spectral density (PSD) of the instantaneous frequency and can be derived by differentiating the phase noise. The phase noise spectrum for L1 and L2 of the DLM is illustrated in Fig. 3.10. The 3-dB linewidth ($\Delta\nu$) estimation can be obtained by analyzing the white noise region, S_0, of the laser's FM noise spectrum, which is

$$\Delta\nu = \pi S_0 \tag{3.11}$$

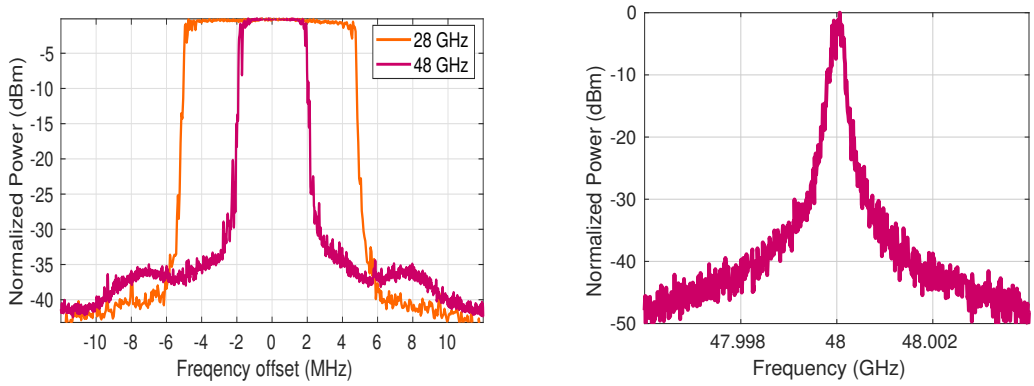

(a) (b)

Fig. 3.11: (a) FO on the 28 GHz and 48 GHz beat tones and (b) electrical spectrum of the 48 GHz beat tone.

The linewidth calculated through the phase noise measurement setup is $\sim$ 12 kHz for both lasers. Hence from this study, it is confirmed that the DLM exhibits very narrow linewidth over a wide wavelength tuning range.

Since the gain sections (SOAs) of L1 and L2 are independent, the optical carriers emitted are non-coherent, giving rise to phase noise and frequency offset (FO) on the resultant RF beat-tone after heterodyning of two laser outputs. The FO caused by the relative drift between laser frequencies can be observed by measuring the detected RF beat signal using the 'max hold' function ($\sim$ 5 mins) on an ESA which plots spectral evolution over the set time period. Fig. 3.11 (a) depicts the FO of $\sim$ 11 MHz on a 28 GHz beat tone and $\sim$ 5 MHz on a 48 GHz beat tone. It is noted that similar FOs are observed as the lasers are tuned to vary the RF beat frequency. Fig. 3.11 (b) presents the RF beat spectrum of two carriers from the dual laser source with 48 GHz separation. The spectral width (−3 dB) of this RF beat tone was measured roughly around $\sim$ 34 kHz, as expected for the beat signal of two independent lasers with linewidths of around 15 kHz.

3.1.3 Device Applications

The flexibility of the DLM, in terms of wavelength tunability and RF signal generation (10 GHz to 1 THz), is depicted in Figs. 3.12 (a), (b) and (c), respectively. The DLM can be used to generate pairs of optical carriers tunable over a wavelength range of 70 nm covering the S-band, C-band and partially the L-band, as discussed in section 3.1, through

optical heterodyning, with Fig.3.12 (a) showing pairs of carriers separated by 56 GHz tuned from 1527 nm to 1553 nm. The power of the optical carriers can be optimized as per the requirements of the heterodyne systems by changing the voltage to the microheaters

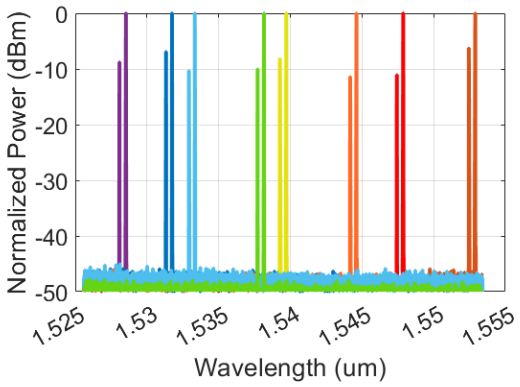

(a)

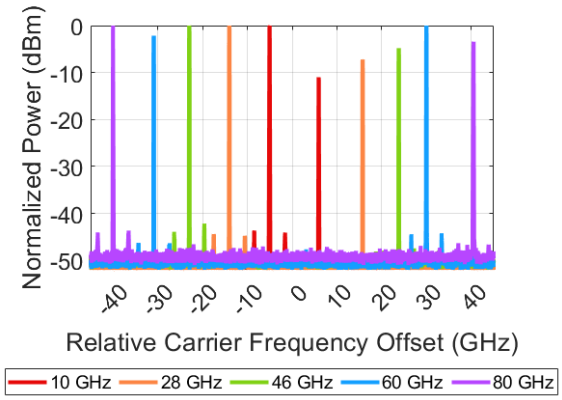

(b)

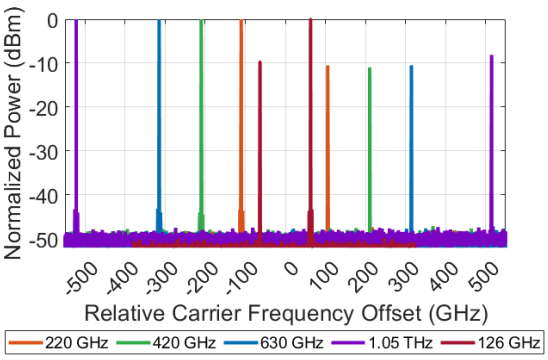

(c)

Fig. 3.12: Thermo-optic tuning of the DLM to generate (a) 56 GHz frequency generation over wavelength, (b) 10 to 90 GHz carrier frequency generation and (c) 100 to 1000 GHz carrier frequency generation.

associated with the tunable couplers of the DLM (see subsection 3.1.2). This wavelength flexibility of the DLM makes it a superior contender among the other optical sources used for heterodyning applications discussed in the introduction. Moreover, the ability to generate optical carrier pairs at various frequency differences offers a versatile way of deploying this device in beyond 5G and 6G, access networks employing K (18-26.5 GHz), Ka (26.5-40 GHz), mmWave (30-300 GHz), Y (325-500 GHz) bands and even the THz range, as presented in Fig. 3.12 (b) and (c).

The DLM offers several advantageous properties, such as low noise and high wavelength tunability. A thorough literature survey performed by authors in [5, 12] suggests that among the various hybrid and heterogeneously integrated laser diodes, the InP-Si_3N_4 hybrid integrated diode laser produces the highest degree of intrinsic coherent output. These features make it highly promising for utilization in high-speed and agile optical communication systems. Some specific applications where this laser module holds potential include:

1. **Direct detection with advanced modulation techniques (such as PAM4/PAM8)**: The laser's low Relative Intensity Noise (RIN) and high optical power make it suitable for direct detection schemes, enabling efficient data transmission in datacenters and access networks.

2. **Optical heterodyning/mmWave generation for ARoF systems**: The laser's low linewidth and wide tuning range are valuable for generating mmWave signals and performing optical heterodyning, which is essential for future ARoF applications.

3. **Gigabit Passive Optical Network (GPON)**: The laser's characteristics, including low RIN, high output powers, and wide tuning range, make it well-suited for use in GPON, enabling high-speed data transmission over passive optical networks.

4. **Coherent communication in optical metro and future optical access networks**: With its narrow linewidth and low RIN, the laser module is highly suitable for coherent communication applications in optical metro and future optical access networks, where precise phase and amplitude information is crucial for reliable data transmission.

Given these strengths, the laser module becomes an ideal source for convergence in various optical communication scenarios. The next section will look into the description of the experimental work conducted with this laser module, showcasing its capabilities and performance in futuristic converged radio/optical transmission systems.

3.2 ARoF mmWave Transmission System

The experimental systems described below are designed to simultaneously exploit the aforementioned advantages of the DLM and leverage the high bandwidth and spectral efficiency of ARoF for mmWave converged access (discussed in section 2.2.2). The DLM is used as a source in two heterodyne ARoF fronthaul link scenarios, incorporating both 10 km fiber and up to 2m wireless transmission. The successful evaluation of these systems elucidates how this source can play a key role in the future optical and wireless integrated C-RANs for beyond 5G and 6G applications and services.

3.2.1 mmWave Receiver for Non-Coherent Heterodyne Systems

Since the carrier pairs generated by the DLM are not coherent, their heterodyne detection can result in the generation of an RF carrier with significant amounts of phase noise and FO (as described in section 2.2.1). To circumvent this issue, the ARoF mmWave converged systems presented in the following section make use of two RF receiver types:

3.2.1.1 PNC receiver

The phase noise cancellation (PNC) receiver [13, 14] allows the RF coherent recovery of the received mmWave signal through the use of a mmWave pilot tone generated through the heterodyne process at the PD stage. The analog phase noise canceling mmWave receiver architecture is depicted in Fig. 3.13. This architecture allows phase noise and FO cancellation at the IF down-conversion stage without the requirement for a standalone receiver LO and is described in detail in [14]. After photodetection, the electrical spectrum shown in Fig. 3.13 is split into two paths. The PNC receiver contains an electrical bandpass filter (EBPF) in each path; a signal filter and a carrier filter which are used to isolate the upper data sideband and mmWave carrier term, respectively. The filtered signal and

carrier terms are then used as the 'RF' and 'LO' inputs to a mmWave mixer, respectively. These filtered components exhibit matching phase noise as a result of being generated through the same photo-mixing process. This allows the filtered carrier term to be used as a phase noise correlated 'LO' which, when mixed with the signal term, produces an IF data signal free from phase noise. This receiver operation allows optical field modulation to be performed at the CO, helping to improve receiver sensitivity. This comes at the cost of a relatively complex, albeit LO-free, mmWave receiver architecture and the additional insertion loss associated with optical field modulation at the CO.

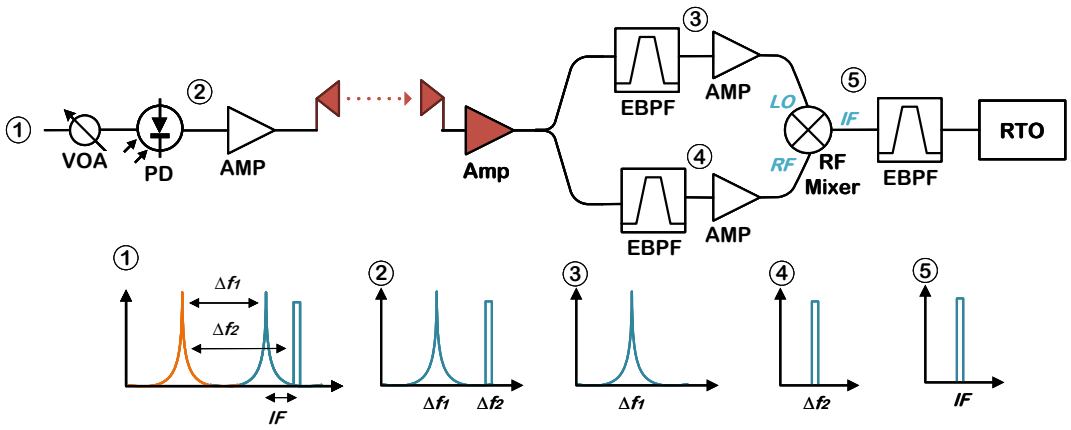

Fig. 3.13: A schematic of PNC receiver [14].

3.2.1.2 Envelope Detector

The envelope detector extracts the envelope of the received signal, recovering amplitude information from a modulated RF carrier. An envelope detector operates by rectifying the modulated signal, which means converting the negative part of the signal into positive one. This rectification is typically done using a diode. The incoming modulated signal is amplitude modulated and on a high RF carrier. By rectifying the signal, all frequency and phase modulation are stripped out with only the amplitude information (i.e. the envelope) remaining. After rectification, a low-pass filter is used to remove the high-frequency components, leaving only the envelope of the signal. The envelope detector provides a simple and low-cost LO-free mmWave receiver solution but is well known to suffer from relatively poor sensitivity. The reason is, as the phase and frequency information is not detected by this receiver, there is a requirement for optical intensity modulation at the CO.

The intensity modulation limits the achievable optical signal-to-carrier ratio and hence the optical receiver sensitivity. However, this requirement – which is enabled through simplistic optical modulation, incurring relatively low insertion losses – also serves to lower the complexity of the overall system design.

3.2.2 Experimental systems for OFDM transmission

To exploit wavelength and frequency flexibility of DLM in the converged optical/mmWave ARoF fronthaul, two types of experimental systems were implemented [13, 15]. The first system depicted in Fig. 3.14 employs the I/Q modulator and PNC receiver to evaluate the wavelength flexible performance of the DLM over ARoF fronthaul. In the second system, represented in Fig. 3.16, the main differences are the use of the intensity modulator and the envelope detector-based receiver, with this setup variant used to evaluate the frequency flexible performance of the DLM over a simplified ARoF fronthaul transmission system. For simplicity, the experimental setups are denoted as system 1 and system 2 to signify the wavelength and frequency flexible optical/mmWave systems, respectively. The PNC receiver is capable of providing superior performance due to higher receiver sensitivity but is bandwidth limited (due to the fixed RF filters used in the circuit) and hence is not used to evaluate the frequency flexibility of the DLM.

3.2.2.1 System 1: λ-flexible optical/mmWave system

In system 1, shown in Fig. 3.14, the DLM is thermo-optically tuned to generate pairs of optical carriers with 56 GHz separation over the C-Band, with optical powers of −3 dBm from laser 1 (L1) and −1 dBm from laser 2 (L2), approximately. Each laser had an isolator connected to the fiber output. L1 is amplified to overcome the losses introduced by the modulation arm of the transmitter. An electrical 5G NR standard compatible 64-QAM OFDM signal (whose parameters are detailed in Table 3.2) was software-generated, up-converted to an IF carrier of 4.75 GHz and loaded on the arbitrary waveform generator (AWG) operating at 20 GSa/s. The signal was amplified and used to drive an I/Q MZM biased close to the null point to perform optical single-sideband (O-SSB) modulation on the optical carrier (L1) and the optical spectrum is shown in Fig. 3.14. Complete suppression of the upper sideband was achieved using an optical bandpass filter (OBPF)

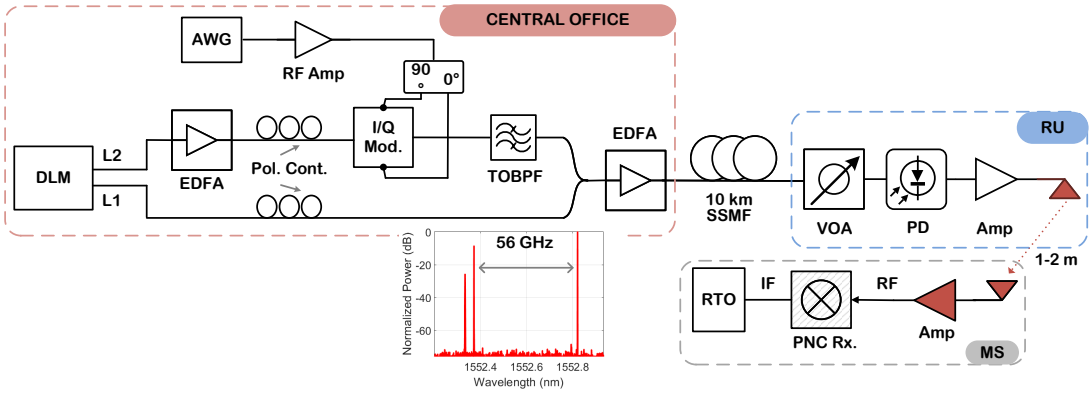

(a) System 1

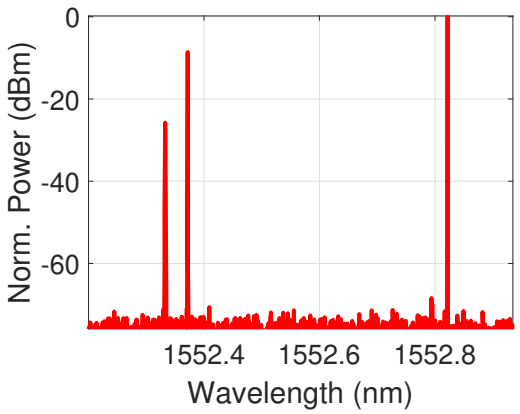

(b) Optical spectrum of narrowband 64-QAM O-SSB modulation

Fig. 3.14: (a) DLM schematic and optical/mmWave experimental ARoF fronthaul system with I/Q modulator and PNC receiver with (b) showing the transmitted optical spectrum of narrowband 64-QAM O-SSB modulation. Elements in red indicate components added to the system for wireless transmission.

following modulation – considering the 20 dB modulator extinction. The modulated and the unmodulated optical carriers, which are 56 GHz apart, are coupled and amplified by the Erbium-doped fiber amplifier (EDFA) to a total power of +3 dBm before propagation through 10 km of SSMF. The two optical carriers beat together at the 70 GHz PIN PD and produce a mmWave carrier at 56 GHz and OFDM sideband at 60.75 GHz (56 GHz + 4.75 GHz). The composite mmWave signal (carrier and data signal) is amplified and then transmitted over a wireless link of 1 - 2 m using a set of 20 dB gain directional horn antennae.

The transmission of the mmWave data signal alongside a phase noise correlated carrier (pilot tone), enables phase noise and FO cancellation using the analog electrical PNC re-

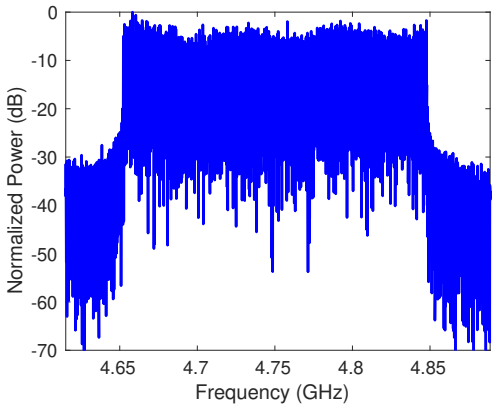

Fig. 3.15: Received IF spectrum of 5G NR

Table 3.2: System 1 & System 2 IF properties

Properties	System 1	System 2	
	5G NR	5G NR	WiGig
QAM order	64	256,512	64
FFT size	2048	2048	512
Total *SC**	800	800	336
SC Spacing	244 kHz	244 kHz	4.88 MHz
Bandwidth	195 MHz	195 MHz	1.64 GHz
Datarate (Gbps)	1.17	1.56,1.76**	9.84

*SC stands for subcarrier

**Values for 256-QAM and 512-QAM respectively

ceiver structure. Mixing of the mmWave carrier and data sideband terms at the PNC stage produces a clean IF OFDM signal (see Fig. 3.15) which is then captured by a real-time oscilloscope (RTO) at 50 GSa/s before offline processing consisting of synchronization, channel estimation and equalization and EVM/BER measurement is performed.

Initially, the wavelength flexibility of the mmWave ARoF system is demonstrated by operating the DLM at four different sets of wavelength pairs across the C-band. Both the lasers from the DML were tuned to achieve a constant relative frequency spacing of 56 GHz while operating at different wavelengths of 1539 nm, 1544 nm, 1548 nm and 1552 nm (shown in Fig. 3.12(a)). One of the optical carriers from these wavelength pairs was single sideband modulated with a 244 kHz subcarrier spacing OFDM signal (5G NR compatible) at 4.75 GHz intermediate frequency in order to generate a 60.75 GHz mmWave signal.

3.2.2.2 System 2: mmWave flexible optical/mmWave system

In system 2, the DLM is thermo-optically tuned to produce the optical carriers with the desired mmWave frequency carrier separation from 55-65 GHz. Each laser had an isolator connected to the fiber output. The inclusion of a single-ended MZM for intensity modulation, coupled with envelope detection, serves to lessen the complexity of the system relative to that of system 1 above. In addition, the intensity modulation operation results in a reduction in modulator insertion losses negating the requirement for the additional EDFA at the transmitter. The single-ended $LiNbO_3$ MZM is fed by two types of IF OFDM signals resembling the 5G NR and Wi-Fi Gigahertz (WiGig) [16] standards. The two IF signals centered at 1.75 GHz, whose properties are given in Table 3.2, are first amplified and then used to drive the MZM which is biased at quadrature for optical double sideband (ODSB) modulation (optical spectra in Fig. 3.16 (b) and (c)). An EDFA amplifies the combined optical spectra before its transmission over fiber. The signal is remotely detected by a PD, which photo-mixes the composite optical signal, generating a mmWave carrier within the V-band range (55-65 GHz) with two OFDM signal sidebands 1.75 GHz away from the carrier. The mmWave generation is limited to this range due to the limited bandwidth of the electrical components at the receiver. This signal is wirelessly transmitted by the antenna over a shorter link length of 1 m, due to lower receiver sensitivity compared to system 1. The received mmWave signal is fed to a 50-75 GHz envelope detector with 3 GHz IF bandwidth which retrieves the amplitude modulated information to generate an IF OFDM signal. This IF signal is then captured by the RTO for further offline processing.

3.2.3 Results & Discussion

3.2.3.1 System 1: λ-flexible performance (5G NR)

Fig. 3.17 (a) shows the EVM performance of this outlined system (system 1) for four different transmission scenarios of O-B2B, 10 km fiber (Fb), 10 km fiber + 1m wireless (Fb + 1 m Wi), and 10 km fiber + 2 m wireless (Fb + 2 m Wi) using all the above-mentioned wavelength pairs. The results indicate that the transmission over 10 km of fiber has a negligible effect on system performance compared to the O-B2B case for all four-

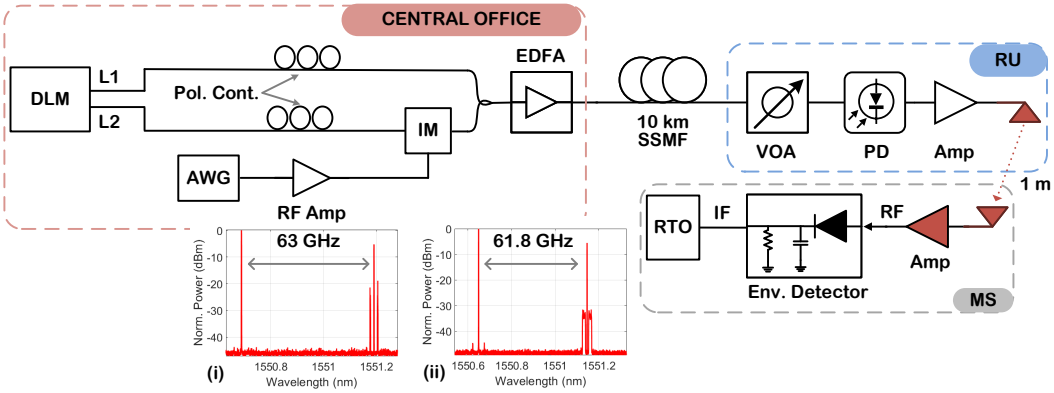

(a) System 2

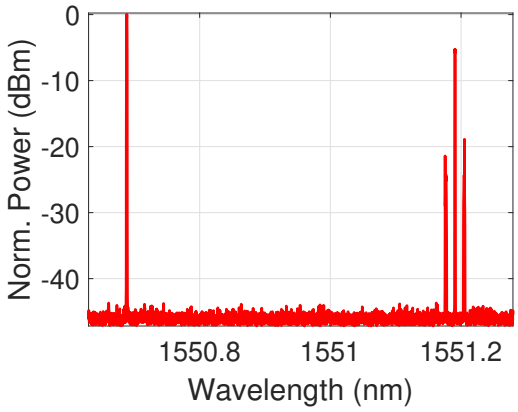

(b) Optical Spectrum of narrowband 256-QAM ODSB modulation

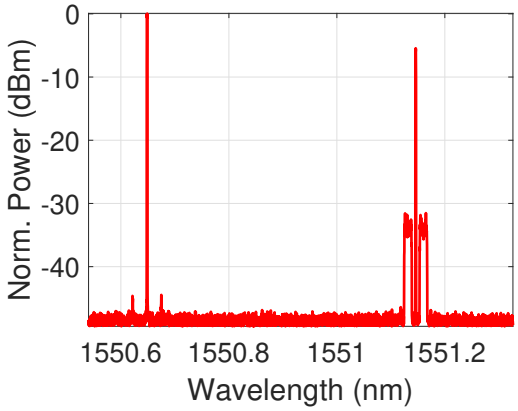

(c) Optical Spectrum of wideband 64-QAM ODSB modulation

Fig. 3.16: (a) DLM schematic and optical/mmWave experimental ARoF fronthaul system 2 having intensity modulator and envelope detector with inset showing with (b) narrowband 256-QAM and (c) wideband 64-QAM ODSB modulations.

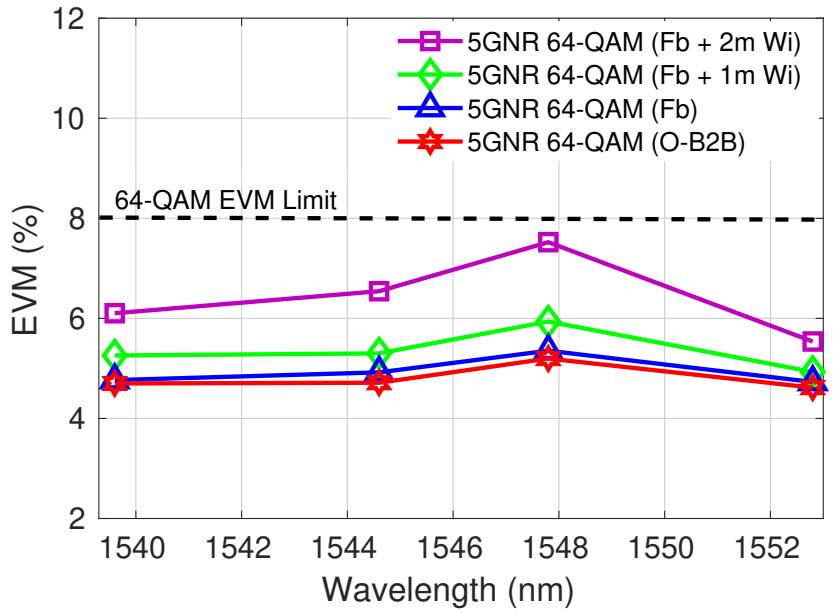

(a) EVM versus wavelength

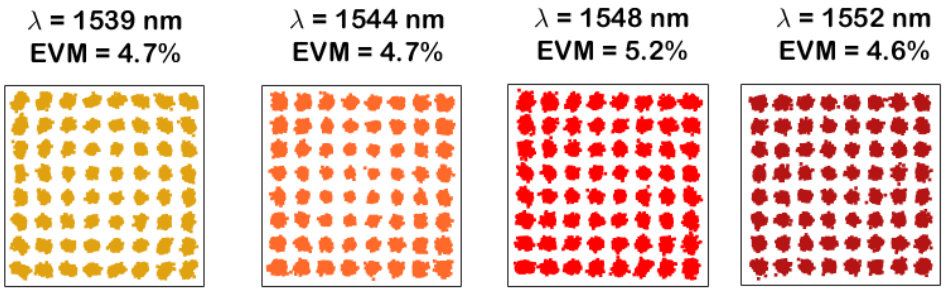

(b) OB2B demodulated signal constellations

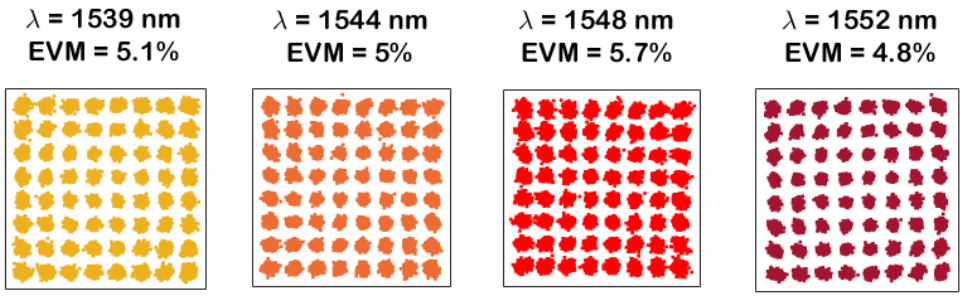

(c) 10 km fiber and 1 m wireless link demodulated signal constellations

Fig. 3.17: (a) EVM performance of the received signal with respect to the wavelength. (b) and (c) shows constellations of the OB2B and 10 km fiber and 1 m wireless link demodulated 60.75 GHz mmWave signal and EVM values respectively.

wavelength pairs at a received optical power (ROP) of -2 dBm. For wireless transmission, the two horn antennae (each with a passband of 55-65 GHz) along with an additional receiver electrical booster amplifier were added to the system. The line-of-sight wireless link was manually adjusted to maximize the received power for transmission distances of 1 and 2 m. Fig. 3.17 (a) shows that the addition of a 1 m wireless link following 10 km fronthaul transmission (Fb + 1m Wi, green curve) results in a small ($\sim$0.5%) degradation in EVM across all tested wavelength pairs. This degradation can be attributed to the reduced electrical SNR at the receiver due to additional noise from the booster amplifier. Nevertheless, excellent performance below 6% was achieved in all cases over the full fiber-wireless link.

Increasing the wireless distance to 2 m (Fb + 2m Wi, purple curve) results in a further 1 - 1.5% degradation in EVM across the wavelength range. This degradation can be attributed to the combined effects of marginally elevated PD nonlinearity (as the ROP, in this case, was increased to 0.5 dBm to obtain a reasonable signal level at the PNC receiver), as well as additional signal attenuation over the increased wireless link distance. Again, EVM performance between 6 and 7.8%, which is below the 8% EVM limit for 64-QAM, indicates the successful transmission of 1.17 Gb/s 5G NR compatible subcarrier spacing OFDM signals. It should be noted that a more advanced wireless mmWave link design, such as beam-forming operation using a phased array antenna (PAA), could greatly increase the achievable wireless transmission distance for the presented system [17]. The constellation results in Fig. 3.17 (b), representing EVMs between 4.6% and 5.2% at different wavelengths for OB2B scenarios, indicate the successful generation, and demodulation of the 5G NR compatible mmWave OFDM signal over an ARoF heterodyne fronthaul link across the C-band. The constellation results for signal transmission over 10 km fiber and 1 m wireless link is depicted Fig. 3.17 (c). The constellation points are more scattered in fiber-wireless link compared to OB2B because the Gaussian noise is added to the signal by the wireless channel.

3.2.3.2 System 2: mmWave flexible performance (5G NR)

While the wavelength flexibility demonstrated by tuning the DLM to operate at four different optical carrier pairs over C-band plays an important role from an optical network

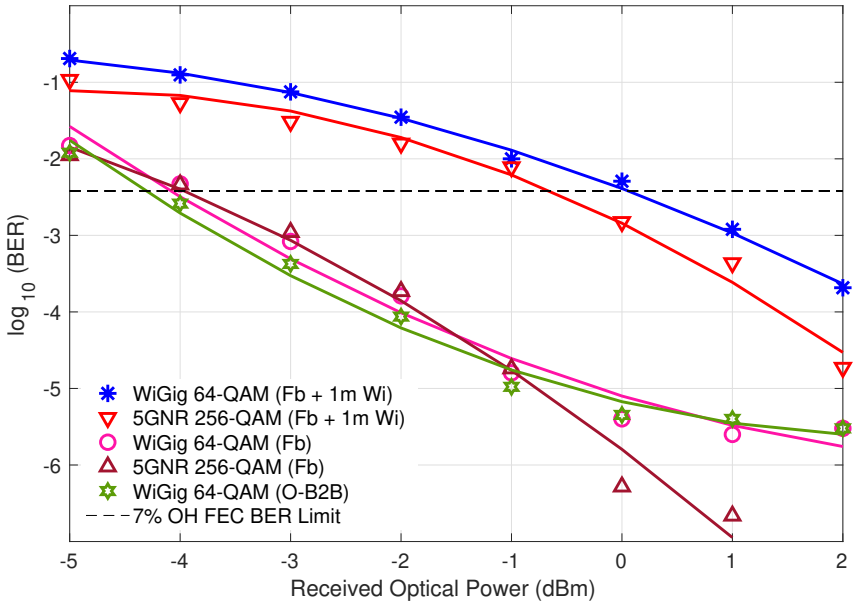

(a)

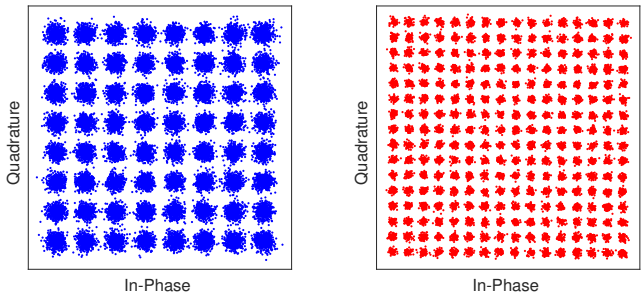

(b) (c)

Fig. 3.18: (a)BER versus ROP over both fiber and wireless, only fiber and back-to-back links. The constellation of demodulated (b) 61.8 GHz mmWave 64-QAM WiGig and (c) 256-QAM 5G NR (red) signals, respectively, for the case of Fb + 1m Wi transmission at +2 dBm ROP.

design perspective, the mmWave carrier frequency flexibility is important for an efficient design of the wireless link. In this subsection, variable frequency mmWave signal generation within the V-band range of 58.3 GHz to 64.3 GHz, using optical carriers at roughly around 1552 nm wavelengths, is demonstrated over an ARoF fronthaul system incorporating the envelope detector-based receiver. Fig. 3.18 shows the BER performance after demodulation of the 256-QAM 61.8 GHz 5G NR OFDM (mobile) signal with respect to ROP on the PD for two different transmission scenarios: 10 km fiber (Fb) and 10 km fiber + 1m wireless (Fb + 1m Wi) .

It was observed that the transmission over the optical back to back link and 10 km fiber link had similar BER performance over different received optical powers. The results also show excellent performance in the case of 10 km fiber transmission with BER as low as 8.46×10^{-6} for 1 dBm optical power falling on the PD. As expected, the BER degrades with reduced ROP and reaches the 7% overhead (OH) FEC limit of 2.3×10^{-3} at –4 dBm. The results shown in Fig. 3.18(a) further indicate performance degradation with ∼3 dB penalty in receiver sensitivity once the wireless transmission is introduced in the link (Fb + 1m Wi case). This performance difference is attributed to the combined effect of SNR degradation due to additional noise from the booster amplifier and reduced electrical power on the receiver envelope detector. Nevertheless, performance below the FEC limit is achieved over the full link demonstrating the successful mobile signal transmission at a data rate of 1.56 Gb/s. A received constellation of the demodulated 64-QAM WiGig and 256-QAM 5G NR data is also shown in Fig. 3.18(b) and (c), respectively, for the case of Fb + 1m Wi transmission with an ROP of 2 dBm.

In order to demonstrate the variable frequency mmWave signal generation, both the lasers from DLM were finely tuned to obtain 9 different carrier spacings from 55-64.3 GHz. Fig. 3.19(b) shows the EVM performance of 256-QAM data modulated 5G NR OFDM signals at each of the generated mmWave frequencies after transmission over 10 km fiber and 1 m wireless (Fb + 1m Wi). The system shows a uniform performance (below the 3.5% EVM limit for a 256-QAM signal) across the frequency span, with the lowest EVM of 2.4% observed at the carrier frequency of 64.3 GHz (with a BER of 8.46×10^{-6}). The slight improvement in system performances, compared to those presented in section 3.2.3.1 over system 1, stems from the improved OSNR as the second EDFA was not required with this system configuration. In order to further increase the data rate, 512-QAM data was modulated on the OFDM subcarriers, and its performance is shown at two different mmWave frequencies in Fig. 3.19. In this case with Fb + 1m Wi transmission, EVM values of 2.5% and 2.4% were measured at 58.3 GHz (constellation in Fig. 3.19) and 64.3 GHz frequencies, respectively, delivering a datarate of 1.76 Gb/s.

RF/mmWave carrier frequency flexibility is paramount for wireless systems due to the use of closely spaced frequency channels. The results presented in this subsection show the capabilities of the employed DLM to generate mmWave signals in the V band

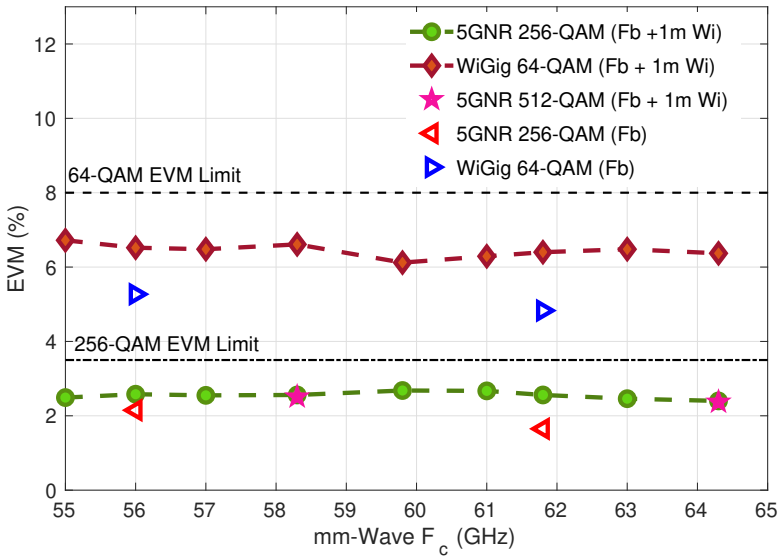

(a)

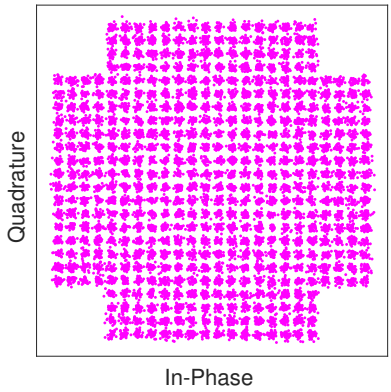

(b)

Fig. 3.19: (a) EVM as a function of mmWave Fc is set at 2 dBm ROP. (b) The received constellation for the 512-QAM 5G signal at 58.3 GHz.

with ∼1 GHz of granularity achieved through precise wavelength tuning. The choice of operating the system in the 55-64.3 GHz frequency band was dictated by the availability of various RF, mmWave and optoelectronic components. In practice, any frequency up to 1.05 THz can be generated with the employed DML as shown by the tuning spectrum in Fig. 3.12(b).

3.2.3.3 System 2: mmWave flexible performance (WiGig)

The results presented in the previous two subsections show the successful transmission of 195 MHz bandwidth 5G NR compatible OFDM signals designed for mobile applications. In order to achieve higher data rates, up to 10 Gb/s for 5G and beyond 5G services, wider bandwidth signals are required. While there is no standard defined for higher channel bandwidth mobile telephony applications yet, the 60 GHz wireless gigabit standard (WiGig IEEE802.11ad [16]) gives some indication of the possible future specifications. The IEEE 802.11ad standard for indoor broadband services specifies the use of four 2.16 GHz bandwidth channels ($\sim$1.83 GHz data signal bandwidth) for data transmission in the unlicensed frequency band between 57 GHz to 66 GHz. In order to demonstrate a higher data rate system, WiGig standard compatible bandwidth OFDM signals over the envelope detector-based mmWave ARoF system 2 are transmitted.

The BER performance of the 61.8 GHz 1.64 GHz bandwidth WiGig signal with variable ROP is shown in Fig. 3.18 for three transmission scenarios of O-B2B, Fb, and Fb + 1m Wi. The results indicate that the transmission over 10 km fiber does not have any significant effect on the performance of the signal compared to the O-B2B case. In both of these cases, the BER degrades to above the FEC limit at an ROP of −4 dBm – similar to the 5G NR transmission case. At higher ROPs in the Fb transmission scenarios, an error floor emerges in the case of the WiGig signal at 61.8 GHz but is not evident for the 5G NR signal. This effect can be attributed to the impact of the wider signal bandwidth. This results in further performance degradation, with a 4 dB penalty in receiver sensitivity, where wireless transmission is introduced in the link. The 1 dB receiver sensitivity penalty between WiGig and 5G NR transmission for Fb + 1m Wi case, as seen in Fig. 3.18, can be attributed to the different SNR requirements for the QAM formats used, as well as the differing signal bandwidths.

Here again, fine wavelength tunability of the DLM (as presented in subsection 3.1.2) is exploited to demonstrate the flexibility of the presented system to successfully generate mmWave signals within the channel frequencies mentioned in the WiGig standard. Fig. 3.19 shows the EVM performance of the outlined Wi + Fb transmission system with respect to the variable mmWave carrier frequency from 55-64.3 GHz for an ROP of +2 dBm

– similar to the 5G NR case. The results indicate minimal variation in the EVM (between 6.1% to 6.7%) for different mmWave channel frequencies. These results demonstrate the successful transmission of the 9.84 Gbps signals in all transmission cases, once again highlighting the ability of the system to support centralized and flexible provisioning of future mmWave services.

The use of a low linewidth and photonic integrated laser module along with FO agnostic receivers in the system enables excellent performance for the WiGig and 5G NR compatible multicarrier OFDM signals which exhibit relatively low subcarrier spacings. But, in general, the single carrier approach (available as a waveform option for WiGig services [18]) can lessen the requirements for precise FO and phase noise cancellation at the receiver [19] at the cost of reduced spectral efficiency.

3.3 Conclusion

As mentioned in chapter 1, photonic integration will play a key role in the development of cost-effective links as many transmitters and modulators can be integrated on a single chip. The experimental work described in this chapter involved the characterization of an integrated DLM that can be tuned over 100 nm while maintaining the SMSR over 50 dB and the RIN values around −160 dB/Hz. The DLM exhibits narrow linewidth and low phase noise indicating the device's potential to provide low noise carriers for use in future optical access networks and coherent communication systems. The tuning characteristics of the device make it an excellent candidate for optical heterodyne systems. The two experimental works presented in this chapter demonstrate the ability of a hybrid integrated InP-Si_3N_4 DLM to provide flexible wavelength and RF carrier assignment, for remote mmWave generation through heterodyne detection. The first system deploys DLM in a heterodyne ARoF system with an analog PNC receiver circuit. Excellent performances of $\sim$ 5% EVM are achieved on all test wavelengths over the full fiber fronthaul link and a 1 m wireless distance, with negligible degradation compared to the back-to-back cases. The results demonstrate how an integrated DLM can provide a highly re-configurable silicon-based platform for the successful delivery of 5G ARoF mmWave services – in this case delivering a raw mobile data rate of 1.17 Gb/s at 60.75 GHz.

A further simplified and cost-effective system is developed using an envelope detector-based receiver. The system performs exceptionally well, with all recorded EVMs below 3% and 7% for the transmission of 256-QAM 5G NR and 64-QAM WiGig signals, respectively, and exhibits excellent uniformity in EVM performance with both signals exhibiting a variance of less than 1% across the frequency range. Although the DSB nature of the signal transmission here limits achievable spectral efficiency, the results show that this can be somewhat offset by the successful transmission of OFDM signals with higher-order QAM, up to 512 levels. While the RF tunability demonstrated in this work is over a portion of the V-band, the use of higher speed photodiodes [20] and electrical components [21], in conjunction with the DLM presented here, can facilitate ARoF systems operating in the 100 GHz to 1 THz range. The integrated SiP approach provides the potential for a smaller form factor, greater cost efficiency and a higher yield device fabrication ultimately paving the way for a fully integrated optical/mmWave transceiver. In the next chapter 4, the wide tunability and low noise features of DLM in combination with advanced system design are discussed.

References

[1] C. G. Roeloffzen, L. Zhuang, C. Taddei, A. Leinse, R. G. Heideman, P. W. van Dijk, R. M. Oldenbeuving, D. A. Marpaung, M. Burla, and K.-J. Boller, "Silicon nitride microwave photonic circuits," *Optics express*, vol. 21, no. 19, pp. 22 937–22 961, 2013.

[2] C. G. H. Roeloffzen, M. Hoekman, E. J. Klein, L. S. Wevers, R. B. Timens, D. Marchenko, D. Geskus, R. Dekker, A. Alippi, R. Grootjans, A. van Rees, R. M. Oldenbeuving, J. P. Epping, R. G. Heideman, K. Worhoff, A. Leinse, D. Geuzebroek, E. Schreuder, P. W. L. van Dijk, I. Visscher, C. Taddei, Y. Fan, C. Taballione, Y. Liu, D. Marpaung, L. Zhuang, M. Benelajla, and K.-J. Boller, "Low-Loss Si_3N_4 TriPleX Optical Waveguides: Technology and Applications Overview," *IEEE J. Select. Topics Quantum Electron.*, vol. 24, no. 4, pp. 1–21, Jul. 2018. [Online]. Available: http://ieeexplore.ieee.org/document/8259277/

[3] J. P. Epping, A. Leinse, R. M. Oldenbeuving, I. Visscher, D. Geuzebroek, D. Geskus, A. van Rees, K. J. Boller, M. Theurer, M. Möhrle, C. G. Roeloffzen, and R. G. Heideman, "Hybrid integrated silicon nitride lasers," in *Physics and Simulation of Optoelectronic Devices XXVIII*, vol. 11274. International Society for Optics and Photonics, 2020, p. 112741L.

[4] Y. Lin, C. Browning, R. B. Timens, D. H. Geuzebroek, C. G. Roeloffzen, M. Hoekman, D. Geskus, R. M. Oldenbeuving, R. G. Heideman, Y. Fan, K. J. Boller, and L. P. Barry, "Characterization of hybrid inp-triplex photonic integrated tunable lasers based on silicon nitride (Si_3N_4/SiO_2) microring resonators for optical coherent system," *IEEE photonics journal*, vol. 10, no. 3, pp. 1–8, 2018.

[5] K.-J. Boller, A. van Rees, Y. Fan, J. Mak, R. E. M. Lammerink, C. A. A. Franken, P. J. M. van der Slot, D. A. I. Marpaung, C. Fallnich, J. P. Epping, R. M. Oldenbeuving, D. Geskus, R. Dekker, I. Visscher, R. Grootjans, C. G. H. Roeloffzen, M. Hoekman, E. J. Klein, A. Leinse, and R. G. Heideman, "Hybrid Integrated Semiconductor Lasers with Silicon Nitride Feedback Circuits," in *Photonics*, vol. 7, no. 1. Multidisciplinary Digital Publishing Institute, 2020, p. 4.

[6] G. P. Agrawal, *Fiber-optic communication systems*. John Wiley & Sons, 2012.

[7] G. E. Obarski and J. D. Splett, "Transfer standard for the spectral density of relative intensity noise of optical fiber sources near 1550 nm," *JOSA B*, vol. 18, no. 6, pp. 750–761, 2001.

[8] L. A. Coldren, S. W. Corzine, and M. L. Mashanovitch, *Diode lasers and photonic integrated circuits*. John Wiley & Sons, 2012.

[9] T. Okoshi, K. Kikuchi, and A. Nakayama, "Novel method for high resolution measurement of laser output spectrum," *Electronics letters*, vol. 16, no. 16, pp. 630–631, 1980.

[10] T. N. Huynh, L. Nguyen, and L. P. Barry, "Phase noise characterization of SGDBR lasers using phase modulation detection method with delayed self-heterodyne measurements," *Journal of lightwave technology*, vol. 31, no. 8, pp. 1300–1308, 2013.

[11] K. Kikuchi, "Effect of 1/f-type FM noise on semiconductor-laser linewidth residual in high-power limit," *IEEE Journal of Quantum Electronics*, vol. 25, no. 4, pp. 684–688, 1989.

[12] Y. Fan, A. van Rees, P. J. van der Slot, J. Mak, R. Oldenbeuving, M. Hoekman, D. Geskus, C. G. Roeloffzen, and K.-J. Boller, "Ultra-narrow linewidth hybrid integrated semiconductor laser," *arXiv preprint arXiv:1910.08141*, 2019.

[13] D. Dass, A. Delmade, L. Barry, C. G. Roeloffzen, D. Geuzebroek, and C. Browning, "Flexible optical and millimeter-wave analog-rof transmission with a silicon-based integrated dual laser module," in *2021 European Conference on Optical Communication (ECOC)*. IEEE, 2021, pp. 1–4.

[14] C. Browning, A. Delmade, Y. Lin, J. Poette, H. H. Elwan, and L. Barry, "Phase noise robust optical heterodyne system for reduced complexity millimeter-wave analog radio-over-fibre," in *European Conference on Optical Communication*, Sept. 2019.

[15] D. Dass, A. Delmade, L. Barry, C. G. Roeloffzen, D. Geuzebroek, and C. Browning, "Flexible v-band mmwave analog-rof transmission of 5g and wigig signals using an inp-sin integrated laser module," in *2021 International Topical Meeting on Microwave Photonics (MWP)*. IEEE, 2021, pp. 1–4.

[16] B. Schultz, "802.11 ad–wlan at 60 ghz–a technology introduction," *Rohde & Schwarz*, 2013.

[17] I. F. Akyildiz, C. Han, and S. Nie, "Combating the distance problem in the millimeter wave and terahertz frequency bands," *IEEE Communications Magazine*, vol. 56, no. 6, pp. 102–108, 2018.

[18] B. Schulz, "802.11 ad–WLAN at 60 GHz–A Technology Introduction. White Paper," 2017.

[19] P. T. Dat, A. Kanno, N. Yamamoto, and T. Kawanishi, "Seamless convergence of fiber and wireless systems for 5G and beyond networks," *Journal of Lightwave Technology*, vol. 37, no. 2, pp. 592–605, 2018.

[20] S. M. Koepfli, M. Baumann, S. Giger, K. Keller, Y. Horst, Y. Salamin, Y. Fedoryshyn, and J. Leuthold, "High-Speed Graphene Photodetection: 300 GHz is not the Limit." in *European Quantum Electronics Conference*. Optica Publishing Group, 2021, p. ei_1_3.

[21] H. Hamada, T. Tsutsumi, H. Sugiyama, H. Matsuzaki, H.-J. Song, G. Itami, T. Fujimura, I. Abdo, K. Okada, and H. Nosaka, "Millimeter-wave InP device technologies for ultra-high speed wireless communications toward beyond 5G," in *2019 IEEE International Electron Devices Meeting (IEDM)*. IEEE, 2019, pp. 9–2.

Chapter 4

Advanced Converged Optical Transmission Systems

The incessant growth in required network capacity can only be catered for by the enhancement and convergence of fixed-line and wireless networks through the adoption of new communication techniques and flexible technologies. This chapter will explore advanced systems that leverage SiP technology to enhance reconfigurability within the overall network infrastructure. One key component utilized in these systems is the low noise characteristics exhibited by the DLM such as extremely low RIN (~ -165 dB/Hz) and linewidth ($\sim$ 10 kHz) which are discussed extensively in subsection 3.1.2. These features of the DLM are exploited for transmission of the multiple multiplexed waveforms that are compatible with cutting edge PON, Wi-Fi and beyond 5G technologies. The amalgamation of digital and analog signals has the potential to enable the transmission of vast bandwidths of information across the future converged optical access networks with high spectral efficiency. Previous work [1] and [2] have shown the coexistence of next-generation PON and 5G networks providing high throughput fixed-line and wireless fronthauls. The hybrid transmission of broadband signaling with mmWave OFDM over a HetNet downlink is demonstrated in [3]. In the first section of this chapter, the first demonstration of unamplified transmission using digitally multiplexed PAM-8, and 64-QAM OFDM signals resembling WiGig and 5G NR standards over a 10 km fronthaul RoF link in a C-RAN scenario using DLM is presented.

SiP PIC designs have proven to show a high degree of flexibility in the past and present

research works [4, 5, 6, 7, 8, 9] and this is also demonstrated through experimental results presented in the previous chapter 3. The concluding section of this chapter illustrates the improved network reconfigurability achieved by incorporating SiP PIC elements into the system. An experimental demonstration showcases a highly flexible wavelength and space-switched ARoF fronthaul transmission, specifically designed for a mmWave emerging 6G waveform over a C-RAN. A spread spectrum multiplexing technique – OCDM – which is highly resilient to inter-channel interference and enables enhanced channel estimation is utilized in the fronthaul transmission demonstration.

4.1 Hybrid DRoF and ARoF mmWave systems

4.1.1 Multiwave Signal Generation

The experimental work presented in this section focuses on the convergence of fixed-line and wireless networks by consolidating various services. In a practical networking scenario, these services can be electrically multiplexed at the CO. However, due to the limited availability of electrical components at the time of the experiment, a digital multiplexing approach is employed utilizing software tools. By digitally multiplexing the different services, the experiment demonstrates the feasibility of combining multiple services over a single transmission medium. The waveform multiplexing technique, either digital or electrical, allows for the efficient utilization of available resources and enables seamless integration of diverse services, such as data transmission, voice communication, video streaming, and more. In this work, the selected services are expected to be provided by PON, Wi-Fi and 5G technologies. However, the services are not limited to these technologies and there is ample scope to integrate visible light communication (VLC) and free space optical (FSO) communication into the transmission system presented in this section. The three types of waveforms that are generated independently are:

1. **OFDM**, compatible with **5G NR** standards (see subsections 1.2.1 and 2.1.2)

2. **OFDM**, compatible with **Wi-Fi** standards (see subsections 1.2.2 and 2.1.2)

3. **PAM**, suitable for broadband access over **PON** (see subsections 1.2.3 and 2.1.2)

Recently the researchers have extensively employed PAM in VLC and FSO links in order to spectrally enhance the bandwidth utilization in these technologies [10, 11, 12]. The software tools utilized in this experimental work play a critical role in enabling digital multiplexing, providing necessary algorithms and processing capabilities to combine and manage different services. To generate a digitally multiplexed signal that combines the aforementioned waveforms, all waveforms have a common sampling rate. This ensures effective multiplexing and allows the generated digital samples to be converted into the electrical signal by the AWG used for the experimental work presented later in this chapter. To facilitate this process, the following equations are presented, representing the relationship between different types of waveforms. These equations serve as guidelines to (re)sample the waveforms and ensure that they align properly during the multiplexing process. The equations are given as follows:

$$DP^{OFDM} = N_{Sym}^{OFDM}(W_{FFT} + W_{CP})R_{US}^{OFDM} \tag{4.1}$$

$$DP^{PAM} = N_{sym}^{PAM}R_{US}^{PAM} \tag{4.2}$$

where DP is number of datapoints/samples, N_{Sym} is the number of symbols and R_{US} is the upsampling rate. These are common properties of PAM and OFDM waveforms. In equation 4.1, W_{FFT} and W_{CP} are the size of the FFT block and CP respectively and these properties are specific to OFDM waveform generation only. The R_{US} is described in terms of the ratio of the desired sampling rate of the system, F_{system}, and the base sampling rate, Fs, of a waveform (without resampling), see 4.3. The equation presenting the upsampling ratio R_{US} is given below, followed by the upsampling rate equations of OFDM and PAM waveforms, i.e. R_{US}^{OFDM} and R_{US}^{PAM} respectively. The R_{US}^{PAM} can also be represented in terms of the ratio between the system's sampling rate and the PAM's symbol rate ($SymR^{PAM}$).

$$R_{US} = \frac{F_{system}}{F_s} \tag{4.3}$$

$$R_{US}^{OFDM} = \frac{F_{system}}{F_s^{OFDM}} \tag{4.4}$$

$$R_{US}^{PAM} = \frac{F_{system}}{F_s^{PAM}} = \frac{F_{system}}{SymR^{PAM}} \tag{4.5}$$

The selection of the parameter R_{US} determines the scaling of the sampling rate for each waveform and can be used to ensure a common sample rate for the system. To facilitate ease in DSP, R_{US} is typically chosen as an integer value. This simplifies the mathematical operations involved in processing the waveforms. Another important factor in the process is ensuring that the same number of samples is generated for each type of waveform. This requires calculating the number of symbols for each waveform. A symbol refers to a distinct entity (single carrier) or unit (multi-carrier) within a waveform that carries specific information. By determining the number of symbols for each waveform and generating an equal number of samples, it ensures proper alignment of the waveforms which is vital for effective multiplexing and subsequent signal processing. The following equations represent the procedure of calculating the number of symbols for each waveform and also show their interdependence for multiplexing. In order to multiplex the three waveforms, each of the waveforms should have the same amount of datapoints/samples, hence forming waveforms vectors of equal dimensions. Hence Eqns. 4.1 and 4.2 can be re-written as follows:

$$N_{sym}^{OFDM1} = \frac{N_{sym}^{PAM} R_{US}^{PAM}}{(W_{FFT}^{OFDM1} + W_{CP}^{OFDM1}) R_{US}^{OFDM1}} \tag{4.6}$$

$$N_{sym}^{PAM} = \frac{N_{bits}^{PAM}}{log_2(M)} \tag{4.7}$$

where N_{bits}^{PAM} is the number of bits in the PAM signal and M is the order of PAM signal and represents the number of discrete levels in PAM. The two types of OFDM signals, say OFDM1 and OFDM2, employed in the digital multiplexing procedure represent 5G NR and Wi-Fi applications respectively and using Eqn. 4.1 can be represented as follows:

$$DP^{OFDM1} = N_{Sym}^{OFDM1}(W_{FFT} + W_{CP}) R_{US}^{OFDM1} \tag{4.8}$$

$$DP^{OFDM2} = N_{Sym}^{OFDM2}(W_{FFT} + W_{CP}) R_{US}^{OFDM2} \tag{4.9}$$

In order to multiplex these two waveforms, Eqns.4.8 and 4.9 can be re-written as follows:

$$N_{Sym}^{OFDM2} = \frac{N_{Sym}^{OFDM1}(W_{FFT} + W_{CP}) R_{US}^{OFDM1}}{(W_{FFT} + W_{CP}) R_{US}^{OFDM2}} \tag{4.10}$$

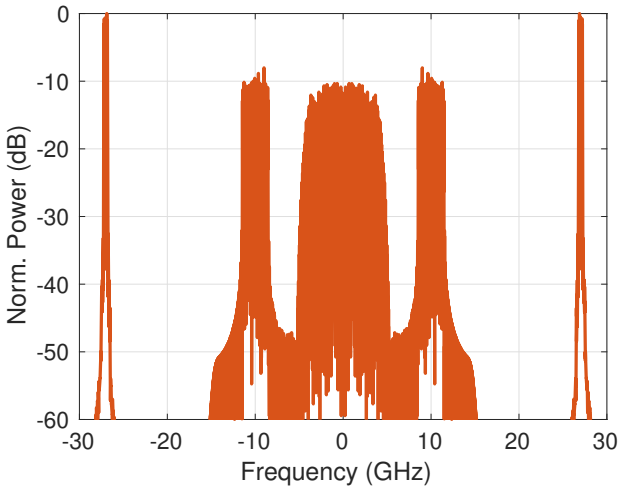

(a) MW-1

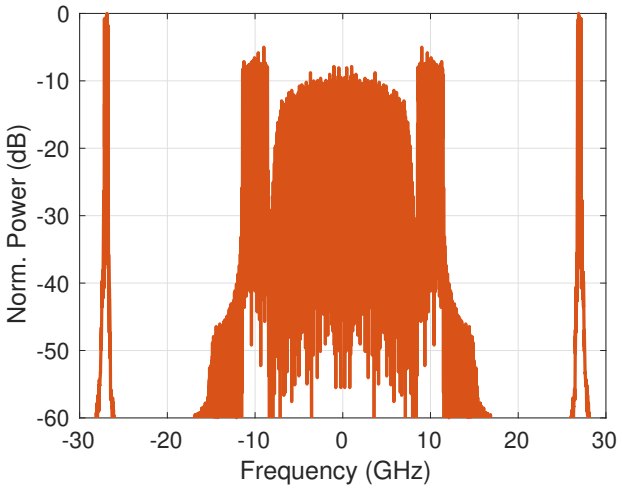

(b) MW-2

Fig. 4.1: The two types of transmitted MW signals.

For example, if N_{sym}^{OFDM1} is set to 4, $W_{FFT}+W_{CP}$ to 1040 (i.e. 1024+16), and the R_{US}^{OFDM1} and R_{US}^{PAM} to 90 and 6 respectively, then using the above equations the number of PAM symbols will be 62400. And by substituting the value of $W_{FFT}^{OFDM2}+W_{CP}^{OFDM2}$ to 1040 (i.e. 1024+16) and R_{US}^{OFDM2} to 9, the N_{Sym}^{OFDM2} obtained from the above equations is 40. This example is processed using the software tools and the multiplexed waveform signal is generated. The two types of digitally multiplexed signals are shown in Fig. 4.1. The first multiple waveform signal (MW-1), shown in Fig. 4.1 (a), constitutes a 7.5 GBd PAM-8, a wideband OFDM and narrowband OFDM waveforms which are centered at 0 GHz, 10 GHz and 27 GHz respectively. To enhance the information rate, another MW

signal, named MW-2, is generated (see Fig. 4.1 (b) that incorporates a higher baudrate PAM-8 signal of a 15 GBd PAM-8 the same two OFDM signals as in MW-1. These two types of multiplexed signals will be used in the experimental setup described later in subsection 4.1.3.

4.1.2 Network Scenario

Section 1.4 provided an overview of different network scenarios that enable the convergence of fixed-line and wireless networks. This subsection focuses on demonstrating the implementation of multiplexed services on a single transmission link within a network scenario. Fig. 4.2 represents one such network scenario. In this configuration, PON technology is utilized to transmit the multiple waveform (MW) signal that combines multiple waveforms, including a potential waveform for PON such as higher-order PAM (see subsection 2.1.2), along with 5G and Wi-Fi-compatible OFDM waveforms. The network scenario involves the consolidation of CU and DU with the OLT at the CO, and the RU and ONU at the antenna site, which can be either FTTB or Fiber-to-the-Room (FTTR). The MW signal can be sent over 10-20 km optical fiber and the power splitter (PS) splits the signal into 1:n ratio. In Fig. 4.2, the two outputs of PS are fed to two floors of a building. The received signals can be first processed by the combination ONU and PS which further divides the signal into different paths. Now each of the service types, such as 5G, Wi-Fi or Ethernet can be optically filtered from the composite MW signal (see the example shown in Fig. 4.1) and processed at the appropriate receiver. In the example scenario in Fig. 4.2, the 5G receiver is represented by 'RU + PS' which can further (electrically) split into data and voice services for wireless (including mmWave) antennae transmission. An ethernet block shows the connection with a Wi-Fi router, a desktop, a printer and smart TV, showcasing the access to the internet to these devices. A Wi-Fi router can be directly connected to the fiber out of the ONU for broadband access to mobile stations (MS) like laptops, and tablets in the premises [13, 14, 15]. A VLC block is also shown to process a higher order PAM as intended in its recent research work [12].

This FTTB/FTTR scenario showcases a fusion of various services that were introduced at the beginning of this section. These services encompass high-capacity PON, Wi-Fi, 5G, and VLC. The amalgamation of these services on a single transmission link

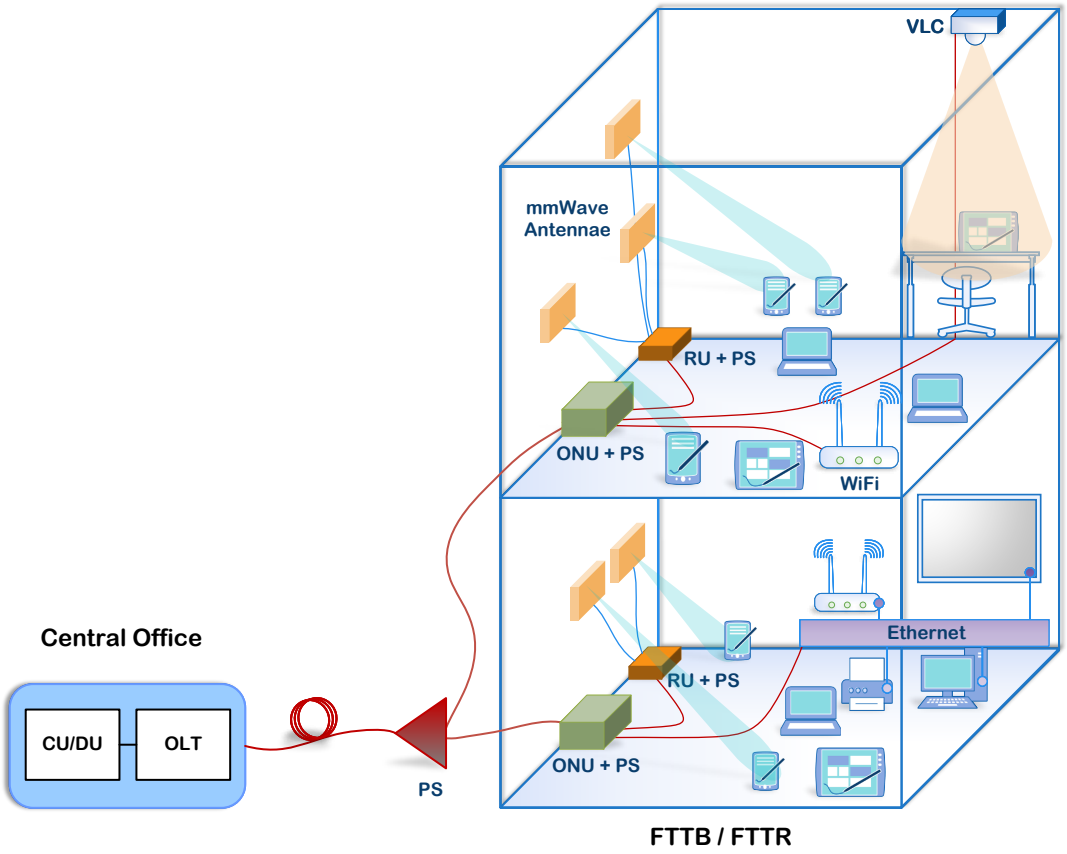

Fig. 4.2: A network scenario for MW Hybrid DRoF and ARoF mmWave system.

enables the efficient utilization of network resources and facilitates seamless communication across different platforms.

4.1.3 Multiwave Transmission System

In this subsection, hybrid optical access by the transmission of a signal constituting baseband PAM-8, 10 GHz WiGig and 27 GHz 5GNR waveforms over a 10 km RoF link. A schematic of the experimental setup demonstrating converged DRoF and ARoF optical access in C-RAN architecture is shown in Fig. 4.3. A SiP based DLM, described in detail in [8], generates an extremely low RIN (~ -169 dB/Hz) optical carrier with $\sim$10 dBm power at 1551.72 nm. The DLM fiber output was connected to an optical isolator to avoid back scattering related losses. As described previously, the digital multiplexing of three independent waveforms — 7.5/15 GBd PAM-8 (with quadratic pre-distortion) at baseband (DRoF), and WiGig and 5G NR standard compatible QAM-64 OFDM (ARoF)

at 10 GHz and 27 GHz, respectively — is performed to produce a unique MW signal. In cases where 7.5/15 GBd PAM-8 are digitally stitched with WiGig and 5G NR, these signals are named MW-1/MW-2, respectively. The generated digital samples are converted to an electrical signal using an AWG, operating at 90 GSa/s with 33 GHz electrical bandwidth. The amplified electrical signal drives the quadrature-biased 40 Gbps single ended $LiNbO_3$ MZM to modulate the optical carrier generated by the DLM. The optical spectrum of the two MW signals with 7.5 GBd and 15 GBd PAM-8 are shown in Fig. 4.3 (b). The modulated signal is transmitted over 10 km standard SSMF and received by a 70 GHz PIN PD. The generated photocurrent is amplified and captured using a 100 GSa/s RTO band-limited to 33 GHz. The properties of the modulation schemes employed in this work are shown in Table. 4.1.

4.1.4 Result & Discussion

The unamplified RoF transmission of MW signals is evaluated in terms of BER and EVM with respect to the ROP for 7.5/15 GBd PAM-8, 2.9 GHz bandwidth WiGig and 488 MHz bandwidth 5G NR. The optical transmission power was 0.5 dBm. The optical transmission without fiber reel and with 10 km fiber reel were observed to be the same. The results after 10 km SMF, presented in Fig. 4.4 (a), show that the lowest BER obtained is 1.1×10^{-3} for 7.5 GBd PAM-8 in MW-1, which is below the 7% hard-decision (HD) FEC limit (3.8×10^{-3}). The system's limit is tested by MW-2 transmission with 15 GBd PAM-8 and the deployed transmitter-receiver matched RRC (see subsection 2.1.2) filtering at $\sim$ 9 GHz is used to avoid interference with WiGig centered at 10 GHz.

A higher relative power is allocated to PAM-8 in MW-2 (compared to MW-1) to improve its performance. However, this value is lower than the power of 15 GBd PAM-8 in the case where it is transmitted alone (i.e. without the adjoining ARoF signals) and

Table 4.1: Properties of MW signal

Property	Digital	WiGig	5G NR
Modulation	PAM-8	QAM-64 OFDM	QAM-64 OFDM
Datarate (Gbps)	22.5(MW-1) / 45(MW-2)	17.5	2.9
Bandwidth (GHz)	7.5(MW-1) / 9(MW-2)	2.9	0.488
RF Carrier (GHz)	0	10	27

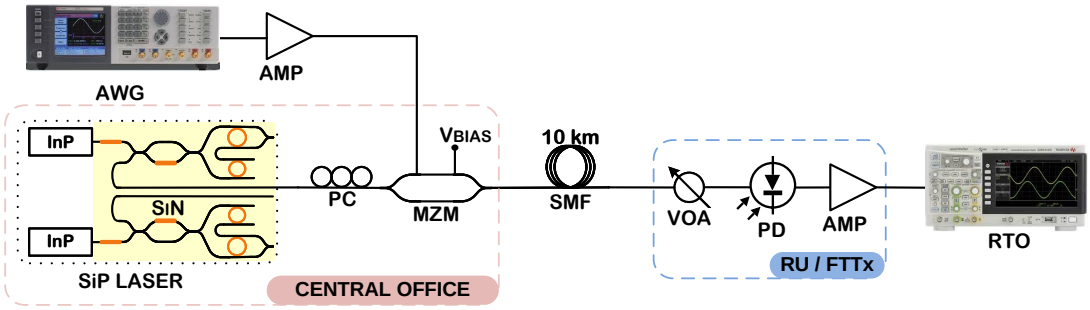

(a) Schematic of experimental setup

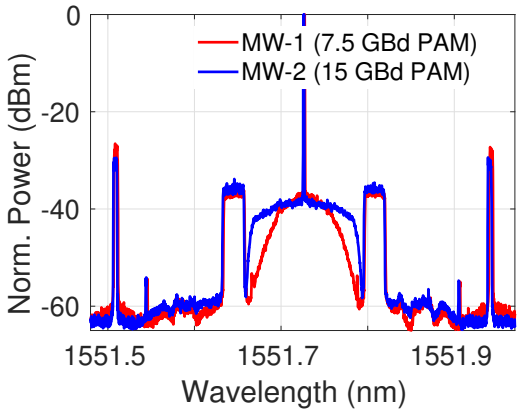

(b) Optical spectra of MW-1 & MW-2

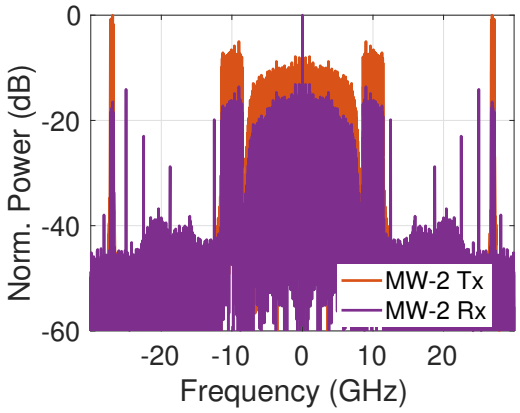

(c) Electrical spectra of transmitted and received MW-2

Fig. 4.3: Experimental setup of MW RoF transmission over 10 km SMF, with inset (a) showing details of each waveform and (b) and (c) showing MW optical and electrical spectra respectively.

hence, degradation of $\sim$ 4 dB in receiver sensitivity at the FEC limit is observed. The EVM performance of WiGig and 5G NR, presented in Fig. 4.4 (b), shows EVMs as low as 6.5% and 5.1%, respectively (well below the 8% QAM-64 EVM limit). There is a negligible performance difference between WiGig in MW-1 and MW-2 compared to 5G

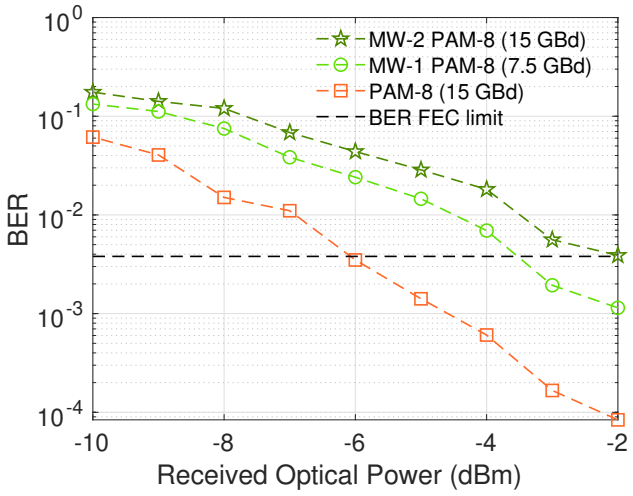

(a)

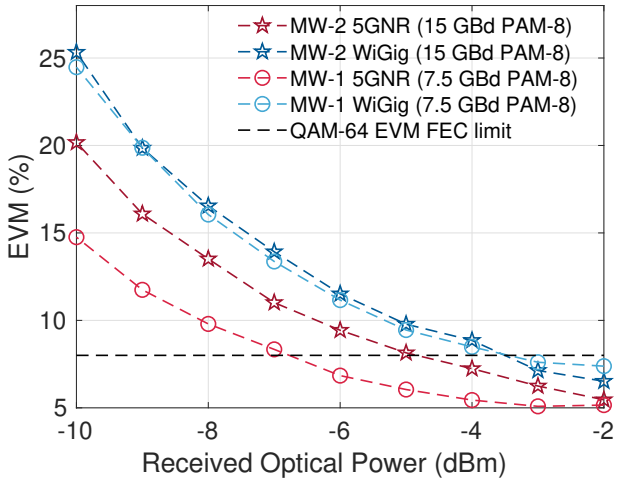

(b)

Fig. 4.4: For RoF transmission over 10 km SMF (a) shows BER performance over ROP for 7.5 GBd and 15 GBd PAM-8 extracted from MW-1 and MW-2 respectively as well as for single 15 GBd PAM-8 signal and (b) shows EVM performance at different ROPs for 5GNR and WiGig extracted from MW-1 and MW-2.

NR for the same conditions. Due to the reallocation of signal power in MW-2, it is noted in Fig. 4.1.3 (b) that a lower relative power is allocated to 5G NR in MW-2 (compared to MW-1), thus impacting its signal to noise ratio adversely, as seen in Fig. 4.1.3 (c). Hence, a degradation in receiver sensitivity by $\sim$ 2 dB for 5G NR in MW-2 is observed at the EVM limit. Nonetheless, the EVM performance for 5G NR in MW-2 is recorded within the standard 3GPP limits for ROPs of more than -5 dBm.

From these results, it is concluded that optimization of power distribution among three

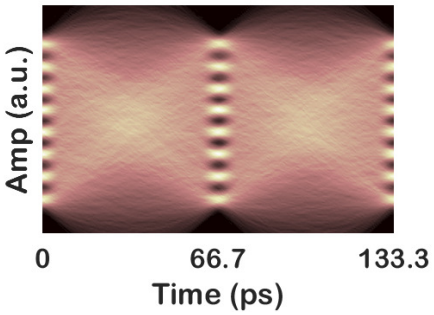

(a) Eye diagram of PAM-8

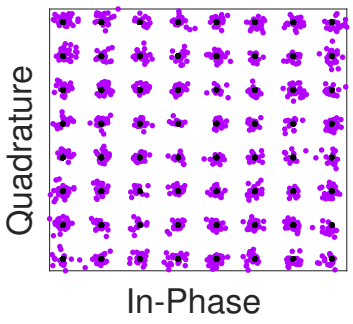

(b) Constellation diagram of 5G NR

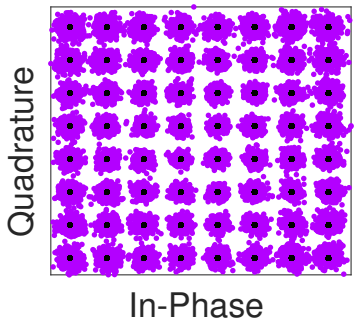

(c) Constellation diagram of WiGig

Fig. 4.5: (a) Shows the eye diagram 15 GBd PAM-8 extracted from MW-2 at the ROP of -2 dBm at the PD. (b) and (c) show the overlapped transmitted and received constellations of 5G NR and WiGig signals respectively that are extracted from MW-2 signal for ROP of -2 dBm.

types of waveforms in the MW signals is vital as the error performance is highly dependent on the power allocated to each waveform. The successful hybrid multi-level DRoF and ARoF transmission demonstrated in this work is ultimately enabled by the low noise and high output power features exhibited by the SiP based DLM.

4.2 Low Noise Ultra-Flexible SiP Switching Platform for mmWave Systems

4.2.1 Optical Switching & Routing

An optical switch is a device used to route an optical signal from one channel to another within a specific range. It offers tunable transmission windows and serves as a crucial component for optical cross-connections, optical add/drop multiplexing, network mon-

itoring, and automatic system protection. Optical switches utilize various implementation technologies, including mechanical, thermo-optical, acousto-optic, electro-optical, magneto-optical, liquid crystal, and MEMS-based switches. With the increasing demand for high-speed and large-capacity optical communication, traditional electronic switches are gradually being replaced by all-optical switches available in the market. Some optical waveguide couplers that are used for manufacturing the SiP optical switches [16, 17, 18, 19, 20, 21, 22] are:

1. **Mach-Zenhder Interferometer (MZI)**: MZI switches are versatile interferometric switch elements that are ideal for space switching in WDM systems. A typical 2×2 MZI switch cell consists of two 3 dB couplers and a dual-waveguide arm with a phase shifter. The phase shifter can be adjusted by changing the refractive index using a heater due to the thermo-optic (TO) effect or a p-i-n junction diode due to the electro-optic (EO) effect. By varying the phase difference between the arms, the output signal can be switched between one of the two ports.

2. **Microring Resonator (MRR)**: MRR switches are resonant switch elements used for wavelength selective filtering in WDM systems. Compared to MZI switches, MRR switches have a smaller footprint and lower power consumption, making them suitable for high-density switches. A typical 2×2 add-drop switch cell consists of an MRR, two bus waveguides, and an optical phase shifter (either EO or TO). The input signal can be switched to the drop port or the through port depending on its alignment with the resonance of the MRR. If the input optical signal, say λ_1, matches the MRR resonance, it is directed to the drop port. The optical signal which is not in resonance with MRR, say λ_2, is sent to the through port.

3. **Micro-Electro-Mechanical Systems (MEMS)**: MEMS optical switches are miniature mechanical devices used to control the routing of optical signals. These switches consist of a movable mirror or prism that can be controlled by electrostatic or electromagnetic forces. The movable element is suspended on a flexible substrate and can be actuated to change the optical path. The principle behind MEMS optical switches is the movement of the mechanical element. When the mirror or prism is at rest, the optical signal follows a specific path. By applying voltage or current to

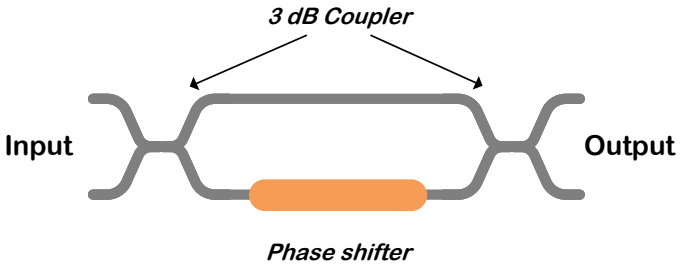

(a) MZI

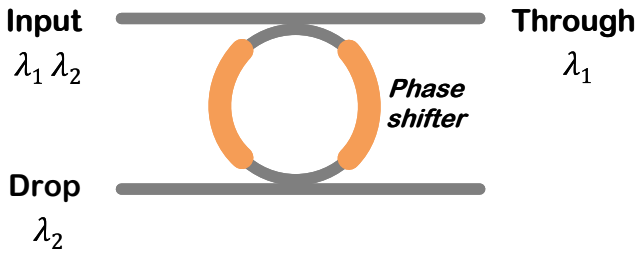

(b) MRR

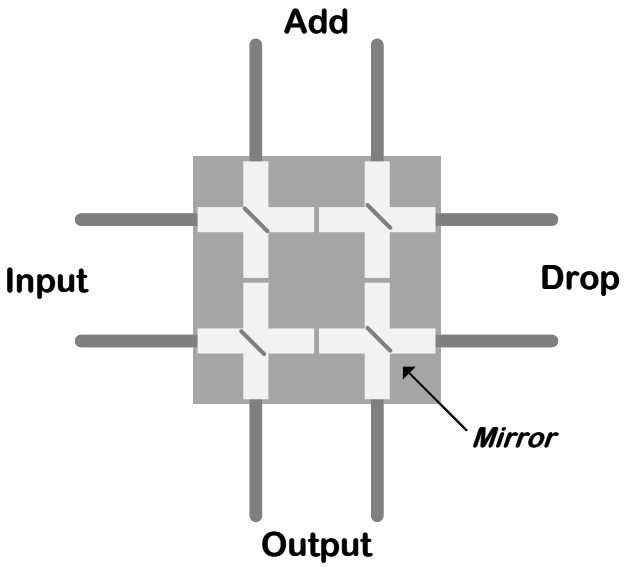

(c) MEMS

Fig. 4.6: Layout of waveguide couplers for optical switches.

the actuation mechanism, the movable element can be deflected, altering the optical path and directing the signal to a different output port.

The key network elements employed for optical switching and routing are as follows:

1. **Arrayed Waveguide Grating (AWG)**: It is a passive component specifically utilized in WDM optical networks and illustrated in Fig. 4.7 (a). It serves the crucial function of both wavelength multiplexing and demultiplexing. The AWG consists of arrays of optical waveguides that spatially separate or demultiplex the wavelengths of an input WDM signal, or combine and multiplex multiple input wavelengths into a single output WDM signal. This separation or combination is achieved by carefully designing the path differences in the waveguides, resulting in wavelength dispersion and the spatial separation of each wavelength. As the dispersed wavelengths propagate through the AWG, they undergo interference, leading to wavelength-selective constructive and destructive interference patterns. The output waveguides then deliver the separated or combined wavelengths of light accordingly.

2. **Wavelength Selective Switch (WSS)**: It is an active optical routing and switching element that is specifically used in WDM optical networks. As shown in Fig. 4.7 (b), it selectively adds, drops or routes a wavelength, that is based on the principle of wavelength filtering and redirection. It can be constructed using MZIs, MRRs, MEMS or liquid crystal on silicon (LCoS) etc. The LCoS based WSS incorporates a switch engine that utilizes an array of phase-controlled pixels to steer beams by creating a linear optical phase retardation in the desired direction. This type of WSS offers high channel isolation, low insertion loss and high speed switching.

3. **Reconfigurable Optical Add Drop Multiplexer (ROADM)**: It is an active component utilized in WDM systems to facilitate the dynamic routing of optical signals and is depicted in Fig. 4.7 (c). It empowers network operators to selectively add or drop specific wavelengths at different nodes within the network. ROADM devices offer remarkable flexibility in wavelength channel management, enabling the reconfiguration of optical paths without the requirement for physical adjustments.

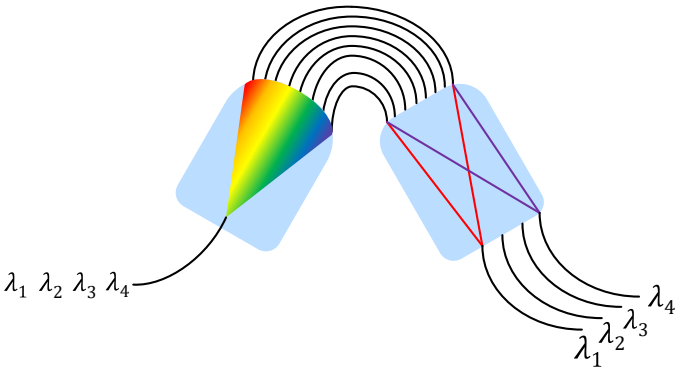

(a) AWG

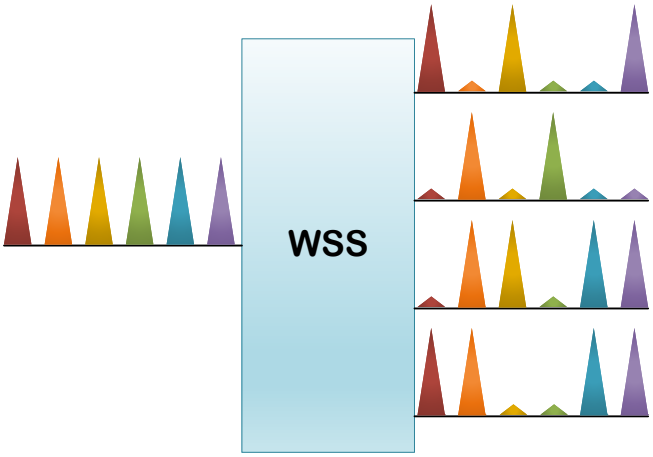

(b) WSS

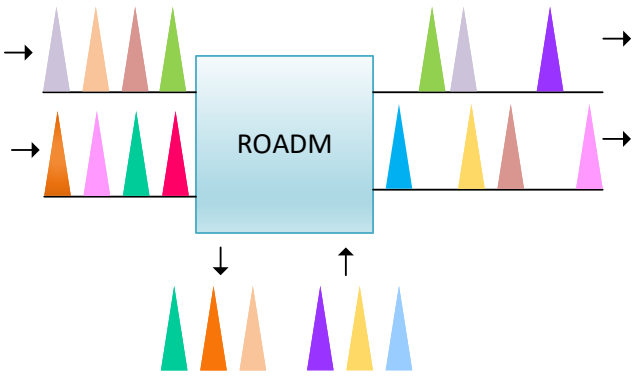

(c) ROADM

Fig. 4.7: Optical switching and routing elements.

They typically incorporate a WSS along with optical amplifiers to enhance signal quality and integrity.

4.2.2 SiP Optical Switch: Functionality and Network Topologies

The SiP MRR based optical wavelength/space switch, used for te experimental work described below, is a chip that incorporates a switch-and-select architecture, consisting of two add/drop linear switching arrays connected via a passive shuffle network. Each array consists of N 1×N/N×1 switching units with MRR add-drop filters serving as demultiplexers. By thermally tuning the MRR resonances using drive voltages, specific add/drop wavelengths can be selected. This configuration ensures non-blocking connectivity and enables the formation of customized input/output paths. The 4×4 SiP MRR-based switch-and-select layout is shown in Fig 4.8. Optical terminations are implemented at through ports to eliminate reflections, while multimode waveguide crossings are utilized in the shuffle network for low-loss and low-crosstalk performance. The placement of thermo-optic MRRs at a 100 μm pitch minimizes thermal crosstalk, and the measured resonance shift exhibits a thermal efficiency of 1 nm/mW. Additionally, a 3 dB passband with ap-

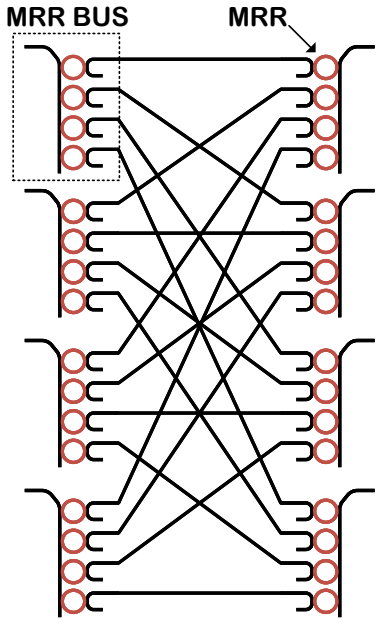

Fig. 4.8: Schematic of 4x4 SiP switch.

proximately 24 GHz bandwidth has been observed [23, 24, 25].

4.2.2.1 Switch Network Topologies

To fully understand the operation and capabilities of the integrated MRR-based device is to consider the various switch network topologies that it enables:

1. **Broadcasting**: The point-to-multipoint transmission of information signals is accomplished through a 1×4 MRR configuration. In this setup, the input signal at a specific wavelength (λ_1) is divided into four switch outputs. To configure the SiP switch, all the MRRs in one bus at the input and the associated MRRs in different buses at the output (see Fig. 4.9 (a)) are thermally tuned to be close to the same resonance. This tuning process involves adjusting the center frequency of the MRRs based on Vernier filtering, allowing a specific wavelength to pass through. At the input bus, the first MRR directs a portion of the signal to the drop port, while the remaining portion is forwarded to the through port. This process continues until the last MRR in the MRR bus [23]. This functionality resembles that of a power splitter in PON networks. Such a topology finds applications in video streaming, real-time data distribution, and network synchronization.

2. **Multicasting**: It is also a point-to-multipoint information transmission topology, similar to broadcasting. However, it differs from broadcasting in that the SiP switch is configured to route the input wavelength of the switch to selected output ports. For instance, the MRRs are thermally tuned to a 1×2 configuration by aligning two MRRs from a bus at the input and the associated MRRs in different buses at the output of the switch to the same resonance. This topology is illustrated in Fig. 4.9 (b). With this type of topology, different services on dedicated wavelengths can be split and broadcast.

3. **Wavelength Switching**: It is also a point-to-multipoint information transmission topology, however, the switch is fed with a WDM signal as shown in Fig. 4.9 (c). In this example, the MRR input-output pairs are configured such that the first MRR in a bus drops one wavelength from the WDM signal, sending the rest along the MRR bus and the through port. The next MRR in the same bus is configured to drop

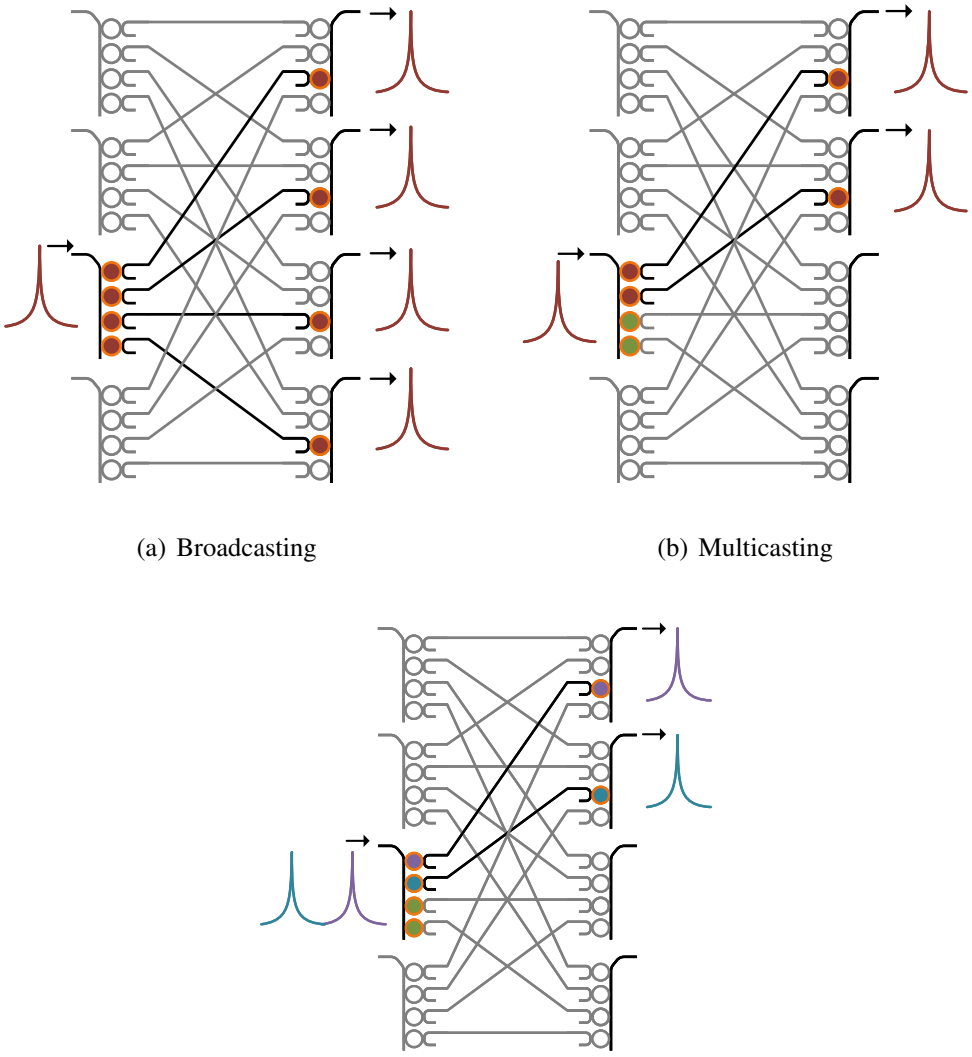

(a) Broadcasting

(b) Multicasting

(c) Wavelength switching

Fig. 4.9: Depiction of various network topologies in which the optical switch can be implemented.

another wavelength. The associated output MRRs are tuned to corresponding input MRRs routing signals at specific wavelengths (colored signals in Fig. 4.9 (c)) out of the switch. This topology can be used in a multi-service environment as discussed in the previous section 4.1 for a case where DRoF and ARoF services share the same network transmission link but are multiplexed over different wavelengths.

4. **Space Switching**: It is a multipoint-to-multipoint topology where the SiP switch is configured to enable the space switching functionality as a "bar" or "cross" state as shown in Fig. 4.10. This topology supports the centralization of resources in the

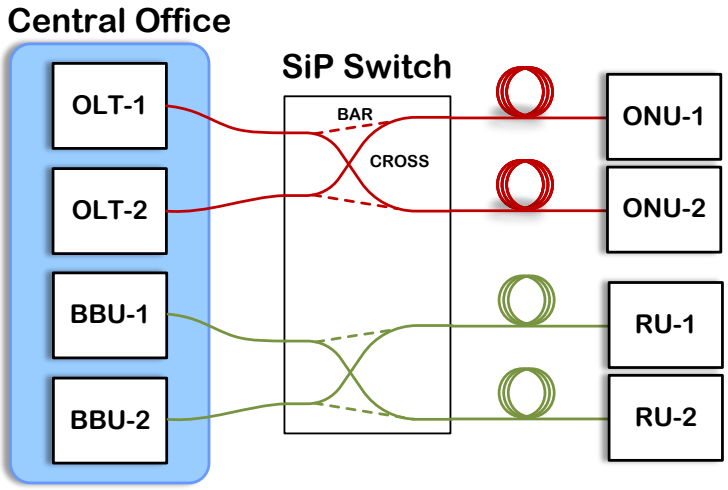

Fig. 4.10: Illustration of physical placement of the switch deployed for space switching in the network.

access network and can be implemented in scenarios where a CO contains multiple CUs and DUs, which are collectively called BBUs (refer to subsection 1.2.1), and OLT pools. An information carrying optical carrier from one pool can be switched to the desired RU or ONU.

4.2.2.2 SiP Switching Technologies for RoF

Highly wavelength flexible SiP integrated circuits can provide low noise, low crosstalk, high yield and small footprint when compared to discrete semiconductor components [26], and these advantages have been exploited by recent works focusing on RoF for C-RAN and converged service applications [27]. In [28], the transmission of multi-band IF ARoF signals through a low cross-talk wavelength and space flexible SiP MRR based optical switch is demonstrated. Xia et al. successfully deployed a similar SiP switch technology in support of a reconfigurable converged fixed-line and wireless network with DRoF technology [23]. A Si_3N_4 MRR based ROADM has been used in [29] to show the coexistence of multi-service mmWave ARoF and DRoF transmission in C-RAN, while a SiP MRR based smart edge in [30] enables the transmission of ARoF with WDM in a converged optical access network scenario. This smart edge, located within the PON remote node, intercepts PON traffic and adds 5G signals to transmissions that are being sent to and from ONUs. The examples of recent research activities above demonstrate

how innovations in integrated photonics technology can be leveraged for advanced networking. In future converged networks, advances in WAN and WLAN technologies must also be supported through these emerging optical systems. In the context of ARoF in particular, new modulation formats and waveform designs must be accommodated through the optical channel.

4.2.3 OCDM waveform

In the wireless domain, much research effort is focussed on the development of new waveform designs that are resilient to harsh channel environments typically encountered at higher radio frequencies [31]. One such multi-carrier waveform is OCDM [32]. Through its use of a Fresnel transform (FnT), OCDM differs from the 5G waveform of choice – OFDM – such that information is encoded on a set of orthogonal chirps rather than frequency subcarriers. The signal's inherent spread-spectrum-like nature offers robustness to channel fading effects and Doppler shifts and it is seen as a promising candidate for next-generation mmWave mobile communications. OCDM also facilitates the use of chirp-based CE and it is shown previously how this feature enables enhanced performance (compared to frequency domain CE) in an optical heterodyne/mmWave ARoF system [33].

4.2.4 OCDM/OFDM transmission over ultra-flexible SiP laser & switch fabric

This experimental work described in this section demonstrates an ultra-flexible fronthaul system underpinned by the unique combination of a low noise SiN-InP MRR-based tunable laser source and a low crosstalk 4×4 SiP MRR-based optical wavelength/space switch for mmWave ARoF fronthaul provisioning with the emerging OCDM waveform. Also, the successful transmission of a multi-band OFDM signal constituting a narrowband signal resembling the 5G NR standard for mobile traffic and a wideband signal for broadband Wi-Fi service in the ultra-flexible ARoF fronthaul system is demonstrated, thus showing the system's viability in a multi-service environment.

In the C-RAN architecture-based experimental setup, shown in Fig. 4.11 (a), the CO

includes a widely tunable and low-noise TriPleX technology-based laser (a full description of the device is given in [6]). This laser is similar to the DLM described in chapter 3. The laser consists of a gain section made of an SOA and a cavity including a phase section and two Si_3N_4 MRRs (as highlighted in orange in Fig. 4.11 (a) which are thermally controlled via microheaters. Control voltages to the microheaters associated with the two MRRs are used to tune the laser across the C-band. This widely tunable laser has a low RIN (~ -140 dB/Hz) and a narrow linewidth ($\sim$ 40 kHz) at a gain current of 70 mA as reported in [6].

In this experiment, four separate wavelengths having $\sim$7 dBm optical power were used (spectra shown in Fig. 4.11 (b)) with the laser's gain current set to 150 mA. An optical isolator is connected to the output of the laser. The laser's output is modulated by two types of RF signals via an MZM (bandwidth $\sim$35 GHz) biased at quadrature. Utilizing the ARoF technique to modulate RF signals directly onto the optical carrier avoids digital/analog conversions while preserving the bandwidth efficiency and fidelity of the original RF data signal. The two types of software-generated signals are – (i) a single-band (SB) 64-QAM OCDM/OFDM signal centered at 24 GHz (see Fig. 4.11 (a)) and (ii) a multi-band (MB) 64-QAM OFDM signal consisting of a 5G NR compatible signal at 24 GHz combined with a Wi-Fi compatible signal at 10 GHz (see Fig. 4.11 (b)), whose detailed features are given in Table. 4.2.

A 60 GSa/s AWG is used to produce an RF signal for laser modulation via the MZM, thus generating a DSB optical signal, which is then transmitted to a single port of the SiP MRR based 4$\times$4 optical switch. The low crosstalk switch with maximum crosstalk avoidance of up to 50 dB and whose design is depicted in the setup in Fig. 4.11 (a) (see further details in [34, 23]) allows all-optical transmission from a single input port to every output port through a designated MRR pair. Each port of the switch consist of four MRRs that are designed to be in different resonant frequency. The switch's operation is wavelength selective by appropriate thermal tuning of the resonances of each of the four MRR filters associated with each port. In the context of this C-RAN type demonstration, this functionally offers switch-and-select functionality for fronthaul transmission links to/from the CO. Combining this with the tuning capability of the laser provides a high degree of high bandwidth all-optical reconfigurability in the network.

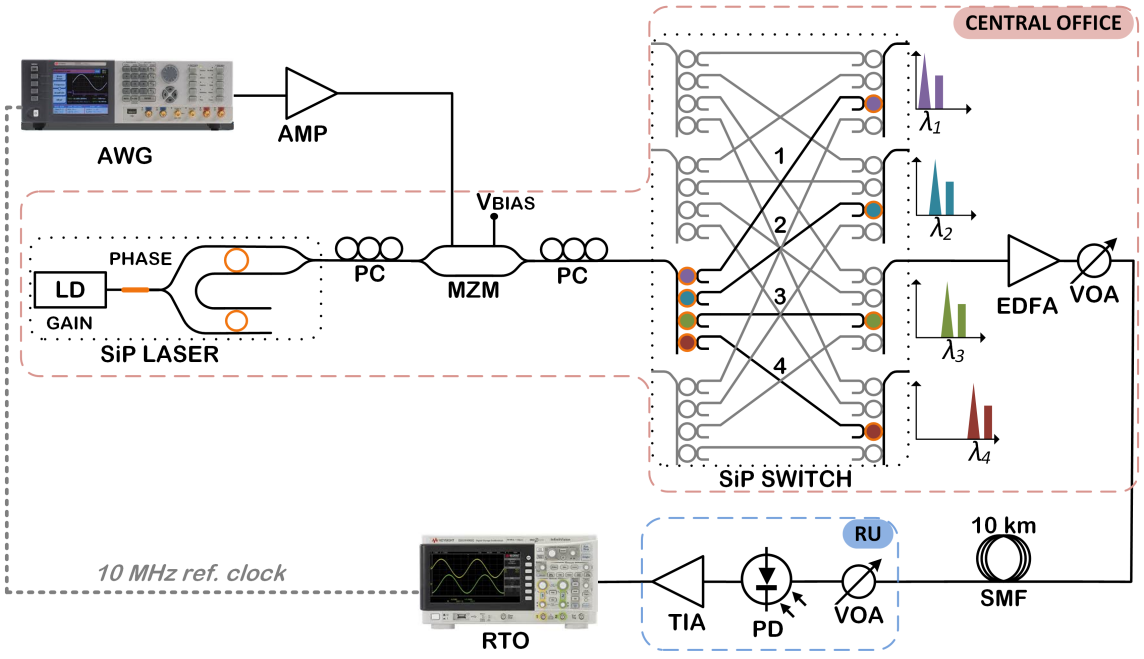

(a)

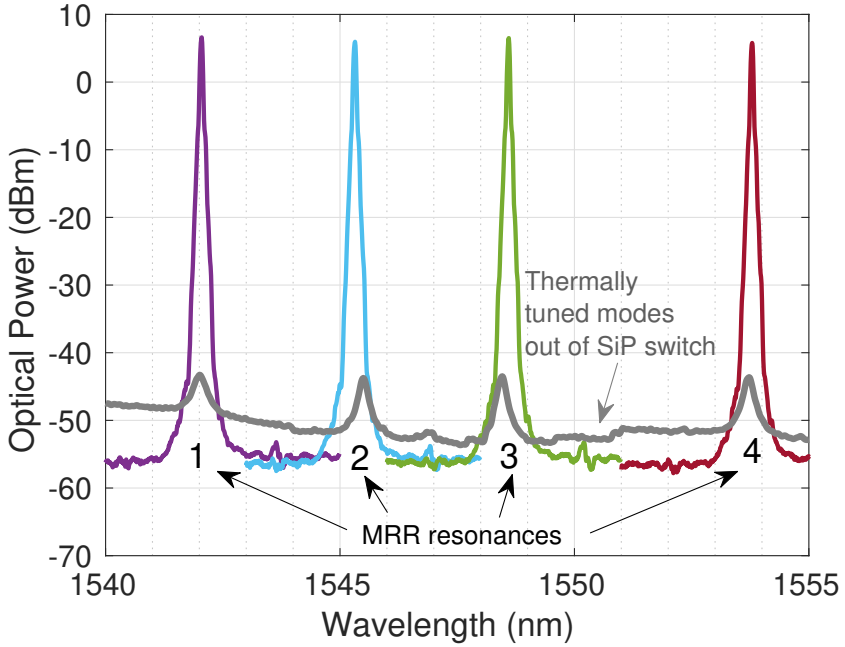

(b)

Fig. 4.11: (a) Experimental setup with tunable SiP based MRRs at the laser and switch (microheaters highlighted in orange), (b) shows the output of the laser tuned in turn to generate four wavelengths and the corresponding measured resonances of the four MRRs of SiP switch in this experiment (shown in grey).

In the example networking scenario implemented in this work, the resonant wavelength of the input and output MRR pairs associated with switch paths 1, 2, 3 and 4 (see

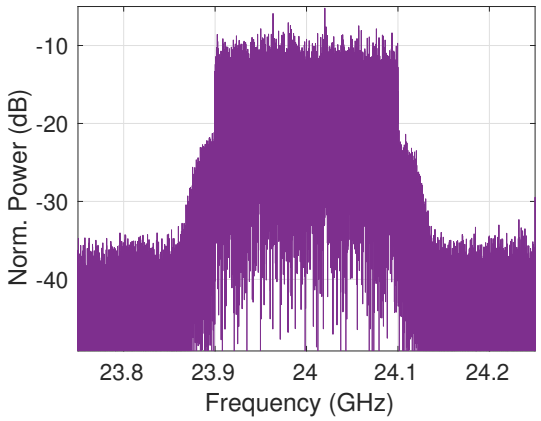

(a)

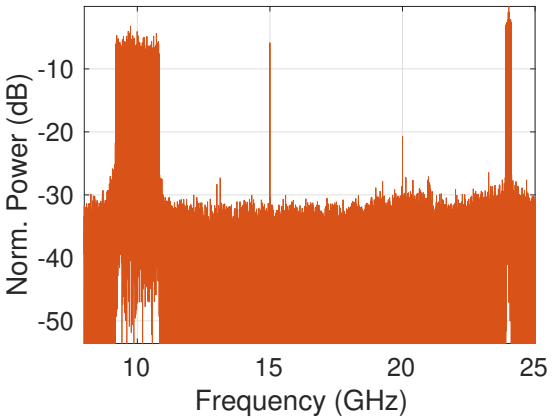

(b)

Fig. 4.12: Received electrical spectra of (a) 64-QAM OCDM at 24 GHz and (b) multi-band OFDM signal constituting Wi-Fi and 5G NR compatible signals at 10 GHz and 24 GHz respectively.

Table 4.2: SB OCDM/OFDM and MB OFDM signal properties

Properties	OCDM/OFDM	MB-OFDM 5G NR	MB-OFDM Wi-Fi
(I)DFnT/(I)DFT*	1024	2048	2048
Symbol Rate	244.14 kHz	244.14 kHz	4.88 Mhz
Chirps/Subcarrier	820	800	336
QAM-Level	64	64	64
Bandwidth	200.2 MHz	195.3 MHz	1.64 GHz
Data rate	1.2 Gbps	1.17 Gbps	9.84 Gbps
Carrier Frequency	24 GHz	24 GHz	10 GHz

*Inverse discrete Fresnel transform/Inverse discrete Fourier transform

Fig. 4.11 (a)) were tuned to a specific configuration (see grey colored input MRR resonances in Fig. 4.11 (b)). In this way, a connection from the input port to a particular output port is achieved by transmission of an associated wavelength across the C-band. In this scenario, each switch output port (representing the connection to a separate fronthaul link served by the CO) can be addressed by appropriate tuning of the TriPleX hybrid integrated laser; thereby introducing an additional layer of networking flexibility on top of the wavelength/space switching capabilities of the SiP switch alone. This operation allows the optical transmitter/service at the CO to be connected to any local fronthaul link regardless of the SiP switch state.

The optical signal routed out of the switch port is amplified by an EDFA to compensate for losses ($\sim$10-15 dB) which are primarily attributed to coupling to/from the SiP chip. The edge coupling loss of 6 dB/facet is reported for a looped pair of MRRs [23]. Path-dependent losses are also introduced by on-chip bends in Si waveguides in the switch fabric and variations in the fabrication process. The output signal is then transmitted over 10 km of SSMF. A VOA is utilized to regulate the optical power falling on a 40 GHz PIN PD with an integrated transimpedance amplifier (TIA), which is situated at the RU and responsible for converting the incident light into an electrical signal in this direct detection system. A 100 GSa/s RTO captures the electrical signal, which is then processed offline to evaluate the EVM performance in all test cases i.e. all four configured switch paths/output ports.

4.2.5 Results & Discussion

The received electrical spectrum of the transmitted 64-QAM OCDM signal via path 1 (at 1542 nm) is shown in Fig. 4.12 (a). The EVM performance is evaluated with respect to ROPs, shown in Fig. 4.13, for four wavelengths routed via four configured paths of the wavelength/space switch. The performance for optical back to back and 10 km fiber transmission were comparable, hence only the transmission over 10 km fiber is presented. EVM percentages below the 8% 64-QAM limit for ROPs higher than -5 dBm are observed, with the lowest EVM of 4.9% (BER of 3.2×10^{-5}) recorded for the 64-QAM OCDM signal received on the 1545 nm carrier (switch path 2) at an ROP of -1 dBm. The effect of chromatic dispersion due to fiber transmission can be observed for fiber lengths

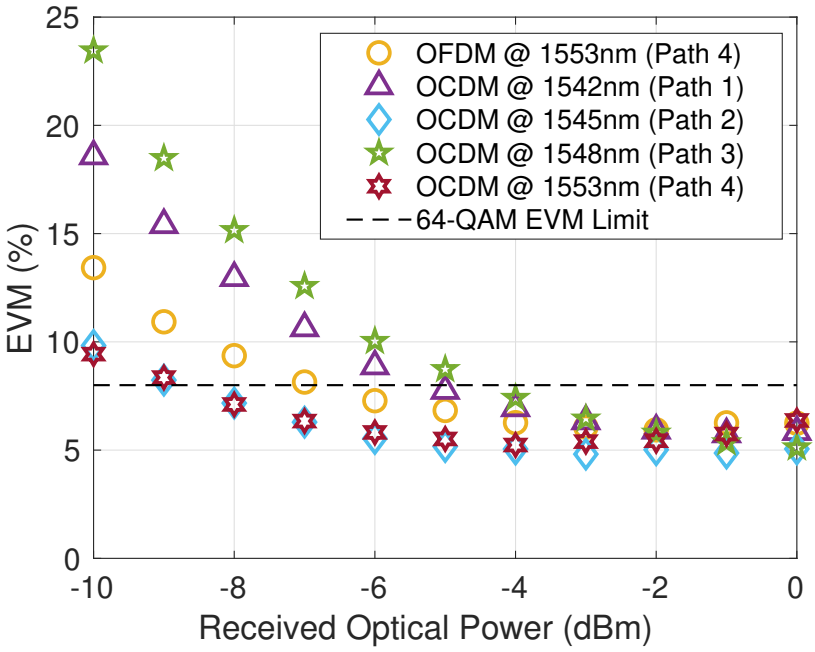

Fig. 4.13: EVM performance evaluation over varied optical power incident on PD.

of more than 20 km fiber, but for ARoF access network applications this transmission distance is unsuitable. Due to the switch path-dependent losses imposed by fabrication tolerances, coupling and bending losses from on-chip Si waveguides and slight thermal fluctuations impacting MRR tuning, signals traversing each switch path experience different losses, leading to a variation in optical power observed at each output port. This directly impacts the OSNR at each wavelength as signals at the output of the switch are fed to the booster EDFA, ultimately leading to the disparity in the performance curves presented in Fig. 4.13. This effect leads to a maximum receiver sensitivity degradation of $\sim$4 dB at the 8% EVM limit when comparing OCDM performances at 1548 nm (path 3) with that received at 1553 nm (path 4).

In all cases at higher ROPs i.e. from -3 to 0 dBm, the EVM performances converge to $\sim$5% as the limitations imposed by the optical receiver (shot noise and non-linearity) begin to dominate the system performance. The clear 64-QAM constellations of OCDM signals received at -2 dBm via the four tested SiP switch paths/wavelength conditions are color-coded with respect to the wavelengths and are shown in Fig. 4.14, indicate excellent performance. To compare OCDM with current 5G technology, an equivalent 24 GHz 1.2 Gbps 64-QAM OFDM mobile signal was also transmitted at 1553 nm and routed via switch path 4 with the same conditions as for the best performing OCDM signal for a

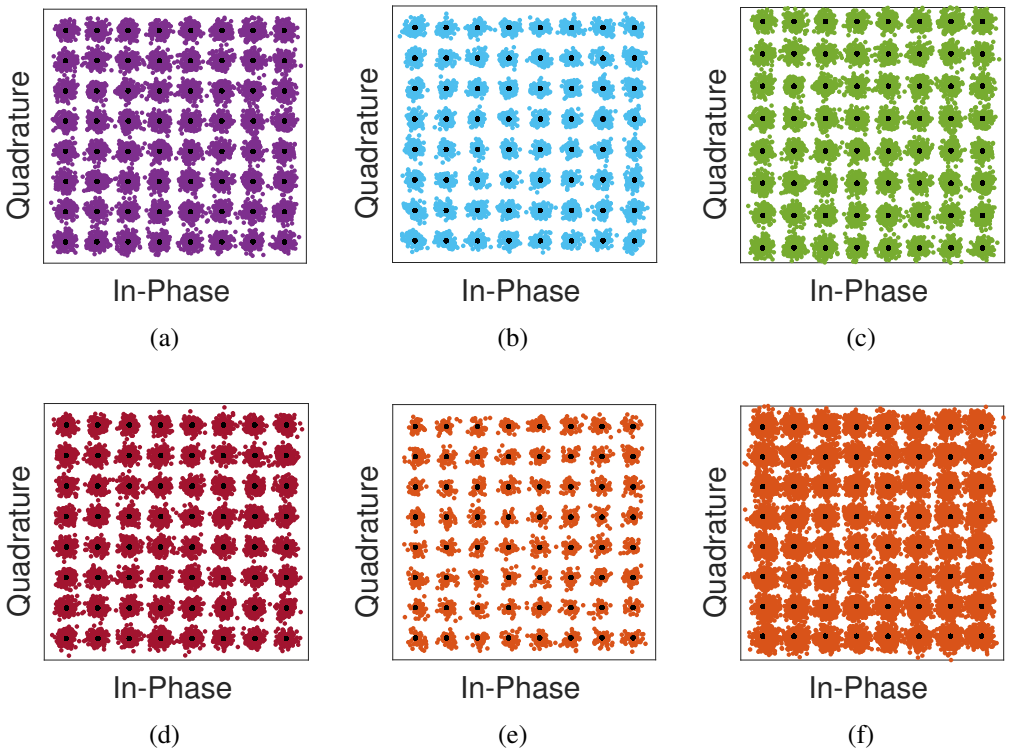

Fig. 4.14: Overlapped transmitted and received constellations of 64-QAM OCDM at four wavelengths, i.e. 1542 nm, 1545 nm, 1548 nm and 1553 nm, coming out of switch paths (a) 1, (b) 2, (c) 3 and (d) 4 respectively and the multi-band 64-QAM OFDM compatible to (e) 5G NR and (f) Wi-Fi standards at 1548 nm wavelength, all observed at ROP of −2 dBm incident on PD.

fair comparison. In this case, where standard OFDM frequency domain CE is utilized, the performance curve ("○" in Fig. 4.13) indicates a 2 dB degradation in receiver sensitivity with respect to OCDM (for the same networking conditions) at the 8% EVM limit. This result highlights the performance enhancement enabled through the use of OCDM's pulse compression-based CE technique [35], providing a superior channel estimation in this system dominated by Gaussian noise processes and is completely independent of the switch path the signal goes through.

A multi-band/multi-service ARoF signal composed of two wireless services; a narrowband 1.2 Gbps 64-QAM OFDM signal adhering to the 5G NR mobile standard at 24 GHz IF and a wideband 10 Gb/s 64-QAM OFDM Wi-Fi standard compatible signal at 10 GHz IF is also transmitted. Fig. 4.12 (b) shows the received electrical spectrum of the multi-band signal transmitted through path 3 in the optical switch. The EVM performance of the composite signal transmitted through switch paths 3 and 4, with an ROP of −2 dBm, is shown in Fig. 4.15. Best EVMs 6.1% and 6.6% are achieved for 5G NR and

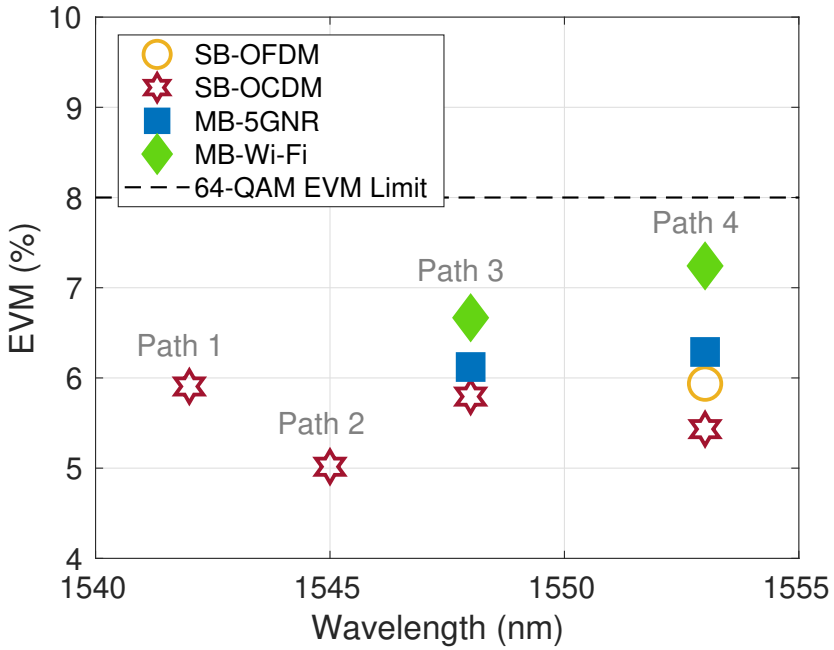

Fig. 4.15: EVM performance evaluation over wavelengths switched in C-band at −2 dBm ROP falling on PD.

Wi-Fi services, respectively, through switch path 3 (carrier wavelength 1548 nm). This divergence in performance between the two services is also observed for transmission through switch path 4 and this is expected given the relatively larger bandwidth of the Wi-Fi service, compared to that of 5G NR (see Table 4.2). The same channel estimation was used for SB-OFDM as for SB-OCDM was used in this experiment. The 0.4% EVM difference between SB-OFDM and SB-OCDM for path 4 in Fig. 4.15 is attributed to ambient temperature variance during the measurement, rather than channel or signal-dependent effects. It is noted that there is wavelength related instability due to the thermal tuning of the MRRs. The overlapped constellation of transmitted and received 5G NR and Wi-Fi signals are shown in Fig. 4.14 (a)and (b), respectively. The overall EVM performance of multi-band OFDM signal at 1548 nm and 1553 nm wavelengths is well below the 64-QAM EVM limit.

4.3 Conclusion

The advanced converged wireless-optical transmission systems utilizing SiP technology offer a promising solution to meet the growing network capacity demands. By integrating

fixed-line and wireless networks and leveraging the advantages of SiP, these systems enable seamless transmission of multiple waveforms, catering to applications such as PON, Wi-Fi, and future 6G networks. This convergence sets the stage for more efficient and adaptable communication networks in the digital age. In a successful demonstration, a multi-service optical access with a low noise SiP-based optical source showcased the coexistence of digital and analog RoF in a converged optical access network scenario. The system's flexibility allows modulation at different mmWave frequencies, making it suitable for VLC, FSO, and satellite communication as well.

In the context of future access networks for beyond 5G/6G technology, optical reconfigurability plays a crucial role in the development of interoperable, energy-efficient, and cost-effective networks. The presented results illustrate how wavelength/space flexible SiP components can be deployed in a C-RAN architecture to achieve all-optical fronthaul switching/routing directly from a RAN central office. The flexible SiP platform showcased its capability to support ARoF transport of emerging 6G waveform (OCDM) at mmWave frequencies with an impressive performance in all test cases. Additionally, the system demonstrated dynamic multi-service delivery in a C-RAN network, which is essential for interoperability in future access networks. To enhance energy efficiency, future improvements can include implementing a feedback control system to stabilize the MRRs. Overall, the proposed system and experimental results highlight the potential of fully integrated SiP systems in developing truly converged and flexible future access networks.

References

[1] C. Browning, E. P. Martin, A. Farhang, and L. P. Barry, "60 GHz 5G Radio-Over-Fiber Using UF-OFDM With Optical Heterodyning," *IEEE Photonics Technology Letters*, vol. 29, no. 23, pp. 2059–2062, 2017.

[2] L. Li, X. Zhang, D. Kong, M. Bi, S. Jia, W. Hu, and H. Hu, "Digital-analog hybrid optical access integrating 56-Gbps PAM-4 signal and 5G mmWave signal by spectral null filling," *Journal of Lightwave Technology*, vol. 39, no. 5, pp. 1278–1288, 2020.

[3] A. V. Martí, N. Vokić, T. Zemen, and B. Schrenk, "Hybrid CAP/mm-wave OFDM Vector Modulation for Photonic Frequency Conversion in a Single-Sideband Feeder," in *2022 Optical Fiber Communications Conference and Exhibition (OFC)*. IEEE, 2022, pp. 1–3.

[4] C. G. Roeloffzen, L. Zhuang, C. Taddei, A. Leinse, R. G. Heideman, P. W. van Dijk, R. M. Oldenbeuving, D. A. Marpaung, M. Burla, and K.-J. Boller, "Silicon nitride microwave photonic circuits," *Optics express*, vol. 21, no. 19, pp. 22 937–22 961, 2013.

[5] C. G. H. Roeloffzen, M. Hoekman, E. J. Klein, L. S. Wevers, R. B. Timens, D. Marchenko, D. Geskus, R. Dekker, A. Alippi, R. Grootjans, A. van Rees, R. M. Oldenbeuving, J. P. Epping, R. G. Heideman, K. Worhoff, A. Leinse, D. Geuzebroek, E. Schreuder, P. W. L. van Dijk, I. Visscher, C. Taddei, Y. Fan, C. Taballione, Y. Liu, D. Marpaung, L. Zhuang, M. Benelajla, and K.-J. Boller, "Low-Loss Si_3N_4 TriPleX Optical Waveguides: Technology and Applications Overview," *IEEE J. Select. Topics Quantum Electron.*, vol. 24, no. 4, pp. 1–21, Jul. 2018. [Online]. Available: http://ieeexplore.ieee.org/document/8259277/

[6] Y. Lin, C. Browning, R. B. Timens, D. H. Geuzebroek, C. G. Roeloffzen, M. Hoekman, D. Geskus, R. M. Oldenbeuving, R. G. Heideman, Y. Fan *et al.*, "Characterization of hybrid InP-TriPleX photonic integrated tunable lasers based on silicon nitride (Si_3N_4/SiO_2) microring resonators for optical coherent system," *IEEE Photonics Journal*, vol. 10, no. 3, pp. 1–8, 2018.

[7] K.-J. Boller, A. van Rees, Y. Fan, J. Mak, R. E. M. Lammerink, C. A. A. Franken, P. J. M. van der Slot, D. A. I. Marpaung, C. Fallnich, J. P. Epping, R. M. Oldenbeuving, D. Geskus, R. Dekker, I. Visscher, R. Grootjans, C. G. H. Roeloffzen, M. Hoekman, E. J. Klein, A. Leinse, and R. G. Heideman, "Hybrid Integrated Semiconductor Lasers with Silicon Nitride Feedback Circuits," in *Photonics*, vol. 7, no. 1. Multidisciplinary Digital Publishing Institute, 2020, p. 4.

[8] D. Dass, M. T. Costas, L. P. Barry, S. O'Duill, C. G. Roeloffzen, D. Geuzebroek, G. Carpintero, R. C. Guzman, and C. Browning, "28 gbd pam-8 transmission over a 100 nm range using an inp-si 3 n 4 based integrated dual tunable laser module," *Optics Express*, vol. 29, no. 11, pp. 16 563–16 571, 2021.

[9] L. Gonzalez-Guerrero, R. Guzman, M. Ali, A. Zarzuelo, J. C. Cuello, D. Dass, C. Browning, L. Barry, I. Visscher, R. Grootjans *et al.*, "Injection locking properties of an dual laser source for mm-wave communications," *Journal of Lightwave Technology*, vol. 40, no. 20, pp. 6685–6692, 2022.

[10] Y.-W. Chen, R. Zhang, C.-W. Hsu, and G.-K. Chang, "Key enabling technologies for the post-5G

era: Fully adaptive, all-spectra coordinated radio access network with function decoupling," *IEEE Communications Magazine*, vol. 58, no. 9, pp. 60–66, 2020.

[11] M. F. Ali, D. N. K. Jayakody, S. Garg, G. Kaddoum, and M. S. Hossain, "Dual-hop mixed FSO-VLC underwater wireless communication link," *IEEE Transactions on Network and Service Management*, vol. 19, no. 3, pp. 3105–3120, 2022.

[12] T. Z. Gutema, H. Haas, and W. O. Popoola, "Bias point optimisation in LiFi for capacity enhancement," *Journal of Lightwave Technology*, vol. 39, no. 15, pp. 5021–5027, 2021.

[13] X. Wu, Y. Zeng, X. Si, X. Wang, and X. Liu, "Fiber-To-The-Room (FTTR): Standards and Deployments," in *2023 Optical Fiber Communications Conference and Exhibition (OFC)*. IEEE, 2023, pp. 1–3.

[14] C. He, Y. Liu, Y. Huang, M. Zhi, Y. Zeng, Z. Ren, X. Wang, and P. Li, "Q-band Millimeter Wave Communication: Enabling 10 Gb/s Home Network in Fiber-to-The-Room Scenario," in *2021 IEEE MTT-S International Wireless Symposium (IWS)*. IEEE, 2021, pp. 1–3.

[15] X. Liu and F. Buchali, "Intra-symbol frequency-domain averaging based channel estimation for coherent optical OFDM," *Optics express*, vol. 16, no. 26, pp. 21 944–21 957, 2008.

[16] X. Tu, C. Song, T. Huang, Z. Chen, and H. Fu, "State of the art and perspectives on silicon photonic switches," *Micromachines*, vol. 10, no. 1, p. 51, 2019.

[17] X. Chen, J. Lin, and K. Wang, "A review of silicon-based integrated optical switches," *Laser & Photonics Reviews*, p. 2200571, 2023.

[18] J. Joo, J. Park, and G. Kim, "Cost-effective $2\backslash$times $2 silicon nitride mach - zehnder interferometric (mzi) thermo-optic switch,''$ *IEEE Photonics Technology Letters*, $vol.\,30, no.\,8, pp.740--743, 2018.$

[19] J. Rakshit, T. Chattopadhyay, and J. Roy, "Design of ring resonator based all optical switch for logic and arithmetic operations–a theoretical study," *Optik*, vol. 124, no. 23, pp. 6048–6057, 2013.

[20] L. Lu, L. Zhou, Z. Li, D. Li, S. Zhao, X. Li, and J. Chen, "$4\backslash$times $4 silicon optical switches based on double - ring - assisted mach - -zehnder interferometers,''$ *IEEE Photonics Technology Letters*, $vol.\,27, no.\,23, pp.2457--2460, 2015.$

[21] X. Ma and G.-S. Kuo, "Optical switching technology comparison: optical mems vs. other technologies," *IEEE communications magazine*, vol. 41, no. 11, pp. S16–S23, 2003.

[22] K. Biswas and A. Sarkar, "Mems-based optical switches," *Optical Switching: Device Technology and Applications in Networks*, pp. 93–106, 2022.

[23] J. Xia, T. Li, Q. Cheng, M. Glick, M. Crisp, K. Bergman, and R. Penty, "A Future Proof Reconfigurable Wireless and Fixed Converged Optical Fronthaul Network Using Silicon Photonic Switching Strategies," *Journal of Lightwave Technology*, 2022.

[24] M. Bahadori, A. Gazman, N. Janosik, S. Rumley, Z. Zhu, R. Polster, Q. Cheng, and K. Bergman, "Thermal rectification of integrated microheaters for microring resonators in silicon photonics platform," *Journal of Lightwave Technology*, vol. 36, no. 3, pp. 773–788, 2017.

[25] M. Bahadori, S. Rumley, R. Polster, and K. Bergman, "Loss and crosstalk of scalable mzi-based switch topologies in silicon photonic platform," in *2016 IEEE Photonics Conference (IPC)*. IEEE, 2016, pp. 615–616.

[26] P. Dong, Y.-K. Chen, G.-H. Duan, and D. T. Neilson, "Silicon photonic devices and integrated circuits," *Nanophotonics*, vol. 3, no. 4-5, pp. 215–228, Aug. 2014. [Online]. Available: https://www.degruyter.com/view/journals/nanoph/3/4-5/article-p215.xml

[27] X. Guan, W. Shi, J. Liu, P. Tan, J. Slevinsky, and L. A. Rusch, "Silicon photonics in optical access networks for 5G communications," *IEEE Communications Magazine*, vol. 59, no. 6, pp. 126–131, 2021.

[28] C. Browning, Q. Cheng, N. C. Abrams, M. Ruffini, L. Y. Dai, L. P. Barry, and K. Bergman, "A silicon photonic switching platform for flexible converged centralized-radio access networking," *Journal of Lightwave Technology*, vol. 38, no. 19, pp. 5386–5392, 2020.

[29] E. Ruggeri, C. Vagionas, R. Maximidis, G. Kalfas, D. Spasopoulos, N. Terzenidis, R. M. Oldenbeuving, P. W. van Dijk, C. G. Roeloffzen, N. Pleros *et al.*, "Reconfigurable Fiber Wireless fronthaul with A-RoF and D-RoF co-existence through a Si3N4 ROADM for Heterogeneous mmWave 5G C-RANs," *Journal of Lightwave Technology*, vol. 40, no. 16, pp. 5514–5521, 2022.

[30] X. Guan, R. Dubé-Demers, W. Shi, and L. A. Rusch, "Heterogeneous optical access networks: Enabling low-latency 5g services with a silicon photonic smart edge," *Journal of Lightwave Technology*, vol. 39, no. 8, pp. 2348–2357, 2021.

[31] M. Alsabah, M. A. Naser, B. M. Mahmmod, S. H. Abdulhussain, M. R. Eissa, A. Al-Baidhani, N. K. Noordin, S. M. Sait, K. A. Al-Utaibi, and F. Hashim, "6G wireless communications networks: A comprehensive survey," *IEEE Access*, vol. 9, pp. 148 191–148 243, 2021.

[32] X. Ouyang and J. Zhao, "Orthogonal chirp division multiplexing," *IEEE Transactions on Communications*, vol. 64, no. 9, pp. 3946–3957, 2016.

[33] C. Browning, X. Ouyang, D. Dass, G. Talli, and P. Townsend, "Orthogonal chirp-division multiplexing for performance enhanced optical/millimeter-wave 5G/6G communications," in *2021 Optical Fiber Communications Conference and Exhibition (OFC)*. IEEE, 2021, pp. 1–3.

[34] Q. Cheng, L. Y. Dai, N. C. Abrams, Y.-H. Hung, P. E. Morrissey, M. Glick, P. O'Brien, and K. Bergman, "Ultralow-crosstalk, strictly non-blocking microring-based optical switch," *Photonics Research*, vol. 7, no. 2, pp. 155–161, 2019.

[35] X. Ouyang, C. Antony, G. Talli, and P. D. Townsend, "Robust channel estimation for coherent optical orthogonal chirp-division multiplexing with pulse compression and noise rejection," *Journal of Lightwave Technology*, vol. 36, no. 23, pp. 5600–5610, 2018.

Chapter 5

Flexible Short-reach Intra-Datacenter Transmission

As discussed in chapter 1, the increasing demand for bandwidth, driven by technological advancements and cloud services, is fueling the evolution of data communications networks. High-capacity and spectrally efficient systems are crucial to meet this demand caused by technologies like cloud computing, ultra-high-definition video streaming, AR/VR, telemedicine, cloud storage and IoT.

The IEEE P802.3db (400 GbE Task Force) standard is rapidly being deployed for short-reach fiber networks such as intra-DC links that can support bitrates of up to 400G, using coarse wavelength division multiplexing (CWDM) with eight wavelength channels each operating with PAM-4 at 50 Gbps [1]. Looking ahead, the Ethernet alliance roadmap indicates that the future link speeds are envisioned to be more than 1 Tb/s [2]. Considering the future proliferation of intra-DC interconnects, providing Terabit-scale operation across a DC network poses a major challenge. To address this issue of scalability, many works have highlighted the need to harness more spectrally efficient transmission technologies, as well as the deployment of flexible networking in the optical domain using dynamic wavelength switching/routing (which overcomes the bandwidth limitations associated with current electronic switching technologies) [3, 4].

While optical coherent solutions have recently been proposed in the literature [5, 4], the associated cost of deployment may be prohibitive in the mid-term. Another option, which maintains the cost-effectiveness of (and provides a greater level of backward com-

patibility with) today's systems, involves harnessing the spectral efficiency offered by dense WDM (DWDM) networking in the C-band in combination with PAM-8 transmissions [6, 7]. Due to the SNR requirements for PAM-8 transmission, a major hindrance to the development of transceivers in such DWDM IM/DD systems is the RIN of the optical source which limits performance [8]. Furthermore, the optical sources commonly used in DC transceivers (vertical cavity surface emitting lasers (VCSELs) and distributed feedback (DFB) lasers), exhibit limited wavelength tunability, making them incompatible with optical switching platforms which are predicated on transceiver wavelength versatility. Such proposed systems can exploit wavelength switching alone [9], or in tandem with optical space switching [10].

It is clear that in order to maximize DC network scalability afforded by a DWDM PAM platform, the development of a mass producible optical source - which supports higher order PAM transmission, exhibits flexibility in the optical domain and is compatible with surrounding integrated photonics - is critical. Optical devices based on photonic integration have shown the potential to be a key element of such evolved optical networks and have drawn a lot of attention in recent years. As discussed in the previous chapter 4, the development of silicon-based optical sources in particular has the potential to enable fully integrated transceiver solutions and is the subject of much research with various approaches described in [11, 12, 13]. Outside of the SiP approach, compact laser designs such as the fiber Bragg grating (FBG)-based sources in [8] provide extremely low RIN (-165 dBc/Hz), while the liquid crystal-based device in [14] gives full C-band tunability.

Recent works have examined the viability of PAM-8 transmissions in short-reach IM/DD systems. Experiments in [6] target a data center interconnect (DCI) application, using an ECL to demonstrate 40 GBd PAM-8 transmissions with the aid of a Volterra non-linear equalizer (VNLE) at the receiver. VCSELs have also been shown to support PAM-8 in some cases; with [15] demonstrating 28 GBd transmission over 25 km of single mode fiber with the aid of injection locking/linear EQ, and [16] overcoming laser noise effects via transmitter side probabilistic shaping (PS) to achieve 33.3 GBd transmission in multi-mode fiber (MMF) system. The authors of [17] demonstrate 37.4 GBd PAM-8 transmissions using a DFB in combination with a SiP modulator and frequency response EQ. In some recent work, authors have proposed simplistic digital post-compensation for

56 GBd PAM-8 DCI transmission using an Electro Absorption Modulator (EAM) [18], and have demonstrated the use of a hybrid integrated MRR based tunable laser source for flexible PAM-4 short-reach systems [19].

In this chapter, a photonic integrated DLM is shown to support 28 GBd PAM-8 transmissions over an ultra-wide wavelength range of 100 nm using only simplistic DSP to achieve performance below the 7% FEC limit. The discretely tunable device, DLM (discussed extensively in section 3.1). Section 5.1 discusses the short-reach datacenter interconnects and 5G cloudification and describes the experimental setup and outcomes of the experiment of the short-reach datacenter transmission in subsections 5.1.2 and 5.1.3 respectively. This chapter is concluded in the subsection 5.1.4.

5.1 Short-reach Datacenter Interconnects

5.1.1 Datacenter Interconnects and 5G Cloudification

A DCI is a technology that provides high capacity link between two or more datacenters to pool resources, balance workloads, replicate data, and enable disaster recovery. The DCI is categorized based on short ($<$ 5 km), medium ($<$ 100 km) and long distance ($\sim$ 100s km) transmission. The evolution of the speeds of the DCI has been very fast paced since the year 2010, as depicted in Fig. 5.1. The 100G channel speed was first achieved in 2010 by deploying coherent technology in the DCNs. Recently, the deployment of 400G coherent technology in real inter-DCIs was achieved in the year 2018. In the current scenario, extensive research on the transmission of 800G with pluggable transceivers, multicore fiber and Si based photonic integration has been portrayed in these works [20, 21, 22].

This rise in the demand for higher bandwidths from DCNs is led by the advent of technologies such as 5G, cloud computing and AI (discussed in section 1.3) which has led to a shift towards decentralization of DCNs. A disaggregated DCN corresponds to a network architecture wherein the various resources and functionalities of the network infrastructure are decoupled, allowing for increased flexibility and customization in building and managing the network. Hence, the network operators have the ability to exert effective control and reconfigure their networks, enabling end-to-end optimization tailored to their

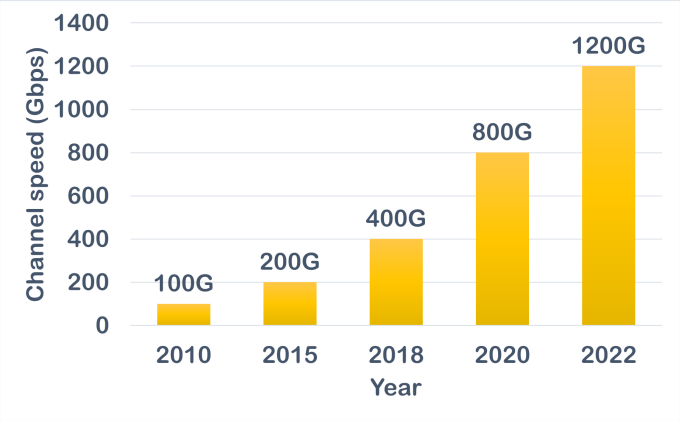

Fig. 5.1: DCI channel speed evolution over the past decade [23].

specific requirements [23].

Moreover, decoupling the DCN resources and functionality produces a decentralized DCN, which is a distributed model that encompasses cloud, edge, and end devices. The complementary capabilities of the edge cloud and core cloud enable seamless collaboration of data, applications, AI algorithms, and management. Some 5G applications necessitate low-latency computing and localized service processing that leads to increased demand for lightweight and flexible edge cloud sites [24]. Additionally, certain functions of the mobile core network are being decentralized and moved closer to the content sources, enabling faster and more efficient processing.

Furthermore, network operators can quickly deploy and scale network functions, reduce reliance on dedicated hardware, and optimize resource utilization through the virtualization of 5G components like CU with the NFV technology described in section 1.3. This enables efficient network management and rapid service provisioning while facilitating network automation and programmability. Fig. 5.2 illustrates a decentralized DCN converged with 5G technology, where the CU is virtualized for time-sensitive applications.

Researchers in [25] have recently highlighted the potential of increasing the modulation order of PAM from PAM-4 to PAM-6, offering the advantage of reduced bandwidth occupancy in 1 km intra-datacenter interconnects. This development has invigorated the interest in analyzing the feasibility of PAM-8 transmissions over these short-reach DC links and the following section explores this.

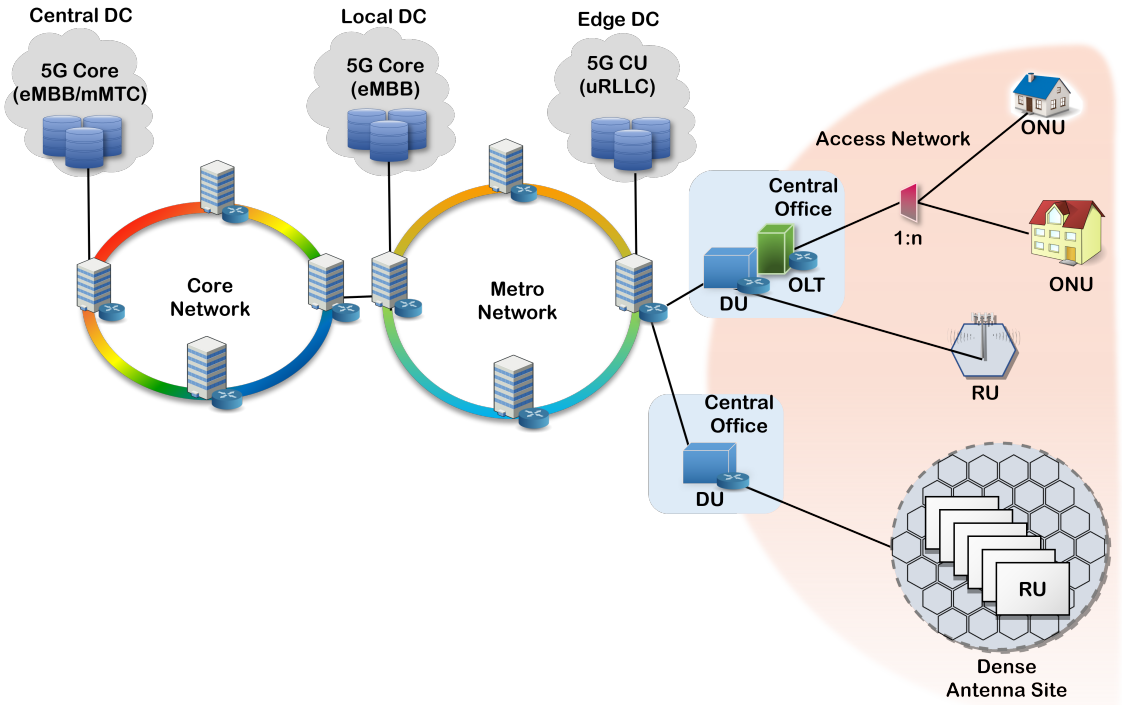

Fig. 5.2: Datacenter and access network convergence.

5.1.2 Intra-Datacenter PAM-8 Transmission

The short-reach PAM-8 experimental setup is shown in Fig. 5.3. Using the tuning maps presented in the chapter 3 section 3.1, the tuning sections of each laser were optimized to obtain an optical carrier with the desired wavelength, power and SMSR. L1 was used to generate wavelengths in the S-band and L2 was used to generate wavelengths in the C-band, with roughly 10 dBm output power achieved for all operating wavelengths. To achieve this output power the gain currents of L1 and L2 were set to 170 mA and 100 mA respectively, as depicted in Fig. 3.5 presented in subsection 3.1.2. The two laser outputs were attached to isolators in order to avoid back reflections in the laser cavity.

A pseudorandom PAM-8 signal of length 2^{15} symbols was generated offline using MATLAB. The PAM signal was then predistorted, see Fig.5.4, through symbol level adjustment in order to compensate for the non-linear transfer function of the Sumitomo 40 GHz single ended $LiNbO_3$ MZM used. The 28 GBaud PAM-8 electrical signal was generated by the Keysight M9502A AWG operating at 84 GSa/s and amplified before driving the MZM which was biased at quadrature. The output voltage of the AWG, as well as the gain on the linear amplifier, were carefully selected to obtain the MZM drive voltage

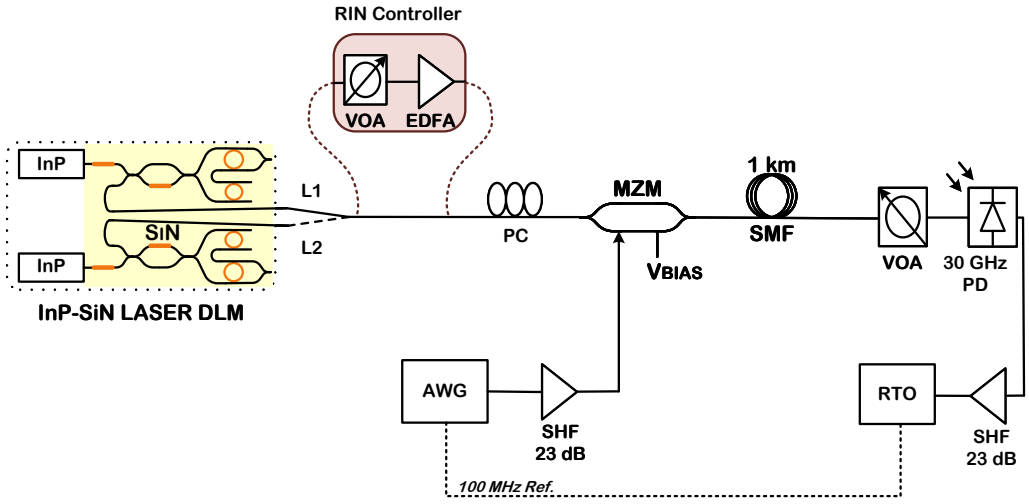

Fig. 5.3: Experimental setup showing the switching between L1 and L2 of the dual module laser.

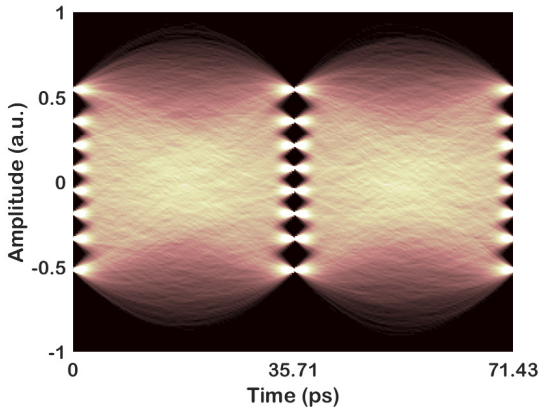

Fig. 5.4: Predistorted PAM-8 signal with linear-quadratic spacing.

required to maximize the extinction of the transmitted optical PAM-8 signal. After modulation of the optical carrier via the MZM, the signal was transmitted through 1 km of SMF. At the receiver, a VOA was used to vary the received optical power falling on a 30 GHz PIN PD. The obtained photocurrent was amplified to allow its capture, at a sample rate of 100 GSa/s, with the Tektronix DPO77002SX RTO.

In order to examine the limitations imposed by RIN in the PAM-8 transmission system, an optical source with variable RIN levels was synthesized. This was achieved by connecting the output of L2 (operating at 1553 nm) to an EDFA through a VOA, shown as RIN controller in Fig. 5.3. By setting the EDFA to have a fixed output power of +10 dBm, the input optical carrier power can be varied by the VOA, thus producing relative

changes in the amplitude noise exhibited by the output optical carrier. This allowed the RIN of the output optical carrier to be precisely controlled while maintaining constant lasing conditions. For further comparisons, an ECL tuned to operate at 1553 nm was also used as a transmitter source for performance evaluation. The received signal was digitally processed offline with different steps including resampling, normalization, equalization, symbol synchronization and PAM-8 decoding. A decision-directed least-mean square (DD-LMS) algorithm (see subsection 2.1.2) was used to train the weights of a 21-tap adaptive filter. After processing, the BER was calculated by counting errors over several captured bit sequences.

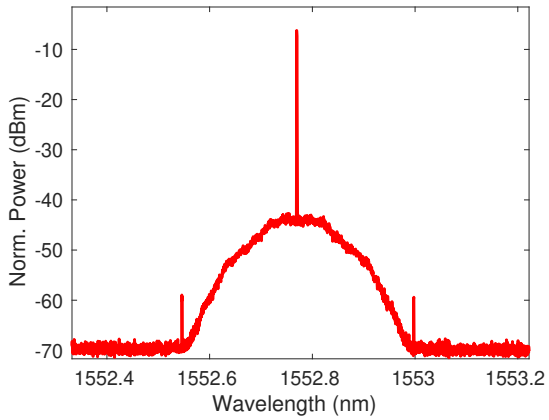

(a)

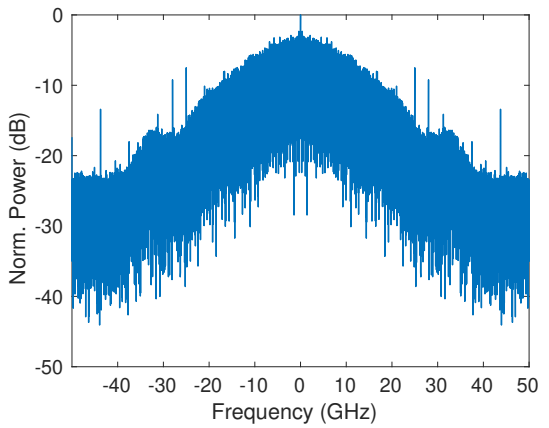

(b)

Fig. 5.5: (a) shows the optical spectrum of PAM-8 signal at PD and (b) shows the electrical spectrum of PAM-8 signal at RTO.

5.1.3 Results & Discussion

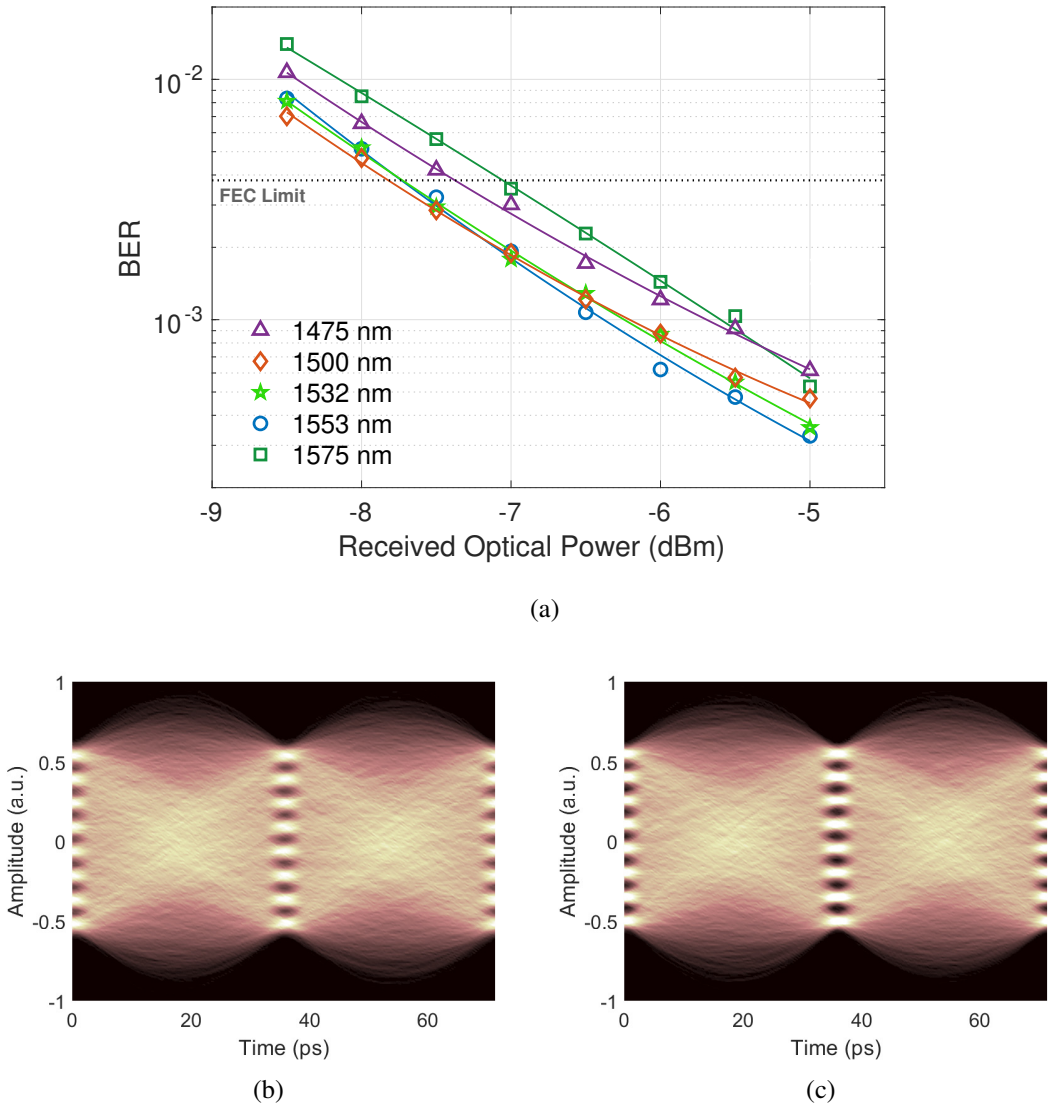

Fig. 5.6: (a) BER versus ROP for various wavelengths after 1 km of SMF. (b) Eye diagram for λ=1553 nm at -7 dBm ROP. (c) Eye diagram for λ=1553 nm at -5 dBm ROP.

The unamplified short-reach PAM-8 system outlined was evaluated in terms of BER with respect to the ROP using a selection of wavelengths from the DLM spanning the full 100 nm range. The received optical and electrical spectra are shown in Fig. 5.5 (a) and (b) respectively. The results after 1 km of SMF, presented in Fig. 5.6 (a), show that in all cases the measured BER was below the 7% FEC limit (3×10^{-3}) for ROPs greater than -7 dBm. Less than 1 dB of variability in received power was found across the whole spectrum for any given BER. The consistency of this performance across an

extremely wide tuning range highlights the potential of the DLM for flexible short-reach communications. Using L2 at 1553 nm, three optical carriers of wavelength, denoted by λ, at 1553 nm with different RIN values were obtained by changing the input power into the 'RIN controller' EDFA while keeping a constant output power, resulting in variable levels of gain and amplified spontaneous emission (ASE) from the EDFA.

A comparison of RIN values for various 'RIN controller' configurations and ECL is shown in Fig. 5.7. The RIN of each configuration was measured using the process outlined in section 3.1. For the cases where RIN was varied using the EDFA with total gains of 20 dB, 24 dB and 29 dB, the obtained RIN values were −144 dB/Hz, −140 dB/Hz and −135 dB/Hz, respectively. The RIN value for the ECL employed in the experiments was −155 dB/Hz.

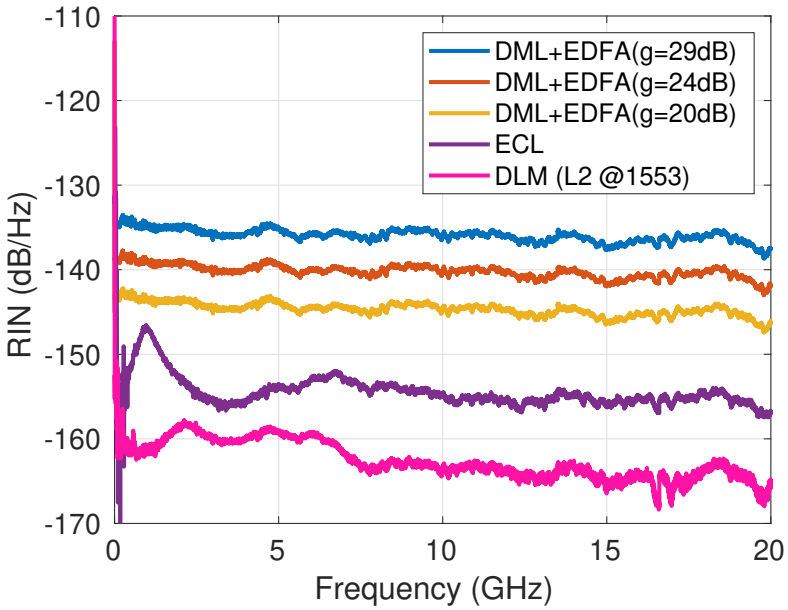

Fig. 5.7: Comparing the RIN values for different settings of RIN controller and ECL.

Fig. 5.8 shows BER versus ROP for each source RIN level evaluated in the short-reach PAM-8 system. In the figure, 'L2' denotes the use of the hybrid laser module alone, while 'L2+EDFA' denotes the use of the hybrid laser module in conjunction with the 'RIN controller' EDFA to obtain the various RIN levels, as described above. The figure shows that while all carriers exhibit similar performances at lower ROPs (due to the impact of receiver thermal noise), transmission with carrier RIN levels of −144 dB/Hz, −140 dB/Hz and −135 dB/Hz results in the emergence of error floors at higher ROPs as

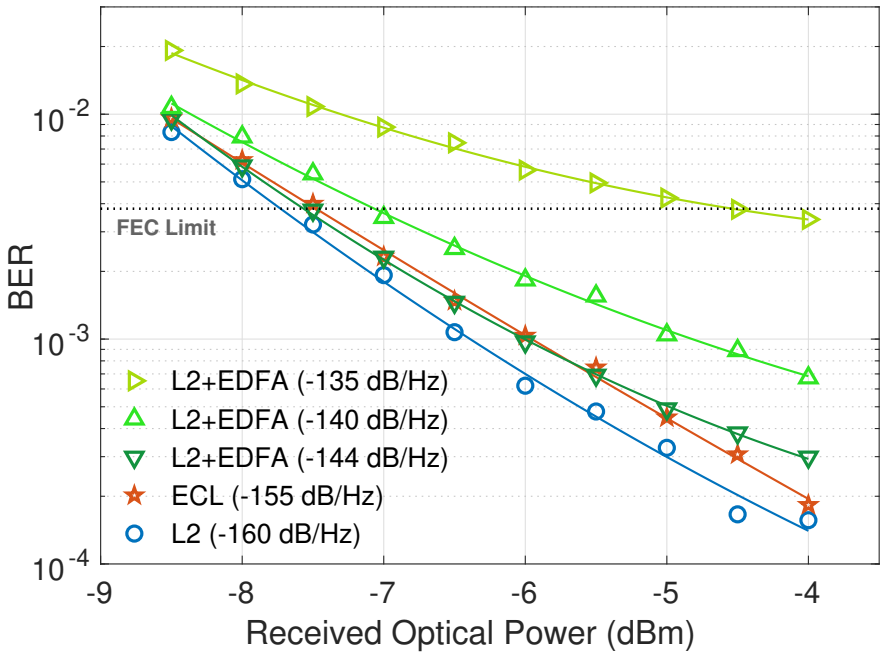

(a)

Fig. 5.8: BER vs ROP for different RIN levels for λ=1553 nm after 1 km of SMF.

RIN becomes the dominant noise process. This highlights the critical impact of RIN on the performance of higher order PAM IM/DD systems. The figure shows that these error floors are alleviated through the use of the low RIN carriers provided by L2 (−160 dB/Hz) and the ECL (−155 dB/Hz). For these RIN levels, [8] confirms that receiver shot noise is the dominant noise process at an ROP of −4 dBm, and in fact, this would be the case for received powers in the range of +3 dBm to +5 dBm (neglecting potential non-linearities due to the PD).

Overall, the superior low noise performance exhibited by the MRR-based hybrid integrated device results in a 3 dB improvement in the receiver sensitivity as compared to the worst case RIN presented (−135 dB/Hz) at the FEC limit. The results also show how the device outperforms a commercial ECL, exhibiting a 0.5 dB improvement in receiver sensitivity at BERs below 1×10^{-3}. The DLM is shown to be capable of supporting unamplified short-reach PAM-8 transmission over its entire wavelength range while maintaining the requirement for low complexity DSP.

5.1.4 Conclusion

With the ongoing increase in bandwidth requirements driven by many internet applications, there is a drive to enhance the capacity and cost effectiveness of short reach DCIs. Optical integration will play a key role in the development of cost-effective links as many transmitters and modulators can be integrated on a single chip. Ensuring these optical transmitters have the required noise levels to handle multi-level signaling is also vital for the deployment of spectrally efficient PAM-N formats. This work has presented an integrated dual laser source that can be tuned over 100 nm with the RIN value around −160 dB/Hz (see section 3.1.2) capable of supporting unamplified short-reach PAM-8 transmission over its entire wavelength range while maintaining the requirement for low complexity DSP.

Overall, the potential for mass production of the PIC-based design approach, the compatibility with surrounding electronic/optical silicon technologies and the facilitation of spectrally efficient IM/DD transmission, point toward the ability of the presented InP-Si_3N_4 DLM to be a key component in a wider cost-efficient and scalable DWDM solution for future DC networks.

Moreover, the transmission system presented in this chapter has been previously successfully deployed for the transmission of converged PON and RoF technologies, as shown in subsection 4.1.3. This noteworthy achievement opens the door to a momentous network convergence encompassing DCNs, PON and the upcoming realms of beyond 5G and 6G networks. The realization of this convergence is facilitated by the seamless integration of SDN and NFV technologies, enabling the efficient provision of optical RoF services. These advancements pave the way for seamless, efficient and highly reconfigurable network infrastructures, bringing together various data storage and communication technologies under a unified and intelligent framework.

References

[1] IEEE P802.3bs 400 Gb/s Ethernet Task Force [Online]. Available = https://www.ieee802.org/3/index.html.

[2] "2020 Roadmap - Ethernet Alliance," 2020 Roadmap - Ethernet Alliance. Available = https://ethernetalliance.org/technology/2020-roadmap/. [Online]. Available: https://ethernetalliance.org/technology/2020-roadmap/

[3] Q. Cheng, M. Bahadori, M. Glick, S. Rumley, and K. Bergman, "Recent advances in optical technologies for data centers: a review," *Optica*, vol. 5, no. 11, pp. 1354–1370, 2018.

[4] X. Zhou, R. Urata, and H. Liu, "Beyond 1 Tb/s Intra-Data Center Interconnect Technology: IM-DD OR Coherent?" *J. Lightwave Technol.*, vol. 38, no. 2, pp. 475–484, Jan. 2020. [Online]. Available: https://ieeexplore.ieee.org/document/8918098/

[5] M. Morsy-Osman, M. Sowailem, E. El-Fiky, T. Goodwill, T. Hoang, S. Lessard, and D. V. Plant, "DSP-free 'coherent-lite' transceiver for next generation single wavelength optical intra-datacenter interconnects," *Optics express*, vol. 26, no. 7, pp. 8890–8903, 2018.

[6] D. Zou, F. Li, Z. Li, W. Wang, Q. Sui, Z. Cao, and Z. Li, "100G PAM-6 and PAM-8 Signal Transmission Enabled by Pre-Chirping for 10-km Intra-DCI Utilizing MZM in C-band," *Journal of Lightwave Technology*, vol. 38, no. 13, Jul. 2020.

[7] H. Liu, R. Urata, X. Zhou, and A. Vahdat, "Evolving Requirements and Trends of Datacenters Networks," in *Springer Handbook of Optical Networks*. Springer, 2020, pp. 707–724.

[8] P. A. Morton and M. J. Morton, "High-Power, Ultra-Low Noise Hybrid Lasers for Microwave Photonics and Optical Sensing," *J. Lightwave Technol.*, vol. 36, no. 21, pp. 5048–5057, Nov. 2018. [Online]. Available: https://ieeexplore.ieee.org/document/8319492/

[9] H. Ballani, P. Costa, R. Behrendt, D. Cletheroe, I. Haller, K. Jozwik, F. Karinou, S. Lange, K. Shi, B. Thomsen, and H. Williams, "Sirius: A Flat Datacenter Network with Nanosecond Optical Switching," ser. SIGCOMM '20. New York, NY, USA: Association for Computing Machinery, 2020, p. 782–797. [Online]. Available: https://doi.org/10.1145/3387514.3406221

[10] A. Gazman, C. Browning, M. Bahadori, Z. Zhu, P. Samadi, S. Rumley, V. Vujicic, L. P. Barry, and K. Bergman, "Software-defined control-plane for wavelength selective unicast and multicast of optical data in a silicon photonic platform," *Optics express*, vol. 25, no. 1, pp. 232–242, 2017.

[11] A. Abbasi, J. Verbist, L. A. Shiramin, M. Verplaetse, T. De Keulenaer, R. Vaernewyck, R. Pierco, A. Vyncke, X. Yin, G. Torfs, G. Morthier, J. Bauwelinck, and G. Roelkens, "100-Gb/s Electro-Absorptive Duobinary Modulation of an InP-on-Si DFB Laser," *IEEE Photonics Technology Letters*, vol. 30, no. 12, pp. 1095–1098, 2018.

[12] S. Chen, W. Li, J. Wu, Q. Jiang, M. Tang, S. Shutts, S. N. Elliott, A. Sobiesierski, A. J. Seeds, I. Ross, P. M. Smowton, and H. Liu, "Electrically pumped continuous-wave III-V quantum dot lasers on silicon," *Nature Photonics*, vol. 10, no. 5, p. 307, 2016.

[13] B. R. Koch, E. J. Norberg, B. Kim, J. Hutchinson, J.-H. Shin, G. Fish, and A. Fang, "Integrated silicon photonic laser sources for telecom and datacom," in *Optical Fiber Communication Conference*. Optica Publishing Group, 2013, pp. PDP5C–8.

[14] J. De Merlier, K. Mizutani, S. Sudo, K. Naniwae, Y. Furushima, S. Sato, K. Sato, and K. Kudo, "Full c-band external cavity wavelength tunable laser using a liquid-crystal-based tunable mirror," *IEEE Photonics Technology Letters*, vol. 17, no. 3, pp. 681–683, 2005.

[15] Y. C. Wang, H. H. Lu, C. Y. Li, P. H. Chew, Y. B. Jheng, W. S. Tsai, and X. H. Huang, "A high-speed 84 gb/s vsb-pam8 vcsel transmitter-based fiber–ivllc integration," *IEEE Photonics Journal*, vol. 10, no. 5, pp. 1–8, 2018.

[16] L. Sun, C. Wang, J. Du, C. Liang, W. Zhang, K. Xu, F. Zhang, and Z. He, "Dyadic probabilistic shaping of PAM-4 and PAM-8 for cost-effective VCSEL-MMF optical interconnection," *IEEE Photonics Journal*, vol. 11, no. 2, pp. 1–11, 2019.

[17] M. Chagnon, M. Osman, M. Poulin, C. Latrasse, J. F. Gagné, Y. Painchaud, C. Paquet, S. Lessard, and D. Plant, "Experimental study of 112 Gb/s short reach transmission employing PAM formats and SiP intensity modulator at 1.3 μm," *Optics express*, vol. 22, no. 17, pp. 21 018–21 036, 2014.

[18] C. Browning, M. Ruffini, B. Cardiff, and L. P. Barry, "Single lane 168 gb/s pam-8 short reach transmission using an eam with receiver skew compensation," in *2018 European Conference on Optical Communication (ECOC)*. IEEE, 2018, pp. 1–3.

[19] C. Browning, M. Ruffini, Y. Lin, R. B. Timens, D. H. Geuzebroek, C. G. H. Roeloffzen, D. Geskus, R. M. Oldenbeuving, R. G. Heideman, Y. Fan, K. J. Boller, and L. P. Barry, "Optically switched 56 GBd PAM-4 using a hybrid InP-TriPleX integrated tunable laser based on silicon nitride micro-ring resonators," in *2018 Conference on Lasers and Electro-Optics (CLEO)*. IEEE, 2018, pp. 1–2.

[20] R. Zhang, K. Kuzmin, Y.-W. Chen, and W. I. Way, "800G/λ Self-Homodyne Coherent Links With Simplified DSP for Next-Generation Intra-Data Centers," *Journal of Lightwave Technology*, vol. 41, no. 4, pp. 1216–1222, 2022.

[21] H. Yu, D. Patel, W. Liu, Y. Malinge, P. Doussiere, W. Lin, S. Gupta, K. Narayanan, I. Hoshino, M. Bresnehan *et al.*, "800 gbps fully integrated silicon photonics transmitter for data center applications," in *Optical Fiber Communication Conference*. Optica Publishing Group, 2022, pp. M2D–7.

[22] H. Sun, M. Torbatian, M. Karimi, R. Maher, S. Thomson, M. Tehrani, Y. Gao, A. Kumpera, G. Soliman, A. Kakkar *et al.*, "800g dsp asic design using probabilistic shaping and digital sub-carrier multiplexing," *Journal of lightwave technology*, vol. 38, no. 17, pp. 4744–4756, 2020.

[23] C. Xie, L. Wang, L. Dou, M. Xia, S. Chen, H. Zhang, Z. Sun, and J. Cheng, "Open and disaggregated optical transport networks for data center interconnects," *Journal of Optical Communications and Networking*, vol. 12, no. 6, pp. C12–C22, 2020.

[24] Huawei, "5g-oriented data center facility." [Online]. Available: https://carrier.huawei.com/~/media/CNBGV2/download/products/network-energy/5G-oriented-Data-Center-Facility-en.pdf

[25] X. Zhou, C. F. Lam, R. Urata, and H. Liu, "State-of-the-art 800g/1.6 t datacom interconnects and

outlook for 3.2 t," in *Optical Fiber Communication Conference*. Optica Publishing Group, 2023, pp. W3D–1.

Conclusion & Future Work

With the ongoing increase in the capacity demanded from the fixed-line and mobile data networks, there is a drive to converge the vast bandwidth provided by optical access networks with the mobility provided by the wireless access networks in order to provide a range of multi-gigabit services to the end-users. The enhancement in storage capacity and communication speed facilitated by high speed, agile and cost-effective datacenters will be another aspect of convergence of the fixed-line/wireless networks. The wavelength flexible optical components supporting multi-gigabit transmissions is one of the key requirements for such converged networks. Adapting to communication techniques, such as optical heterodyning and ARoF, which supports optical-wireless integration in a simple and cost effective manner, will be a critical aspect of future converged networks. The ARoF technology supports simplified RU which is a key requirement for enhancing the number of devices and users in access networks. The components and techniques developed to support converged networks must be compatible with key high capacity communication technologies such as advanced modulation and the use of very high frequency RF carriers.

The experimental work presented in this thesis demonstrates the significant potential of SiP-based technologies in achieving system-level convergence and enhancing network capacity. The integrated DLM, characterized in detail, exhibits excellent performance in terms of tunability, noise levels, and compatibility with optical heterodyne systems. The mmWave frequency transmission systems for high throughput applications are realized with this versatile optical source in combination with advanced detection techniques. The wavelength flexibility feature of this optical source permits the best use of available fiber in a reconfigurable network environment while the ability to vary the RF carrier frequencies can allow different RF standards to be used, also enabling future network upgrades

to higher carrier frequencies in the THz range. The experimental results validate the feasibility of utilizing SiP-based components in a hybrid integrated ARoF mmWave transmission system, enabling flexible wavelength and RF carrier assignment and delivering high-quality signals over both fiber and wireless links.

Moreover, the research underscores the importance of reconfigurability and scalability in optical networks. The reconfigurability is achieved in this work using flexible optical devices such as MRR-based lasers and switches whereas the network scalability is enhanced by employing ARoF technology. The integration of SiP components in a C-RAN architecture enables all-optical fronthaul switching and routing, supporting the transport of emerging 6G waveforms at mmWave frequencies. The experimental results demonstrate the system's dynamic multi-service delivery and its potential for future converged access networks. This dynamic interplay between network elements and emerging technologies opens doors to novel and exciting possibilities, fostering a new era of connectivity and innovation.

In the context of short-reach datacenter interconnects, the thesis emphasizes the role of photonic integration in enhancing the capacity and cost-effectiveness. For datacenter interconnects, ensuring these optical transmitters have the required noise levels to handle multi-level signaling is also vital for the deployment of spectrally efficient PAM-N formats. The integrated DLM, with its wide tunability and low noise characteristics, proves suitable for spectrally efficient PAM-N transmission, meeting the increasing bandwidth requirements of datacenters.

Overall, the research presented in this thesis provides valuable insights into the potential of SiP-based technologies for achieving system-level convergence, enhancing network capacity, and enabling cost-effective and scalable solutions for future converged access networks and datacenter interconnects. This thesis contributes to the advancement of optical networking. It paves the way for developing efficient, reconfigurable and fully converged optical networks for dynamic multi-service delivery in the new digital era.

Future Work

- The multi-service optical access system, utilizing a low noise SiP-based optical source, effectively demonstrated the coexistence of fixed-line and wireless services

within a converged optical access network. Its remarkable flexibility enables the multiplexing of diverse modulation formats, thus facilitating a wide range of services beyond the scope of this study like VLC, FSO, satellite communication, and more. Consequently, the system significantly enhances interoperability among network operators, fostering seamless communication and collaboration. The potential future work can include incorporating these unexplored services in the multi-service optical access system presented in subsection 4.1.3.

- In anticipation of the transition to higher frequency ranges in 6G networks, research in the field of sub-THz frequencies becomes essential. The SiP-based DLM emerges as a valuable tool for generating tunable THz frequencies, reaching up to several THz. By leveraging these capabilities of DLM and integrating it with ARoF and multiple input multiple output (MIMO) technologies, 6G networks can support the high data rates, increased capacity, and diverse applications that are expected in the THz frequency range.

- The production of fully integrated optical transceivers, incorporating lasers, modulators, amplifiers, filters, and switches using Si-based elements, enables mass production due to the widespread availability of silicon. This approach significantly reduces costs, minimizes footprint and opens up possibilities for optical and electronic integration and one example of future work could involve the optical/electronic integration of the phase noise canceling receiver presented in section 3.2, which could enable practical networking demonstrations of this technology.

- The potential architectures proposed for utilizing the optical switch fabric can be deployed on a faster scale, providing greater flexibility and energy efficiency for network operators. Moreover, these architectures enable the transmission of multiplexed waveforms supporting both fixed-line and wireless services through optical switches, which requires thorough analysis. By implementing these architectures, a dynamic multi-service environment can be created, offering increased flexibility and versatility in network operations. Further research can be done to analyze the performance of multiplexed waveforms compatible with fixed-line and wireless services over the optical switch fabric discussed in subsection 4.2.2.2.

- Latency becomes a critical factor as the demand for cloud data storage and access increases especially for high bandwidth time-sensitive applications such as telemedicine, robotic surgeries, and live streaming. These applications require proximity to the cloud datacenter and minimal time consumed by DSP. Hence, the research focused on the combination of faster signal processing techniques, advanced modulation formats and the deployment of ARoF technology in the access network holds great potential in meeting the low latency demands of time-sensitive applications, ultimately improving the overall user experience and enabling efficient cloud-based services.

Appendix A : DLM Configuration

Table of Wavelength, SMSR and Power[1]

Table 5.1: Values corresponding to the Wavelength, SMSR and Power graphs

L1			L2		
Wavelength (nm)	SMSR (dB)	Power (dBm)	Wavelength (nm)	SMSR (dB)	Power (dBm)
1501.44	57.12	-0.46	1552.78	62.64	0.09
1501.44	57.04	-0.42	1552.78	62.82	0.03
1501.44	57.40	-0.41	1552.78	62.42	0.09
1501.44	57.38	-0.43	1552.78	63.69	0.08
1501.44	57.52	-0.41	1552.78	63.73	0.11
1501.44	57.54	-0.38	1552.78	63.00	0.16
1501.44	57.67	-0.38	1552.78	65.00	0.20
1501.44	57.89	-0.38	1552.78	65.00	0.27
1501.44	57.93	-0.38	1552.78	65.00	0.32
1501.44	57.64	-0.39	1552.78	65.00	0.42
1501.44	57.83	-0.47	1552.78	65.00	0.48
1501.44	57.22	-0.61	1552.78	65.00	0.55
1501.44	56.93	-0.85	1552.78	65.00	0.63
1501.44	46.31	-1.23	1552.78	65.00	0.70
1503.02	54.30	-1.74	1552.78	65.00	0.78
1503.02	56.28	-1.28	1552.78	65.00	0.83
1503.04	56.84	-0.80	1552.78	65.00	0.91
1503.04	57.02	-0.30	1552.78	65.00	0.91
1503.04	56.92	0.19	1552.78	65.00	0.94
1503.04	57.25	0.63	1552.78	65.00	0.92
1503.04	57.68	1.13	1552.78	62.48	0.93
1503.04	58.25	1.62	1552.78	61.52	0.88
1503.04	58.79	2.08	1552.78	59.04	0.85
1503.06	59.25	2.54	1552.78	56.21	0.84
1503.06	59.79	2.86	1552.78	54.04	0.80

[1]Both the lasers have a supply of 100 mA to gain section and 15 V to output MZI-TC

1503.06	59.75	2.91	1552.78	54.85	0.67
1503.06	59.92	2.58	1554.48	62.11	1.20
1503.06	59.34	1.78	1554.48	65.00	1.54
1503.06	58.50	0.60	1554.48	65.00	1.84
1504.62	50.55	-3.53	1554.48	65.00	2.13
1504.62	55.62	-2.76	1554.48	65.00	2.40
1504.62	55.73	-2.07	1554.48	64.80	2.61
1504.62	55.97	-1.47	1554.48	61.32	2.67
1504.64	56.38	-0.99	1554.48	14.61	2.26
1504.64	56.84	-0.49	1554.48	5.76	0.34
1504.64	57.09	-0.08	1554.48	2.45	-1.01
1504.64	57.36	0.15	1556.18	61.26	1.64
1504.64	58.02	0.20	1556.18	65.00	2.14
1504.64	58.19	-0.03	1556.18	65.00	2.47
1506.20	53.54	-2.40	1556.20	65.00	2.94
1506.20	57.60	-1.44	1556.20	65.00	3.24
1506.22	57.93	-0.52	1556.20	63.47	3.35
1506.22	58.38	0.25	1556.20	57.89	3.16
1506.22	58.86	1.08	1556.20	12.29	1.97
1506.22	59.34	1.58	1557.90	61.42	1.43
1506.22	58.89	1.24	1557.90	65.00	2.02
1506.22	54.83	-0.25	1557.90	65.00	2.45
1507.80	55.69	-2.80	1557.90	65.00	2.81
1507.80	57.27	-1.76	1557.90	65.00	2.88
1507.80	57.50	-0.87	1557.92	60.26	2.67
1507.80	57.79	-0.28	1557.92	53.62	1.98
1507.80	57.83	-0.14	1559.64	63.71	1.72
1507.80	57.79	-0.61	1559.64	65.00	2.39
1507.80	54.49	-1.60	1559.64	65.00	2.89
1509.38	58.19	-1.07	1559.64	65.00	3.12
1509.38	59.12	-0.18	1559.64	62.20	2.96
1509.38	59.45	0.56	1559.64	58.28	2.18
1509.40	60.01	1.23	1561.36	65.00	2.05
1509.40	58.87	0.90	1561.36	65.00	2.79
1510.96	55.13	-0.95	1561.36	65.00	3.42
1510.96	60.03	0.14	1561.36	62.29	3.77
1510.96	60.74	0.89	1561.36	51.34	3.36
1510.96	60.07	1.08	1563.08	62.90	1.76
1510.98	59.28	0.41	1563.08	65.00	2.58
1510.96	50.28	-1.06	1563.10	65.00	3.27
1512.54	59.68	0.04	1563.10	64.66	3.86
1512.54	61.43	0.81	1563.10	60.64	3.72
1512.56	61.57	1.54	1564.82	8.26	1.01
1512.56	60.57	1.15	1564.82	65.00	3.15

1514.16	52.26	-0.54	1564.82	65.00	3.88
1514.16	60.57	0.54	1564.82	63.82	4.17
1514.18	61.86	1.04	1564.82	16.38	2.90
1514.18	61.12	0.31	1566.56	7.36	1.39
1514.18	54.14	-1.33	1566.56	65.00	4.25
1515.80	55.35	0.31	1566.56	65.00	4.64
1515.82	62.80	1.33	1566.56	8.41	2.23
1515.82	63.38	2.36	1568.30	2.22	-0.77
1515.82	58.19	1.40	1568.30	65.00	3.38
1517.46	57.42	0.16	1568.30	65.00	4.13
1517.46	62.36	1.06	1519.52	7.31	0.09
1517.48	63.53	1.67	1519.52	47.72	0.36
1517.48	57.23	0.89	1570.04	65.00	3.43
1519.08	55.71	-0.92	1570.06	65.00	4.00
1519.10	62.25	-0.47	1521.12	49.73	-0.64
1519.10	62.05	0.10	1521.12	53.48	-1.16
1519.10	57.16	0.43	1571.80	54.61	4.03
1520.66	58.21	0.62	1522.76	50.03	0.87
1520.70	60.92	-0.85	1522.76	61.62	1.30
1475.12	3.06	-7.32	1573.56	10.11	1.73
1522.34	61.30	1.21	1573.58	2.63	0.59
1522.34	66.23	2.86	1524.38	59.28	2.14
1522.34	66.42	2.58	1524.40	45.64	-0.18
1523.96	52.69	0.02	1526.02	53.84	0.25
1523.98	65.27	2.43	1526.04	59.05	1.50
1524.00	66.81	3.33	1526.04	58.45	0.47
1523.98	11.46	-0.26	1527.66	61.31	-0.49
1525.60	62.50	1.83	1527.66	65.00	1.20
1525.60	67.61	2.77	1527.66	64.70	1.09
1525.60	61.94	1.55	1529.30	65.00	0.34
1527.24	60.35	2.08	1529.32	65.00	1.69
1527.24	67.53	3.91	1529.32	55.90	0.17
1501.44	57.12	-0.46	1552.78	62.64	0.09
1501.44	57.22	-0.45	1552.78	63.02	0.10
1501.44	57.33	-0.42	1552.78	62.92	0.09
1501.44	57.25	-0.44	1552.78	62.32	0.13
1501.44	57.13	-0.43	1552.78	63.27	0.12
1501.44	57.08	-0.42	1552.78	62.86	0.15
1501.44	57.40	-0.38	1552.78	62.11	0.15
1501.44	57.18	-0.38	1552.78	61.92	0.15
1501.44	57.39	-0.34	1552.78	59.97	0.16
1501.44	57.11	-0.30	1552.78	58.87	0.18
1501.44	57.44	-0.26	1552.78	56.86	0.19
1501.44	57.24	-0.24	1552.78	53.24	0.13

1501.44	57.20	-0.22	1551.08	63.55	1.88
1501.44	57.60	-0.20	1551.08	65.00	2.07
1501.44	57.57	-0.19	1551.10	65.00	2.35
1501.44	57.79	-0.21	1551.10	65.00	2.59
1501.44	57.69	-0.28	1551.10	65.00	2.83
1501.44	57.65	-0.37	1551.10	65.00	3.03
1501.46	57.75	-0.51	1551.10	65.00	3.20
1501.44	58.09	-0.69	1551.10	65.00	3.32
1501.44	57.54	-0.95	1551.10	65.00	3.37
1501.44	56.96	-1.46	1551.10	65.00	3.38
1501.44	54.56	-2.74	1551.10	65.00	3.31
1499.86	50.22	-2.32	1551.10	65.00	2.98
1499.86	55.31	-1.84	1551.12	57.86	-0.35
1499.88	55.56	-1.36	1549.44	9.21	-0.45
1499.88	55.69	-0.90	1549.44	57.98	0.54
1499.88	55.86	-0.54	1549.46	63.07	1.05
1499.88	56.36	-0.22	1549.46	65.00	1.47
1499.88	56.45	-0.02	1549.46	64.87	1.85
1499.88	57.18	0.04	1549.46	65.00	2.15
1499.88	57.15	-0.10	1549.46	65.00	2.37
1499.88	57.48	-0.46	1549.46	65.00	2.52
1499.88	55.32	-1.49	1549.46	65.00	2.48
1498.32	54.27	-2.02	1549.46	65.00	2.27
1498.32	54.60	-1.72	1549.46	65.00	1.37
1498.32	54.53	-1.27	1547.82	52.32	0.40
1498.32	54.35	-0.97	1547.82	64.72	1.01
1498.32	54.50	-0.52	1547.82	65.00	1.57
1498.34	55.15	-0.12	1547.82	65.00	1.99
1498.34	55.35	-0.48	1547.84	65.00	2.36
1498.32	55.19	-1.86	1547.84	65.00	2.46
1498.32	51.00	-3.86	1547.84	65.00	2.19
1496.80	51.25	-1.49	1547.82	65.00	1.11
1496.80	50.87	-0.92	1546.20	57.88	0.70
1496.80	50.95	-0.49	1546.20	65.00	1.39
1496.80	51.43	-0.19	1546.20	65.00	1.81
1496.80	52.48	-0.75	1546.20	65.00	2.05
1496.80	52.63	-2.66	1546.20	65.00	1.91
1495.30	50.43	-3.59	1546.20	65.00	1.19
1495.30	49.93	-2.72	1546.20	53.70	-0.32
1495.30	49.33	-2.15	1544.56	65.00	0.14
1495.30	48.34	-1.84	1544.56	65.00	0.97
1495.32	47.77	-2.19	1544.56	65.00	1.47
1495.32	47.69	-3.97	1544.56	65.00	1.34
1493.80	47.56	-5.10	1544.56	62.37	0.24

1493.80	46.04	-3.81	1542.92	63.20	-0.77
1493.82	42.86	-2.35	1542.92	65.00	0.03
1493.82	38.25	-1.82	1542.92	65.00	0.46
1493.82	43.82	-3.12	1542.94	64.76	0.34
1492.30	45.66	-3.60	1542.94	59.15	-0.67
1492.32	40.21	-3.31	1541.30	60.58	-1.47
1540.82	18.18	4.57	1541.32	65.00	-0.47
1540.82	23.36	5.26	1541.32	65.00	-0.19
1490.80	48.41	-2.64	1539.66	63.02	1.81
1490.82	56.08	-0.58	1539.66	65.00	3.26
1490.82	57.49	0.25	1539.68	63.87	-1.46
1539.20	21.09	4.56	1539.70	62.31	-0.22
1539.22	0.47	-2.79	1538.06	65.00	1.67
1489.32	54.91	0.76	1538.06	65.00	3.59
1489.32	55.52	1.12	1538.06	65.00	3.91
1489.32	53.87	-0.98	1538.08	57.62	-2.40
1487.82	46.02	-3.50	1536.44	65.00	1.52
1487.82	53.84	-2.46	1536.46	65.00	3.49
1487.82	51.13	-2.11	1536.46	65.00	3.93
1487.82	45.76	-3.04	1536.46	65.00	1.42
1486.32	47.79	-4.92	1534.84	65.00	0.93
1486.32	50.35	-3.01	1534.86	65.00	3.05
1534.36	0.17	-3.13	1534.86	65.00	2.97
1486.34	45.07	-3.90	1533.24	11.42	-1.43
1484.80	48.61	-4.86	1533.26	65.00	0.87
1484.80	51.27	-3.16	1533.26	65.00	1.90
1532.76	2.30	-2.10	1533.26	65.00	0.19
1532.74	2.70	-5.00	1531.64	65.00	-0.29
1483.28	47.24	-3.62	1531.66	65.00	0.83
1531.14	11.19	2.35	1531.66	65.00	0.31
1531.16	65.05	4.40	1530.04	60.86	-1.89
1531.16	64.85	4.21	1530.04	65.00	-0.25
1481.78	41.93	-4.80	1528.40	58.21	-1.30
1529.54	62.72	4.75	1528.42	65.00	1.22
1529.56	65.41	4.87	1528.44	65.00	-0.70
1527.94	51.13	0.62	1526.84	64.30	-0.04
1527.96	61.21	2.30	1526.84	65.00	2.57
1527.96	65.97	3.32	1526.86	59.48	-1.35
1527.96	58.28	2.47	1525.26	61.54	0.35
1526.38	60.27	2.19	1525.26	65.00	1.88
1526.38	61.66	2.54	1523.68	2.66	-4.49
1526.38	56.55	1.63	1523.68	56.51	2.73
1524.80	59.89	0.23	1523.70	65.00	2.57
1524.80	61.95	0.96	1522.10	4.79	-0.49

RIN measurement heater settings

Table 5.2: DLM's heater voltages applied to L1 when gain current is set to 170 mA

Wavelength (nm)	Output MZI-TC (V)	Ring1 (V)	Ring2 (V)
1492	15	6	8.3
1502	15	8	7.8
1512	15	6.8	3.4
1522	15	9.3	2.45
1532	15	2.5	8.85

Table 5.3: DLM's heater voltages applied to L2 when gain current is set to 100 mA

Wavelength (nm)	Output MZI-TC (V)	Ring1 (V)	Ring2 (V)
1522	15	1.8	10.1
1527	15	9.7	1.8
1532	15	2.9	8.8
1537	15	3.6	8.1
1542	15	2.3	6
1547	15	2.5	4.7
1552	15	3.5	3.2
1557	15	4.8	1.5
1562	15	8	5.4
1567	15	10	6.8
1541	15	2.3	6.3

Linewidth measurement heater settings

Table 5.4: DLM's heater voltages applied to L1 when gain current is set to 170 mA

Wavelength (nm)	Output MZI-TC (V)	Ring1 (V)	Ring2 (V)
1501	15	12.64	12.03
1503	15	7.6	7.3
1512	15	6.8	3.4
1522	15	9.3	2.45
1532	15	2.5	8.85
1492	15	6	8.3
1512	15	6.8	3.2

Table 5.5: DLM's heater voltages applied to L2when gain current is set to 100 mA

Wavelength (nm)	Output MZI-TC (V)	Ring1 (V)	Ring2 (V)	Cavity MZI-TC (V)
1522	15	1.8	10	0
1576	15	1.8	10	0
1527	15	9.6	1.8	0
1536	15	2.9	7.6	0
1538	15	3.6	7.6	0
1547	15	1.9	4.5	0
1557	15	4.7	2.3	0
1567	15	10	6.8	12
1518	15	7.5	0.1	3
1532	15	2.9	8.8	0
1542	15	2.3	6	0
1552	15	3.5	3.2	0
1562	15	8	5.4	0